SAND79-7095
Unlimited Release
UC-94d

Microstructure and Hydriding Studies of AB_5 Hydrogen Storage Compounds

MASTER

P. D. Goodell, G. D. Sandrock, E. L. Huston
International Nickel Co., Inc.

Prepared by Sandia Laboratories, Albuquerque, New Mexico 87185 and Livermore, California 94550 for the United States Department of Energy under Contract DE-AC04-76DP00789

Printed January 1980

Sandia National Laboratories

SF 2900-Q(3-80)

DISTRIBUTION OF THIS DOCUMENT IS UNLIMITED

Issued by Sandia Laboratories, operated for the United States Department of Energy by Sandia Corporation.

NOTICE

This report was prepared as an account of work sponsored by the United States Government. Neither the United States nor the Department of Energy, nor any of their employees, nor any of their contractors, subcontractors, or their employees, makes any warranty, express or implied, or assumes any legal liability or responsibility for the accuracy, completeness or usefulness of any information, apparatus, product or process disclosed, or represents that its use would not infringe privately owned rights.

Printed in the United States of America

Available from
National Technical Information Service
U. S. Department of Commerce
5285 Port Royal Road
Springfield, VA 22161

Price: Printed Copy $ 6.75; Microfiche $3.00

DISCLAIMER

This report was prepared as an account of work sponsored by an agency of the United States Government. Neither the United States Government nor any agency Thereof, nor any of their employees, makes any warranty, express or implied, or assumes any legal liability or responsibility for the accuracy, completeness, or usefulness of any information, apparatus, product, or process disclosed, or represents that its use would not infringe privately owned rights. Reference herein to any specific commercial product, process, or service by trade name, trademark, manufacturer, or otherwise does not necessarily constitute or imply its endorsement, recommendation, or favoring by the United States Government or any agency thereof. The views and opinions of authors expressed herein do not necessarily state or reflect those of the United States Government or any agency thereof.

DISCLAIMER

Portions of this document may be illegible in electronic image products. Images are produced from the best available original document.

SAND79-7095 UC-94d

Unlimited Distribution

Printed January 1980

MICROSTRUCTURE AND HYDRIDING STUDIES OF AB_5 HYDROGEN STORAGE COMPOUNDS

by

P. D. Goodell, G. D. Sandrock, and E. L. Huston

International Nickel Co., Inc.
INCO Research and Development Center
Sterling Forest
Suffern, New York
10901

Prepared for

SANDIA LABORATORIES
ALBUQUERQUE, NEW MEXICO
87185

under Contract 13-0524

FINAL REPORT

DISCLAIMER

Th s book was prepared as an account of work sponsored by an agency of the Un ted States Government Ne ther the United States Government nor any agency thereof nor any of their employees makes any warranty express or mpl ed or assumes any legal liab l ty or responsibil ty for the accuracy completeness or usefulness of any information apparatus product or process d sclosed or represents that ts use would not infr nge pr vately owned r ghts Reference herein to any spec fic commercial product process or service by trade name trademark manufacturer or otherw se does not necessar y constitute or mply its endorsement recommendation or favor ng by the United States Government or any agency thereof The views and op n ons of authors expressed herein do not necessar ly state or reflect those of the United States Government or any agency thereof

DISTRIBUTION OF THIS DOCUMENT IS UNLIMITED

FOREWORD

This report summarizes the results by Drs. P. D. Goodell, G. D. Sandrock and E. L. Huston of the International Nickel Co., Inc. (INCO). It contains new data on the microstructure, pressure-composition-temperature, and absorption/desorption kenetics of AB_5 metal hydrides. The most significant result to emerge from the investigation is that many of the AB_5 metal hydrides, especially the $LaNi_5$ related materials, show instantaneous absorption and desorption response in proportion to the amount of cooling or heating which is provided. The data are very timely because of current interest in using metal hydrides for energy conversion, energy storage, and for heating and air conditioning. The kinetic data are extremely valuable for use in the sizing of heat exchange equipment due to a scarcity of information of this sort.

The work was performed under contract to Sandia Laboratories as a joint venture between Sandia and the International Nickel Co. with each sharing a portion of the cost. It was agreed at the start of the contract that the results of the work would be published as a Sandia document to provide a means of placing contractually private information in the public domain.

Sandia initiated this contract as a result of early observations made in the development of a water pump which used solar energy as the power source. The use of metal hydrides as the energy converter seemed feasible because it was known that: (1) Metal hydrides have a large storage capacity for hydrogen; (2) many metal hydrides are stable at room temperature and at hydrogen overpressures ranging from subatmospheric to several atmospheres; (3) the pressure of hydrogen gas in equilibrium with the metal hydride increases exponentially with increasing temperature in a manner analogous to the change of vapor pressure of a liquid with increasing temperature; and (4) the pressure change with temperature for some metal hydrides was greater than the pressure change for liquid Freons in equilibrium with its saturated vapor, consequently, a modest temperature change of 60°C or so was capable of producing enough pressure change to perform the pumping work.

Apparent obstacles to the successful development of the pump and the areas where we needed assistance were: (1) Kinetics of hydrogen absorption were slow; (2) the metal hydride was easily poisoned by contaminants; and (3) alloy life was possibly limited to a few cycles.

It was learned through experimentation that the diffusion of water through a flexible membrane was poisoning the metal hydride and nearly stopping hydrogen absorption. The problem was resolved through Dr. C. J. M. Northrup, Jr. in consultation with INCO personnel. They recommended changing the metal hydride from $CaNi_5$ to a $LaNi_5$ based material that was less sensitive to poisoning and had a greater hydrogen capacity, changing the flexible membrane to a less permeable one, and inserting a water vapor trap in the connecting line. The change in the operational behavior of the pump was spectacular.

The INCO study and pumping experiments agreed when it was reported that within the sensitivity of the measuring apparatus the absorption/desorption kinetics of $LaNi_5$ metal hydride were limited only by the rate of heat transfer into or out of the sample. It was also empirically observed that a bed of $LaNi_{4.7}Al_{0.3}$ hydride survived several thousand cycles without apparent changes in absorption rate

or hydrogen capacity. It was inductively reasoned that an extended lifetime of many thousands of cycles could be expected. The major obstacles to the use of metal hydrides were therefore overcome.

The idea of using metal hydrides as the power conversion device in a heat engine is relatively new. The feasiblity of the concept has been demonstrated with the operation of the solar/hydride engine. A few minor problems may remain to be solved before commercial development proceeds. However, if a need for the items exists, then hardware will surely follow.

A. A. Heckes
Technical Staff Member
Sandia Laboratories

INTENTIONALLY LEFT BLANK

CONTENTS

	Page
INTRODUCTION	
RESEARCH PROGRAM	9
General Approach	9
Compositions Studied	10
Sample Preparation	10
Metallography	11
Static Pressure-Composition Isotherms	[illegible]
Dynamic Test Set-Up	12
Dynamic Pressure-Composition Isotherms	13
Kinetic Tests	13
Comparisons of Kinetic Data	15
Presentation of the Data	16
RESULTS AND DISCUSSION	16
Category 0 - Reference Alloys	16
$LaNi_5$	16
$LaNi_{4.9}Al_{0.1}$	17
$LaNi_3Co_2$	19
Category 1 - Ni Second Phase Particles	20
$LaNi_{5.67}$	20
$LaNi_7$	21
$LaNi_{11.3}$	21
Category 2 - Eutectoid Microstructure	22
$SmCo_5$	22
Category 3 - Other Second Phases	23
$LaNi_{3.8}Fe_{1.2}$	23
$LaNi_{3.5}Cr_{1.5}$	24
$LaNi_4Cr$	24
$LaNi_4Si$	24
$LaNi_4Sn$	24
MNi_4Sn	25
$MNi_{4.3}Al_{0.7}$	25
Category 4 - Substitutional Elements	26
$LaNi_4Cu$	26
$LaNi_{4.5}Pd_{0.5}$	26
$LaNi_{4.7}Sn_{0.3}$	27
$LaNi_{4.8}C_{0.2}$	28
$MNi_{4.3}Mn_{0.7}$	28
Category 5 - Surface Active Elements	29
$LaNi_{4.8}B_{0.2}$	29
$LaNi_{4.9}S_{0.1}$	29
$LaNi_{4.9}Se_{0.1}$	30
Category 6 - Large Diameter Atom Substitutions	30
$Mg_{0.1}La_{0.9}Ni_5$	30
$Ca_{0.2}La_{0.8}Ni_5$	31
$Sr_{0.2}La_{0.8}Ni_5$	31
$Ba_{0.2}La_{0.8}Ni_5$	32
Category 7 - Other Compositions	33
$LaNi_3$	33
Category 8 - Pd Plating	34
Electroless Plated Samples	34
Mechanically Alloyed Specimens	34
COMPARISONS AND CONCLUSIONS	35
Category 0 - Reference Alloys	36
Category 1-6 - Experimental Compositions	37
CONCLUDING REMARKS	39
REFERENCES	40
TABLES	42
FIGURES	48
APPENDIX A: SYSTEM THERMAL EFFECTS	170

INTENTIONALLY LEFT BLANK

INTRODUCTION

Work at Sandia-Albuquerque has resulted in the invention of a number of solar-powered water pumps using metal hydride beds as thermal compressors. As with a number of other concepts that use rechargeable metal hydrides, the following general properties are desired for the hydrides used in the water pumps:

1. Good kinetics, especially the kinetics of charging (or discharging) at low overpressure (or underpressure).
2. High reversible capacity (H/M).
3. Resistance to poisoning, especially from air, water vapor, and various foreign substances (e.g., oil) inherent with common low-cost construction materials.
4. Ability to tailor the PTC (pressure-temperature-composition) relationships to suit particular design requirements (i.e., available solar collector temperature, well depth, and desired output pressure).
5. Easy activation.
6. Flat plateaus.
7. Low hysteresis.
8. Good stability (chemical and mechanical).
9. Low cost.
10. Good reproducibility (i.e., low sensitivity to common production variables).

There must be trade-offs. The best of all properties probably cannot be achieved simultaneously.

It is the purpose of this brief experimental study to survey several new compositions that may be useful for the Sandia hydride water pump. The survey is directed particularly toward dynamic properties (e.g., kinetics), with support work in the area of static PTC properties (capacity, plateau pressures, and hysteresis). In particular, we will attempt to correlate microstructural factors with hydriding behavior.

RESEARCH PROGRAM

General Approach

By mutual agreement, we have decided to concentrate initially on the AB_5 compounds. As a class, the AB_5s seem to have a good combination of high kinetics and poisoning resistance. Although a number of AB_5 compounds have been studied for basic PTC behavior, there is a general lack of quantitative data on kinetics. In addition, most studies have been done on single phase alloys which may not have the best kinetics.

Hydride reaction kinetics, as for any heterogeneous reaction, may be determined by a variety of mechanisms or combinations of steps. Detailed mechanistic analysis, however, is beyond the scope of the present effort. Yet, for practical purposes, the kinetics of hydriding is likely to be most influenced by three factors: (1) heat transfer, (2) surface reactions, and (3) diffusion through the hydride layer. Heat transfer is basically a matter of container engineering and will not be directly considered in this program. Our main efforts were directed toward surface reaction and diffusion behavior. Surface reactions include the adsorption of H_2 molecules, the dissociation reaction $H_2 \rightarrow 2H$, the migration of H atoms on the surface and finally the nucleation of the hydride phase. Once a metal particle has been encased by a growing hydride envelope, these same reactions must be involved with the additional factor of diffusion through the hydride layer. Each of these steps should be broadly sensitive to microstructure, bulk chemistry, and surface chemistry. Thus the approach of this program was to study a series of AB_5 type alloys prepared with microstructural and chemical variations which might improve surface reactions or hydrogen diffusion. The immediate objectives were to (1) achieve more rapid reaction kinetics, and (2) to determine the effect of such variations on the basic static PTC properties most often used to characterize and select hydriding alloys.

Compositions Studied

Thirty-two compositions were made which fell under nine general categories. The categories and aim compositions are shown in Table I. The reasons for selecting the compositions are better discussed during the presentation of the results later. It should be realized, of course, that many of the compositions listed in Table I do not necessarily fit under a single category as shown. For example, many of the ternary elements that result in second phases (Category 3) also have some substitutional solubility in the main AB_5 phase and could also be included in Category 4. Similarly, as will be shown, the Mg, Sr, and Ba large diameter atom substitutions (Category 6) result in substantial quantities of second phases and could also be placed in Category 3. The grouping we have used in Table I is meant to be a compromise between the intent of the experiments and the actual microstructural results obtained.

All of the compositions shown in Table I were examined metallographically. Twenty-one samples (marked with an asterisk in Table I) were selected for hydriding evaluations, both equilibrium (static) P-C and dynamic.

Sample Preparation

With the exception of the $LaNi_{4.5}Pd_{0.5}$ sample, all materials were made by vacuum induction melting in an Al_2O_3 crucible. Heat sizes ranged from 6-20 kg. Although most of

the melting was carried out under full vacuum (10-20 x 10^{-3} torr), the volatile ternary additions (specifically S, Se, Sm, Mg, Ca, Sr, and Ba) were added under a 0.5 atmosphere pressure of argon just before pouring. Melts were cast into 11 cm. diameter ingots using graphite molds. Because of the high cost of Pd, the $LaNi_{4.5}Pd_{0.5}$ sample was made in the form of a 50 g argon-arc-melted button. All heats were chemically analyzed and the results are tabulated in Table II.

Many of the samples were evaluated in the as-cast condition. Some were evaluated in a heat treated condition, as will be discussed in the appropriate context during the presentation of the data. Most samples were readily crushable. Prior to hydriding small samples were crushed in air to about 10 mesh.

Attempts were made to Pd-plate 2 samples each of activated $LaNi_5$ and $LaNi_{4.9}Al_{0.1}$. One technique used was electroless deposition (1,2). A Pd solution was made from the trans-diamminedichloro-palladium (II) salt dissolved in ammonium hydroxide and stabilized with the disodium salt of EDTA. The solution was diluted to achieve a theoretical thickness of 50Å on the 0.2 m^2/g sample surfaces (1.2 wt.% Pd). 50 grams of activated sample (cycled 4 times and dehydrided) were transferred from the hydriding reactor in an argon atmosphere and stirred into the solution at about 50°C. A solution of 0.1M hydrazine dihydrochloride was slowly added which resulted in the reduction of the Pd and its spontaneous deposition directly on the surface of the metal powder. After plating the samples were thoroughly washed in distilled water followed by acetone, vacuum dried, and then exposed to the air.

The second plating technique tried was mechanical alloying. Mechanical alloying is a high energy ball milling technique(3). Our intent was to physically smear ductile Pd on the surfaces of the powder sample. The following charge was loaded into a 3.8 cm. diameter x 5.7 cm. deep spex mill under argon.

1. 12.0 g activated sample (cycled 4 times and dehydrided).
2. 0.144 g of -325 mesh Pd powder.
3. 120 g of 3.2 mm diameter 52100 steel balls.

The charge was milled (vigorously shook) for 5 minutes and the sample removed in air.

Metallography

All compositions were examined metallographically. Samples were mounted in epoxy and polished in a conventional manner using kerosene or water based slurries of silicon carbide, diamond, and alumina. Merica's etch (50-50 nitric-acetic) was used. Photographs were taken on a Leitz MMG metallograph. Selected samples were examined on an ARL electron microprobe analyzer for phase identification. Pd plated samples were examined on a Cambridge S-180 scanning electron microscope.

Static Pressure Composition Isotherms

Static 25°C absorption and desorption isotherms were obtained for most of those samples marked with an asterisk in Table I. These were obtained volumetrically on our Seiverts apparatus, a fairly conventional state of the art unit. In general, the pressure range of about 0.1-68 atmospheres was used. Linde ultra high purity hydrogen (99.999 + %) was used. The sample was activated and cycled a few times before running. Specimen temperature was maintained with a constant temperature water bath around the specimen holder, controlled at 25.0°C ± 0.1°C. Hydrogen was introduced or extracted on a discrete aliquot by aliquot basis (as opposed to the dynamic procedures outlined in the next section). Approximately 8 hours were used to develop each isotherm, insuring thermal equilibrium at each point. The low pressure offset was obtained by heating the samples to 100°C and extracting hydrogen until the pressure was less than about 4 torr (0.005 atm). The static data gives information on plateau pressure, plateau slope, plateau width, hysteresis, and H-capacity. Definitions of these terms are shown in Figure 1.

Dynamic Test Set-Up

Dynamic pressure-composition isotherms and kinetic response were determined using the IRDC, cyclic-contamination-absorption-desorption (CCAD) test apparatus. This equipment allows volumetric determination of hydrogen transfer between the sample in its reaction chamber, and gas supply or take-up chambers. The transfer conditions may be varied to provide: (1) controlled flow rate, or (2) constant reaction pressure. The unit may be cycled repetitively by time programming of automatic valves. The hydrogen transfer is monitored continuously by measurement of the pressure in each of the three chambers which are of known volume and temperature. The pressures and sample temperatures are recorded on a four-pen strip chart recorder. Hydrogen mass transfer is determined from these records after corrections are made for gas nonideality and gas temperature transients, especially in the gas supply chamber.

The sample reactor used for dynamic testing is shown in Figure 2 and several thermal parameters of the system are discussed in Appendix A. The reactor is based on a thin disc sample configuration (0.15 cm. thick x 4.3 cm. dia.) which is in contact with a copper plate (platinum plated to prevent oxygen pick-up). This design provides rapid heat transfer and relatively straightforward thermal modeling. It was selected to enhance detection of kinetic response related specifically to alloy characteristics. In other reactor designs, kinetics can be dominated by slow heat transfer of the system and thereby mask differences in alloy behavior.

The temperature of the sample was measured using an ultra fast response thermocouple located at the mid-thickness of the powder bed. The thermocouple was a grounded junction, chromel-alumel type packed in MgO in a 0.0254 cm. (0.010 in.) diameter, stainless steel sheath. This unit has a response time factor of 0.3 seconds and appears to be the most rapid response device practical for inclusion within the powder sample bed. The experimental results confirmed that this thermocouple is adequate for tracking the response at the reaction rates achieved in the thin disc sample holder (see Appendix A).

Samples for dynamic testing were crushed to between 30 and 80 mesh powder sizes and activated in the reactor. Samples of 8.0 g were used throughout. Activation was performed using an automatic cyclic program on the CCAD apparatus. The charging phase of the cycle was at 20 atm. hydrogen pressure for 15 minutes; discharging was also for 15 minutes. By this procedure, samples could be activated overnight with between 20 to 30 absorption/desorption cycles accumulated prior to testing. This procedure was intended to provide optimum particle breakdown and a subsequently stable powder condition. Additionally, the number of cycles required to achieve at least 90 percent of full charge capability was taken as a semi-quantitative indication of activation ease of the alloy.

Dynamic Pressure-Composition Isotherms

Following activation, pressure-composition isotherms were determined dynamically by using the controlled flow rate hydrogen transfer mode of operation of the CCAD apparatus. The flow rate employed for these tests was 0.0027 g-atoms hydrogen per minute. For the typical 8.0 g sample, this allows characterization of the plateau region of the P-C isotherm in 60 to 70 minutes. The reaction heating or cooling changes the initial sample temperature by 0.3 to 0.4°C and is constant over the plateau. The development of the dynamic P-C isotherms provides a comparison to the static test results and identifies specific pressures to be used in the kinetic tests.

Kinetic Tests

Kinetic tests were performed using the constant pressure hydrogen transfer mode of operation of the CCAD apparatus. Samples were stabilized at a predetermined starting pressure. The sample reactor was then opened to the supply (or take-up) reservoir through a pressure regulator preset at the desired test pressure.

The initial condition for each heat was a pressure just below (or above) the absorption (or desorption) plateau. This minimizes effects due to solid solution reactions but allows reasonably rapid attainment of a stable and reproducible

initial pressure and composition. In practice, the starting pressures and compositions corresponded closely to values defined by the average between the absorption and desorption plateau and are represented by P_1 and P_2 in Figure 1. For the final or test pressure, several levels were evaluated for each alloy. These included pressures corresponding to: (1) the midpoint of the plateau, (2) the end of the plateau, and (3) several increasingly greater (or lower) pressures past the plateau.

As the reaction proceeds after the pressure change is made, the sample temperature changes due to reaction heating (or cooling) . The sample holder, even though of rapid heat transfer design, does not assure true isothermal conditions. The sample temperature, which can be tracked almost instantaneously by the fast response thermocouple, is a useful indicator of the reaction process. This is especially true when heat transfer does not completely dominate reaction kinetics. In this case, the temperature response of the samples should be a function of the reaction rate. The temperature-time profile should approximate the derivative of the reaction-time profile and thus provide additional resolution of alloy differences.

The mass transfer and thermal responses for each test run were recorded as a function of time. Corrections, as required, were made for nonideality and reservoir temperature changes. The resulting time response curves are included in the discussion of the individual alloys. From such curves several types of data were extracted for further correlations. These include time, rate and temperature parameters and are defined in the schematic illustration given in Figure 3.

The time and rate correlation parameters defined in Figure 2 were taken at reaction levels of 0.0 (rate only), 0.05, and 0.08 g-mole hydrogen. For typical samples having H/M ratios near unity, these levels represent slightly less than 50 and 80 percent completion of the reaction. Of these, the time to 0.05 g-mole reacted was taken as the principle parameter to be used for comparison of alloy modifications.

Thermal parameters include the time, t^*, magnitude, T^*, and reaction rate, $\mathring{n}^*$, at the peak temperature deviation. The magnitude, T^*, can be compared to T_{vh}, the Van't Hoff temperature characteristic of the test pressure, and to the nominal (bath) temperature, T_n. For this purpose the ratio $R=(T^*-T_n)/(T_{vh}-T_n)$ is defined at $P=2P_a$. This provides an indication of the relative degree of thermal control of the reaction. For true isothermal conditions, R=0, and intrinsic sample kinetics are represented; if the Van't Hoff temperature is reached, the kinetics are thermally dominated and R=1. Additionally, the reaction rate and temperature data can be used to characterize the thermal properties of both the sample holder and the sample powder bed. This is presented in Appendix A.

Comparisons of Kinetic Data

Several types of comparisons of alloy hydriding kinetics can be developed from the experimental data. "Reduced" and "absolute" pressure correlations are of particular interest. The reduced pressure is taken as the ratio of the test pressure to the plateau pressure. To a rough approximation it can be used as the basis for showing changes in intrinsic kinetics resulting from alloy modification. On the other hand, correlations based on the absolute test pressures reflect the combined effect of changes in intrinsic kinetics and in the reaction plateau pressure. In fact, comparisons based on both types of correlations should be useful with respect to alloy design and alloy reflection for specific applications. To facilitate both types of comparisons, the kinetic data for each alloy is presented as a function of the absolute pressure on a logarithmic scale. Comparisons based on absolute pressure can be made directly from this format. Additionally, the superposition of absolute pressure correlations in such a manner that the plateau pressures are coincident, provides comparison based on reduced pressure. The plateau pressure used to define reduced pressure is taken throughout as the reaction pressure at 0.5 H/M.

Another aspect of the kinetic data correlations involves use of a fixed mass of reactant (0.05 g-atoms) as the basis for comparing alloys, irrespective of differences in their total capacity. This procedure may shift the apparent kinetics in relation to treatments based on fraction of total reaction, (a basis which may in fact be more appropriate for mechanistic evaluations). However, the fixed mass approach was maintained throughout since for most applications, it is the kinetics relative to reaction mass not fraction which is important.

Finally, it should be reiterated that the interpretation of kinetic data must be considered in relation to the nature of the experiments. It may be difficult to separate the influence on reaction kinetics of material and thermal characteristics. The nature of rate controlling mechanisms and the magnitude of the instantaneous driving force may be obscured by the non-isothermal conditions. These are recurring problems in the study of practical kinetics of rapid heterogeneous reactions. Typical functional relations expressing time, pressure, and temperature dependencies which often suggests specific rate controlling steps, may not be appropriate for that purpose and the present conditions. They may nevertheless be instructive as to alloy differences though further experimental work and reaction modeling would be required to support any mechanistic inferences. It should also be recognized that the experiments do not simulate particular application operating conditions and should not be so interpreted. Rather, the kinetic experiments are intended to rank alloy behavior on a comparative basis and illustrate trends of kinetic behavior which could be generally useful in application considerations.

Presentation of the Data

The data will be presented on a section by section, alloy by alloy basis in the order shown in Table I. Nominal stoichiometries will be mostly used in the text and figures. Microstructures will be described, followed by static and dynamic hydriding data for each alloy, if obtained. Finally, alloy to alloy comparisons will be made near the end of the report. Figure numbers will carry the general designation i-j-k, where i is category number, j is the alloy number in that category, and k is the figure number within the series for that alloy.

RESULTS AND DISCUSSION

Category 0 - Reference Alloys

The three reference compositions are (or have been) used in Sandia prototype pumps. Therefore, we were requested to obtain somewhat rather detailed data for these for possible design and performance correlation purposes. The equilibrium data for three reference alloys, nominally $LaNi_5$, $LaNi_{4.9}Al_{0.1}$, and $LaNi_3Co_2$ have been published and were selected to give three distinct plateau pressures. Dynamic tests of these three reference alloys were run in both absorption and desorption modes at each of three or four temperatures. These tests provide extensive characterization of reaction kinetics. They also provide a framework for comparison of the results from other alloys for which testing was necessarily more limited in scope.

$LaNi_5$

The heat prepared has nearly perfect analyzed chemistry. The microstructure, shown in Figure 0-1-1, is exceptionally clean. The few small second phase particles present are probably oxides. The static absorption/desorption isotherms, Figure 0-1-2, show all the characteristics of classic $LaNi_5$ hydride: appropriate plateau pressures, moderate hysteresis, flat plateaus, and good capacity ($H/M_{max}>1$):

The dynamic absorption and desorption isotherms for this heat are given in Figures 0-1-3 and-4 at four temperatures. Comparing these with Figure 0-1-2 shows that the absorption pressures are higher and the desorption pressures lower in the dynamic tests than in the static; the deviation is more pronounced on the absorption side. As a result hysteresis, as defined by $ln(P_a/P_d)$, is 0.43 at 25°C in the dynamic test and only 0.19 in the static tests. Otherwise, the general features of the isotherms are similar. Also, the heat of reaction indicated from the dynamic plateau pressures at 0.5 H/M is 7.6 kcal/g-mole (1.82 KJ/g-mole) which is comparable to values in the literature from static test data.

Typical isobaric kinetic test results at 25°C are presented in Figures 0-1-5, -6, and -7. The values of various kinetic parameters derived from these tests are summarized in Figures 0-1-8 through 0-1-15 for each of the four test temperatures. Comparison of these figures shows that the reaction rate (or time) at any given pressure is a strong function of the nominal temperature. Moreover, the reaction appears to be quite rapid; at a nominal temperature of 25°C, nearly full charging (or discharging) can be accomplished in about 3 minutes at twice (half) the plateau pressure.

It is also evident that the instantaneous temperature varies considerably from the nominal during the reaction. The peak temperature parameters (time and rate) closely track the other reaction parameters, suggesting similar types of relations between all the reacting parameters and the experimental variables. Moreover, in each case, the peak temperature corresponds to the Van't Hoff temperature for the pressure of the test. This is the temperature limit for the reaction and reaction rate, therefore, is determined primarily by the rate of heat transfer of the system (i.e., R=1).

Comparisons of kinetics on a "reduced" pressure basis, i.e., relative to the plateau pressures are shown in Figures 0-1-16 and -17 (only the 0.05 g-mole reacted parameters are shown). These comparisons indicate little or no real dependence of kinetics on the independently varied experimental parameters of temperature or pressure ratio (driving force). This follows directly from the fact that the reaction is so rapid that the system thermal response dominates the kinetics.

These kinetic data, therefore, do not represent the intrinsic kinetics of $LaNi_5$. However, since the system is of high heat transfer design, the results probably represent close to the maximum practically attainable kinetics.

$LaNi_{4.9}Al_{0.1}$

The actual composition of this heat was very close to the nominal. In order to produce as flat a plateau as possible, this alloy was annealed for 4 hours at 1125°C (in argon). The microstructure, shown in Figure 0-2-1, is predominantly the AB_5 phase $La(Ni,Al)_5$ with a small amount of a second phase. This phase was not specifically identified, but in analogy with the mischmetal-nickel-aluminum system(4), it is most likely NiAl. The 25°C static isotherms are shown in Figure 0-2-2. The plateau pressures are somewhat below those of $LaNi_5$, consistent with the literature on Al substitution(5,6). As in the M-Ni system (4), Al-substitution seems to significantly reduce hysteresis in the La-Ni system. The capacity of $LaNi_{4.9}Al_{0.1}$ is comparable to that of $LaNi_5$.

Dynamic absorption and desorption isotherms for this heat are given in Figures 0-2-3 and -4 for three temperatures. These isotherms indicate slightly greater hysteresis in the dynamic test mode than in the static tests. Additionally, the absorption isotherms show a slight over-pressure requirement at the onset of hydriding. The origin of this "onset-overpressure" is not clear, however, it may be speculated as being related to either of two types of phenomenon. One possibility is that it represents a surface barrier such as an oxide film which must be broken down. This would suggest the subtle early stages of poisoning even though UHP H_2 was used throughout. Alternatively, and more likely, the onset-overpressure may be related to nucleation of the hydride phase. In this case, the solid solution phase supersaturates until interfacial and/or strain energy barriers to solid state phase transformation are overcome. For whatever reason, the magnitude of the over-pressure appears dependent on temperature and reaction speed (also alloy composition) and warrants further study.

Isobaric kinetic test results (25°C only) for the $LaNi_{4.9}Al_{0.1}$ alloy are presented in Figures 0-2-5, -6, and -7. These differ from those for $LaNi_5$ in that an S-shape, or incubation type response is evident in absorption. This may be related to the onset-overpressure phenomenon observed in the absorption isotherms.

The various kinetic parameters derived from the time-response curves are summarized in Figures 0-2-8 through 0-2-13. The incubation type effect on absorption is seen in these figures in that the initial reaction rate, $\dot{n}_0$, is less than the reaction rate later in the reaction (e.g., $\dot{n}_{0.05}$); no such effect is observed on desorption. The reaction rates shown for the $LaNi_{4.9}Al_{0.1}$ alloy are slightly slower than those for $LaNi_5$, especially at the lower temperatures. Indeed, the reaction rates do not exceed completely the capacity of the system for reaction heat removal (or supply). This is indicated since the Van't Hoff temperatures are not reached (except for absorption at 45°C). The thermal contribution parameter, R, varies from 0.7 at 25°C to 1.0 at 45°C. Even greater deviation from thermal control are evident from the desorption data; this is because the heat transfer capability of the system is lower under some desorption conditions than it is for absorption (see Appendix A).

Comparisons of the 0.05 g-atom reaction times and rate on a reduced pressure basis are presented in Figures 0-2-14 and -15. These comparisons indicate a more significant temperature effect for both the absorption and desorption reactions than was evident from the $LaNi_5$ data. This is in part a consequence of the generally slower reaction rates of $LaNi_{4.9}Al_{0.1}$ allowing material properties to be more evident. Nevertheless, the reaction kinetics represented by this data reflect combined and varying effects of system heat transfer and intrinsic material response.

$LaNi_3Co_2$

The analyzed composition of this final reference heat again was very close to the aim point. Metallographic examination of an as-cast sample showed some segregation within the essentially single AB_5 phase, so a homogenization annealing treatment (24 hours at 1175°C) was done to give as flat a p[illegible] possible. The micros[illegible] of annealed $LaNi_3Co_2$ is shown in Figure 0-3-1. The material is virtually single phase with a trace (<1%) of a second phase, probably oxide. The static absorption and desorption isotherms, shown in Figure 0-3-2, are very consistent with prior published data on the $LaNi_{5-X}Co_X$ system(7). The plateau is limited to H/M = 0.6, above which there is a long sloping rise in the curves (in effect a substantial H-solubility in the β hydride phase). Plateau pressures are almost an order of magnitude lower than $LaNi_5$ and the plateaus are slightly sloping. Hysteresis is small.

The dynamic absorption and desorption isotherms for this heat are given in Figures 0-3-3 and -4. The dynamic absorption isotherm pressures at 25°C are somewhat higher than for the static pressures; the desorption pressures are similar. Other characteristics are also similar for both the static and dynamic test modes.

Isobaric kinetic absorption test results (at 25°C) are given in Figure 0-3-5 and -6. These results suggest an incubation type response, at least for the higher pressure differential tests. Only limited desorption testing was possible for this alloy due to the very low plateau pressures; one curve is presented in Figure 0-3-7.

The kinetic absorption parameters are summarized in Figures 0-3-8, -9, and -10. By comparison with the $LaNi_5$ and $LaNi_{4.9}Al_{0.1}$ alloy data, the $LaNi_3Co_2$ results show very good absorption rates on an absolute pressure basis. This is primarily a consequence of the low plateau pressure. In contrast, however, comparison on the basis of reduced pressures indicate that, in fact, the intrinsic absorption kinetics of $LaNi_3Co_2$ are much slower than those of the other two reference alloys. It is not surprising, therefore, that the instantaneous excursions from the nominal temperature are not as great as for the other reference alloys. The thermal contribution parameter, R, varies from 0.6 at 45°C down to 0.3 at 25°C. Thus the $LaNi_3Co_2$ data more closely (but not completely) represent the intrinsic dynamic response of the material than does the data for $LaNi_5$ and $LaNi_{4.9}Al_{0.1}$.

Kinetic desorption tests could be run at only one pressure at each temperature. The 0.05 g-atom reaction times and rates for these tests are shown in Figure 0-3-11. From these results and the plateau data, an attempt has been made to

estimate the possible response at other pressures. This was done only to provide some basis for comparisons. It appears, however, that the desorption reaction can be characterized as slow in both absolute and relative terms.

Despite the intrinsically slow response of the $LaNi_3Co_2$ alloy, it appears likely to be a general useful alloy. This is because on an absolute pressure basis, the absorption rates are comparatively fast at each of the temperatures tested.

Category 1 - Ni Second Phase Particles

It is generally agreed that H_2 dissociation ($H_2 \rightarrow 2H$) is a necessary reaction that must occur on the surface of a hydrogen storage compound before the H atoms enter the metal lattice to form a hydride. Ni is an excellent hydrogen dissociation catalyst. This may be the main reason only AB_5 compounds (e.g., $LaNi_5$) have such high kinetics. The following question is then suggested: Would some free Ni particles in the microstructure be even more effective than the Ni bound in the intermetallic (AB_5) phase in catalyzing the dissociation reaction and thereby increasing kinetics?

As shown by the La-Ni phase diagram(8), Figure 1-0-1, there are two obvious ways to create second phase Ni in a $LaNi_5$ matrix. First, because the $LaNi_5$ phase field has width at high temperature but none at low temperature, it should be possible to make a slightly Ni-rich sample (we tried 85.0 wt.% Ni = $LaNi_{5.67}$), solution treat it at some high temperature ($\sim$1270°C), and then age it at a lower temperature (say 1000°C) to produce a Ni dispersion by precipitation from solid solution. The second way is to make even more Ni-rich melts to allow formation of eutectic $LaNi_5$+Ni directly on solidification. Aim compositions tried in the latter approach were $LaNi_7$ (87.5 wt.% Ni), midway between $LaNi_5$ and the eutectic point, and $LaNi_{11.5}$ (92 wt.% Ni), the eutectic composition.

$LaNi_{5.67}$

This heat, designed for the solid state precipitation trials, is close to the aim composition. Microstructures for the as-cast, solution-treated, and aged conditions are shown in Figure 1-1-1. Also shown are saturation magnetic moment measurements and calculated free nickel contents estimated from these measurements (using 54.4 emu/g as the accepted moment for pure Ni). The as-cast structure (Figure 1-1-1a) is predominantly $LaNi_5$ with a small amount of free Ni (3.6 wt.% by magnetic estimates). Solution treating at 1260°C for 24 hours (Figure 1-1-1b) reduced the amount of free Ni to 0.8 wt.%. Finally, following this solution treatment by a 24 hour age at 1000°C (Figure 1-1-1c) results in substantial intergranular and intragranular Ni precipitation (to a level of 11.9 wt.%). In summary, the results are entirely consistent with the published La-Ni phase diagram (Figure 1-0-1).

The solution-treated plus aged sample (Figure 1-1-1c) was selected for hydriding evaluation. The static 25°C isotherms are shown in Figure 1-1-2. Plateaus are fairly flat and hysteresis is comparable to single phase $LaNi_5$. Plateau pressures are slightly higher than $LaNi_5$. Because the free Ni does not hydride, the capacity of aged $LaNi_{5.67}$ is lower than single phase $LaNi_5$. The 15% reduction in capacity below that of $LaNi_5$ is in reasonable agreement with the 12% free Ni estimated from the magnetic measurement.

The dynamic 25°C absorption isotherms is shown in Figure 1-1-3. The plateau pressure is slightly higher than found in the static test and the dynamic results exhibit an "onset-overpressure" characteristic. Several isobaric kinetic test response curves are shown in Figure 1-1-4. These show an incubation type response. The kinetic data are summarized in Figure 1-1-5. The results are slower than those of $LaNi_5$, based on both absolute and reduced pressure comparisons. This is also suggested by thermal contribution parameter, R, which is about 0.4. It appears, therefore, that the free nickel particles did not have the desired effect of increasing the H_2 dissociation speed. Rather, the effect is to decrease the kinetics.

$LaNi_7$

The La-Ni phase diagram (Figure 1-0-1) predicts about a 50-50 mixture of primary $LaNi_5$ and eutectic LaNi+Ni. The microstructure of as-cast $LaNi_7$, Figure 1-2-1, corresponds qualitatively to this prediction.

No hydriding tests were performed on this alloy.

$LaNi_{11.3}$

According to the phase diagram (Figure 1-0-1), this is the eutectic composition. The as-cast microstructure, Figure 1-3-1, is virtually 100% eutectic. The structure consists of fine, irregular lammelae of alternating $LaNi_5$ and Ni. Because of the ductile Ni-network, this composition was relatively difficult to crush.

The 25°C absorption and desorption isotherms are shown in Figure 1-3-2. Because of the approximately 50%-free Ni content, the capacity is only half that of single phase $LaNi_5$. The hysteresis is large. The relative shapes of the isotherms are somewhat unusual; the desorption curve shows a very sloping plateau while the absorption curve shows a relatively flat plateau. Because of the supporting network of ductile Ni, $LaNi_{11.43}$ did not decrepitate much during hydriding.

The dynamic 25°C absorption and desorption isotherms are presented in Figure 1-3-3. They appear very similar to the static isotherms except for slightly higher absorption pressures. Isobaric absorption data are given in Figure 1-3-4 and summarized in Figure 1-3-5. Because of the limited capacity, the 0.05 g-atom H reacted parameters necessarily show poor response.

Category 2 - Eutectoid Microstructure

$SmCo_5$

The Sm-Co phase diagram is shown in Figure 2-0-1. This AB_5 compound is unusual in that it is said to decompose below about 780°C according to the diffusion controlled eutectoid reaction $SmCo_5 \rightarrow Sm_2Co_7 + Sm_2Co_{17}$. Attempts were made to create the three-phase microstructure ($SmCo_5$-Sm_2Co_7-Sm_2Co_{17}) by heat treating to achieve a partial eutectoid reaction.

The sample prepared was close to the aim composition, slightly Sm-rich. The microstructures of as-cast, solution annealed, and aged $SmCo_5$ are shown in Figure 2-1-1. The as-cast microstructure (Figure 2-1-1a) shows predominantly $SmCo_5$ with a few percent of a second phase, probably Sm_2Co_7 because of the slightly Sm-rich composition. Solution annealing at 1225°C (Figure 2-1-1b) dissolves some, but not all of the Sm_2Co_7 phase. Also subtle rows of etch pits became apparent. Aging for 24 hours at 700°C (i.e., below the eutectoid decomposition temperature) did not change the microstructure much (Figure 2-1-1c). The rows of etch pitting are somewhat more evident but there is little evidence of a typical eutectoid microstructure. Another sample was aged for 168 hours at 700°C with no significant change in the microstructure. Thus, the 780°C eutectoid temperature shown in Figure 2-0-1 must be incorrect or the diffusion rates for this reaction are extremely slow at 700°C.

A limited amount of static hydriding data was obtained. The 25°C desorption curve for solution treated $SmCo_5$ is shown in Figure 2-1-2. Also shown are absorption and desorption curves for solution treated plus 24 hour 700°C aged material. There is lower capacity in the aged sample. This is believed to be a result of partial oxidation of the sample because of inadequate atmosphere control during the age (note the oxidized cracks in Figure 2-1-1c) and not a manifestation of any partial eutectoid reaction. The plateaus are extremely flat and the hysteresis is very small. The maximum H/M is only 0.5. In summary, the data is consistent with that previously published for annealed $SmCo_5$(9) and does not show any evidence of the expected eutectoid reaction.

In view of the above negative results, no dynamic hydriding tests were run.

Category 3 - Other Second Phases

The object of this category of melts was to examine the potential role of various second phases. It might be argued that the heterogeneities associated with second phase particles (especially on the surface of activated powder) might serve [illegible] hydride nucleation sites [illegible] circuit H-diffusion paths, thus aiding kinetics.

$LaNi_{3.8}Fe_{1.2}$

The composition of this heat was very close to the aim. It was examined only in the as-cast condition. The as-cast microstructure is shown in Figure 3-1-1a. In addition to the $La(Ni,Fe)_5$ matrix there are substantial amounts of two second phases. Although we did not specifically identify these phases, they appear to be identical to those we have identified earlier in the M-Ni-Fe system(4). By analogy to that system we can be reasonably sure the identification of the second phases in $LaNi_{3.8}Fe_{1.2}$ (Figure 3-1-1a) are as follows: The occasional white islands and the fine eutectic particles are a Fe-rich Fe-Ni solid solution and the large 'twinned' areas are approximately $La_3(Ni,Fe)_{10}$.

The ductile Fe-Ni phase appears to give substantial resistance to decrepitation (particle size breakdown on cycling). After cycling four times the sample used for the static hydriding curves almost completely retained its 10 mesh particle size, although each particle was highly cracked internally, of course (Figure 3-1-1b). This suggests the ductile eutectic Fe-Ni forms a 3-dimensional tree-like network, not unusual for a eutectic. We have noticed this phenomenon before in AB_5 compounds containing a ductile second phase(10). Thus it is possible, with careful design of the microstructure, to produce a decrepitation resistant AB_5 hydride. The static 25°C absorption and desorption curves for as-cast $LaNi_{3.8}Fe_{1.2}$ are shown in Figure 3-1-2. The plateaus are slightly sloped and significantly lower than $LaNi_5$, an expected effect of partial Fe substitution into the AB_5 structure(4). Hysteresis is reasonably low. Because the Fe-Ni and $La_3(Ni,Fe)_{10}$ phases are not useful for reversible 25°C hydrogen storage, the usuable capacity is significantly lower than $LaNi_5$.

The dynamic 25°C absorption isotherm is shown in Figure 3-1-3. The absorption pressures are slightly higher than in the static test but otherwise the isotherms are similar. The usable hydrogen capacity of this alloy is less than 0.6 H/M. However, the isotherms should, in fact, be shifted to higher H/M levels. This is because during activation, the alloy was found to absorb about 0.3 H/M which was not reversible under normal test conditions.

Isobaric kinetic data is shown in Figure 3-1-4 and summarized in Figure 3-1-5. Due to the low plateau and solid solution reaction (giving unstable initial test conditions) the kinetic data is very limited. The estimates shown in Figure 3-1-5 indicate moderate absolute and slow reduced pressure reaction rates. This is supported by a low indicated thermal contribution, R=0.3.

$LaNi_{3.5}Cr_{1.5}$

This material, representing an arbitrary partial substitution of 1.5 atoms of Cr for Ni, resulted in the as-cast microstructure shown in Figure 3-2-1. It is multiphase and extremely complex. The ingot was tough and very difficult to crush, suggesting a significant amount of a ductile solid solution present. No attempt was made to identify the phases or obtain any hydriding data.

$LaNi_4Cr$

After seeing the excessively high second phase content of the preceeding material, another heat was made with only one atom of Cr substitution. The microstructure is shown in Figure 3-3-1. Although the second phase content was slightly reduced below that of $LaNi_{3.5}Cr_{1.5}$, $LaNi_4Cr$ still showed a complex microstructure consisting of at least 50% non-AB_5 phases. Because of this no attempt was made to obtain any hydriding data.

$LaNi_4Si$

A Si-substituted heat, nominally $LaNi_4Si$, was made. The analyzed La content was on the low side but not seriously so (actual $La_{0.90}Ni_{4.04}Si_{0.96}$). The as-cast microstructure, shown in Figure 3-4-1, consisted of roughly equal amounts of two phases. The chemistries of these phases were determined by electron microprobe analysis. The dark, cored (segregated) phase is AB_5 with a microprobe analysis close to the nominal formula $La_{1.0}Ni_{4.0}Si_{1.0}$. The light phase had an approximately A_2B_{13} formula, actually $La_{2.0}Ni_{9.2}Si_{3.8}$.

This composition was not chosen for hydriding tests.

$LaNi_4Sn$

The as-cast microstructure of $LaNi_4Sn$ is shown in Figure 3-5-1. It consists of two phases: (a) a light phase consisting of both large islands and fine eutectic particles, and (b) a darker etching matrix. Microprobe analysis showed the light phase to be the AB_5 composition $La_{1.03}Ni_{4.55}Sn_{0.45}$. The darker phase was found to be a higher Sn + La phase of the approximate stoichiometry $LaNi_{2.9}Sn_{1.6}$.

Attempts were made to obtain 25°C static isotherms. It became soon evident that Sn substitution had drastically lowered the plateau pressure. The plateau was not flat and in the rough vicinity of 0.01 atm at 25°C. Because our Severts apparatus is not very precise in this pressure range, we do not include the data obtained, nor did we run dynamic tests. We did [illegible] ower Sn alloy, nomin[illegible] $_{4.7}Sn_{0.3}$, which we will discuss later in Category 4 (Substitution Elements).

MNi_4Sn

A Sn-substituted AB_5 compound was made using lower cost mischmetal M, rather than La. Based on the potent effect of Sn in lowering the plateau pressure, it was reasoned that Sn substitution might be yet another useful way of lowering the excessively high plateau pressure and hysteresis of MNi_5(4).

The microstructure of as-cast MNi_4Sn is shown in Figure 3-6-1. It is similar to the $La_{1.02}Ni_{3.99}Sn_{1.01}$ composition discussed above (Figure 3-5-1), except it is somewhat coarser. The primary white phase (assumed to be about $MNi_{4.5}Sn_{0.5}$) has a more prismatic morphology. The dark eutectic phase is present. In addition, a small amount of another white phase (perhaps Ni solid solution) is present in the mischmetal version.

No hydriding data was obtained.

$MNi_{4.3}Al_{0.7}$

Al substitution is an effective and economic way of reducing the plateau pressure and hysteresis of MNi_5(4). The procedure usually results in some NiAl second phase particles in the microstructure. We examine here the effect of these particles (and matrix Al-substitution effects) on hydriding behavior.

The analyzed composition of the heat was very close to the aim. In order to flatten the plateau(4) the sample was homogenized for 16 hours at 1125°C. The resultant microstructure is shown in Figure 3-7-1. The matrix is $M(Ni,Al)_5$ and the second phase particles are Ni-rich NiAl.

The static 25°C curves are shown in Figure 3-7-2. Plateau pressure is about 0.6 atm (this value can be varied to any desired level by varying Al content(4)). Hysteresis is small. Capacity is lower than $LaNi_5$ because of the non-hydriding NiAl present.

The dynamic 25°C absorption isotherm is shown in Figure 3-7-3. The plateau pressure appears slightly higher and there is a slight onset-overpressure. Isobaric absorption response is illustrated in Figure 3-7-4 and the kinetic parameters are summarized in Figure 3-7-5. The absorption reaction is quite rapid when compared to other alloys on an absolute pressure basis. This is due in part to the low plateau pressure. Additionally, the reduced pressure reaction rate is also comparatively rapid. Indeed, the reaction rates are sufficiently rapid that the thermal contribution to the observed response is quite significant (R=0.7). On the basis of relatively good reaction rate response and lower raw materials cost, this alloy appears to be an interesting candidate for further evaluation.

Category 4 - Substitutional Elements

In this section we consider a series of ternary modified $A(B,Y)_5$ compounds where the ternary addition Y largely substitutes into the AB_5 structure.

$LaNi_4Cu$

Because the prototype crystal structure for the AB_5 hydrogen storage compounds is the so-called $CaCu_5$ structure it would logically be expected that Cu would completely substitute for Ni in $LaNi_{5-y}Cu_y$. As shown by the microstructure of $LaNi_4Cu$, Figure 4-1-1, this speculation is confirmed. The heat is almost single phased. A few dark particles, probably oxides, and a few oval white particles, probably free Ni-Cu, are present but in almost insignificant quantity. Around some of the white particles there was some fine etch pitting. It is not clear if this is an etching artifact or evidence of a fine precipitate that started to form during cooling of the ingot.

$LaNi_4Cu$ was not selected for hydriding studies. An equilibrium isotherm is given for this alloy in Reference 11.

$LaNi_{4.5}Pd$

Pd, well known for its catalytic activity, was substituted into a $LaNi_5$ heat. Because of the high cost of Pd, only a small 50 g arc melted button was made. Chemical analysis of the melted sample showed it was exactly on composition. However, the microstructure of the button, Figure 4-2-1, showed a slight inhomogeneity from top to bottom, not unusual for arc melted buttons. A small amount of a dark etching second phase was present, sometimes in grain boundaries and sometimes present as discrete particles within a grain. Microprobe analysis of this phase showed that it was a Pd-rich intermetallic compound (or solid solution) of the approximate composition $Pd_{4.1}Ni_{0.4}La_{1.0}$. The

matrix analysis was $La_{1.04}Ni_{4.55}Pd_{0.45}$, i.e. an AB_5 stoichiometry. Thus it appears that the substitutional solubility of Pd in $LaNi_5$ is limited to about 0.5 atom.

The static 25°C isotherms are shown in Figure 4-2-2. The curve shapes are unusual for an AB_5 compound. They are qualitatively like FeTi. There is a flat lower plateau, comparable in pressure to $LaNi_5$ and a sl[illegible]er plateau. Hysteresis is fairly small. Capacity reaches H/M = 1 at high pressure; however, the working range of the lower plateau is limited to only about ΔH/M = 0.46.

The dynamic absorption and desorption isotherms at 25°C are shown in Figure 4-2-3. The absorption pressures are significantly higher than for the static tests, and a major onset-overpressure is observed. Examples of isobaric kinetic tests are given in Figure 4-2-4 and these show an extended incubation type of behavior. Kinetic parameters are summarized in Figure 4-2-5. The thermal contribution to the kinetic response may be characterized as R=0.5, which suggests a considerable decrease in intrinsic kinetic response from $LaNi_5$. This may be due in large part to the loss in effective capacity at small pressure increments over the plateau. Taken together, the kinetic response suggests no obviously beneficial effect of the palladium modifications.

$LaNi_{4.7}Sn_{0.3}$

This heat was made after obtaining the results on the $LaNi_4Sn$ sample discussed earlier and represents an attempt to substitute a lower level of Sn. As shown by the as-cast microstructure, Figure 4-3-1, 0.3 atom of Sn is below the solubility limit. The microstructure is virtually single phase. However, the modulated etching effect implies substantial coring (segregation) during solidification from the melt.

The static 25°C isotherms are shown in Figure 4-3-2. They are consistent with what might be expected from the microstructure. Capacity is good (to max. H/M = 1), consistent with the single phase AB_5 nature of the composition. The plateau is very sloping, consistent with the severe segregation. As with other cases of cored AB_5's(4) the plateau can probably be flattened substantially by homogenization annealing. Finally, as-cast $LaNi_{4.7}Sn_{0.3}$ shows unusually small hysteresis.

Dynamic absorption and desorption isotherms at 25°C are shown in Figure 4-3-3. These indicate a small, very low pressure plateau, followed by an extended variable pressure reaction. Figure 4-3-4 illustrates an isobaric absorption test response curve for this alloy. Kinetic parameters are summarized in Figure 4-3-5. The absolute pressure comparison of reaction rates to that of other alloys indicate good kinetics. The intrinsic kinetics, however, appear to be relatively poor. Any further examination of the kinetics response due to Sn modification should probably be done on homogenized material.

$LaNi_{4.8}C_{0.2}$

The as-cast microstructure is shown in Figure 4-4-1. It is predominantly the AB_5 phase with a small amount of an unidentified, dark etching, second phase, perhaps graphite. Because both La and Ni are not strong carbide formers it is likely some of the C remains in solid solution in the AB_5 phase.

The static isotherms, Figure 4-4-2, show behavior similar to $LaNi_5$, except that the hysteresis is significantly greater. Plateaus are flat and the material has good capacity.

The dynamic absorption and desorption isotherms at 25°C are shown in Figure 4-4-2. For this alloy, the dynamic absorption pressures are greatly above those found in the static test mode; the desorption pressures are slightly lower. This results in a dynamic hysteresis which is greater than that of any other alloys studied in this program.

Examples of isostatic kinetic test response are shown in Figure 4-4-4 and -5. These also exhibit a rather unusual behavior. This is most obvious in the higher speed test results (4-4-5) and suggests an initial very rapid, exothermic reaction which is different from the bulk hydriding reactions. This unusual effect results in a thermal contribution which appears to be greater than the Van't Hoff relation (R = 1.3). The kinetic parameters are summarized in Figure 4-4-6. The intrinsic absorption kinetics of the alloy appear to be very rapid when normalized to the plateau pressure. However, the plateau pressure is so high that the kinetic response on an absolute pressure basis is not outstanding.

$MNi_{4.3}Mn_{0.7}$

Mn substitution is an effective way of lowering the plateau pressure of MNi_5(12). It also increases the air pyrophoricity of activated powder, suggesting it somehow modifies the surface properties. Because of this a sample was evaluated in this study.

The analyzed composition was close to the aim. In order to flatten the plateaus, a sample was annealed for 16 hours at 1150°C. The resultant microstructure is shown in Figure 4-5-1. The sample is nearly single phase with "ghosts" remaining of an as-cast phase that was largely dissolved during the homogenization anneal.

The static isotherms are shown in Figure 4-5-2. They show two atypical characteristics: (a) a substantial H-solubility in the α (metal) phase and (b) a large hysteresis in the plateau ($\alpha+\beta$) region. Total capacity is good ($H/M \approx 1$) but workable plateau width is rather small ($\Delta H/M \approx 0.5$).

Dynamic absorption and desorption isotherms at 25°C are shown in Figure 4-5-3. Considerable hydrogen solubility in the alloy is evident. Isobaric absorption response is shown in Figure 4-5-4. The extensive solid solution reaction gives a temperature response above the Van't Hoff relation. This is evident in the kinetic parameter summary given in Figure 4-5-5.

Category 5 - Surface Active Elements

In this category, we tried small additions of B, S, and Se, elements that are often considered "surface active" because of their tendency to segregate to surfaces such as grain boundaries.

$LaNi_{4.8}B_{0.2}$

The as-cast microstructure of this heat is shown in Figure 5-1-1. It consists of three phases which we have quantified by microprobe analysis: (a) the matrix which is $LaNi_5$ and contains little, if any, B; (b) the massive interdendritic white phase, which is also AB_5, specifically $LaNi_{4.4}B_{0.6}$; and the fine, interdendritic eutectic phase $NiB_{0.9}La_{0.1}$ (i.e. a La containing NiB). In the case of phases (a) and (b), it is not at all obvious why the B segregates so thoroughly to one of two AB_5 phases present. Presumably the $LaNi_{4.4}B_{0.6}$ phase does not have the usual AB_5 crystal structure ($CaCu_5$).

No hydriding data was obtained on this sample. In retrospect, this is unfortunate. It might be especially interesting to prepare single phase $LaNi_{4.4}B_{0.6}$ and examine hydriding behavior.

$LaNi_{4.9}S_{0.1}$

This was an attempt to make a $LaNi_{4.9}S_{0.1}$ composition. The actual composition that resulted was $La_{0.94}Ni_{4.998}S_{0.002}$, much lower in S. It is now obvious that the solubility of S in $LaNi_5$ is much lower than 0.1 atom, probably because of the strong sulfide forming tendency of La. The low La level is believed to be a result of La sulfide slag formation during melting. The small sulfur level that was retained in the melt, however, resulted in the dramatic microstructure shown in Figure 5-2-1. A very fine precipitate (probably a La-rich sulfide) is profusely distributed throughout the microstructure.

Hydriding tests were not performed on this sample because of fear that H_2S would form and lead to contamination of our apparatus. If the particles are very stable La-sulfides, H_2S probably would not form. If, on the other hand, H_2S does form it probably would result in self-poisoning of the specimen.

$LaNi_{4.9}Se_{0.1}$

The solubility of Se in molten $LaNi_5$ is also much less than 0.1 atom, but it is significantly higher than S. The analyzed composition of this heat was $La_{0.99}Ni_{4.97}Se_{0.03}$. The microstructure, Figure 5-3-1, is qualitatively similar to the S-doped LaNi discussed above.

This composition also was not subjected to hydriding tests for fear of H_2Se formation and apparatus contamination.

Category 6 - Large Diameter Atom Substitutions

In this series we attempted the partial substitution (for La) of the Group IIA elements Mg, Ca, Sr, and Ba. If successful we hoped to see the effect of varying the size of the substitution atom and any effect that might have on hydriding properties. The CN 12 metallic radii for these elements are (in Å): Mg = 1.60, Ca = 1.97, Sr = 2.15, and Ba = 2.22.

$Mg_{0.1}La_{0.9}Ni_5$

The analyzed Mg-content of the heat ($Mg_{0.19}La_{0.91}Ni_5$) was high because we overcompensated for the Mg evaporation during melting. The microstructure, Figure 6-1-1, shows a fairly fine second phase. Microprobe analysis shows the second phase to have the approximate formula $LaMg_{1.85}Ni_{9.26}$. Disappointingly the microprobe shows the matrix to be essentially free of Mg (i.e. simply $LaNi_5$). Thus Mg does not appear to substitute into $LaNi_5$.

The static absorption and desorption curves, Figure 6-1-2, are similar to $LaNi_5$. They differ slightly in that the plateaus are slightly higher, more sloping than $LaNi_5$ and have a slightly smaller hysteresis. Capacity is below that of $LaNi_5$ because of the second phase present.

The dynamic absorption isotherm at 25°C is shown in Figure 6-1-3. The absorption pressures are higher than observed in the static isotherm, and there is an onset-overpressure. Except for the reduced capacity caused by second phases, the isotherm is very similar to that for nickel-rich, $LaNi_5$ **(e.g. Figure 1-1-3).**

Isobaric absorption kinetic test results are illustrated in Figure 6-1-4 and the kinetic parameters are summarized in Figure 6-1-5. These results, also, are very similar to those for nickel-rich $LaNi_5$ **(e.g. Figure 1-1-5).** The absolute reaction is slower than for $LaNi_5$ in both absolute and relative comparison.

$Ca_{0.2}La_{0.8}Ni_5$

The as-cast microstructure of this composition, Figure 6-2-1, is virtually single phase, confirming our previous observations of complete Ca solubility in the AB_5 rare earth-nickel compounds(4,10).

The static 25°C curves are shown in Figure 6-2-2. Hysteresis is low and the plateaus are slightly sloping consistent with the usual coring seen in as-cast Ca-substituted AB_5(4). Pressures are, over most of the plateau, slightly below $LaNi_5$. Capacity is slightly higher than $LaNi_5$, reaching 1.1 H/M max. Interestingly this slightly higher H-capacity at the 0.2 atom Ca level was seen before in the $Ca_xMi_{-x}Ni_{5-y}Cu_y$ quaternary system(13).

The dynamic absorption isotherm at 25°C is shown in Figure 6-2-3. The absorption pressures are somewhat higher than for the static isotherm and the high capacity is also evident. Several isobaric absorption kinetic test curves are shown in Figure 6-2-4 and the kinetic parameters are summarized in Figure 6-2-5. Compared to single phase $LaNi_5$ absorption, the $Ca_{0.2}La_{0.8}Ni_5$ alloy reacts considerably more slowly. This is evident from absolute and reduced pressure comparisons as well as from the thermal contribution parameter (R = 0.3). The reduced intrinsic kinetics of this alloy are of considerable interest since the calcium has clearly dissolved in the matrix.

$Sr_{0.2}La_{0.8}Ni_5$

The microstructure of the Sr-substituted composition is shown in Figure 6-3-1. Microprobe analysis of the matrix indicated that little, if any, Sr had substituted into the AB_5 phase. The interdendritic phase was predominantly a Ni-2 wt.% Sr solid solution. Associated with this phase were regions leached out during polishing and etching. This is probably indicative of the presence of a higher Sr (water soluble) phase. The main point, somewhat disappointing, is that the AB_5 phase seems to have no significant substitutional solubility for Sr.

As expected from the above microstructural observations, the static 25°C isotherms of $Sr_{0.2}La_{0.8}Ni_5$, Figure 6-3-2, are very similar to $LaNi_5$. The only noticeable differences are a slight rounding of the left knee of the curves and a generally smaller hysteresis.

The dynamic absorption isotherm at 25°C is shown in Figure 6-3-3. Absorption pressures are slightly higher than in the static isotherm. The metal phase hydrogen solubility appears to be increased over that of $LaNi_5$. Isobaric absorption kinetic test results are illustrated in Figure 6-3-4. These curves show a high initial reaction rate and temperature increase, a response which appears typical of the metal solid solution reaction. Kinetic parameters are summarized in Figure 6-3-5.

$\underline{Ba_{0.2}La_{0.8}Ni_5}$

This heat behaved differently from all the other heats during melting. As soon as the Ba was added to the melt vigorous crucible attack occurred with substantial slag formation. As a result the Ba content is somewhat below the aim level and there is a larger Al residual (Table II).

The as-cast microstructure, Figure 6-4-1, is similar to the Sr-substituted composition discussed above. Again microprobe analysis showed the AB_5 matrix to be virtually Ba-free. The eutectic phase is a Ni solid-solution containing 3-4 wt.% Ba. Voids in the polished and etched microstructure are again believed to be the remnants of a leached out Ba-rich phase. Thus, as for Mg and Sr, Ba also appears to have negligible substitutional solid solubility in $LaNi_5$.

The static isotherms, Figure 6-4-2, are, as expected, similar to $LaNi_5$. They show slightly higher plateau pressures and slopes.

Dynamic absorption and desorption isotherms at 25°C are shown in Figure 6-4-3. They indicate rather greater hysteresis than does the static data and, show a similarly high slope reduced capacity. Isobaric kinetic test results are shown in Figure 6-4-4 and the kinetic parameters are summarized in Figure 6-4-5. The kinetic parameters indicate similar intrinsic reaction speed to that of other alloys in the group IIA addition series. However, the thermal contribution to kinetic control appears larger (R = 0.8). This difference may be due to the more sloping character of the plateau.

Category 7 - Other Compositions

$LaNi_3$

This composition was not part of the overall study. We were asked to prepare about 20 kg of $LaNi_3$ for undisclosed Sandia evaluation. As we will show, this is not easily done and represents an excellent example of an exercise in "metallurgical patience".

Referring to the La-Ni phase diagram (Figure 1-0-1) we see that the solidification is non-congruent as with $LaNi_5$ and most other AB_5's. Rather $LaNi_3$ solidifies by a series of peretectic reactions. The first phase to precipitate from the melt is $LaNi_5$ which causes the remaining liquid to become more and more La-rich. At 995°C some La_2Ni_7 forms peretectically followed by some $LaNi_3$ (also peretectically at 955°C). By this time the remaining liquid is very rich in La and must cool to 795°C where $LaNi_2$ forms by yet another peretectic. Thus, even though the melt we made has almost perfect overall composition, the resultant as-cast microstructure, Figure 7-1-1a, was a complex non-equilibrium mixture of at least these four phases.

To achieve single phase $LaNi_3$ the alloy must be annealed for long times at temperatures below the $LaNi_3$ peretectic temperature (955°C). We first tried annealing (in argon) at 927°C for two weeks. Even at this temperature there was some remelting of La-rich regions, a small part of which drained to the bottom of the furnace and was lost. The microstructure of the remaining solid material after 2 weeks at 927°C is shown in Figure 7-1-1b. The structure was about 75-80% $LaNi_3$. Increasing the annealing time to 4 weeks, Figure 7-1-1c, resulted in about 90% $LaNi_3$. This is an improvement, but we are clearly reaching a point of diminishing returns. As per x-ray diffraction analysis, the remaining two second phases are La_2Ni_7 and $LaNi_2$.

This illustrates a typical problem with many of the non-AB_5, rare earth-transition metal phases which commonly form by relatively low temperature peretectics. Because of the low temperatures involved, solid state, homogenization annealing (diffusion controlled) is slow. In retrospect, a better procedure would have been to solidify rapidly in a thin Cu chill mold to achieve a very fine microstructure, thus reducing diffusion distances. This would not completely solve the problem, however. The main problem is one of nature which has dictated a La-Ni phase diagram with a series of troublesome peretectic reactions accompanied by a rapidly decreasing liquidus temperature with increasing La content.

Category 8 - Pd Plating

Electroless Plated Samples

Scanning electron micrographs of electroless Pd-plated $LaNi_5$ and $LaNi_{4.9}Al_{0.1}$ are shown in Figure 8-1/2-1. Qualitative EDAX spectra were used to locate the position of Pd on the surface. Some of the Pd seems to have deposited as small islands on the surface, represented by the small particles that are bright in the secondary electron images. However, EDAX spectra taken on the general particle surfaces show a weak Pd peak indicating there was also some general deposition of Pd in addition to the islands.

Static 25°C isotherms were taken only for the Pd-plated $LaNi_5$ specimen. These, shown in Figure 8-1-2, were very similar to unplated $LaNi_5$ (Figure 0-1-2).

Numerous dynamic testing and cycling was done with the Pd-plated sample. However, the results were not encouraging and reduction of the test data was carried only to the point of making some limited comparisons. These are presented in Table III. These data are based on the time to absorb 0.05 g-atom of H at 1.2 times the plateau pressure. The long air exposure data was taken after the activated sample had been Pd-treated and then left open to air for about 7 days. Clearly the Pd-plating provided some initial advantage, but good kinetics were achieved after about 5 additional cycles irrespective of the Pd-treatment. The samples were then further exposed to air for 16 hours, and the Pd-treatment did not appear significant.

These results suggest that Pd may provide some protection prior to testing, but that cycling renders it ineffective. Either it spalls off or is bypassed by cracking.

Mechanically Alloyed Specimens

First attempts to smear Pd on activated $LaNi_5$ and $LaNi_{4.9}Al_{0.1}$ surfaces were not successful. Scanning electron micrographs are shown in Figure 8-1/2-3. The ball milling has resulted in a much finer particle size. EDAX analysis did not detect any Pd on the particle surface. Apparently, the ductile Pd formed clumps and was not smeared on the AB_5 surfaces.

Pd coating of $LaNi_5$ by mechanical alloying (M.A.) was tested for dynamic response and the results included in Table III with those for electro-deposited (E.D.) Pd. These results suggest simply that the finer particle size is more sensitive to damage in air; no effect of Pd is evident.

COMPARISONS AND CONCLUSIONS

Thus far, we have presented the microstructure and hydriding results on an alloy by alloy basis. In this section we will attempt to make comparisons among alloys. Such comparisons must, of necessity, be somewhat arbitrary because the comparisons can be made in a number of ways. The optimum comparison depends on the details of the application intended. In making the comparisons discussed below we tried to keep in mind the basic operational intent of the Sandia water pump and thus will concentrate on basic PTC properties (such as plateau pressures, hysteresis and workable capacity) and especially charging kinetics at low overpressures. In addition to these engineering properties we have tried to make comparisons such that insights into fundamental material trends can be derived for potential use in further alloy development for this or any other hydride application.

Static absorption and desorption curves are well known to those in the field and tabular comparisons of resultant data are quite straightforward. In Table IV we compare all the alloys tested in terms of static 25°C plateau pressures, plateau slopes, hysteresis, and workable Δ H/M.

Dynamic data, of the type we have generated here, are virtually absent in the AB_5 literature; thus we present our comparisons in ways not generally seen before by those in the field. Alloy-to-alloy comparisons of selected dynamic data are presented in Tables V and VI for the reference alloys and all the tested experimental alloys, respectively. These data are selected from the curves presented earlier and consist of (a) dynamic plateau pressures, (b) reaction times, and (c) a thermal contribution factor R.

The dynamic plateau pressures are those determined from the 60-70 minute continuous tests and can be easily visualized and compared to the static tests.

The reaction time data are the key kinetic comparisons. They are presented on both "absolute" and "reduced" bases. On a reduced basis the applied pressure during charging (or backpressure during discharging) is effectively constant at some multiple (or fraction) of the appropriate plateau pressure. The "absolute" pressure comparisons are useful for comparing predicted alloy behavior in an actual device which must operate in "absolute" pressures. The "reduced" comparisons are more useful for alloy-to-alloy comparison of mechanistic behavior (e.g., surface reactions, H-diffusion, etc.), because the applied pressure ratio (or backpressure) represents a constant effective overpressure (or underpressure) for each particular alloy.

The thermal contribution parameter R is a new term that can be used as a semiquantitative measure of intrinsic kinetics. R is defined in Table V. In brief, it is derived from the maximum temperature charge monitored by the thermocouple during charging. If the temperature of the bed quickly reached the expected Van't Hoff temperature for the applied pressure (R=1.0) then the reaction rate is intrinsically so fast that it cannot be quantitatively isolated from the heat transfer properties of the thin specimen holder. The lower the measured value of R, the more the data represents intrinsic kinetics and not heat transfer of the specimen holder.

Before comparing materials, it is well to discuss some general comparisons between the static and dynamic P-C curves. As might be expected, static and dynamic tests give similar capacities and roughly similar isotherm shapes. Invariably, however, the hysteresis is significantly larger for the dynamic P-C curves. The absorption pressures are higher and the desorption pressures lower in the dynamic tests, although the effort tends to be more pronounced on the absorption side. Because the temperature excursions for these slow (60-70 minute) tests were typically less than 0.3°C, this phenomenon is quite real and seems to be absent in the literature on AB_5 hydrides. From a practical device point of view, (i.e., a dynamic situation), it is more important to determine the dynamic P-C curves; in fact, the classic static curves widely published in the literature may be very misleading from a design point of view. All the kinetic experiments and parameters compared in Tables V and VI are based on dynamic, not static, P-C curves.

Category 0 - Reference Alloys

The most detailed comparisons were made on the three reference alloys $LaNi_5$, $LaNi_{4.9}Al_{0.1}$, and $LaNi_3Co_2$. All three alloys are nearly single phase. Plateau pressures decrease in the order $LaNi_5$, $LaNi_{4.9}Al_{0.1}$, $LaNi_3Co_2$ as expected from the previous literature on these materials. Usable capacities for $LaNi_5$ and $LaNi_{4.9}Al_{0.1}$ are similar and significantly higher than $LaNi_3Co_2$. On an absolute pressure basis, the absorption and desorption rates generally increase in the order $LaNi_5$, $LaNi_{4.9}Al_{0.1}$, $LaNi_3Co_2$ (Table V). [The infinite rates listed in Table V, of course, represent situations where the temperature is too high (or low) for charging (or discharging) at the applied pressure (or backpressure).] This is an expected result of the decrease in plateau pressures associated with alloy order. On a reduced pressure basis, however, the trend is quite opposite. $LaNi_5$ is extremely fast; in fact R-values were 1.0 for all the $LaNi_5$ tests, signifying that even for this specimen holder we are not able to isolate the true reaction kinetics of $LaNi_5$. $LaNi_{4.9}Al_{0.1}$ was intrinsically slower than $LaNi_5$ and $LaNi_3Co_2$ was even slower. The marked differences in the intrinsic kinetics of these three reference alloys are better shown in the time vs. reduced pressure curves of Figure 4.

The reduced R-values measured for $LaNi_{4.9}Al_{0.1}$ and $LaNi_3Co_2$, accompanied by an increased test temperature dependence for these two materials (Table V), further confirms the conclusion of decreased intrinsic kinetics.

Some speculation should be provided on the possible reasons for the unmistakeable decrease in intrinsic kinetics with the [illegible] $LaNi_{4.9}Al_{0.1}$, $LaNi_3$[illegible] the case of $LaNi_3Co_2$, it can be suggested that Co is not as effective an $H_2 \rightarrow 2H$ dissociation catalyst as Ni and that removing a significant fraction of the Ni reduces the rate of this critical step. The role of the small Al-addition in $LaNi_{4.9}Al_{0.1}$ is less obvious. Perhaps the light Al atoms tend to segregate to the first few monolayers on the surface, effectively reducing the Ni concentration on the surface and inhibiting the H_2-2H reaction slightly. Because Al tends to form oxide films in the presence of oxygen, we may even be seeing the subtle early stages of surface poisoning even through we used UHP H_2 (5 ppm maximum O_2 content). Longer cycling tests would help to confirm these speculations. In any event these new kinetic observations seem to open a whole new field of speculation and experimentation. In a practical sense all three reference alloys seem to have fast enough kinetics, relative to heat exchanger design considerations, to be of practical use in the water pump.

Categories 1 to 6 - Experimental Compositions

Comparison of reaction kinetics of 15 AB_5 alloy modifications is shown in Table VI. These results are more limited than those for the three reference alloys, including only absorption data at 25°C. Obviously, in any cyclic application, desorption kinetics must be considered also. However, absorption kinetics appeared to be limiting in several pump designs and were therefore selected for alloy comparisons. In this connection, inclusion of the reduced pressure comparison, by normalizing the effect of changing plateau pressure on kinetics, should help identify the manner in which the alloy modifications affect the reaction kinetics.

As shown by Tables IV and VI the experimental alloys show a wide variety of hydriding properties. With one or two possible exceptions, to be discussed, the practical properties (especially dynamic) are inferior to $LaNi_5$. There are enough interesting differences, however, to warrant a brief discussion relative to our original objectives of using chemical and microstructural variations to modify the behavior of AB_5 compounds.

In Category 1 the inclusion of free Ni particles in a $LaNi_5$ matrix clearly does not increase kinetics as hoped; in fact, a significant decrease of kinetics was found. This strongly suggests that free metallic Ni is not as effective as a $H_2 \rightarrow 2H$ dissociation catalyst as Ni bound in the $LaNi_5$

intermetallic compound. If the Ni is in the form of a ductile eutectic network ($LaNi_{11.5}$) kinetics are especially slow, the "sheets" of Ni probably acting as H-diffusion barriers.

In Category 3, Fe-substitution to produce second phases reduces kinetics as well as capacity. $MNi_{4.3}Al_{0.7}$ shows reasonably good kinetics, but clearly below that of $LaNi_5$. Capacity is reduced. However, because of the relative low cost of the mischmetal, this alloy is probably a very promising one if it were normalized on a cost basis. The role of the NiAl particles in kinetics, relative to the change from La to M, has not been clearly established.

The substitutional compositions show a variety of effects. Pd and Sn substitutions seem to show no overall advantages (although the Sn substituted sample is difficult to compare because of the highly sloped plateau). From a kinetic point of view, the mischmetal container $MNi_{4.3}Mn_{0.7}$, like $MNi_{4.3}Al_{0.3}$, appears to be an attractive low cost substitute for $LaNi_5$. Its main disadvantages are high hysteresis and low Δ H/M (Table IV).

The C-substituted $LaNi_{4.8}C_{0.2}$ is one of the most interesting of the compositions studied. It was the only composition studied that seemed to have reduced kinetics at least as fast as $LaNi_5$. The measured R-factor was actually greater than 1.0. This does not necessarily mean this material violated the Van't Hoff plat; rather, there appeared to be an abnormal exothermic burst in the early stage of charging. C atoms probably occupy interstitial sites in the $CaCu_5$ structure that are competitive with H-sites, a possible explanation for the higher hysteresis. It is not at all clear why C has such a beneficial effect on kinetics, whether it is a surface effect or a bulk diffusion effect. A number of secondary (covalent?) interactions between C and H atoms can be speculated.

In the Category 6 series (Group IIA substitutions) only Ca substitute significantly into the $LaNi_5$ structure. However, all the Category 6 compositions had somewhat lower intrinsic kinetics than $LaNi_5$ (Table VI). Interestingly, $Ca_{0.2}La_{0.8}Ni_5$ (the only substitution that worked) had significantly lower kinetics than $Mg_{0.1}La_{0.9}Ni_5$, $Sr_{0.2}La_{0.8}Ni_5$, and $Ba_{0.2}La_{0.8}Ni_5$. This poses interesting questions. Is this a catalytic effect (i.e., La is more effective than Ca for H_2 dissociation) or can the effect be attributed to lattice strain resulting from Ca substitution? Why does Ca increase the usable Δ H/M over that of $LaNi_5$? Again the kinetics of this alloy, although slower than that of $LaNi_5$, are probably sufficient for water pump applications.

CONCLUDING REMARKS

As far as we know, this is the first study that has attempted to systematically relate intrinsic AB_5 as hydriding kinetics to chemical and microstructural factors. In fact, we believe it is the first effort that has begun to isolate the true kinetics of these remarkable materials. It has resulted in more questions than it was answered and, indeed, we would have expected no more from such a brief study. It has told us at least four main fundamental things:

1. It is possible to measure, at least semiquantitatively, the intrinsic kinetics of many AB_5 compounds.

2. There are chemical and microstructure effects that significantly influence intrinsic kinetics. We certainly do not always know why.

3. $LaNi_5$, historically one of the first AB_5 hydrides, has extraordinarily fast kinetics and may in fact represent the "ultimate", at least for practical purposes (neglecting economics).

4. There are a number of modified AB_5s that seem to have adequate kinetics for rapid cycle devices (i.e., have kinetics faster than any likely practical heat exchange situation).

REFERENCES

1) R. N. Rhoda and A. Madison: "Palladium Plating by Chemical Reduction", U.S. Patent 2,915,406, December 1,1959.

2) R. N. Rhoda: "Palladium Deposition", U.S. Patent 3,724,022, September 20, 1976.

3) J. S. Benjamin: "Composite Metal Powder", U.S. Patent 3,591,362, July 6, 1971.

4) G. D. Sandrock: "Development of Low Cost Nickel-Rare Earth Hydrides for Hydrogen Storage", Proc. 2nd World Hydrogen Energy Conference, August, 1978, IAHE, Vol. 3, pp. 1625-1656.

5) J. C. Achard, A. Percheron-Guegan, H. Diaz, F. Briancourt, and F. Demany, "Rare Earth Ternary Hydrides-Hydrogen Storage Application", Proc. Second International Congress on Hydrogen in Metals, Paper 1E12, Paris, 1977.

6) M. H. Mendelsohn, D. M. Gruen, and A. E. Dwight, "$LaNi_{5-x}Al_x$ in a Versatile Alloy System for Metal Hydride Applications", Nature, Vol. 269 (1977), p. 45-46.

7) H. H. vanMal, K.H.J. Buschow, and F. A. Kuijpers: "Hydrogen Absorption and Magnetic Properties of $LaCo_{5x}Ni_{5-5x}$ Compounds", J. Less Common Metals, Vol. 32 (1973), pp.289-296.

8) K.H.J. Buschow and H. H. VanMal: "Phase Relations and Hydrogen Absorption in the Lanthanum-Nickel System", J. Less Common Metals, Vol. 29 (1972), pp. 203-210.

9) H. Zijlstra and F. F. Westendorp: "Influence of Hydrogen on the Magnetic Properties of $SmCo_5$", Solid State Communications, Vol. 7 (1969), pp. 857-859.

10) G. D. Sandrock: "A New Family of Hydrogen Storage Alloys Based on the System Nickel-Mischmetal-Calcium", Proc. 12th IECEC, 1977, Vol. I, pp. 951-958.

11) H. H. VanMal, K.H.J. Buschow, and A. R. Miedema: "Hydrogen Absorption in $LaNi_5$ and Related Compounds: Experimental Observations and Their Explanation", J. Less Common Metals, Vol. 35 (1974), pp. 65-76.

12) C. E. Lundin and F. E. Lynch: "Modification of Hydriding Properites of AB_5 Type Hexagonal Alloys Through Manganese Substitution", Proc. Miami Alternative Energy Sources Conference, December, 1977.

13) G. D. Sandrock: "A Survey of the Hydrogen Storage Properties of Nickel-Copper-Mischmetal-Calcium Alloys", Proc. Miami Alternate Energy Sources Conference, December, 1977.

14) C. Herget and H.-G. Domazer: "Methods for the Production of Rare Earth-3rd Metal Alloys with Particular Emphasis on the Cobalt Alloys", Goldschmidt Informiert, Th. Goldschmidt A.G., Essen, Vol. 4/75 (1975), No. 35, pp. 3-33.

TABLE I

COMPOSITIONS STUDIED

Category No.	Category	Aim Compositions
0	Reference	$LaNi_5$*; $LaNi_{4.9}Al_{0.1}$*; $LaNi_3Co_2$*
1	Ni Second Phase Particles	$LaNi_{5.67}$*; $LaNi_7$, $LaNi_{11.5}$*
2	Eutectoid Microstructure	$SmCo_5$*
3	Other Second Phases	$LaNi_{3.8}Fe_{1.2}$*; $LaNi_{3.5}Cr_{1.5}$, $LaNi_4Cr$, $LaNi_4Si$, $LaNi_4Sn$*; MNi_4Sn, $MNi_{4.3}Al_{0.7}$*
4	Substitutional Elements	$LaNi_4Cu$, $LaNi_{4.5}Pd_{0.5}$*; $LaNi_{4.7}Sn_{0.3}$,* $LaNi_{4.8}Co_{0.2}$*; $MNi_{4.3}Mn_{0.7}$*
5	Surface Active Elements	$LaNi_{4.8}B_{0.2}$, $LaNi_{4.9}S_{0.1}$, $LaNi_{4.9}Se_{0.1}$
6	Large Diameter Atom Substitutions	$Mg_{0.1}La_{0.9}Ni_5$*; $Ca_{0.2}La_{0.8}Ni_5$,* $Sr_{0.2}La_{0.8}Ni_5$*; $Ba_{0.2}La_{0.8}Ni_5$*
7	Other Compositions	$LaNi_3$
8.	Pd Plating	Electroless: $LaNi_5$*; $LaNi_{4.9}Al_{0.1}$* Mechanical Alloying: $LaNi_5$*; $LaNi_{4.9}Al_{0.1}$*

M = Mischmetal (nominally 48-50 Ce, 32-34 La, 13-14 Nd, 4-5 Pr, and 1.5 other rare earths, in weight percent)

* = Indicates those compositions evaluated for hydriding behavior.

TABLE II

CHEMICAL ANALYSES

Category No.	Heat No.	Aim Composition	Actual Composition	Analysis, Wt.% La	M	Ni	O	N	C	Other
0	T-82108	$LaNi_5$	$La_{1.00}Ni_5$	31.95	-	67.7	0.025	0.0038	0.006	-
0	T-82118	$LaNi_{4.9}Al_{0.1}$	$La_{1.00}Ni_{4.91}Al_{0.09}$	32.0	-	66.8	0.017	0.002	0.004	0.54Al
0	T-82895	$LaNi_3Co_2$	$La_{0.97}Ni_{3.01}Co_{1.99}$	31.5	-	41.2	0.021	0.003	0.008	27.4Co,0.24Cu
1	T-82885	$LaNi_{5.67}$	$LaNi_{5.63}$	29.3	-	69.7	0.023	0.004	0.006	0.021Al
1	T-82886	$LaNi_7$	$LaNi_{7.05}$	24.9	-	74.2	0.032	0.004	0.013	0.011Al
1	T-82887	$LaNi_{11.5}$	$LaNi_{11.43}$	16.6	-	80.2	0.025	0.004	0.022	0.008Al
2	T-82863	$SmCo_5$	$Sm_{1.02}Co_5$	-	-	-	0.041	0.006	-	34.2Sm,65.9Co
3	T-82890	$LaNi_{3.8}Fe_{1.2}$	$La_{0.99}Ni_{3.81}Fe_{1.19}$	31.9	-	52.0	0.054	0.005	0.031	15.5Fe,0.009Al
3	T-82893	$LaNi_{3.5}Cr_{1.5}$	$La_{1.05}Ni_{3.51}Cr_{1.49}$	33.8	-	47.6	0.066	0.008	0.010	17.85Cr,0.14Sn
3	T-82920	$LaNi_4Cr$	$La_{0.98}Ni_{4.01}Cr_{0.99}$	32.2	-	55.6	0.020	0.008	0.005	12.2Cr
3	T-82891	$LaNi_4Si$	$La_{0.90}Ni_{4.04}Si_{0.96}$	32.3	-	61.5	0.030	0.004	0.011	6.99Si,1.19Al
3	T-82892	$LaNi_4Sn$	$La_{1.02}Ni_{3.99}Sn_{1.01}$	28.55	-	47.0	0.040	0.003	0.008	24.0Sn,0.12Si
3	T-82922	MNi_4Sn	$M_{0.99}Ni_{4.01}Sn_{0.99}$	-	28.4	48.0	0.020	0.009	0.031	23.9Sn
3	T-81785	$MNi_{4.3}Al_{0.7}$	$M_{0.98}Ni_{4.30}Al_{0.70}$	-	33.5	61.4	0.029	0.005	0.043	4.6Al,1.1Fe
4	T-82894	$LaNi_4Cu$	$La_{0.98}Ni_{4.04}Cu_{0.96}$	31.0	-	53.2	0.026	0.005	0.006	13.9Cu,0.50Cr
4	T-82896	$LaNi_{4.5}Pd_{0.5}$	$La_{1.00}Ni_{4.50}Pd_{0.50}$	30.3	-	57.75	0.034	0.004	-	-
4	T-82921	$LaNi_{4.7}Sn_{0.3}$	$La_{0.99}Ni_{4.70}Sn_{0.30}$	30.6	-	61.2	0.016	0.005	0.006	7.8Sn
4	T-82919	$LaNi_{4.8}Co_{0.2}$	$La_{0.97}Ni_{4.78}Co_{0.22}$	32.2	-	67.1	0.017	0.005	0.63	-
4	T-80854	$MNi_{4.3}Mn_{0.7}$	$M_{0.98}Ni_{4.3}Mn_{0.69}$	-	32.1	59.4	0.14	0.022	-	8.8Mn
5	T-82897	$LaNi_{4.8}B_{0.2}$	$La_{0.95}Ni_{4.83}B_{0.17}$	31.2	-	66.7	0.036	0.004	0.017	0.435B,0.027Al
5	T-82898	$LaNi_{4.9}S_{0.1}$	$La_{0.94}Ni_{4.998}S_{0.002}$	29.9	-	67.2	0.018	0.004	0.009	0.015S,0.012Al
5	T-82899	$LaNi_{4.9}Se_{0.1}$	$La_{0.99}Ni_{4.97}Se_{0.03}$	31.8	-	67.8	0.021	0.003	0.006	0.051Se,0.010Al
6	T-82889	$Mg_{0.1}La_{0.9}Ni_5$	$Mg_{0.19}La_{0.91}Ni_5$	29.6	-	68.8	0.014	0.003	0.004	1.08Mg
6	T-82888	$Ca_{0.2}La_{0.8}Ni_5$	$Ca_{0.21}La_{0.81}Ni_5$	26.9	-	70.55	0.039	0.008	0.013	1.91Ca,0.018Al
6	T-82900	$Sr_{0.2}La_{0.8}Ni_5$	$Sr_{0.18}La_{0.80}Ni_5$	26.3	-	69.7	0.051	0.010	0.009	3.8Sr,0.021Al
6	T-82901	$Ba_{0.2}La_{0.8}Ni_5$	$Ba_{0.13}La_{0.77}Ni_5$	25.5	-	70.0	0.19	0.006	0.034	4.1Ba,0.22Al
7	T-82918	$LaNi_3$	$LaNi_{2.99}$	44.1		55.7	0.066	0.001	0.027	

TABLE III

EFFECT OF Pd TREATMENT
ON ABSORPTION KINETICS*

*Time in seconds to charge
0.05 g-mole H at P $\approx 1.2 P_a$ at 25°C

ALLOY	ORIGINAL	LONG AIR EXPOSURE		SHORT AIR EXPOSURE	
		(Fresh)	(Cycled)	(Fresh)	(Cycled)
$LaNi_5$	67	1620	120	250	153
$LaNi_5$ + Pd(E.D.)	-	600	141	280	138
$LaNi_5$ + Pd(M.A.)	-	>3000	510	>2000	330
$LaNi_{4.9}Al_{0.1}$	120	∞	120	-	-
$LaNi_{4.9}Al_{0.1}$ + Pd(E.D.)	-	351	102	216	138

TABLE IV

COMPARATIVE STUDY OF STATIC HYDRIDING RESULTS

Category No.	Composition	Condition*	25°C Static Isotherm Data**				
			Pa	Pd	(Slope)d	Hysteresis	Plateau ΔH/M
0	$LaNi_5$	AC	2.0	1.65	0.09	0.19	0.84
0	$LaNi_{4.9}Al_{0.1}$	ST	1.3	1.2	0.20	0.08	0.83
0	$LaNi_3Co_2$	ST	0.27	0.23	0.77	0.16	0.52
1	$LaNi_{5.67}$	ST+A	2.9	2.4	0.18	0.19	0.68
1	$LaNi_{11.5}$	AC	4.4	1.7	2.15	0.95	0.30
2	$SmCo_5$	ST+A	4.7	4.3	0.00	0.09	0.33
3	$LaNi_{3.8}Fe_{1.2}$	AC	0.48	0.42	1.34	0.13	0.38
3	$MNi_{4.3}Al_{0.7}$	ST	0.67	0.58	0.57	0.14	0.46
4	$LaNi_{4.5}Pd_{0.5}$	AC	2.4	2.1	0.12	0.13	0.46
4	$LaNi_{4.7}Sn_{0.3}$	AC	0.62	0.60	2.53	0.03	0.68
4	$LaNi_{4.8}Co_{0.2}$	AC	2.8	1.95	0.39	0.36	0.80
4	$MNi_{4.3}Mn_{0.7}$	ST	2.85	1.75	0.36	0.49	0.38
6	$Mg_{0.1}La_{0.9}Ni_5$	AC	2.45	2.25	0.70	0.09	0.72
6	$Ca_{0.2}La_{0.8}Ni_5$	AC	1.8	1.55	0.86	0.15	0.90
6	$Sr_{0.2}La_{0.8}Ni_5$	AC	1.85	1.65	0.37	0.11	0.68
6	$Ba_{0.2}La_{0.8}Ni_5$	AC	3.4	2.9	0.58	0.16	0.75
8	See Table III						

* AC = As Cast; ST = Solution Treated (annealed); A = Aged

** See Fig. 1 for definition of terms

TABLE V

COMPARATIVE SUMMARY OF REFERENCE ALLOY DYNAMIC HYDRIDING RESULTS

Composition	Condition	Nom. Test Temp. °C	Dynamic Plateau Pressures P_a atm	P_d atm	Time (sec.) to 0.05 g-atom H reacted (0.45 H/M) Absorption Absolute 2 atm	Absorption Absolute 5 atm	Absorption Reduced 1.2 P_a	Absorption Reduced 2 P_a	Desorption Absolute 1 atm	Desorption Absolute 0.3 Atm	Desorption Reduced 0.8 P_d	Desorption Reduced 0.5 P_d	Thermal Contribution, R, at 2 P_a(b)
$LaNi_5$	AC	15	1.66	0.88	45	4.4	51	12	∞	13	47	19	1.0
		25	2.31	1.50	∞	7.6	65	9.5	30	9.6	43	20	1.0
		35	3.33	2.38	∞	16	44	7.8	17	8.0	57	19	1.0
		45	4.76	3.54	∞	90	40	7.0	12	7.0	44	19	1.0
$LaNi_{4.9}Al_{0.1}$	ST	25	1.63	1.09	130	11	130	25	900	4.6	250	72	0.7
		35	2.42	1.70	∞	14	90	16	50	26	110	43	0.8
		45	3.54	2.72	∞	24	54	10	23	15	76	29	1.0
$LaNi_3Co_2$	ST	25	0.35	0.24	23	6.4	1000	150	∞	∞	(c) (600)	(300)	0.3
		35	0.56	0.39	21	6.2	800	63	∞	(360)	(400)	(200)	0.4
		45	0.82	0.60	21	5.0	160	35	∞	(130)	(300)	(130)	0.6

(a) AC = As-Cast; ST = Solution treated.

(b) $R = (T_{max}-T_N)/(T_{VH}-T_N)$ where T_N = Nominal Test Temperature, T_{VH} = Van't Hoff Temperature, Values of R = 1 imply complete thermal control of reaction kinetics, R = 0 implies no thermal control.

(c) Values in Parentheses are Estimates.

TABLE VI

COMPARATIVE SUMMARY OF DYNAMIC HYDRIDING RESULTS AT 25°C [a]

Cat. No.	Composition	(b) Condition	Cycles to Activate	Dynamic Plateau Pressures P_a (atm)	Dynamic Plateau Pressures P_d (atm)	Time(sec.) to Absorb 0.05 g-atom H (0.45 H/M) Absolute 2 atm	Absolute 5 atm	Reduced $1.2P_a$	Reduced $2P_a$	Thermal Contribution, R, at $2P_a$(c)
0	$LaNi_5$	AC	4	2.31	1.50	∞	7.6	65	9.5	1.0
0	$LaNi_{4.9}Al_{0.1}$	ST	9	1.63	1.16	130	11	130	[illegible]	0.7
0	$LaNi_3Co_2$	ST	4	0.35	0.24	23	6.4	1000	1[illegible]5	0.3
1	$LaNi_{5.67}$	ST+A	10	3.40	-	∞	47	111	22	0.4
1	$LaNi_{11.5}$	AC	11	(5.4)	(3.6) [d]	∞	∞	∞	>1000	-
3	$LaNi_{3.8}Fe_{1.2}$	AC	1	0.82	-	350	80	(2000)	510	(0.3)
3	$MNi_{4.3}Al_{0.7}$	ST	4	0.95	-	32	6	150	35	0.7
4	$LaNi_{4.5}Pd_{0.5}$	AC	5	3.81	2.38	∞	45	75	105	0.5
4	$LaNi_{4.7}Sn_{0.3}$	AC	2	0.61	0.41	(7)	16	(500)	(1[illegible])	(0.2)
4	$LaNi_{4.8}Co_{0.2}$	AC	24	5.10	2.52	∞	90	28	[illegible]	1.3
4	$MNi_{4.3}Mn_{0.7}$	ST	5	3.61	1.50	∞	43	100	22	0.7
6	$Mg_{0.1}La_{0.9}Ni_5$	AC	16	3.47	-	∞	52	120	24	0.4
6	$Ca_{0.2}La_{0.8}Ni_5$	AC	3	2.18	-	∞	32	170	42	0.3
6	$Sr_{0.2}La_{0.8}Ni_5$	AC	2	1.97	-	500	19	170	32	0.6
6	$Ba_{0.2}La_{0.8}Ni_5$	AC	4	4.08	2.72	∞	90	120	20	0.8

(a) Nominal Test Temperature.
(b) AC = As Cast; ST = Solution Treated (annealed); A = Aged
(c) See Definition in Table V
(d) Values in Parentheses are Estimates.

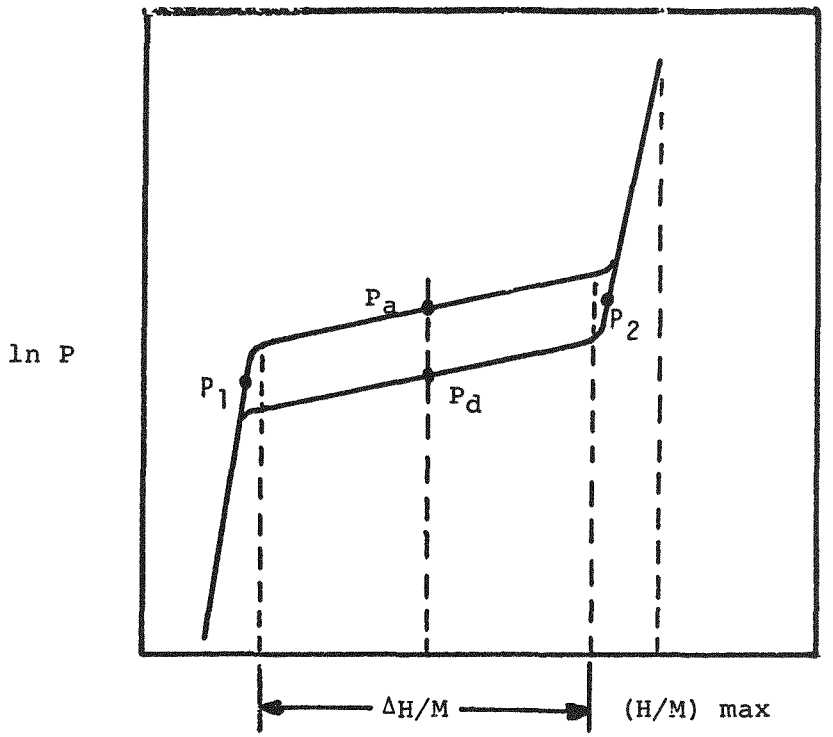

$\Delta H/M$ = Plateau Width (Usable Capacity)

(H/M) max = Maximum Capacity

P_d = Desorption Pressure at Mid-Plateau, atm.

P_a = Absorption Pressure at Mid-Plateau, atm.

$\frac{d \ln P_d}{d(H/M)}$ = Desorption Plateau Slope (at plateau midpoint).

$\ln \frac{P_a}{P_d}$ = Hysteresis (at plateau midpoint).

P_1, P_2 = Kinetic Test Starting Pressures

Figure 1. Definitions of Hydriding Properties (Especially Used in Table III)

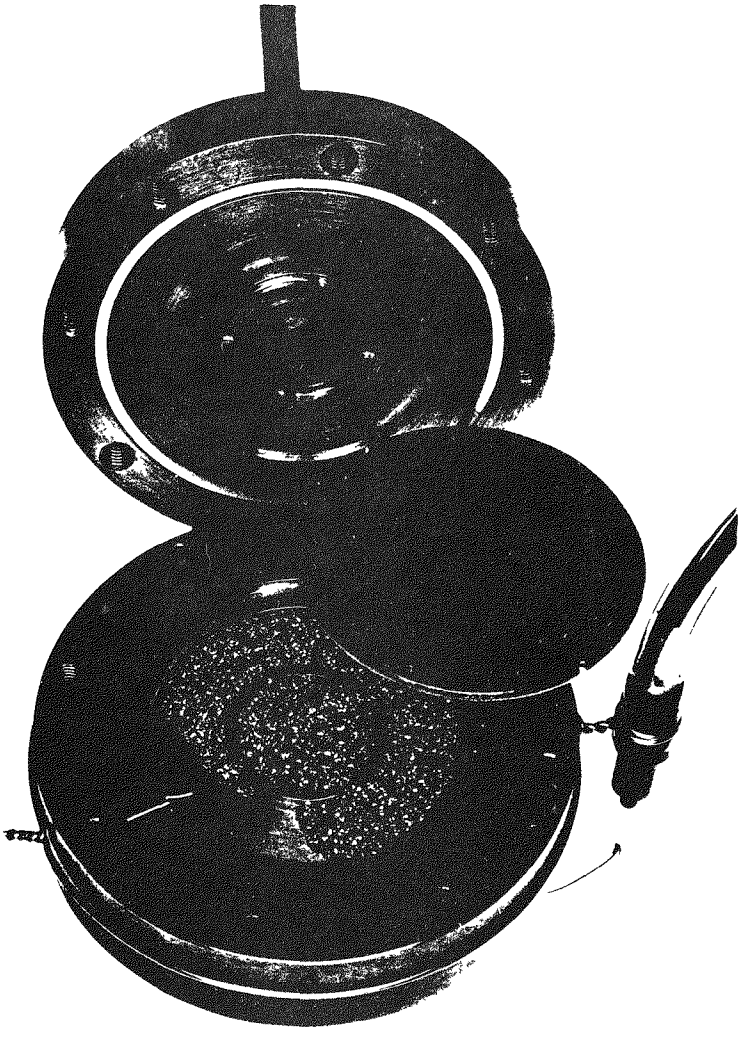

Figure 2. Photograph of the thin disc sample holder used for the dynamic hydriding tests. The sample powder has been partially removed to show the position of the rapid response thermocouple (at arrow).

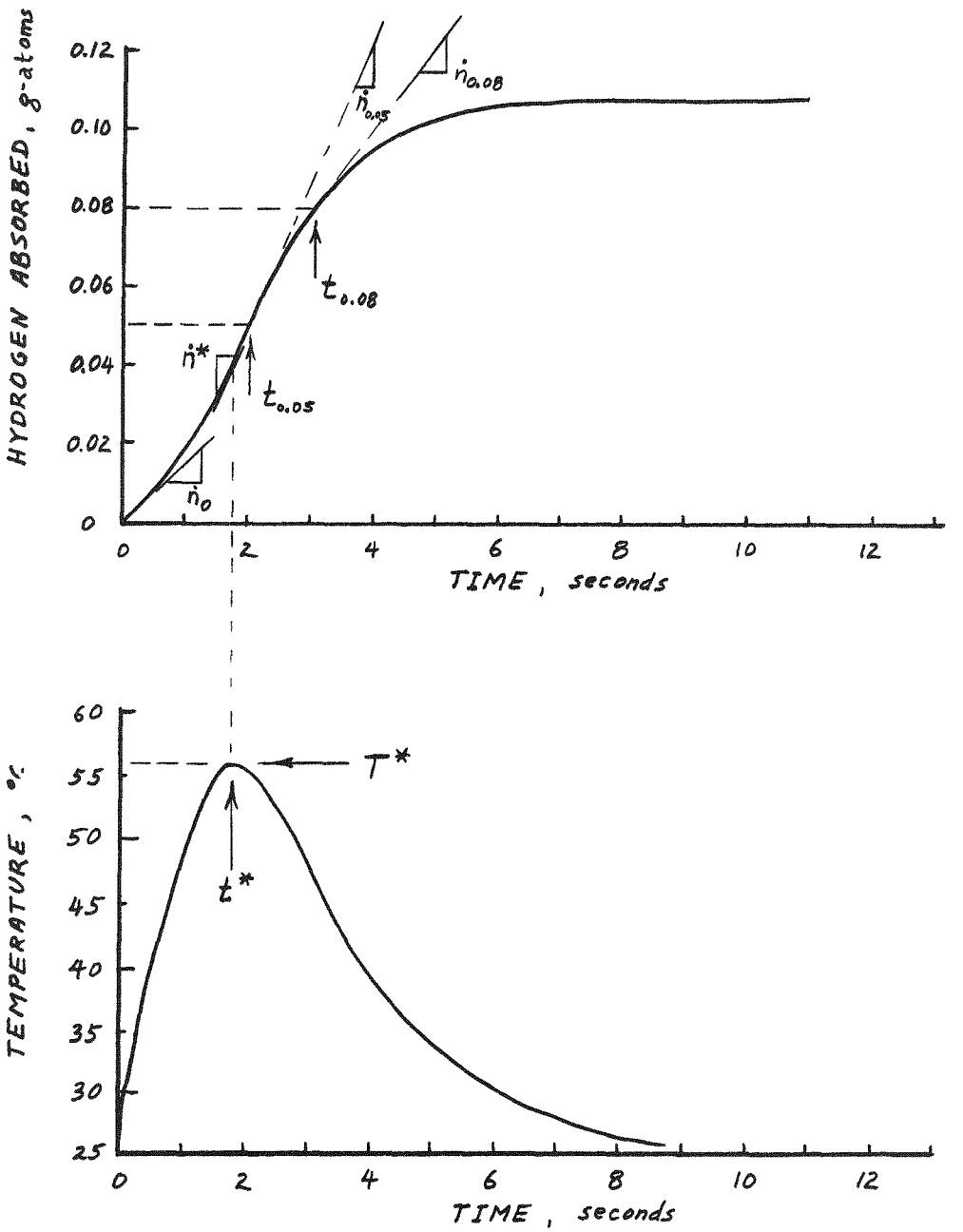

Figure 3. Schematic illustration of kinetic test reaction and temperature response curves showing the definitions of the derived parameters used to characterize the reaction.

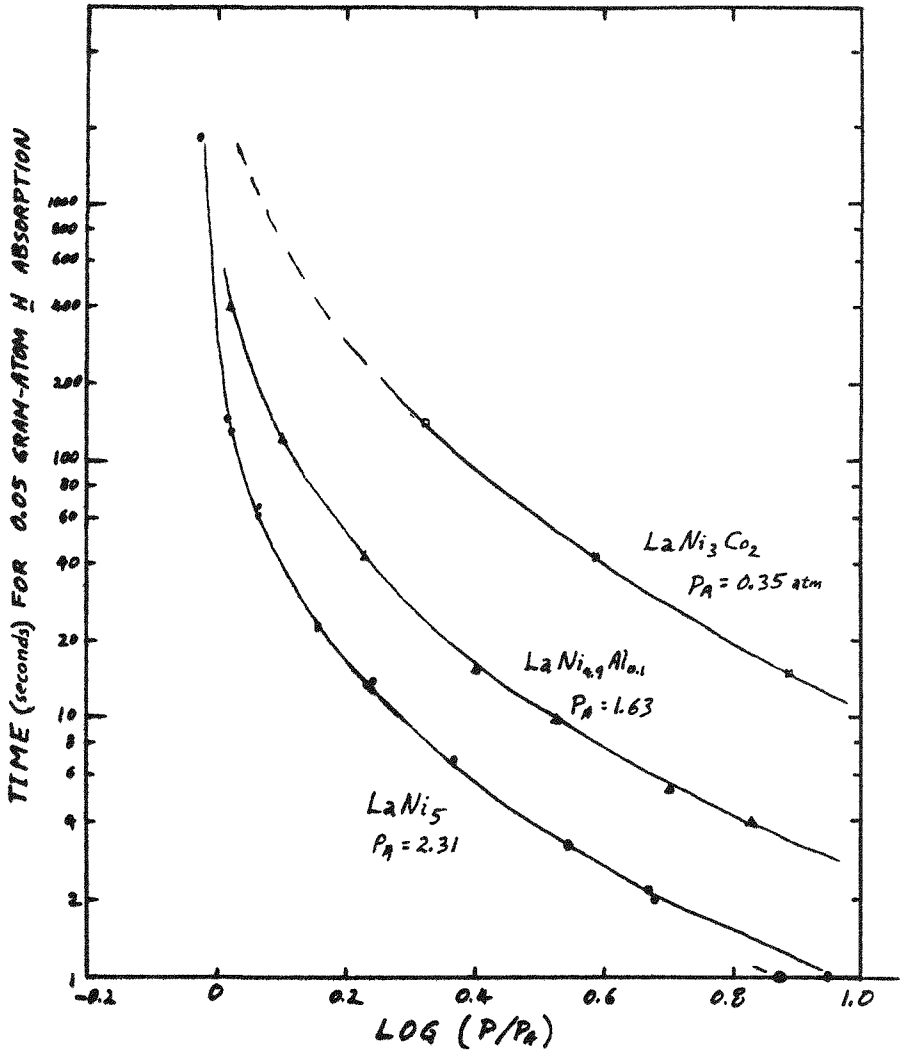

Figure 4. Reduced pressure comparison of absorption kinetics for the three reference alloys at 25°C.

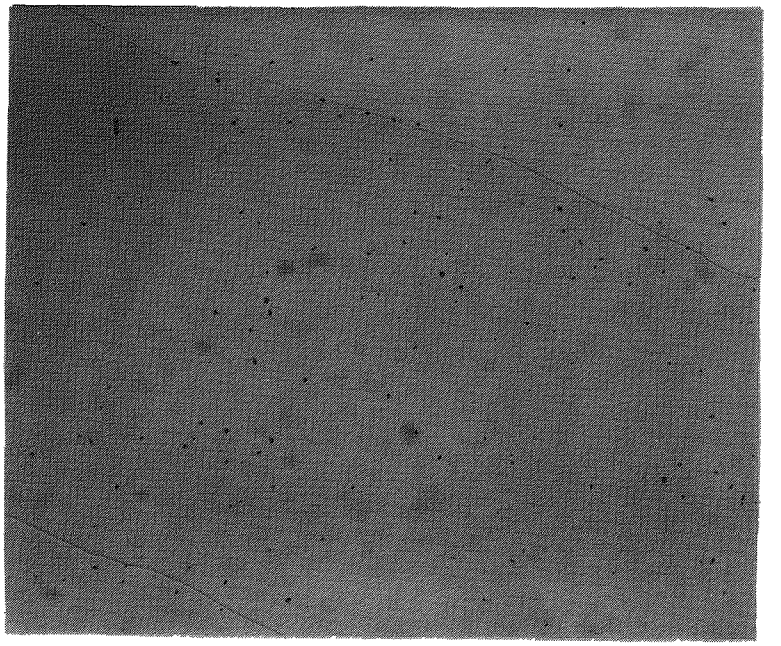

PN 1-71132 200X

Figure 0-1-1. As-Cast Microstructure of $LaNi_5$.

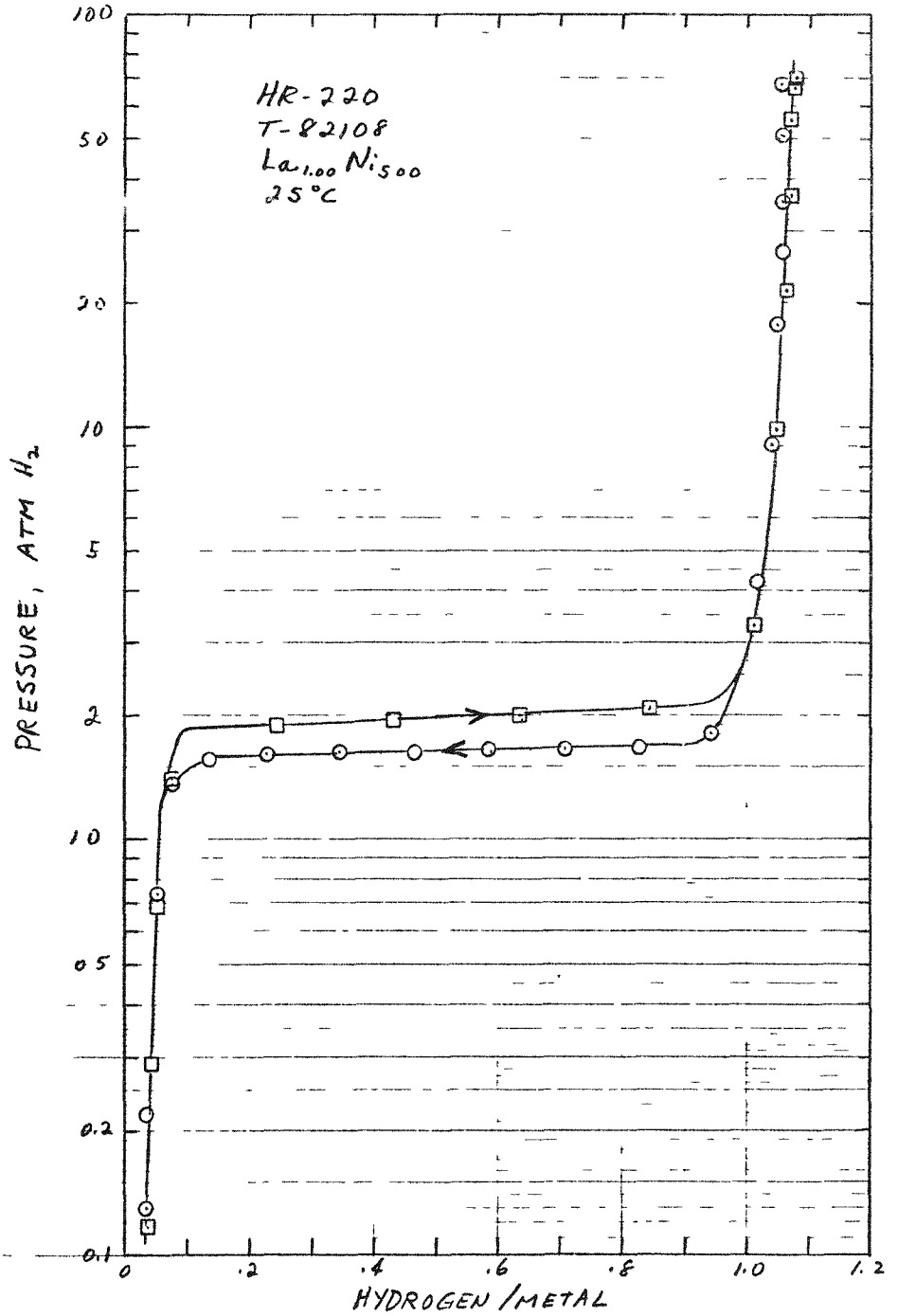

Figure 0-1-2. Static 25°C Isotherms for As-Cast $LaNi_5$.

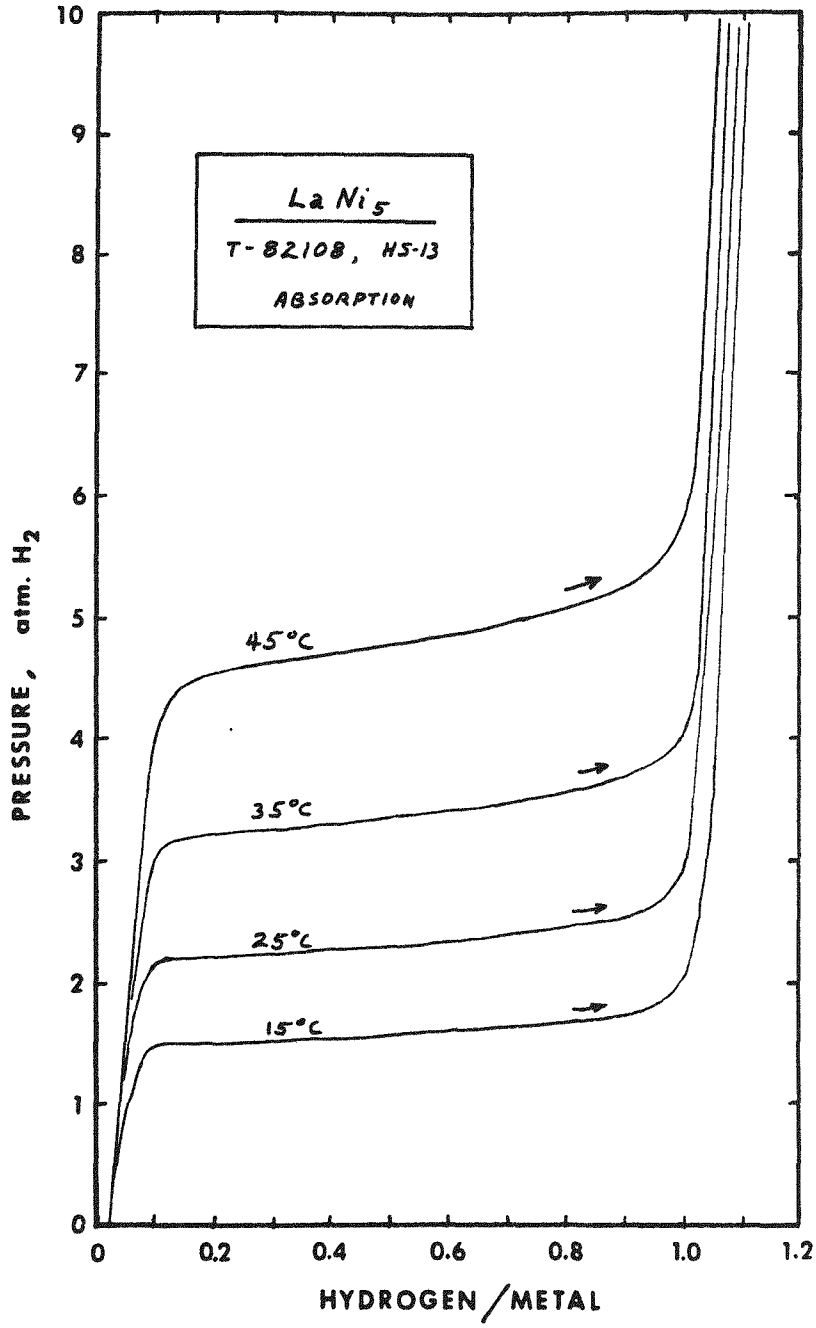

Figure 0-1-3. Dynamic pressure-composition absorption isotherms for $LaNi_5$ determined at a reaction rate of 0.0027 g-atom H/min. (0.024 H/M/min.). Actual temperatures are about 0.3°C higher than the indicated nominal.

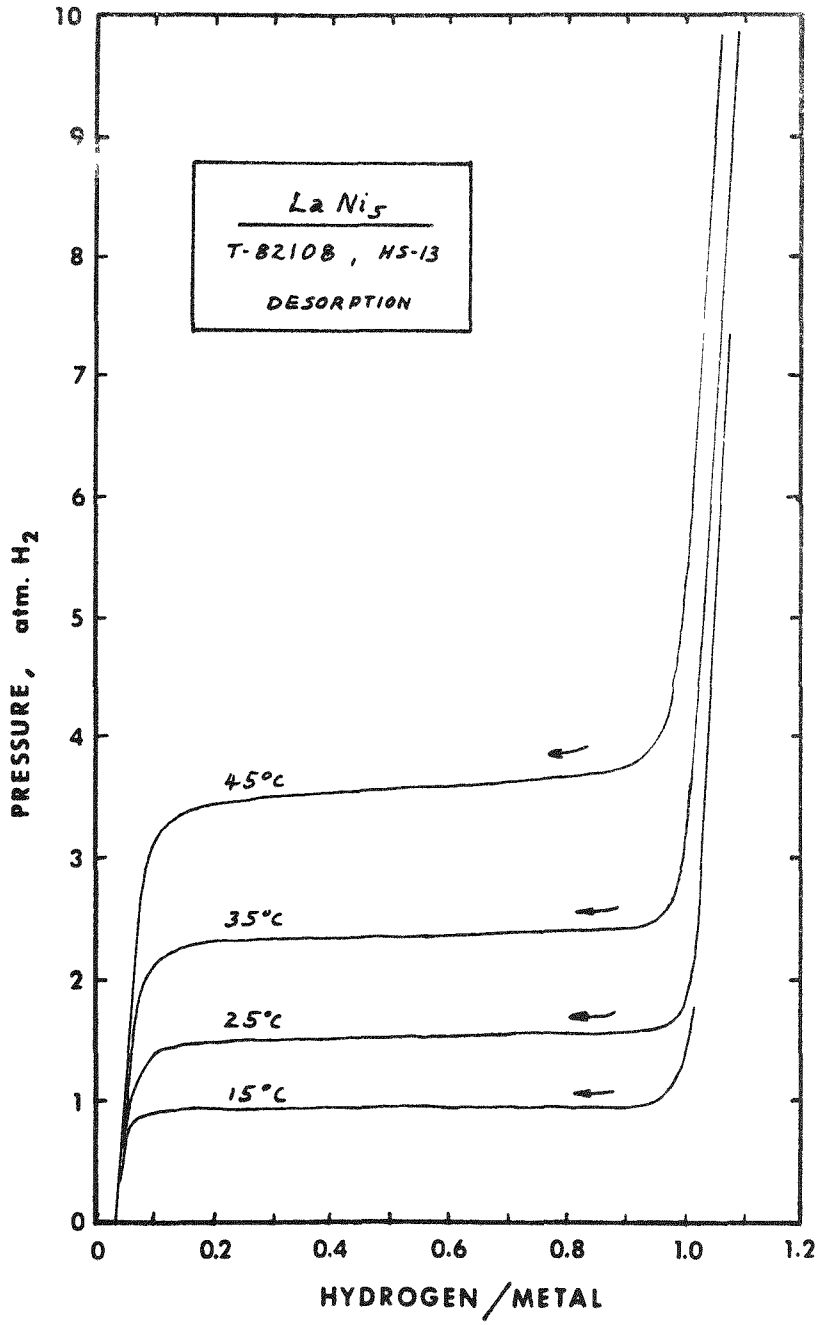

Figure 0-1-4. Dynamic pressure-composition desorption isotherms for $LaNi_5$ determined at a reaction rate of 0.0027 g-atom/min. (0.024 H/M/min.). Actual temperatures are about 0.3°C lower than the indicated nominal.

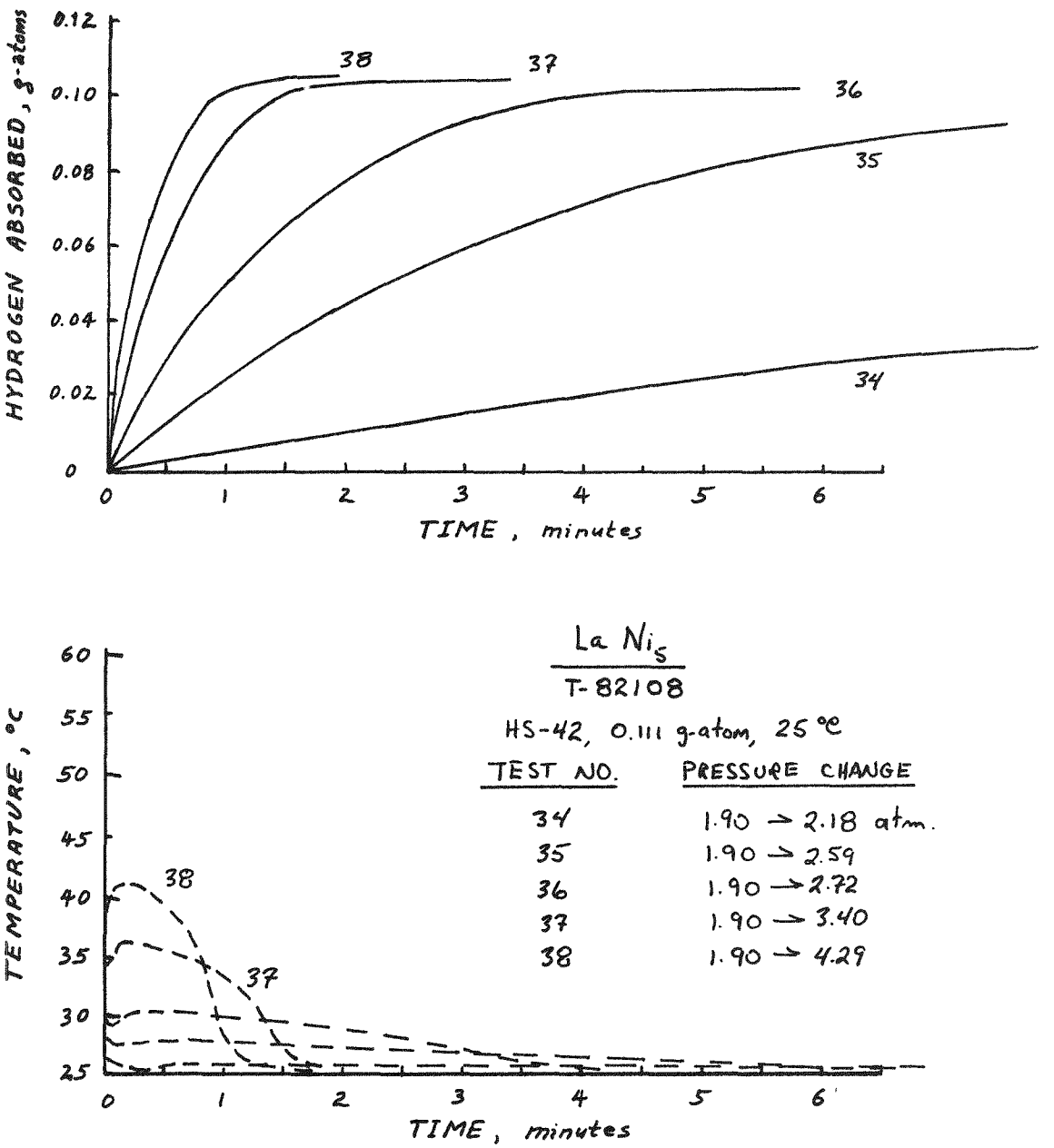

Figure 0-1-5. Time response data for the reaction mass and instantaneous temperature during isobaric absorption at a nominal temperature of 25 C.

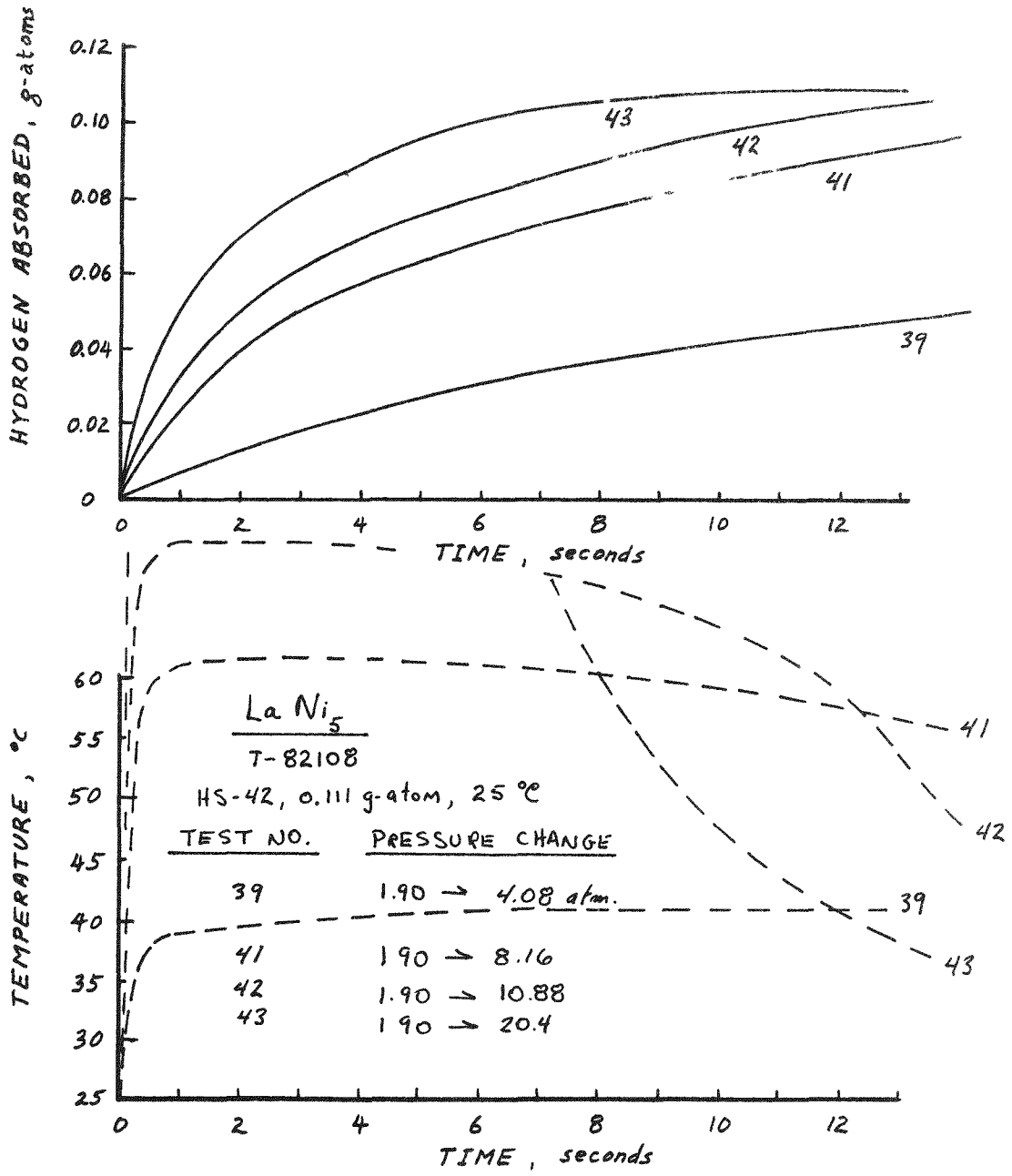

Figure 0-1-6. Time response data for the reaction mass and instantaneous temperature during isobaric absorption at a nominal temperature of 25 C.

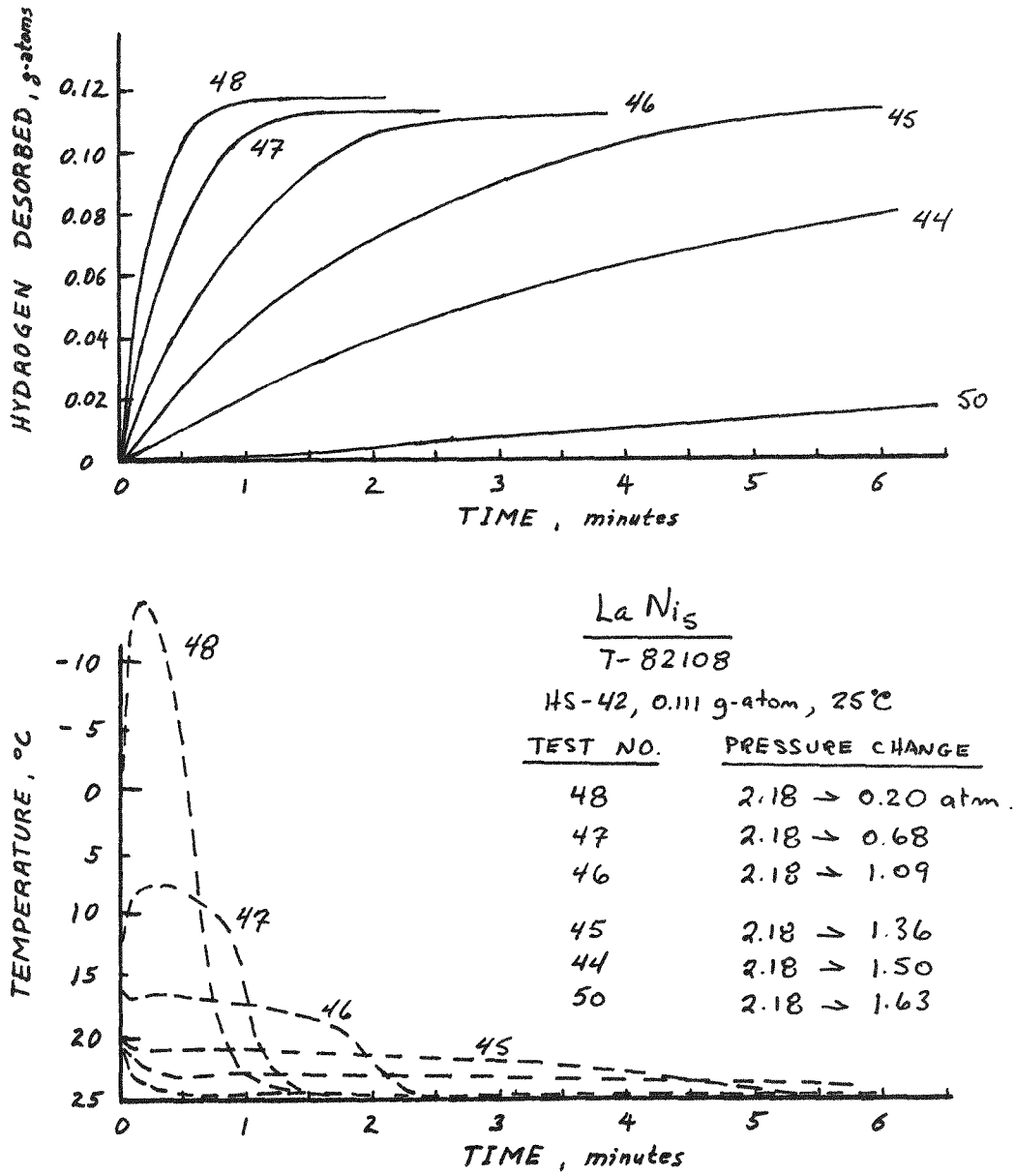

Figure 0-1-7. Time response data for the reaction mass and instantaneous temperature during isobaric desorption at a nominal temperature of 25 C.

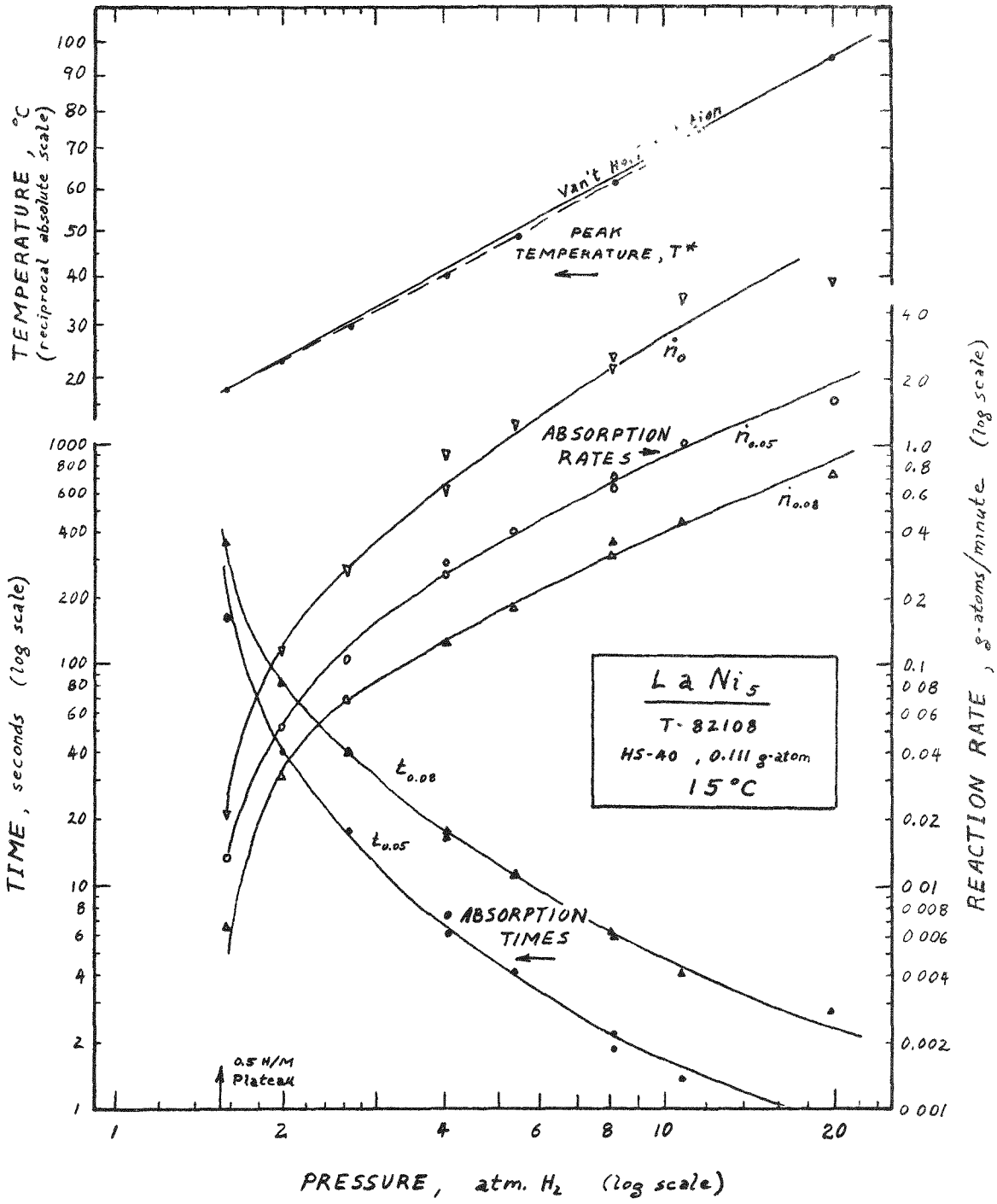

Figure 0-1-8. Summary of $LaNi_5$ absorption kinetic data at 15°C showing the maximum temperature excurstion as well as the reaction rate and time parameters.

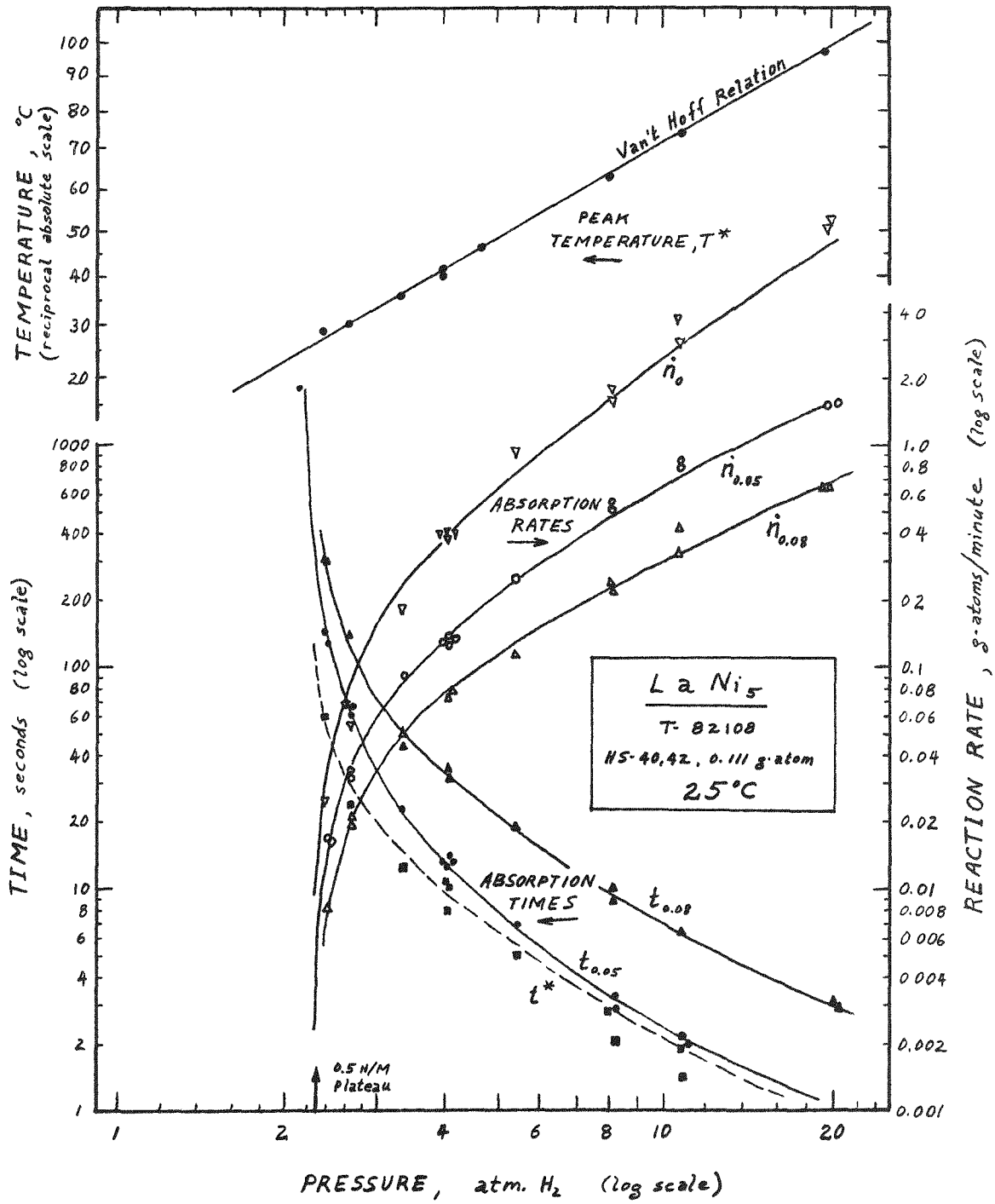

Figure 0-1-9. Summary of $LaNi_5$ absorption kinetic data at 25°C showing the maximum temperature excursion as well as the reaction rate and time parameters.

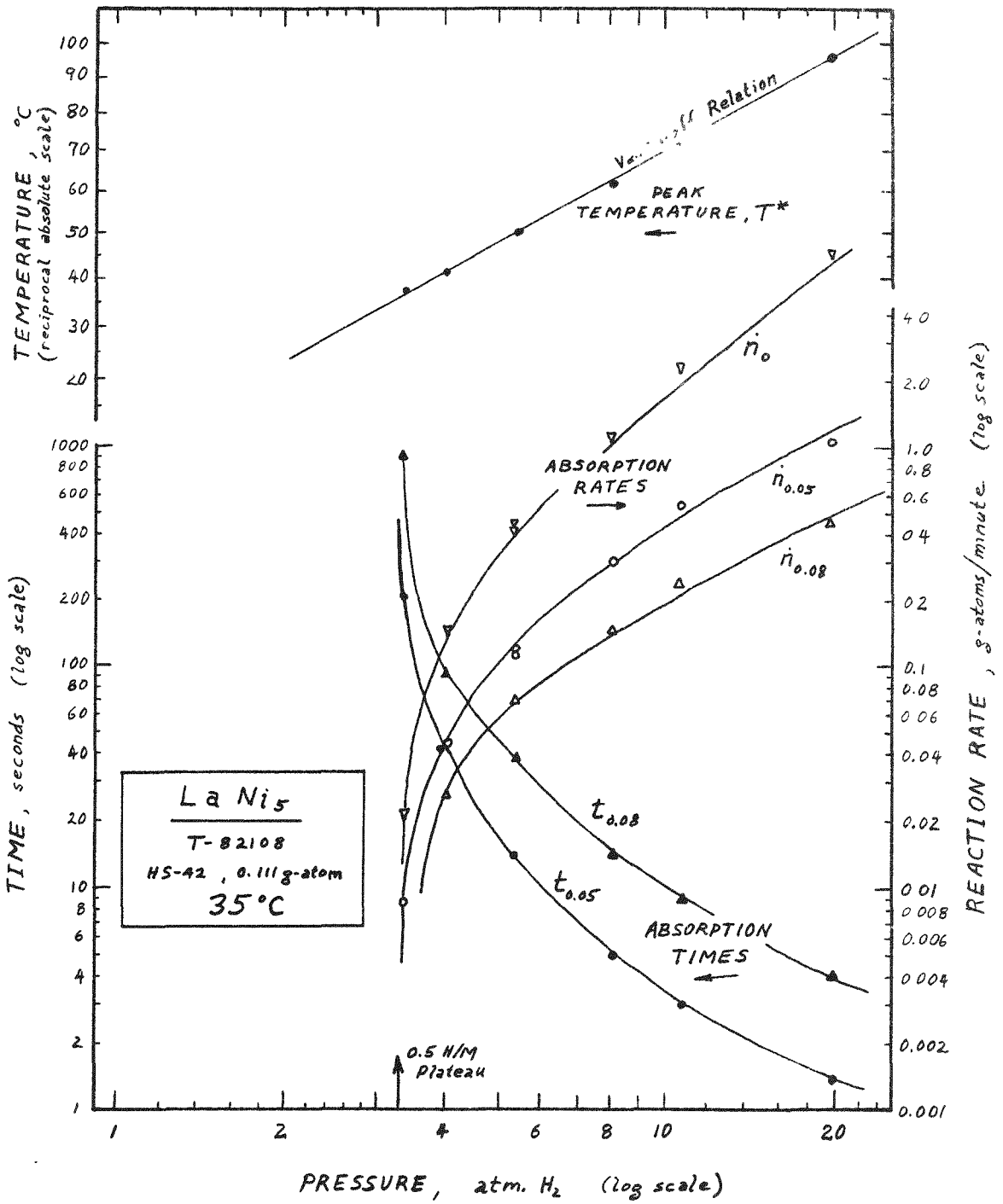

Figure 0-1-10. Summary of $LaNi_5$ absorption kinetic data at 35°C showing the maximum temperature excursion as well as the reaction rate and time parameters.

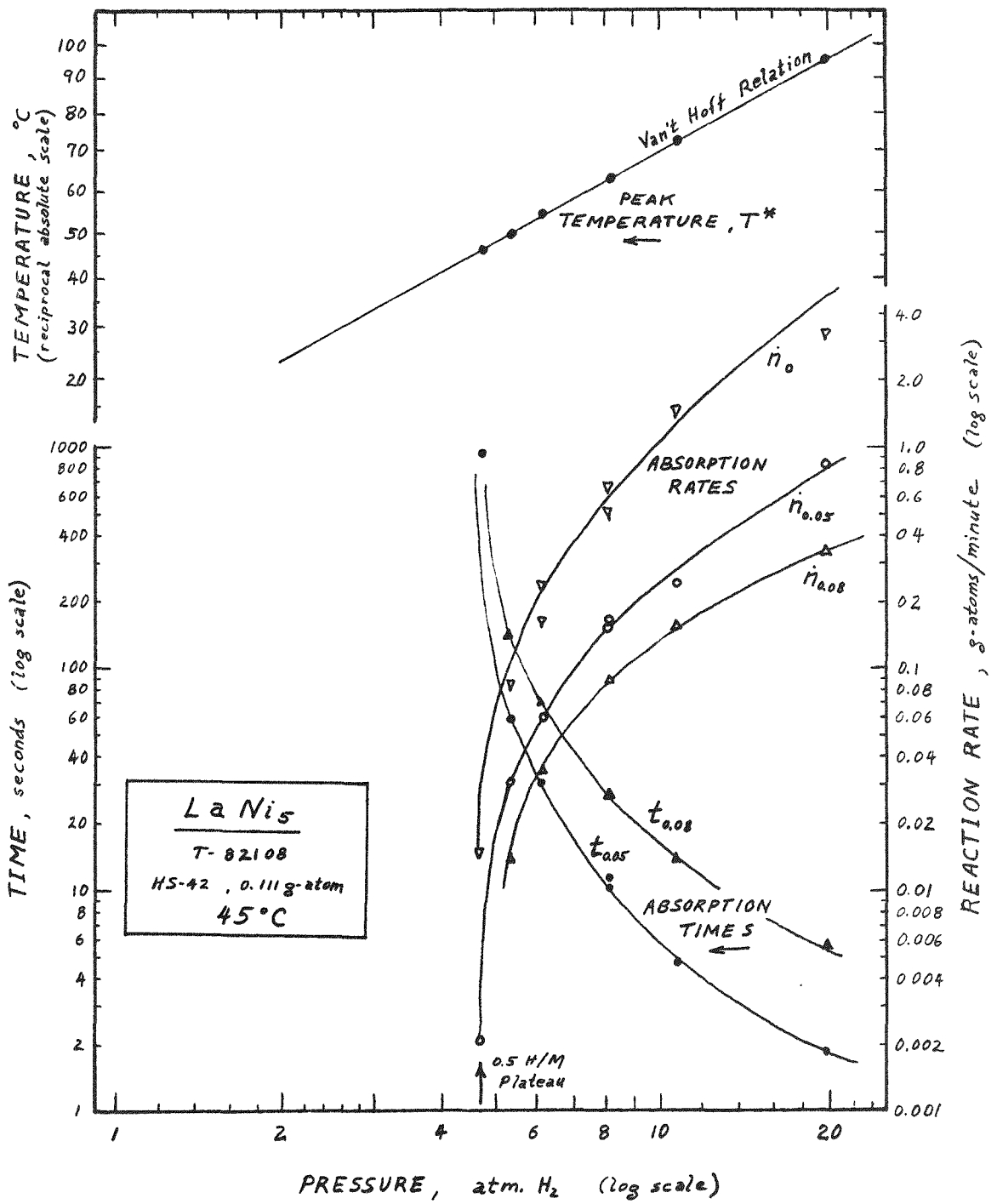

Figure 0-1-11. Summary of $LaNi_5$ absorption kinetic data at 45°C showing the maximum temperature excursion as well as the reaction rate and time parameters.

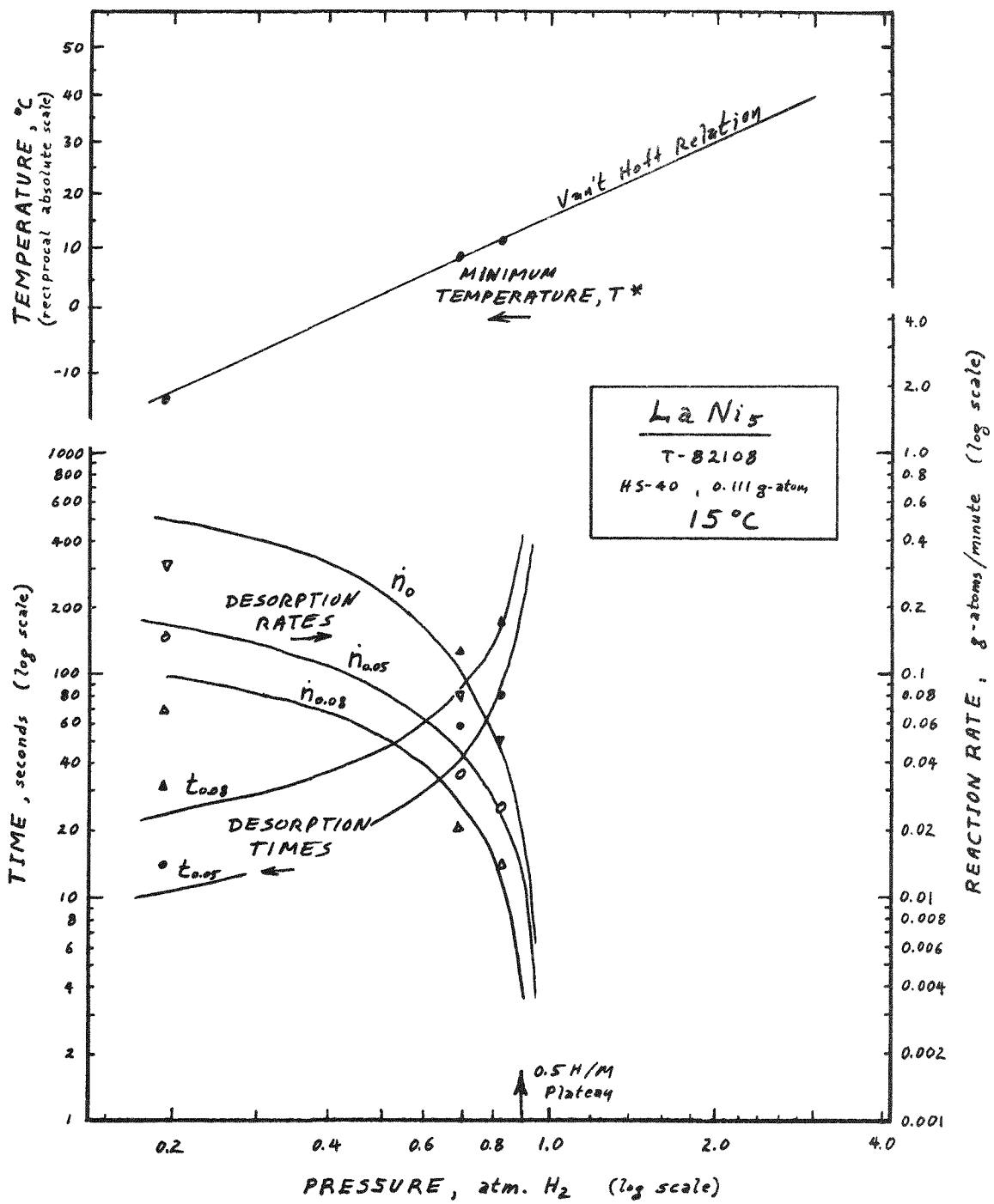

Figure 0-1-12. Summary of $LaNi_5$ desorption kinetic data at 15°C showing the minimum instantaneous temperature and the reaction rate and time parameters.

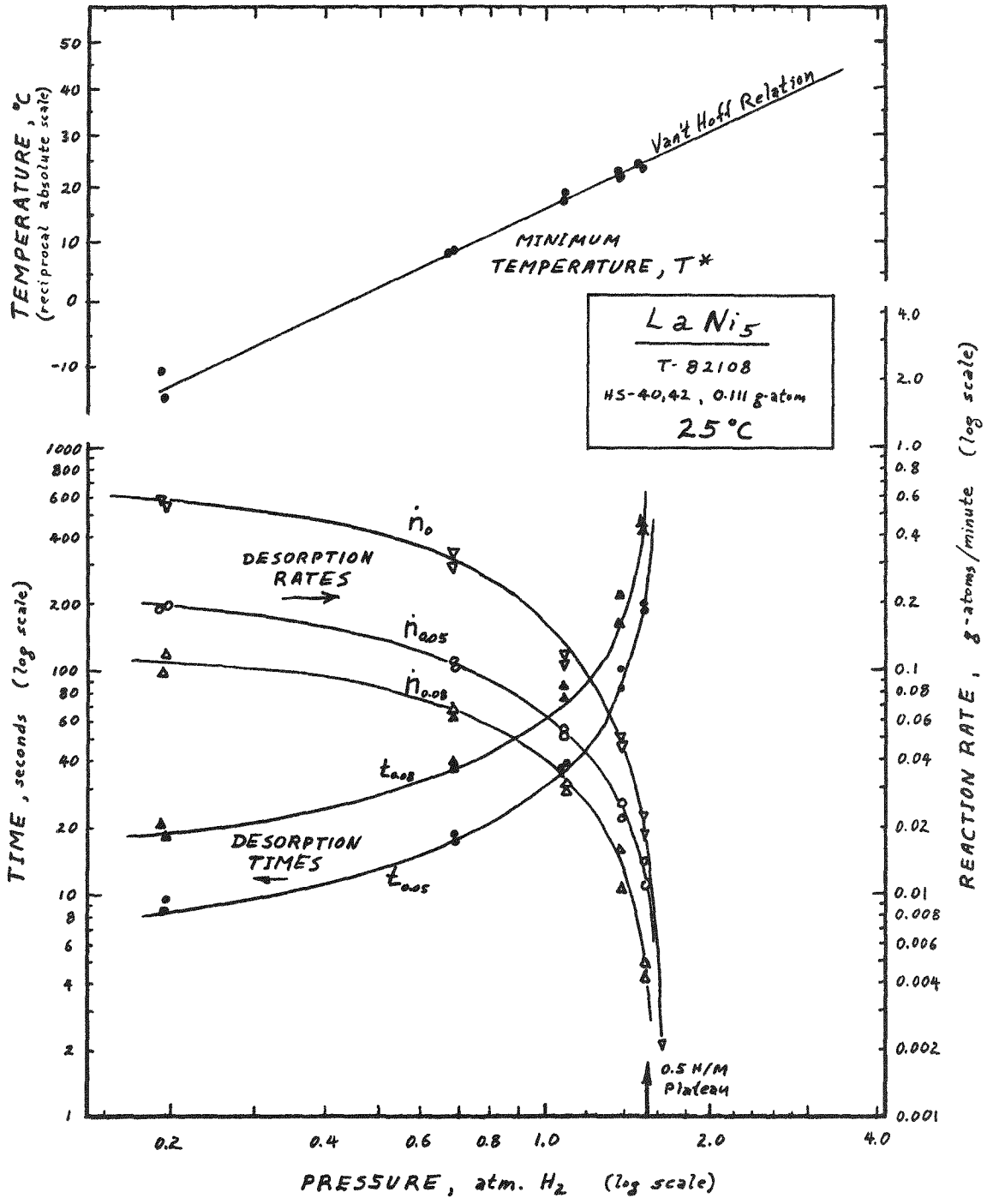

Figure 0-1-13. Summary of $LaNi_5$ desorption kinetic data at 25°C showing the minimum instantaneous temperature and the reaction rate and time parameters.

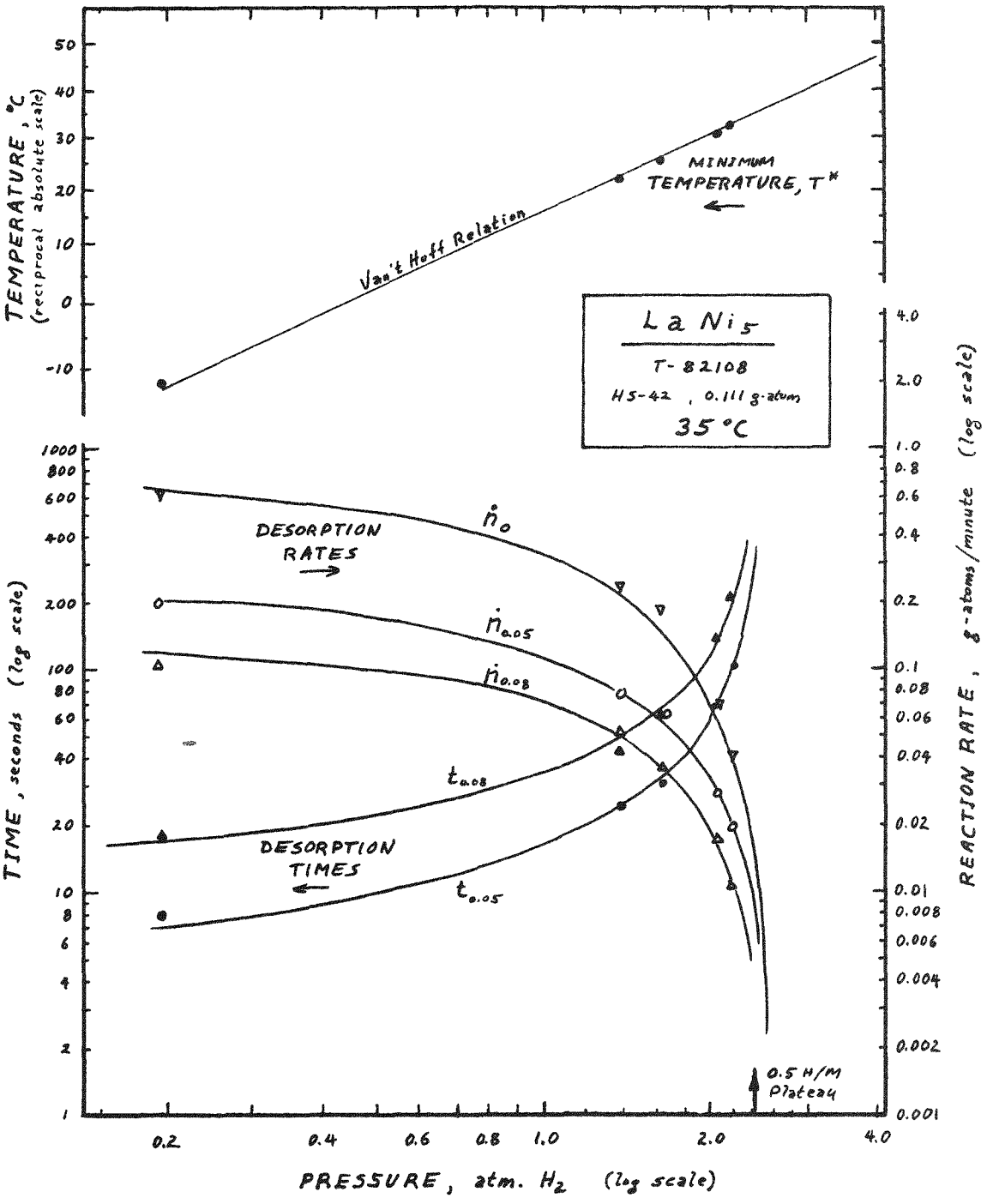

Figure 0-1-14. Summary of $LaNi_5$ desorption kinetic data at 35°C showing the minimum instantaneous temperatures and the reaction rate and time parameters.

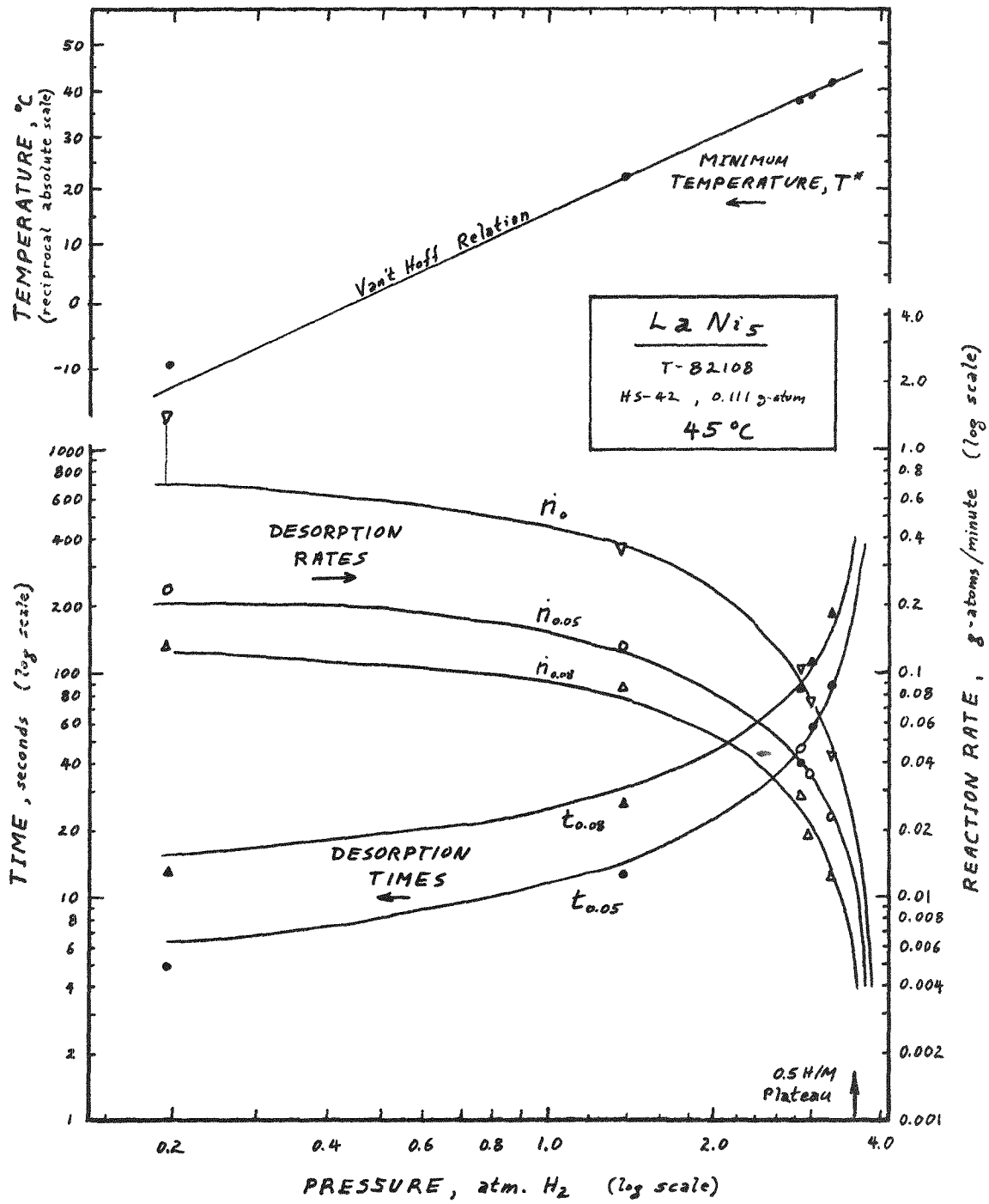

Figure 0-1-15. Summary of $LaNi_5$ desorption kinetic data at 45°C showing the minimum instantaneous temperatures and the reaction rate and time parameters.

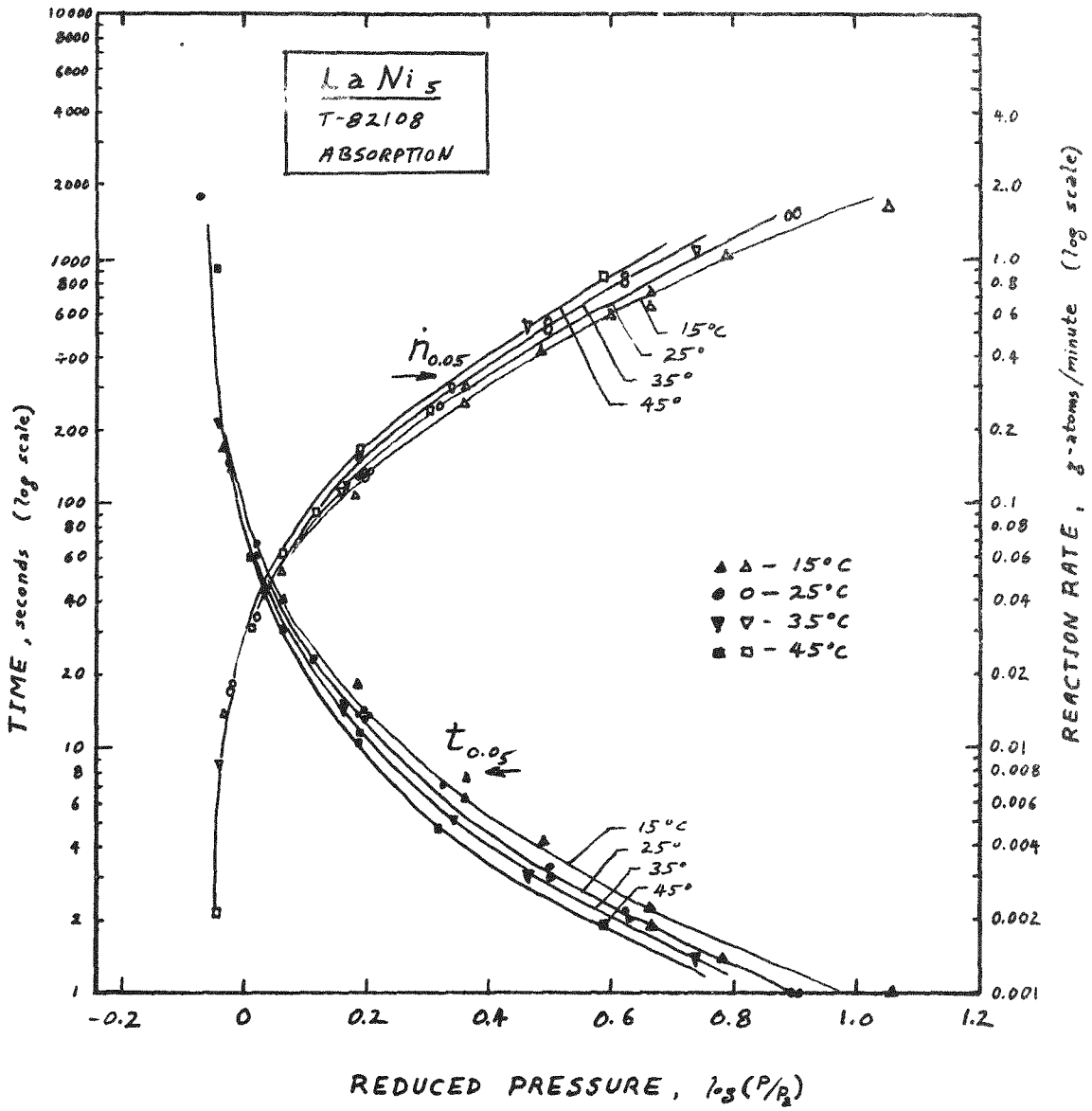

Figure 0-1-16. Comparison based on reduced pressure of $LaNi_5$ absorption kinetic data showing the rate and time to 0.05 g-atom H reacted at all pressures and temperatures tested.

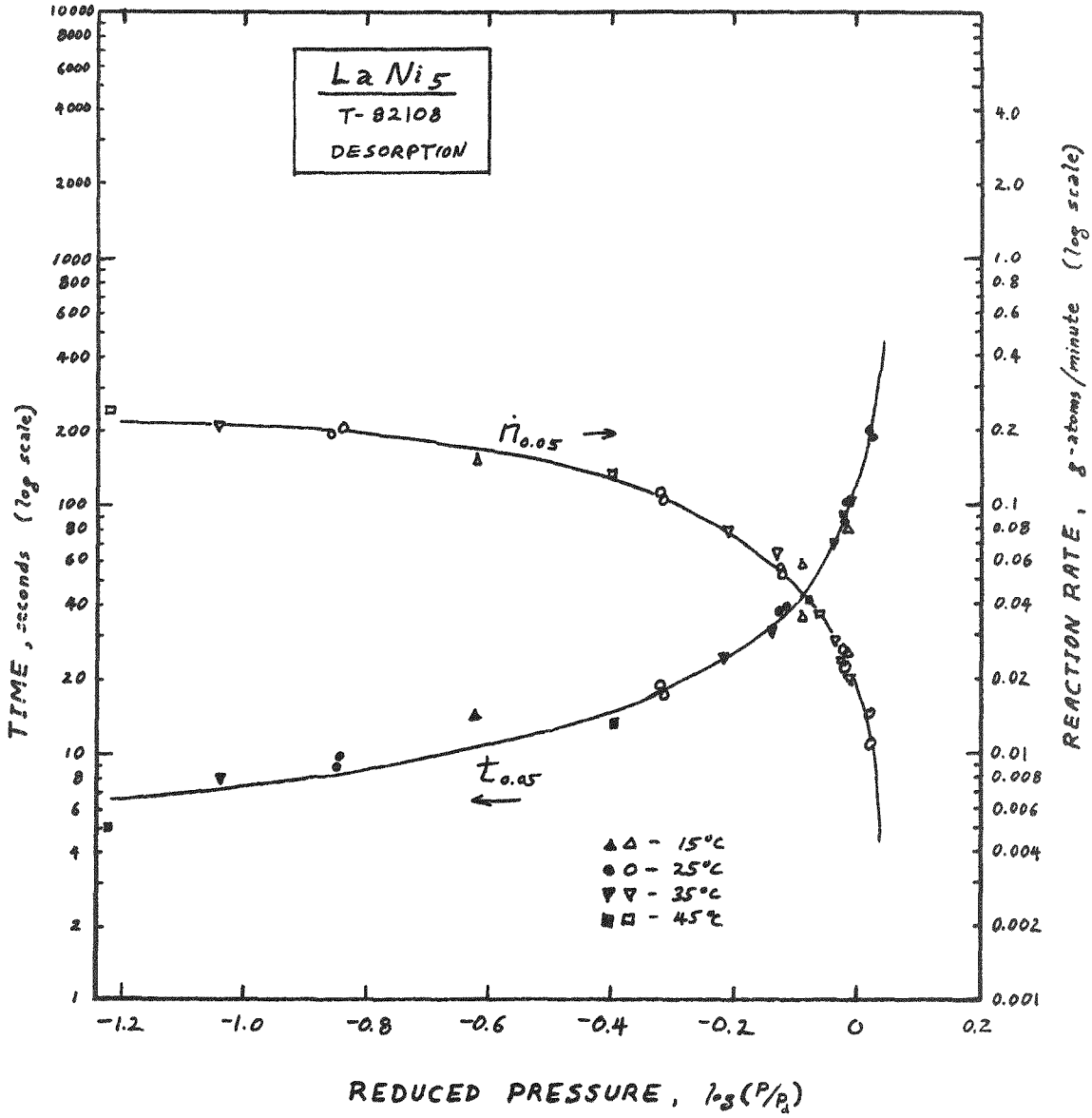

Figure 0-1-17. Comparison based on redcued pressure of $LaNi_5$ desorption kinetic data showing the rate and time to 0.05 g-atom H desorbed at all pressures and temperatures tested.

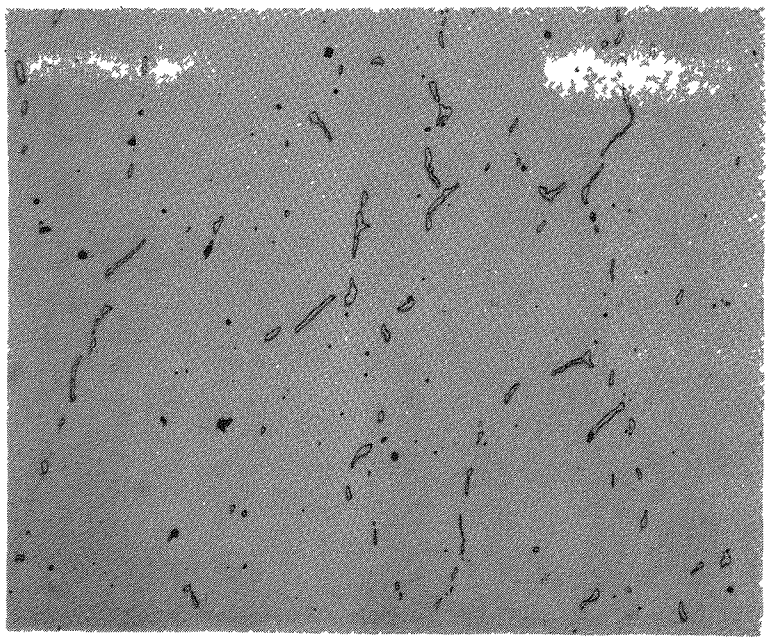

PN 1-72541 200X

Figure 0-2-1. Microstructure of $LaNi_{4.9}Al_{0.1}$, Annealed 4 Hours at 1125°C.

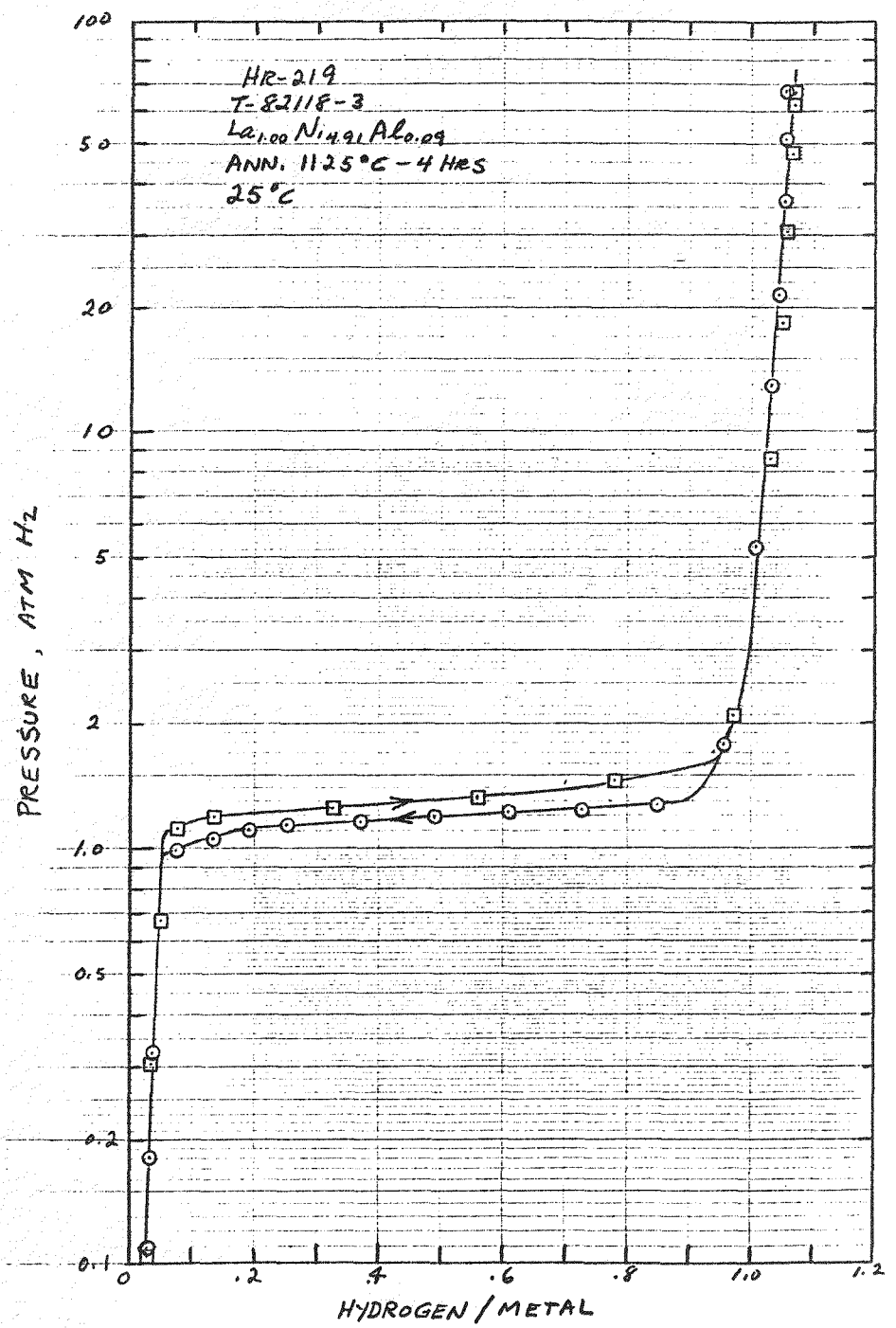

Figure 0-2-2. Static 25°C Isotherms for $LaNi_{4.9}Al_{0.1}$, Annealed 4 Hours at 1125°C.

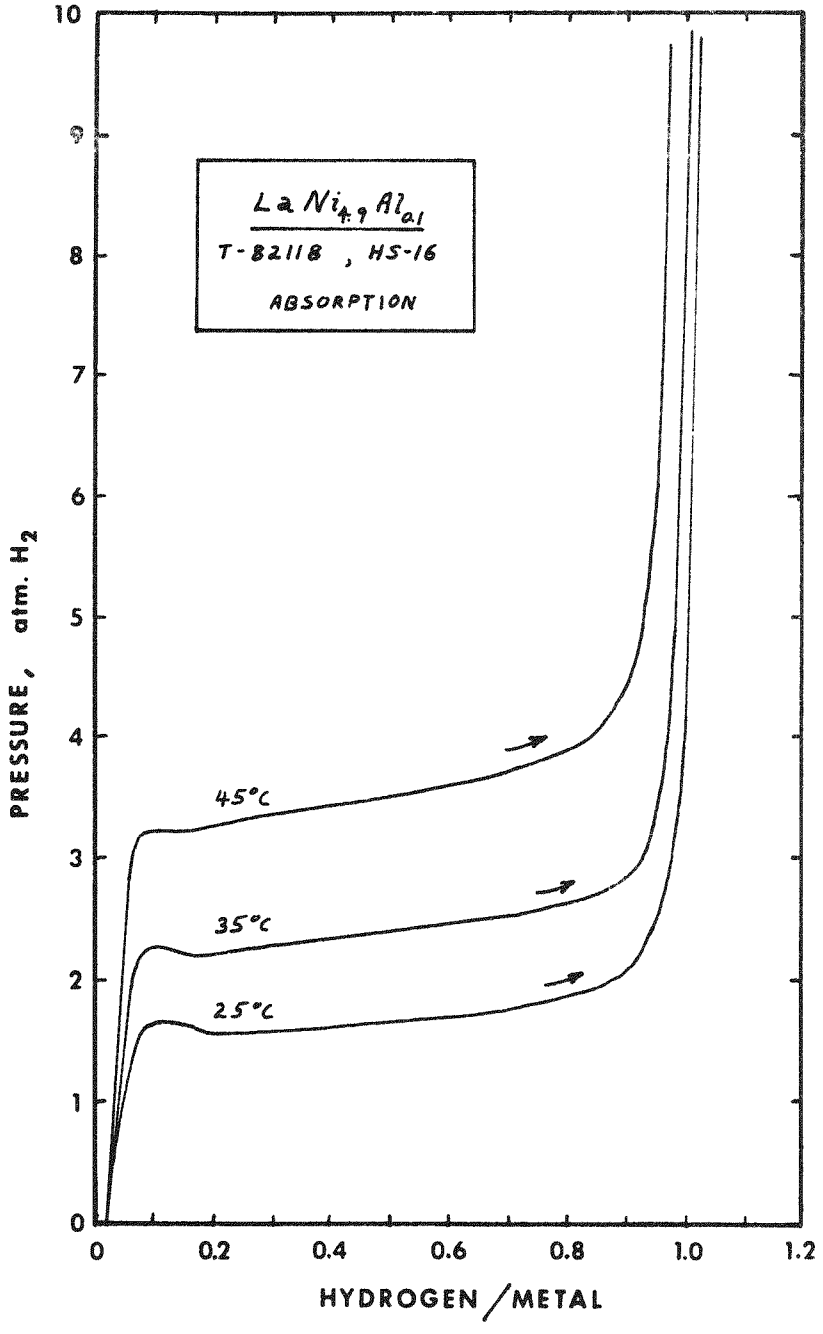

Figure 0-2-3. Dynamic pressure-composition absorption isotherms for $LaNi_{4.9}Al_{0.1}$ determined at a reaction rate of 0.0027 g-atom H/min. (0.024 H/M/min.). Actual temperatures are about 0.3°C higher than the indicated nominal.

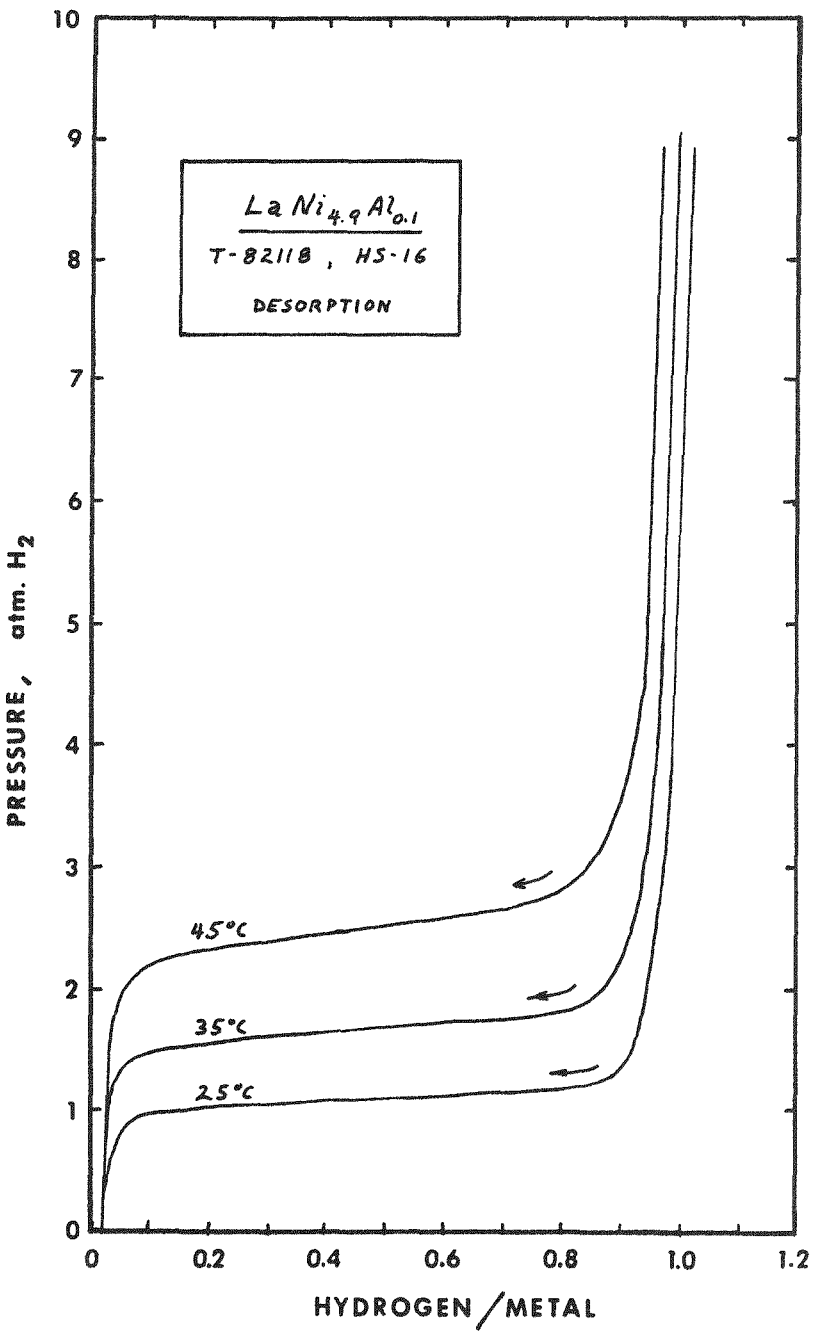

Figure 0-2-4. Dynamic pressure-composition desorption isotherms for $LaNi_{4.9}Al_{0.1}$ determined at a reaction rate of 0.0027 g-atom/min. (0.024 H/M/min.). Actual temperatures are about 0.3°C lower than the indicated nominal.

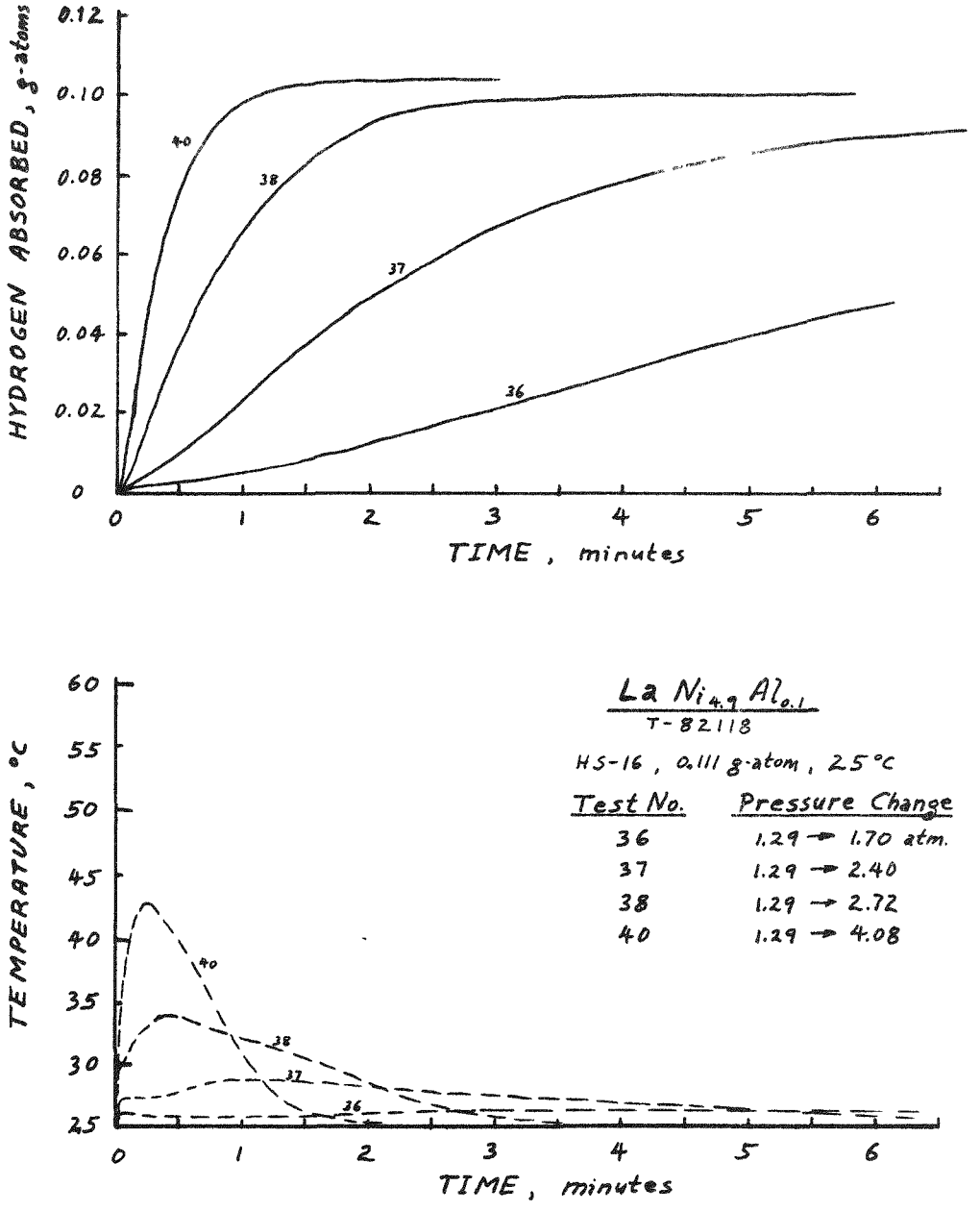

Figure 0-2-5. Time response data for the reaction mass and instantaneous temperature during isobaric absorption at a nominal temperature of 25 C.

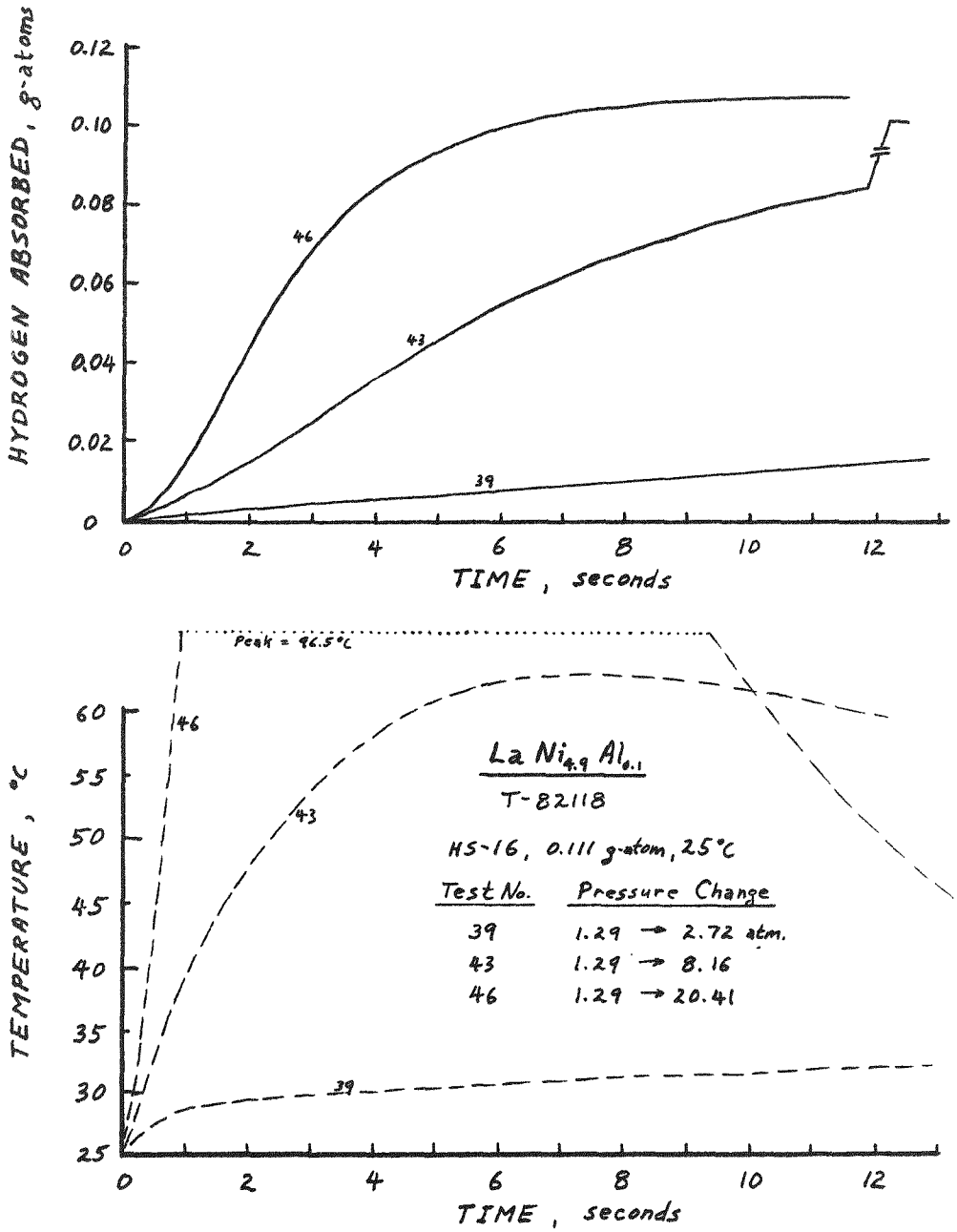

Figure 0-2-6. Time response data for the reaction mass and instantaneous temperature during isobaric absorption at a nominal temperature of 25 C.

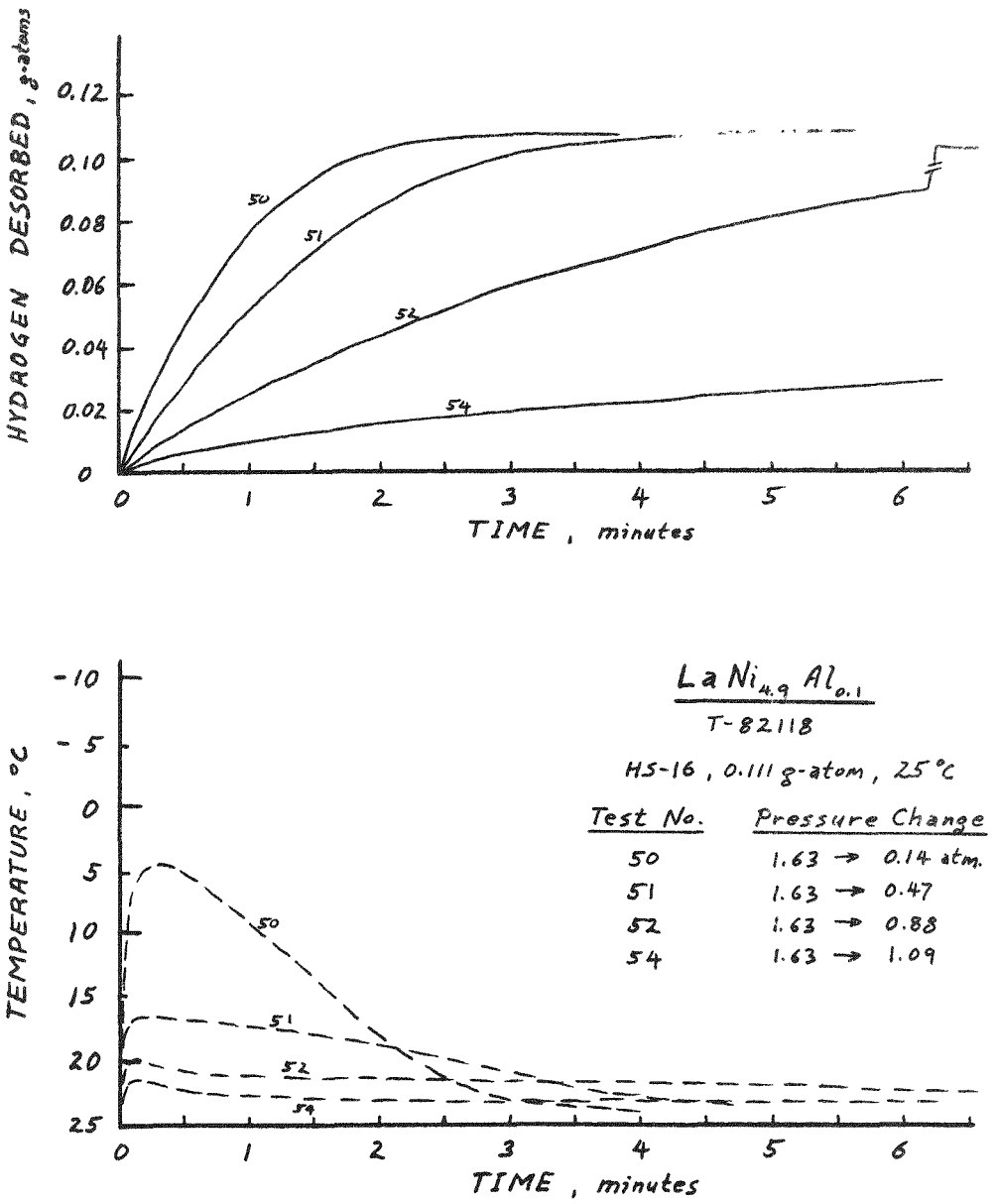

Figure 0-2-7. Time response data for the reaction mass and instantaneous temperature during isobaric desorption at a nominal temperature of 25 C.

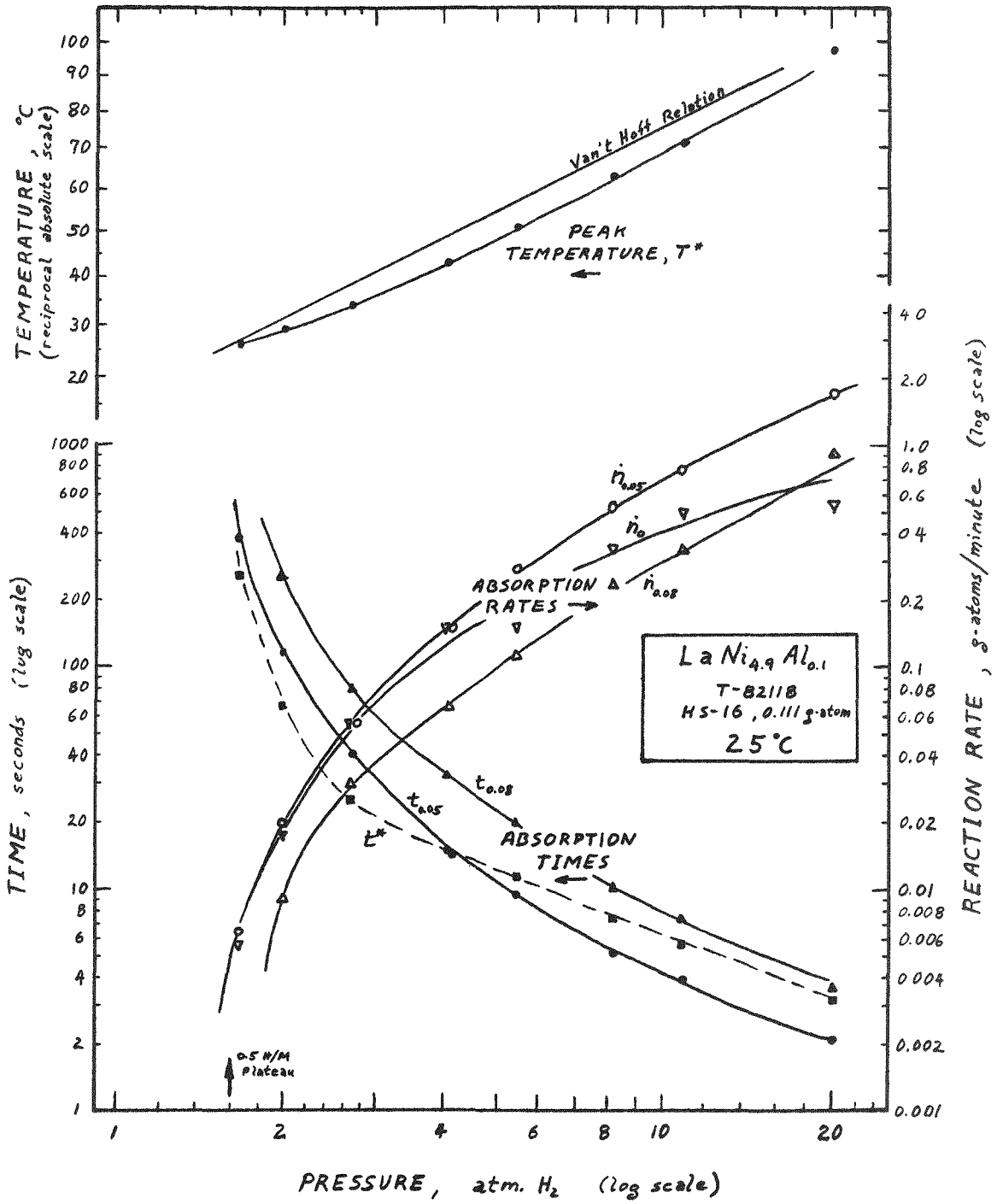

Figure 0-2-8. Summary of $LaNi_{4.9}Al_{0.1}$ absorption kinetic data at 25°C showing the maximum temperature excursion as well as the reaction rate and time parameters.

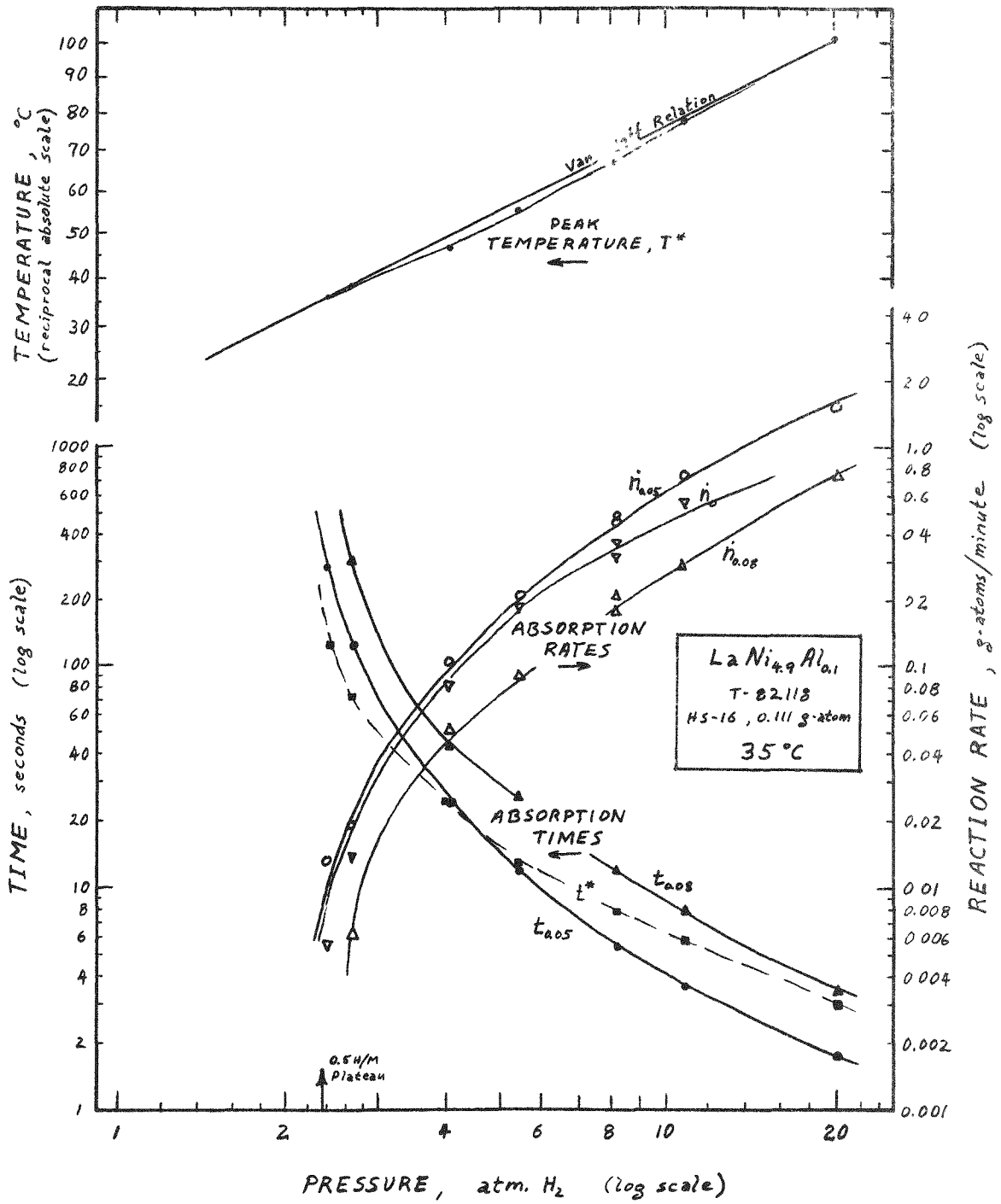

Figure 0-2-9. Summary of $LaNi_{4.9}Al_{0.1}$ absorption kinetic data at 35°C showing the maximum temperature excursion as well as the reaction rate and time parameters.

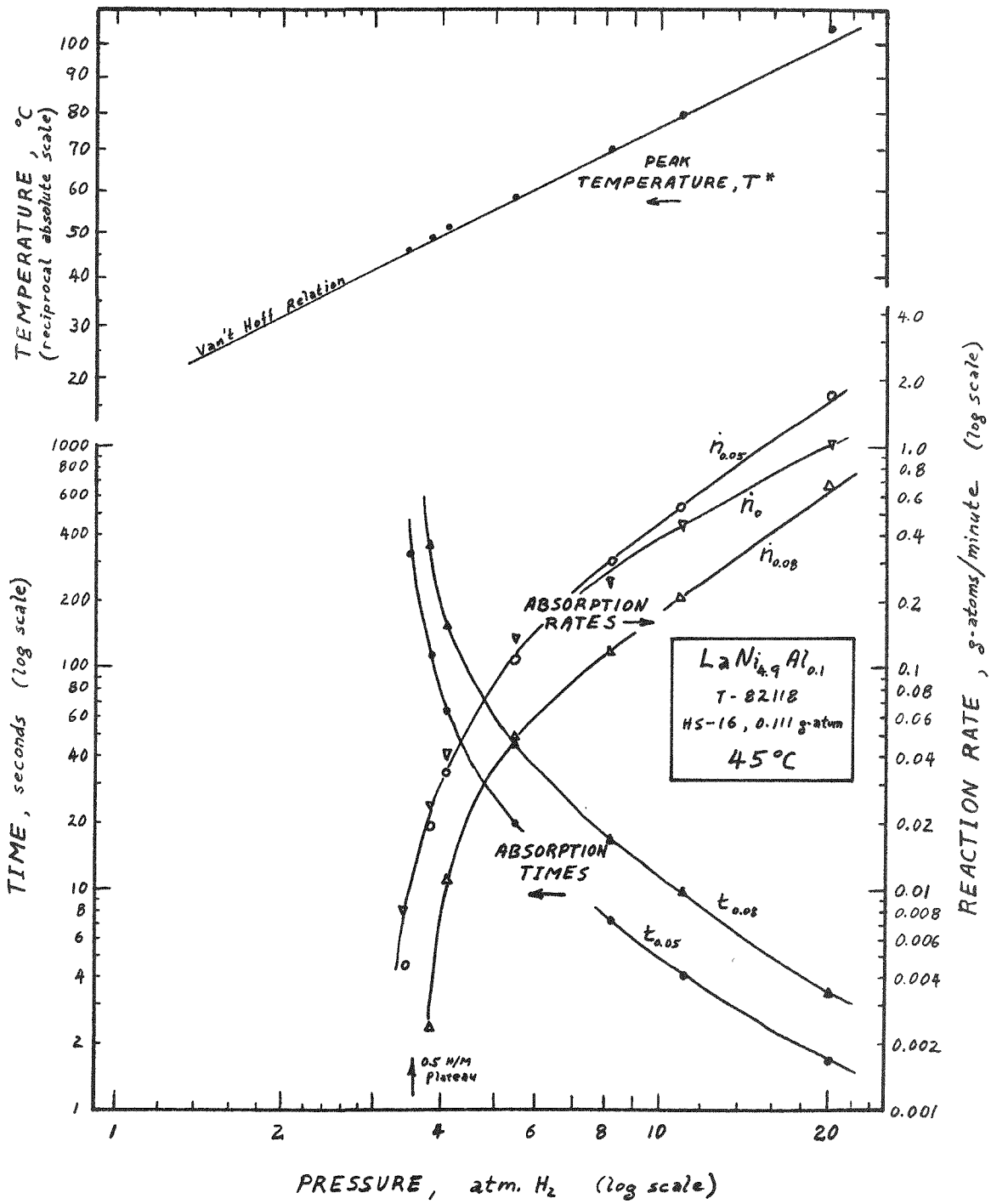

Figure 0-2-10. Summary of $LaNi_{4.9}Al_{0.1}$ absorption kinetic data at 45°C showing the maximum temperature excursion as well as the reaction rate and time parameters.

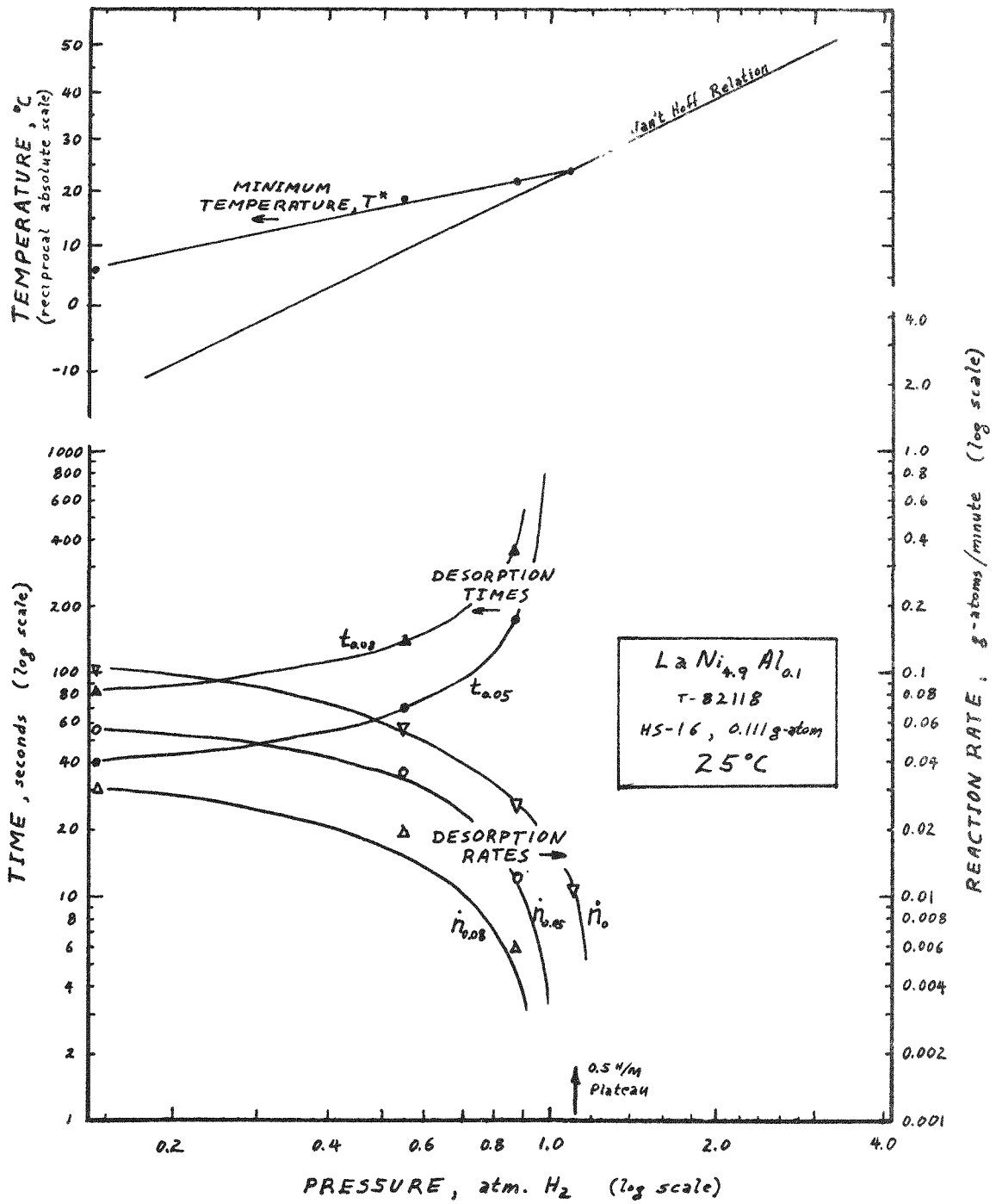

Figure 0-2-11. Summary of $LaNi_{4.9}Al_{0.1}$ desorption kinetic data at 25°C showing the minimum instantaneous temperature and the reaction rate and time parameters.

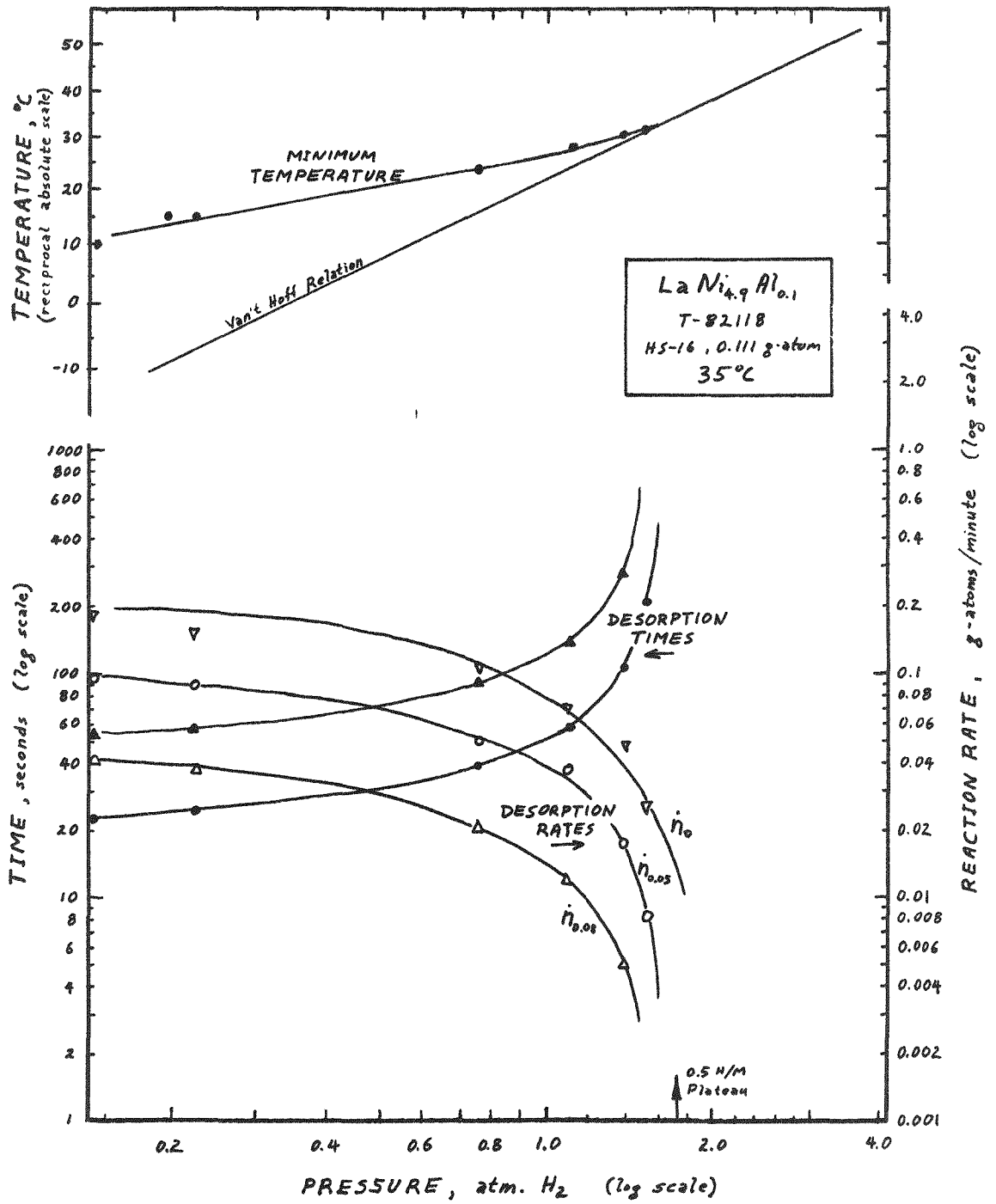

Figure 0-2-12. Summary of $LaNi_{4.9}Al_{0.1}$ desorption kinetic data at 35°C showing the minimum instantaneous temperature and the reaction rate and time parameters.

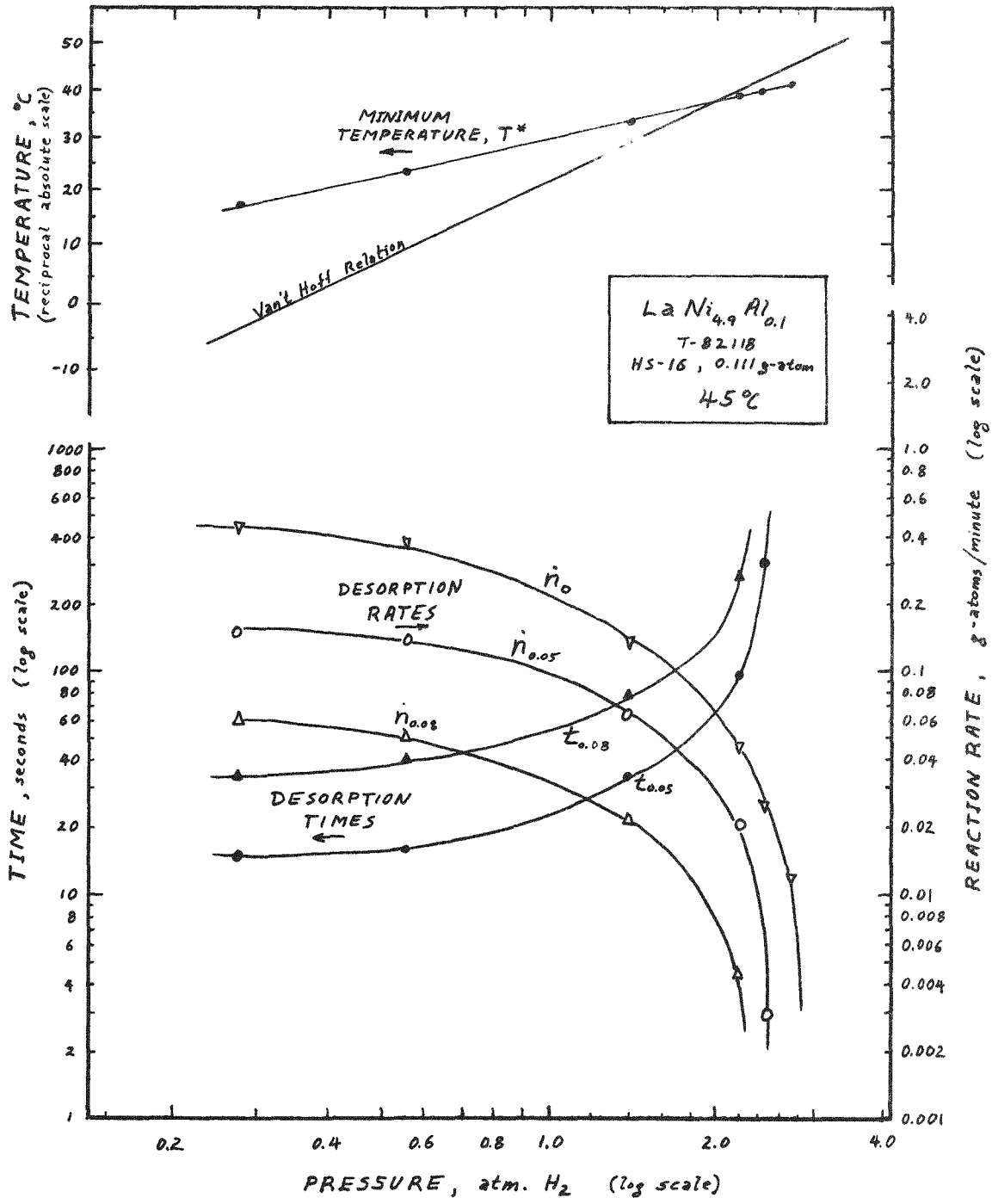

Figure 0-2-13. Summary of $LaNi_{4.9}Al_{0.1}$ desorption kinetic data at 45°C showing the minimum instantaneous temperature and the reaction rate and time parameters.

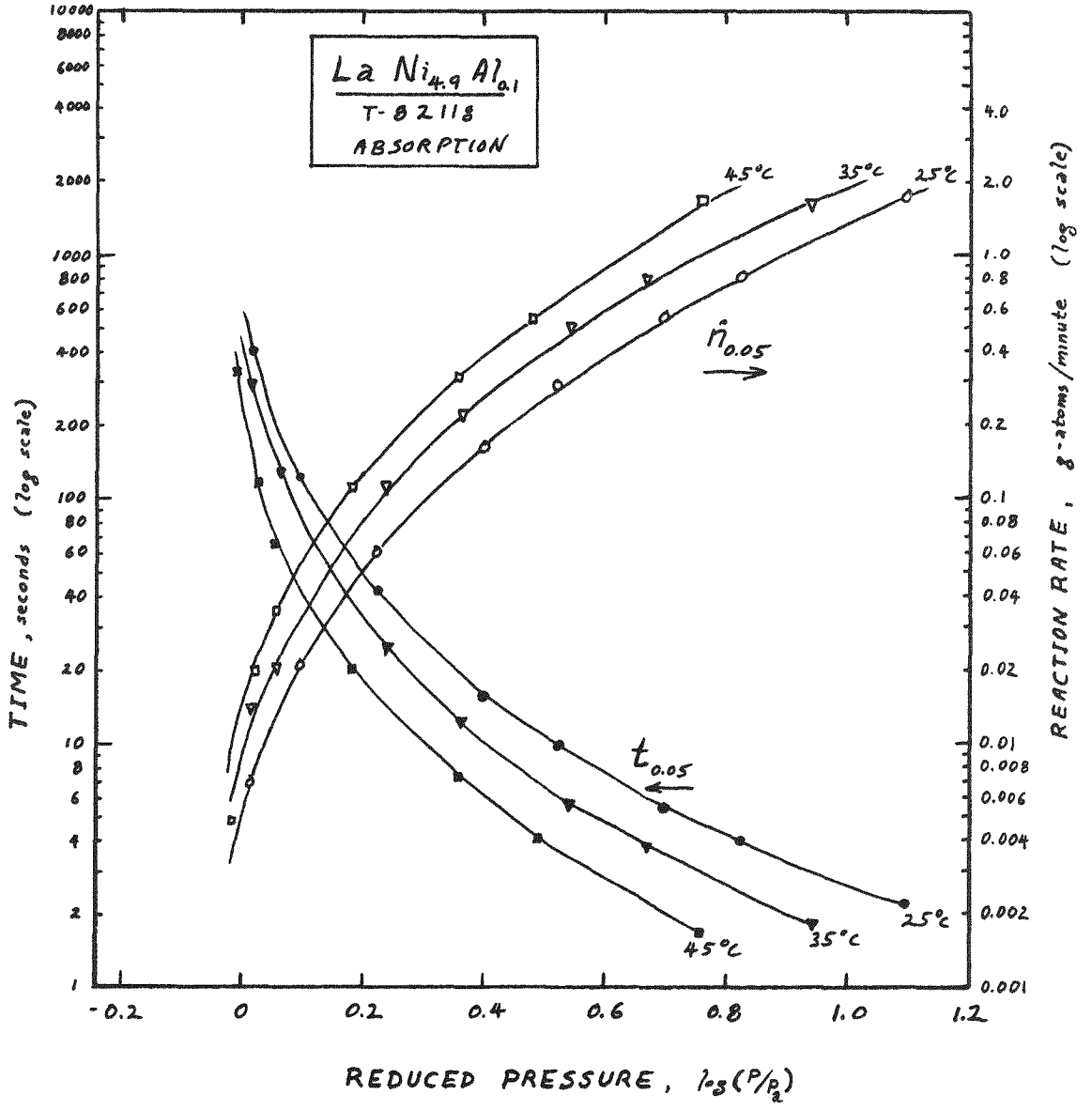

Figure 0-2-14. Comparison based on reduced pressure of $LaNi_{4.9}Al_{0.1}$ absorption kinetic data showing the rate and time to react 0.05 g-atom H at all pressures and temperatures tested.

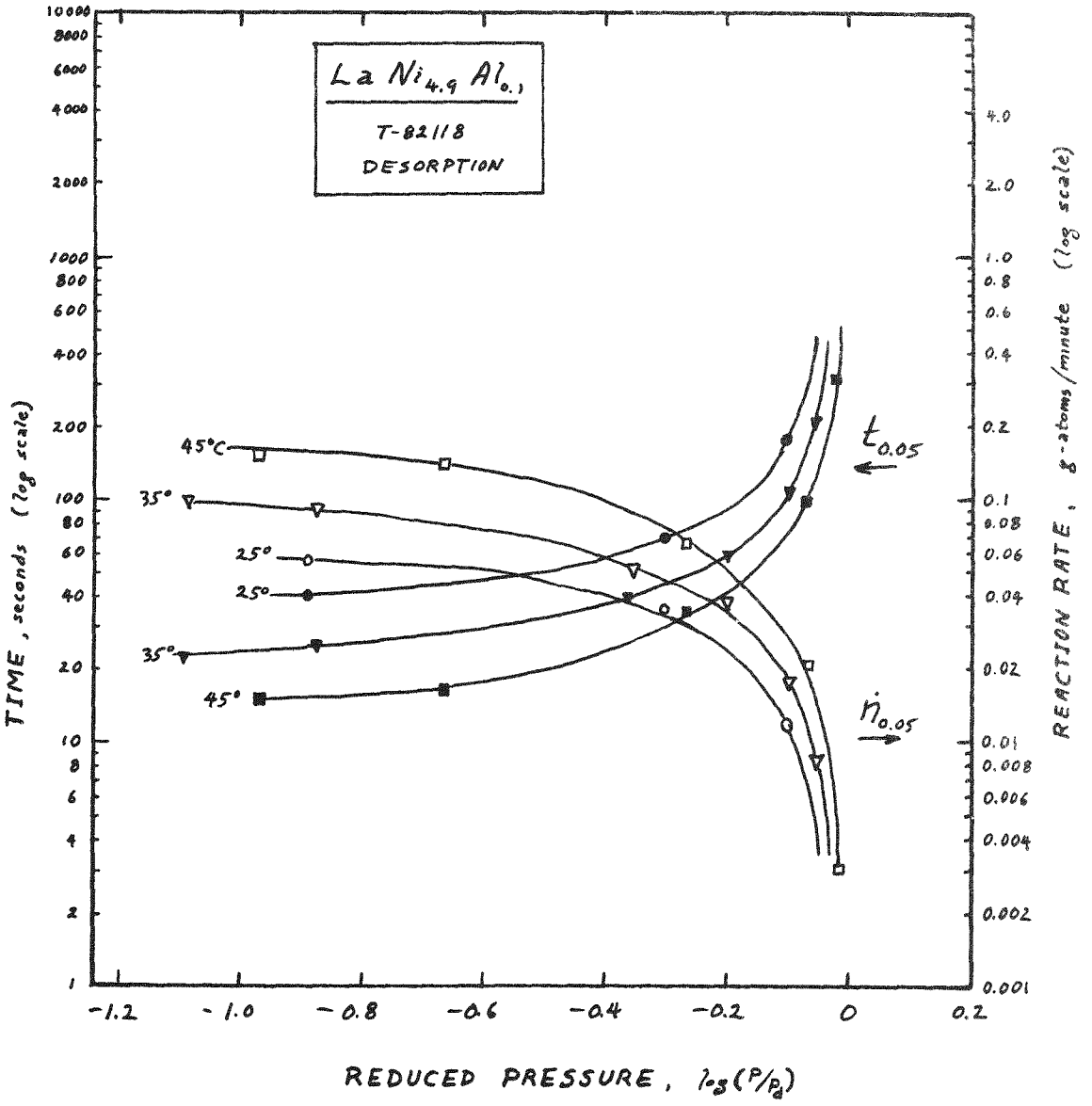

Figure 0-2-15. Comparison based on reduced pressure of $LaNi_{4.5}Al_{0.1}$ desorption kinetic data showing the rate and time to desorb 0.05 g-atom H at all pressures and temperatures tested.

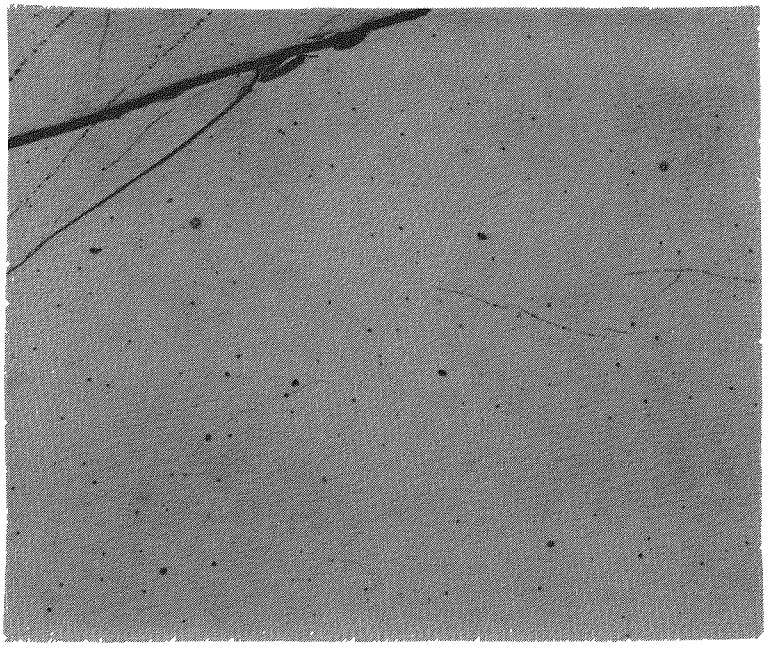

PN 1-72781 250X

Figure 0-3-1. Microstructure of $LaNi_3Co_2$, Annealed 24 Hours at 1175°C.

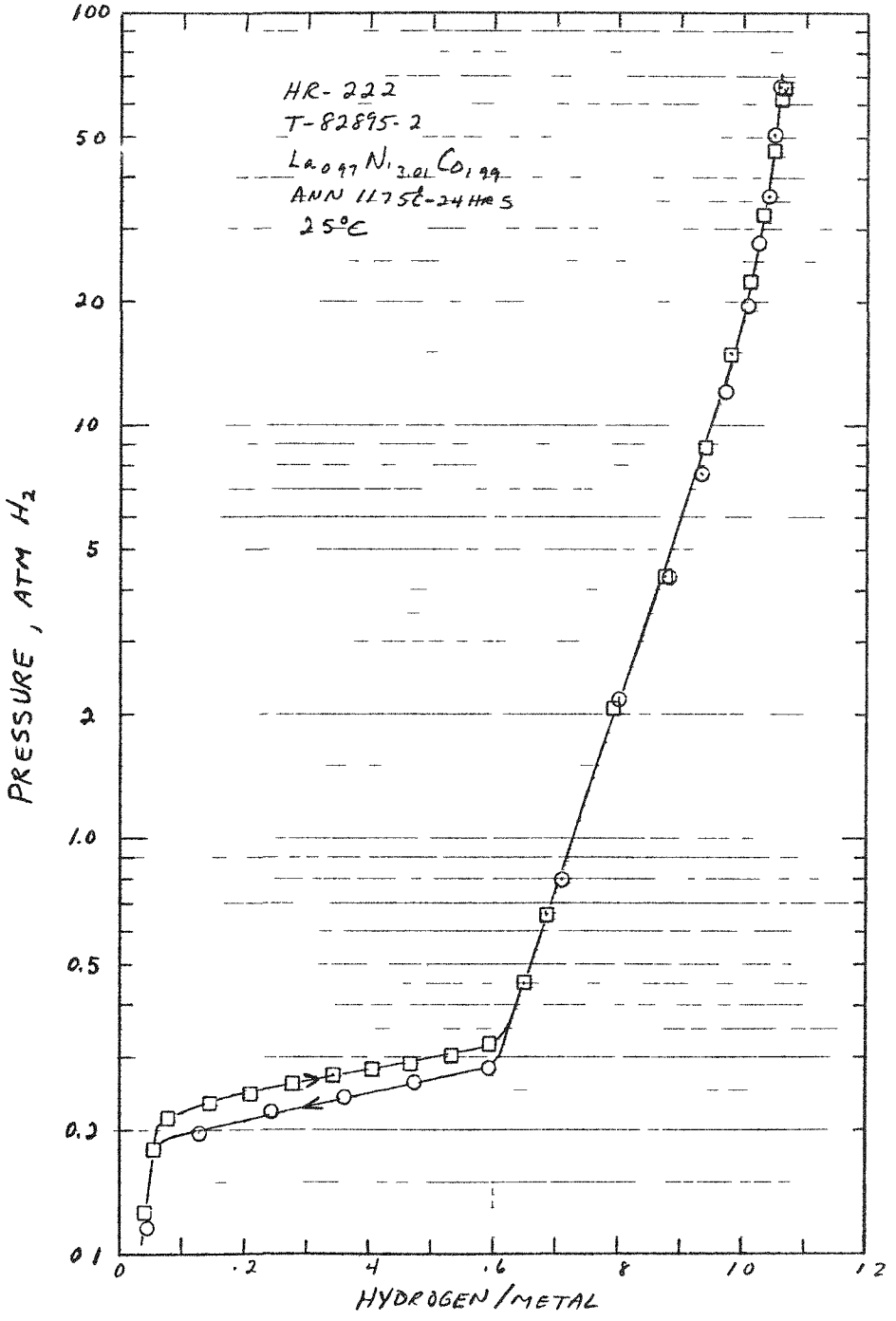

Figure 0-3-2. Static 25°C Isotherms for $LaNi_3Co_2$, Annealed 24 Hours at 1175°C.

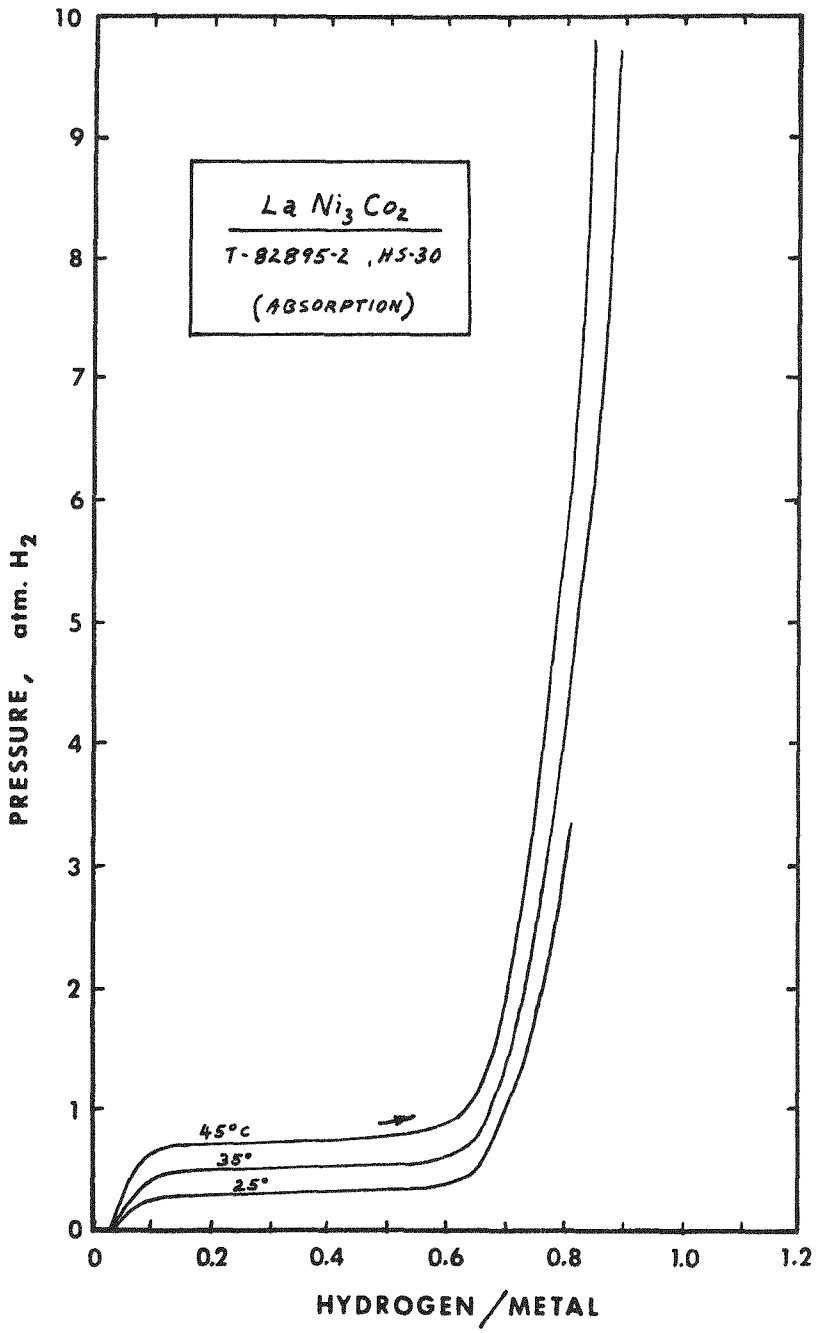

Figure 0-3-3. Dynamic pressure-composition absorption isotherms for $LaNi_3Co_2$ determined at a reaction rate of 0.0027 g-atom H/min. (0.024 H/M/min.). Actual temperatures are about 0.3°C higher than the indicated nominal.

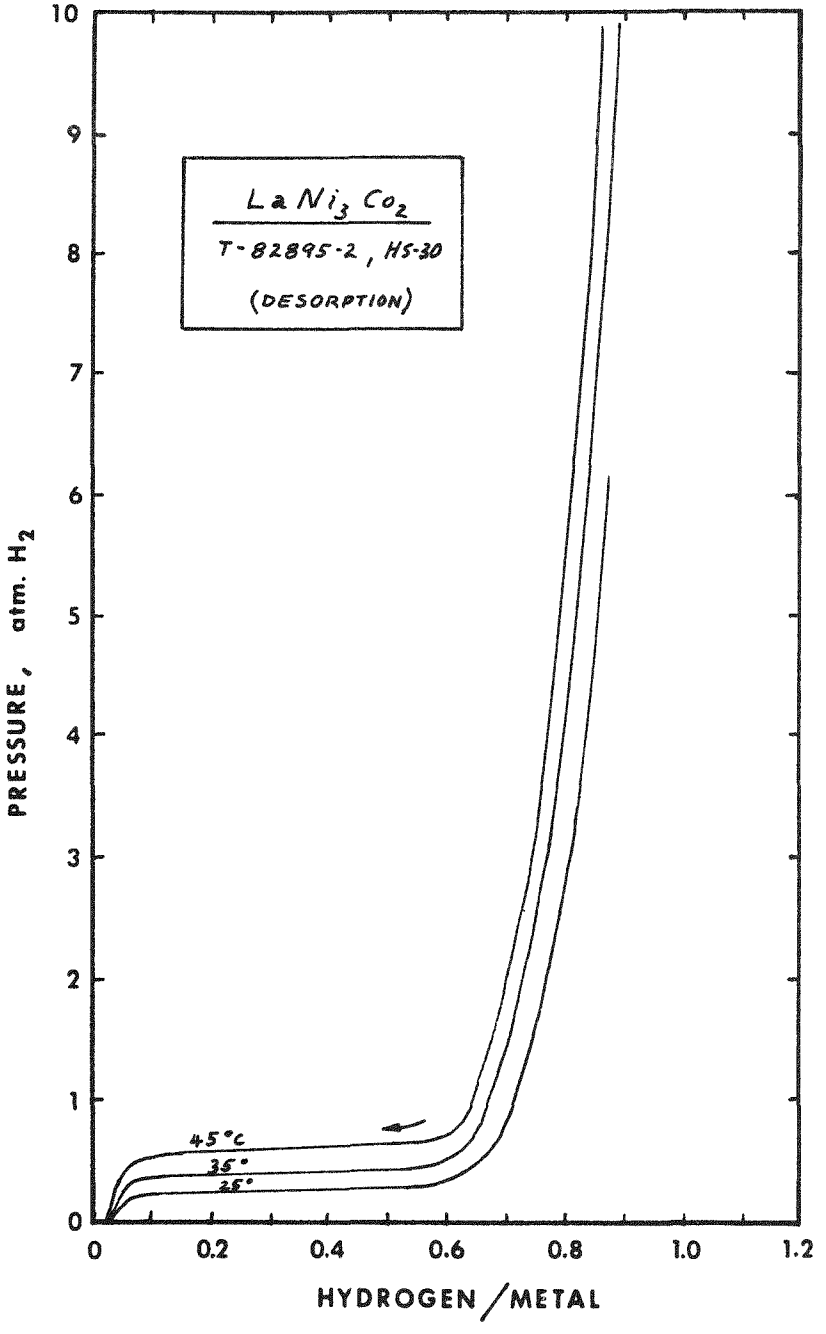

Figure 0-3-4. Dynamic pressure-composition desorption isotherms for $LaNi_3Co_2$ determined at a reaction rate of 0.0027 g-atom/min. (0.024 H/M/min.). Actual temperatures are about 0.3°C lower than the indicated nominal.

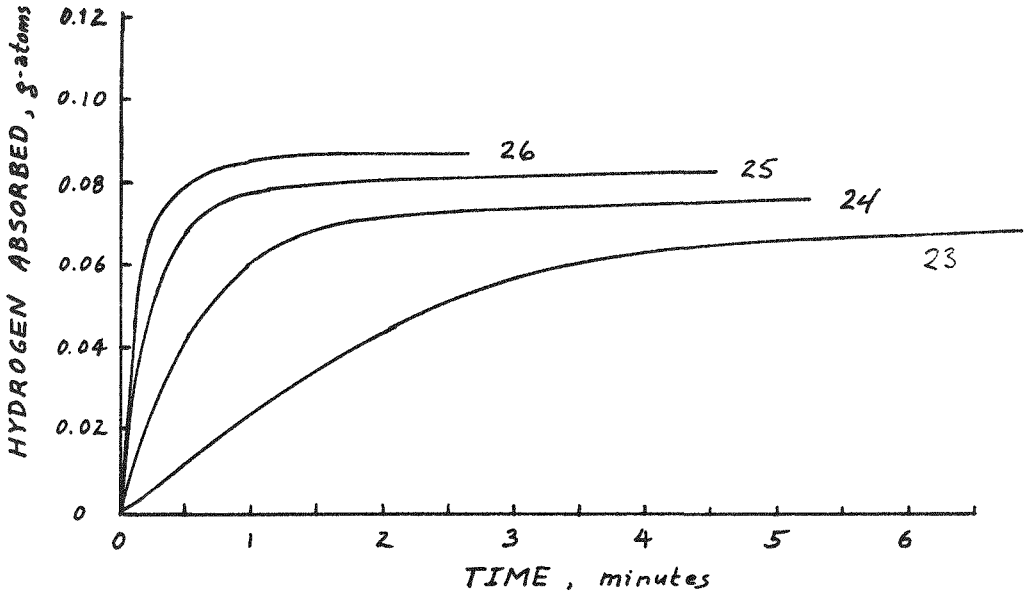

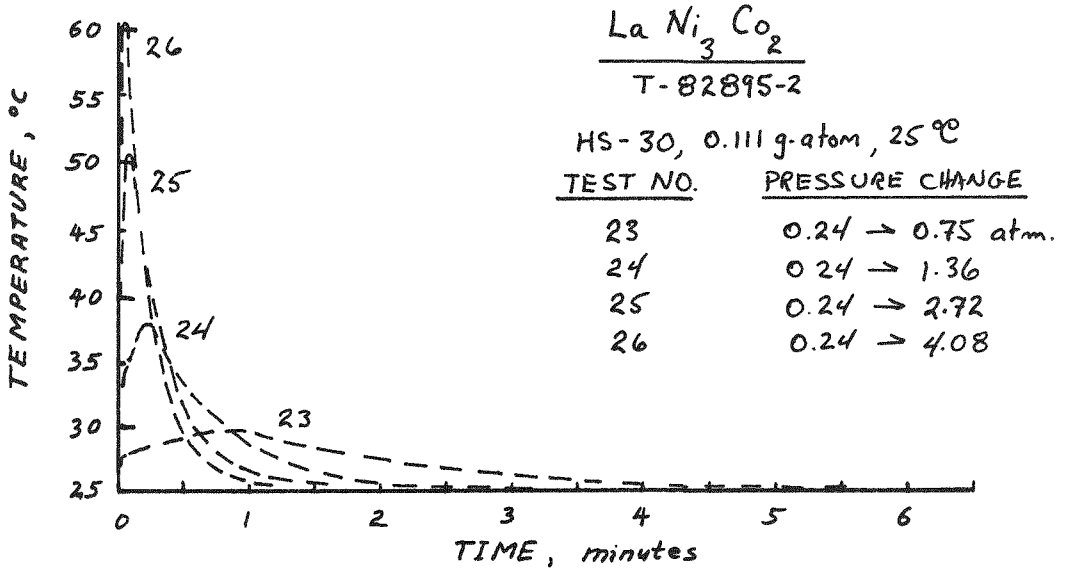

Figure 0-3-5. Time response data for the reaction mass and instantaneous temperature during isobaric absorption at a nominal temperature of 25 C.

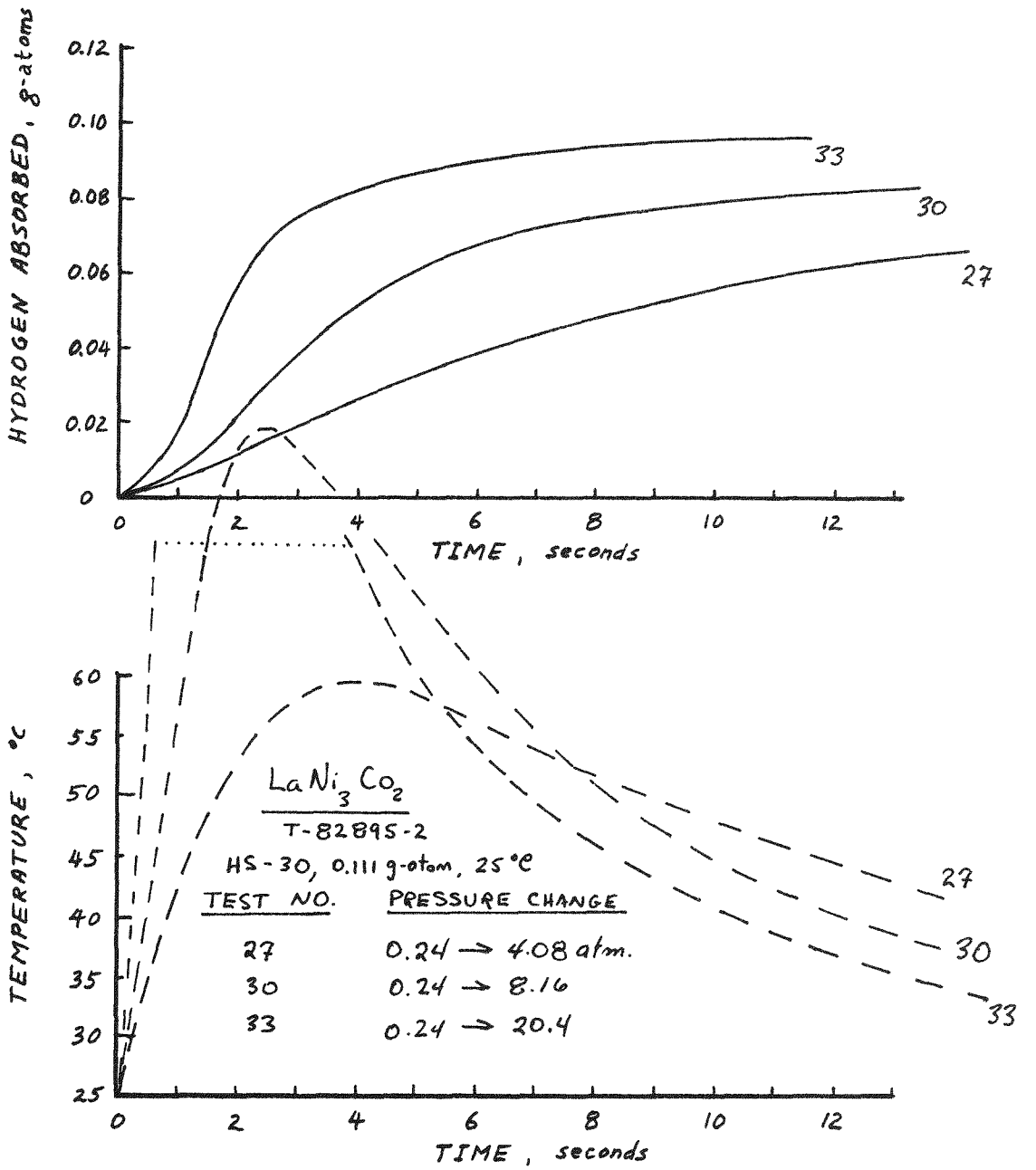

Figure 0-3-6. Time response data for the reaction mass and instantaneous temperature during isobaric absorption at a nominal temperature of 25 C.

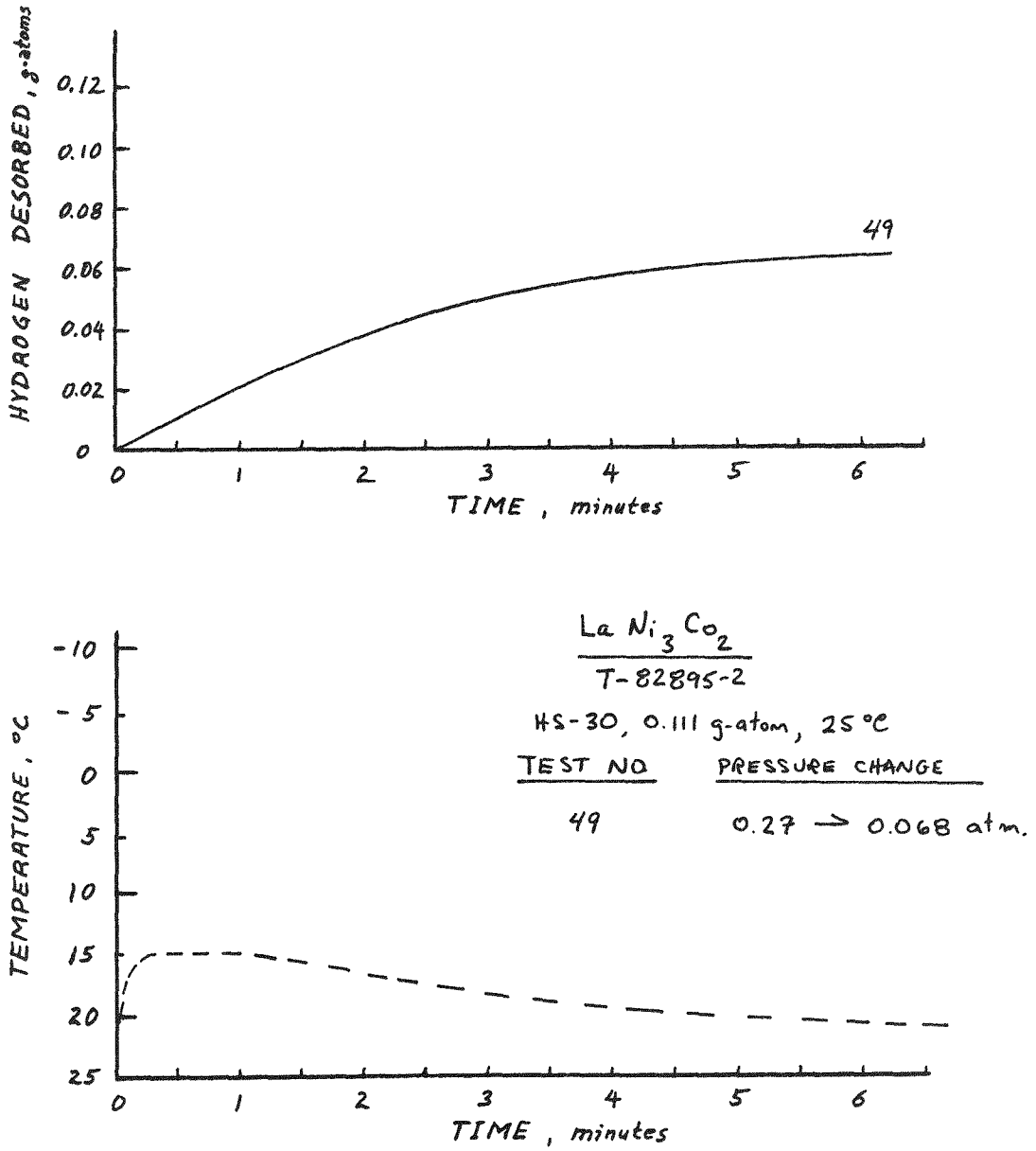

Figure 0-3-7. Time response data for the reaction mass and instantaneous temperature during isobaric desorption at a nominal temperature of 25 C.

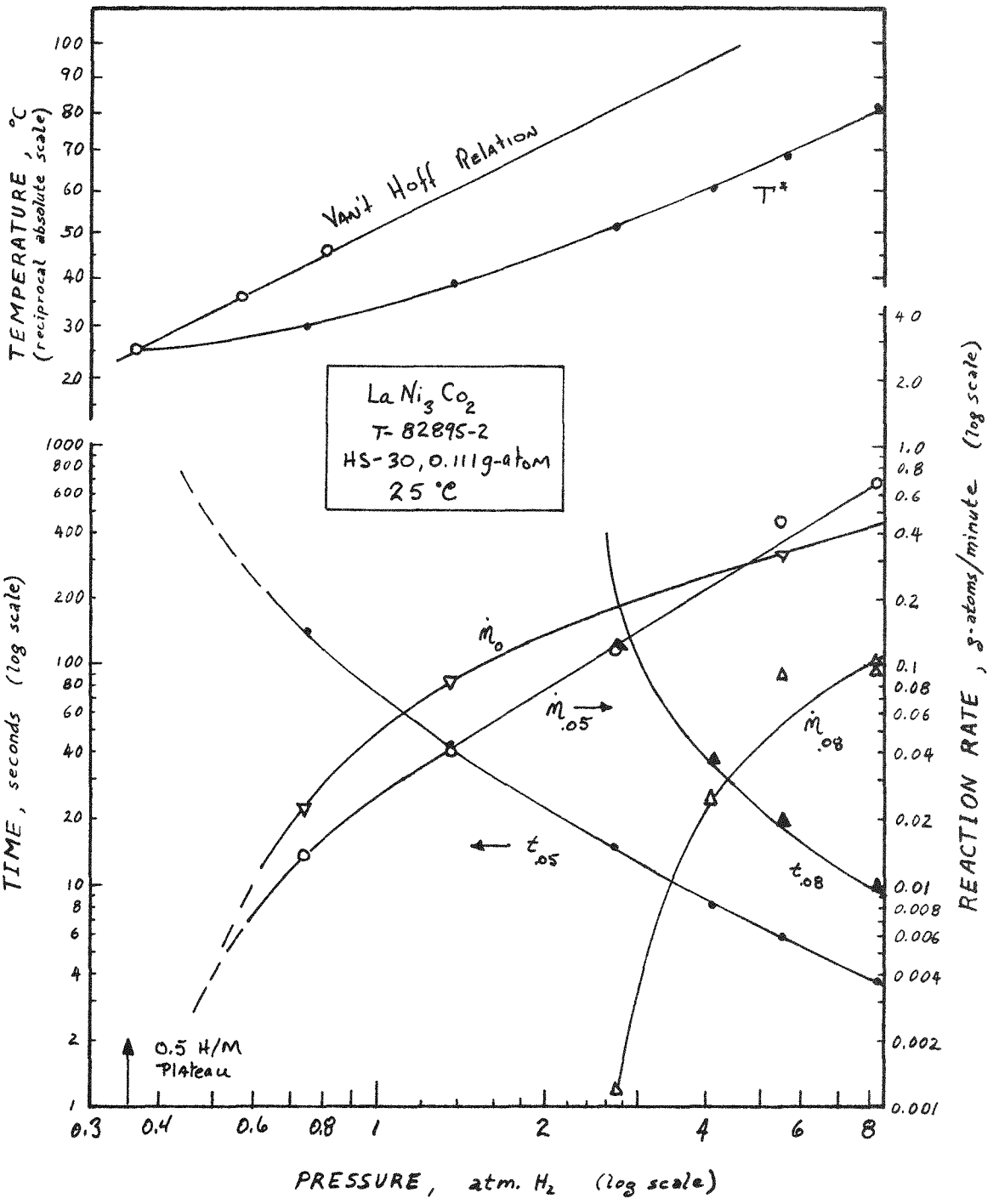

Figure 0-3-8. Summary of $LaNi_3Co_2$ absorption kinetic data at 25°C showing the maximum temperature excursion as well as the reaction rate and time parameters.

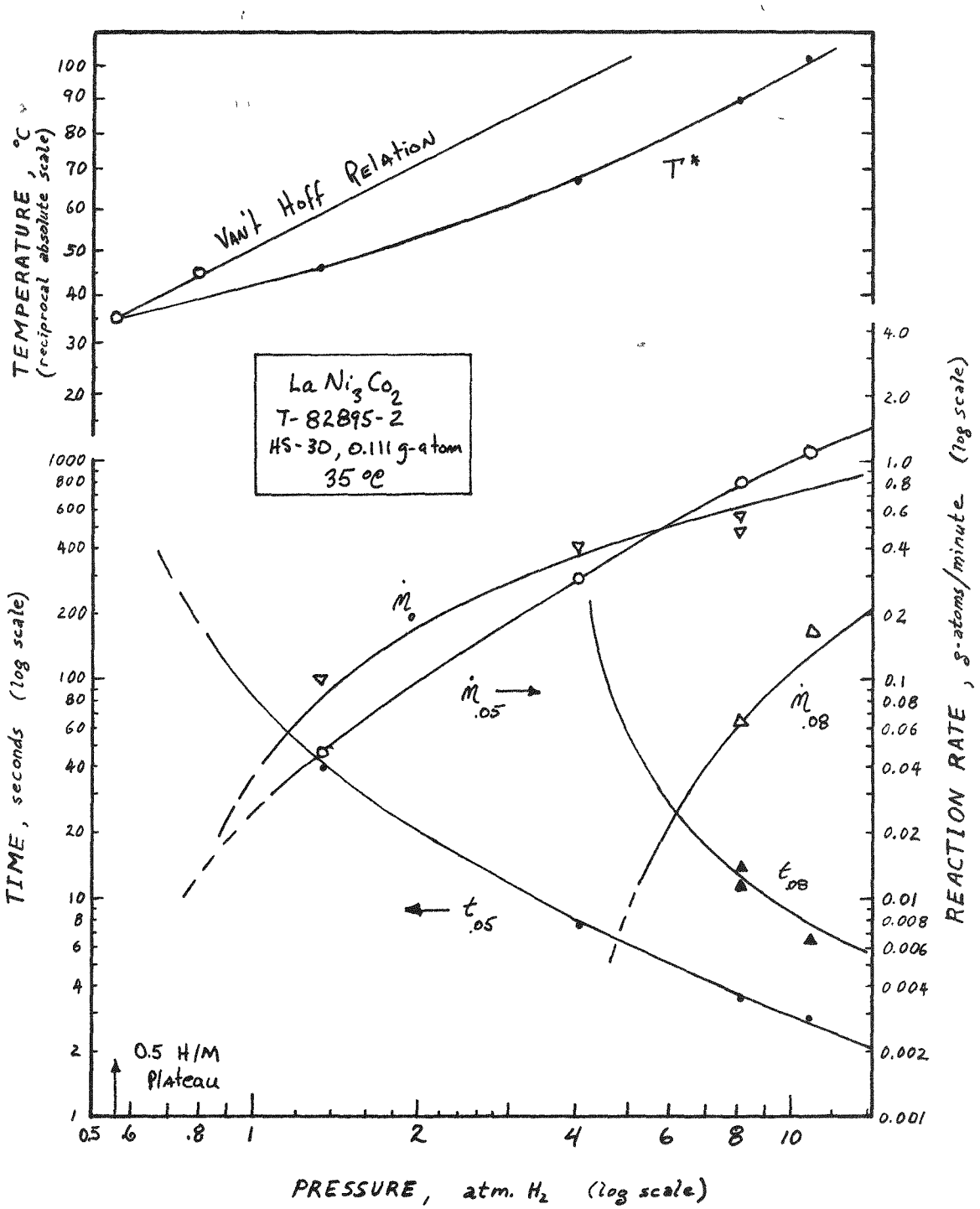

Figure 0-3-9. Summary of $LaNi_3Co_2$ absorption kinetic data at 35°C showing the maximum temperature excursion as well as the reaction rate and time parameters.

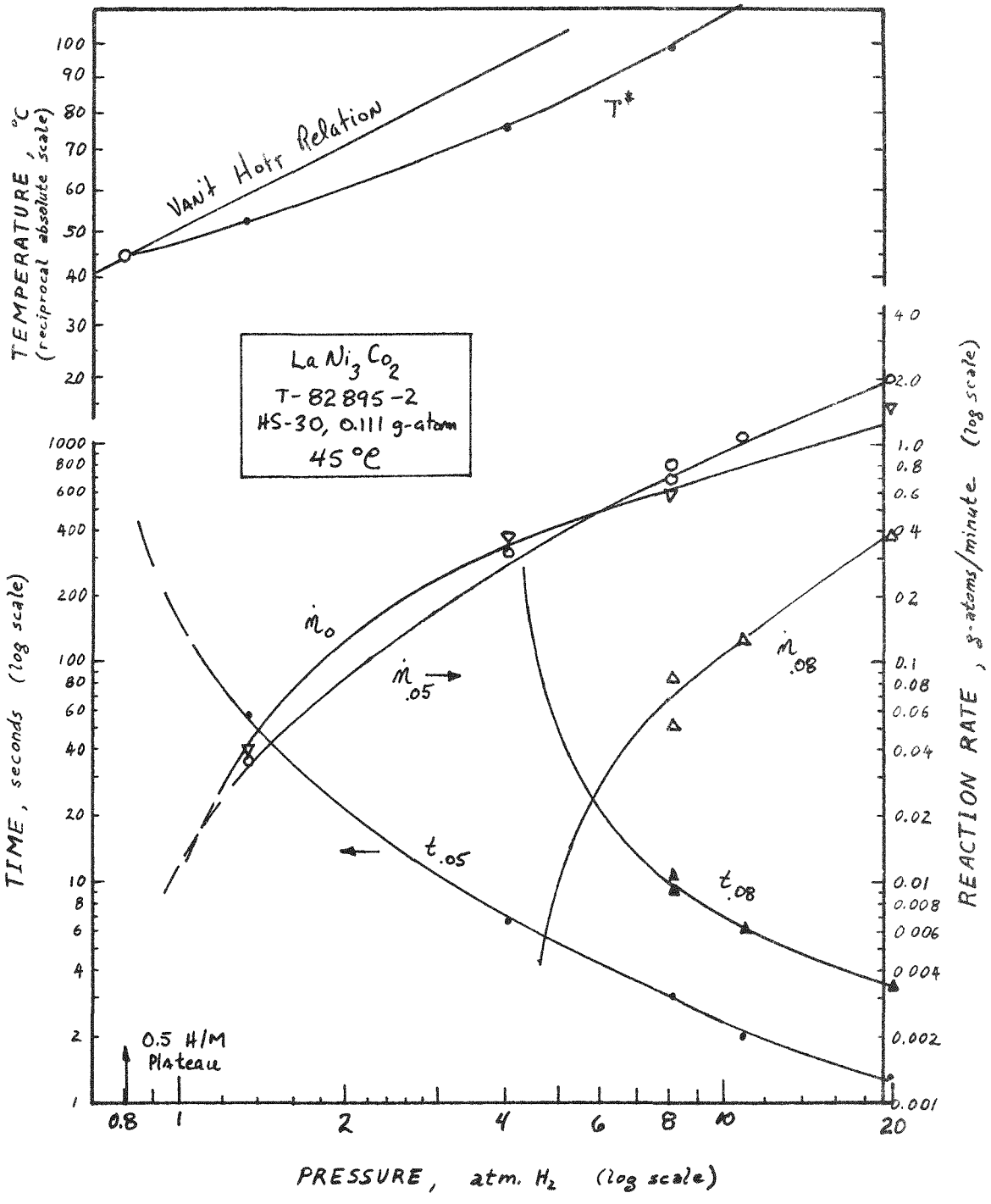

Figure 0-3-10. Summary of $LaNi_3Co_2$ absorption kinetic data at 45°C showing the maximum temperature excursion as well as the reaction rate and time parameters.

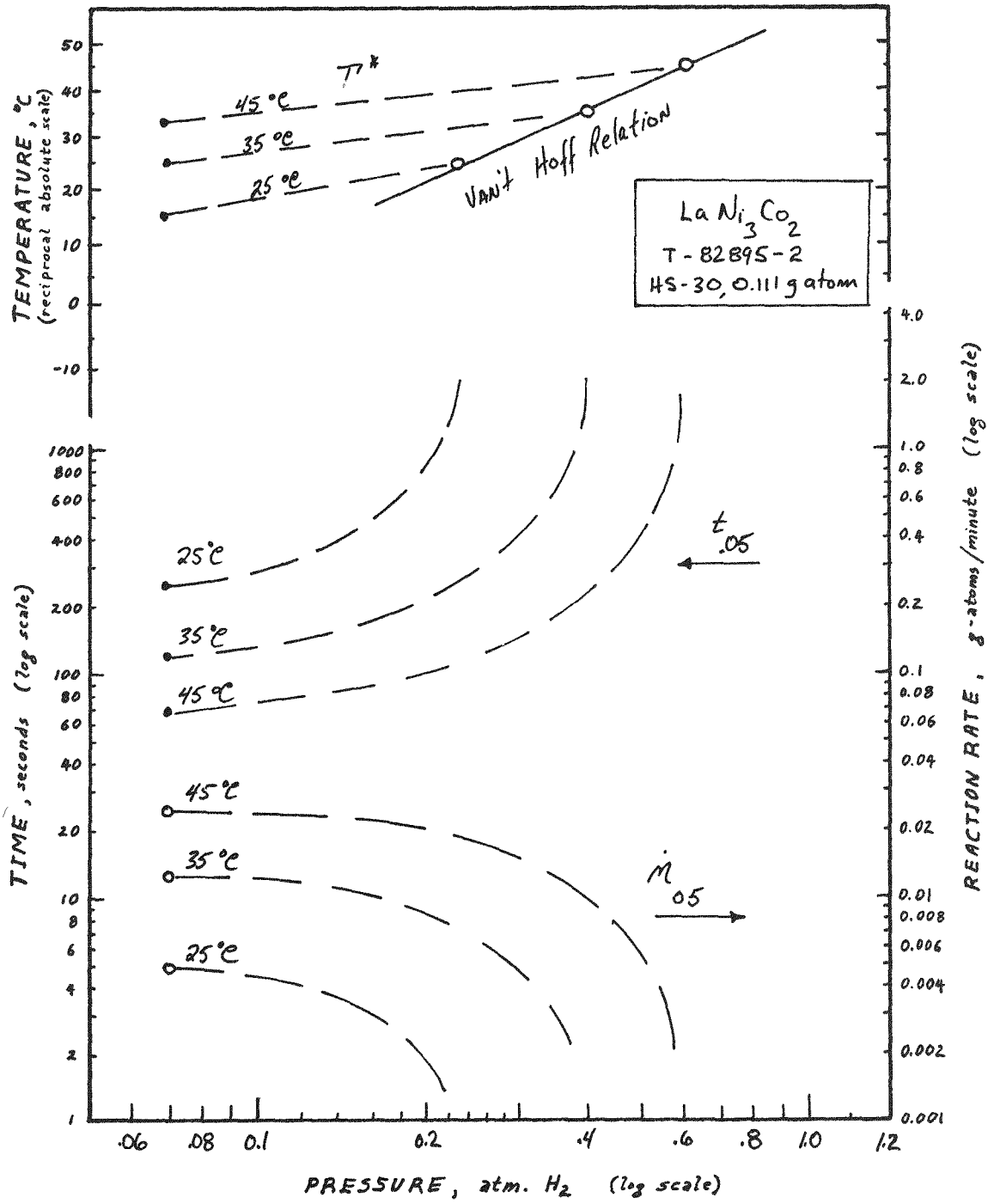

Figure 0-3-11. Summary of desorption kinetic data showing the maximum temperature excursion as well as the reaction rate and time at 0.05 g-atoms hydrogen reacted (~0.5 H/M).

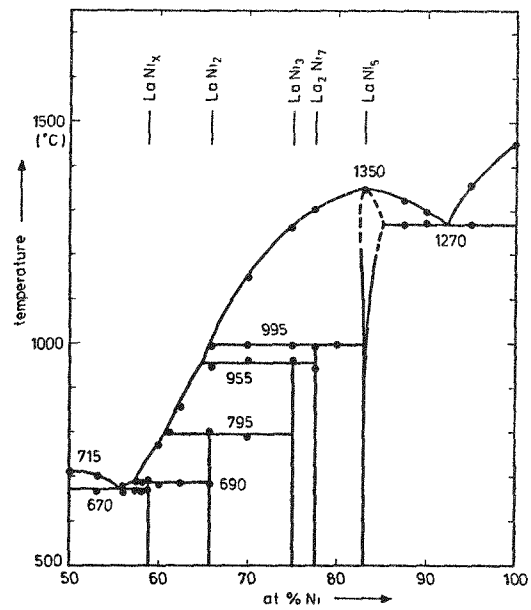

Figure 1-0-1. La-Ni Phase Diagram(8).

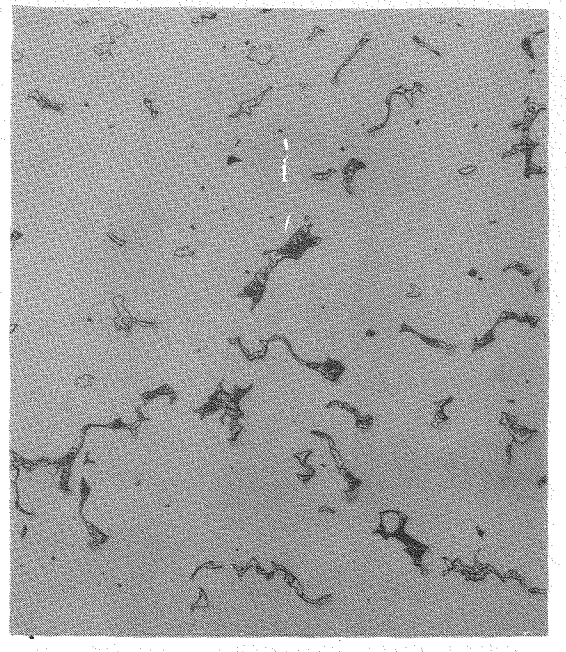

PN 1-72842 250X

(a) As-Cast
σ_s=1.98 emu/g
(3.6 wt.% free Ni)

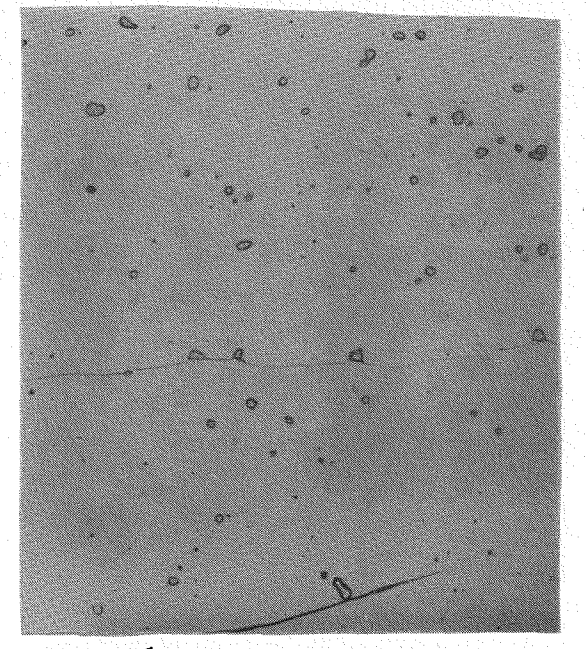

PN 1-73671 250X

(b) S.T. 24 Hours at 1260°C
σ_s=0.46 emu/g
(0.8 wt.% free Ni)

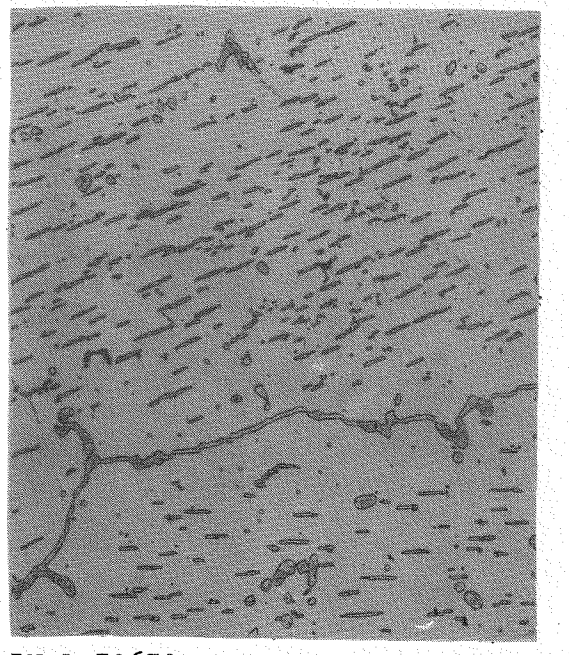

PN 1-73673 250X

(c) S.T. + Aged 24 Hrs.@ 1000°C
σ_s=6.45 emu/g
(11.9 wt.% free Ni)

Figure 1-1-1. Microstructures and Magnetic Moments for $LaNi_{5.67}$.

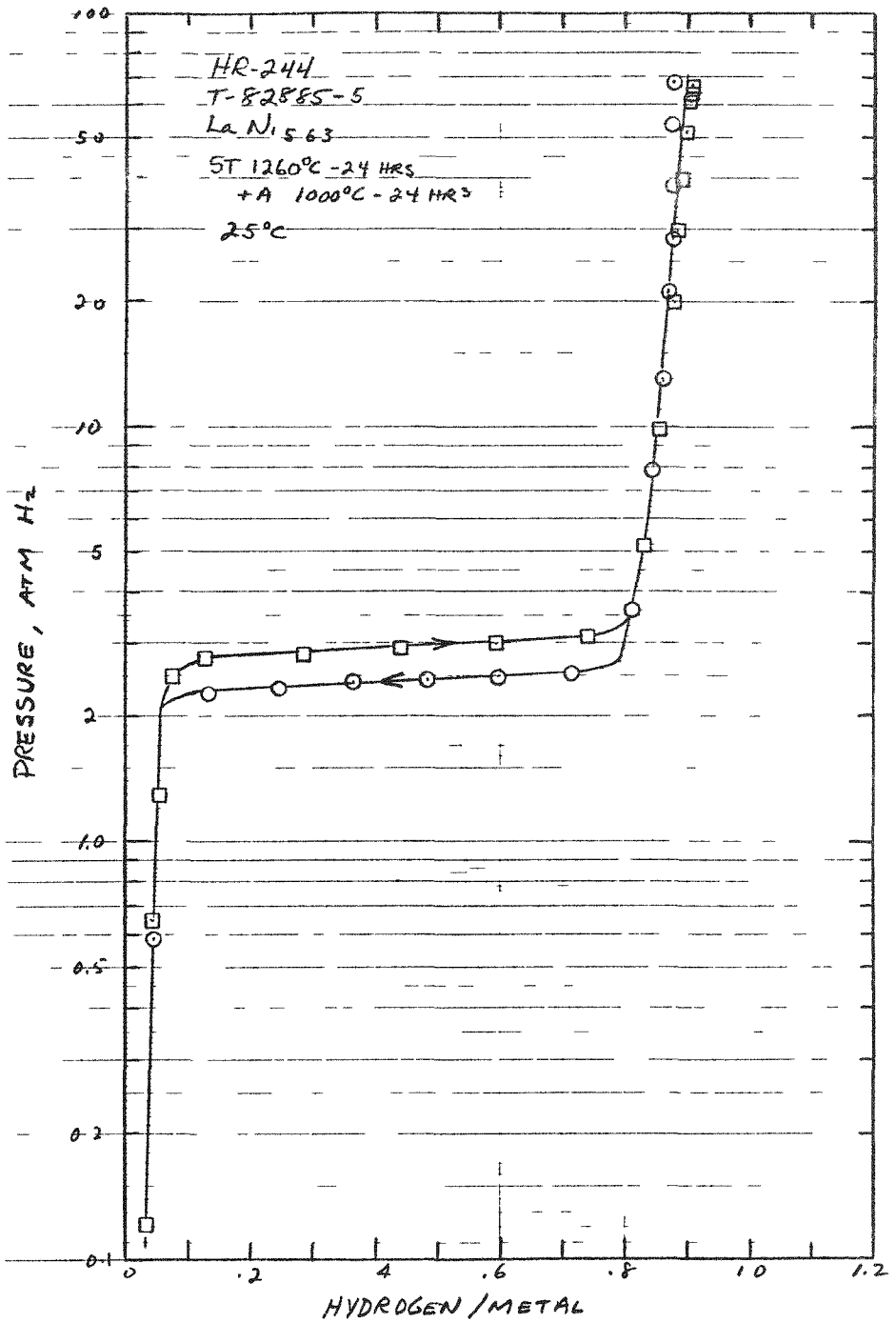

Figure 1-1-2. Static 25°C Isotherms for $LaNi_{5.67}$, Solution Treated at 1260°C and Aged at 1000°C.

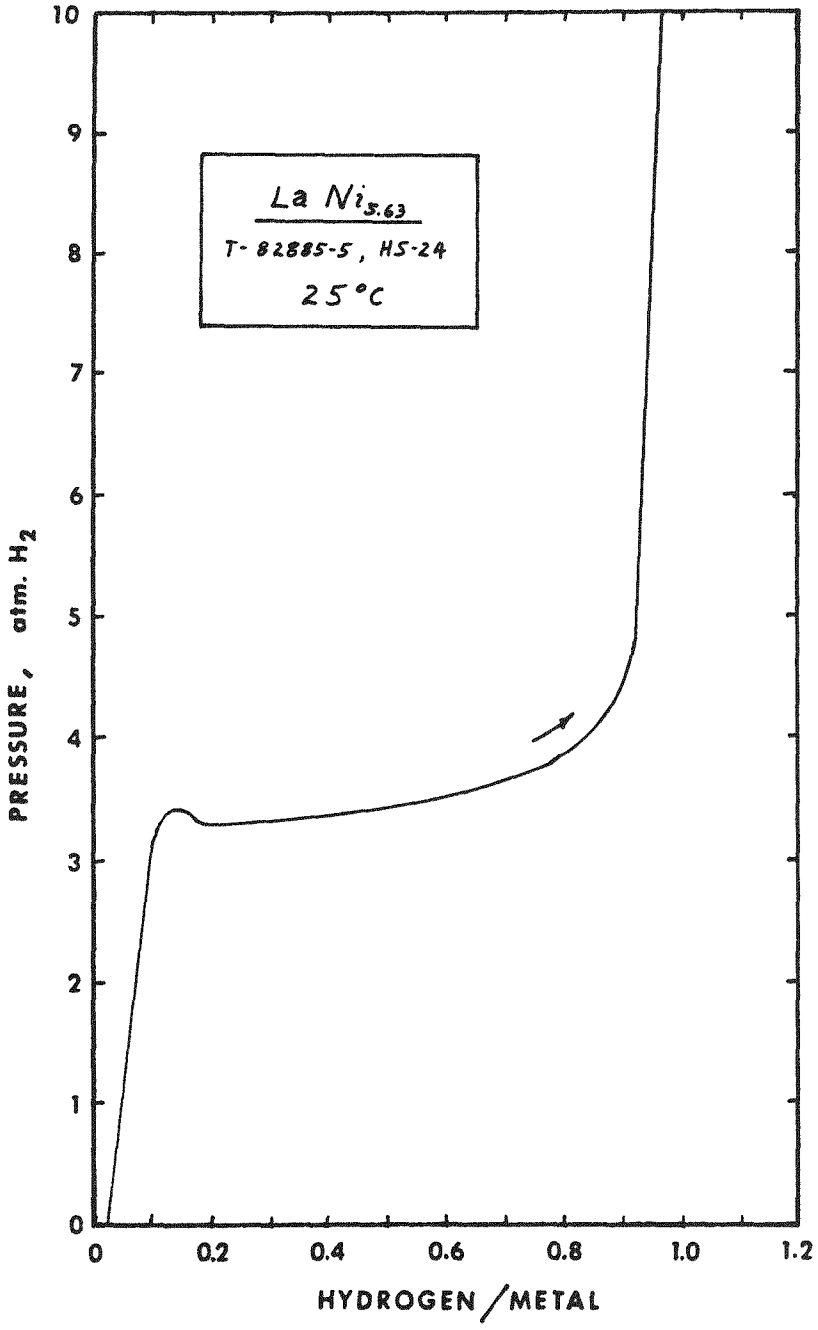

Figure 1-1-3. Dynamic pressure-composition absorption isotherm determined at a reaction rate of 0.0027 g-atom H/min. The actual temperature is about 0.3°C higher than the indicated nominal.

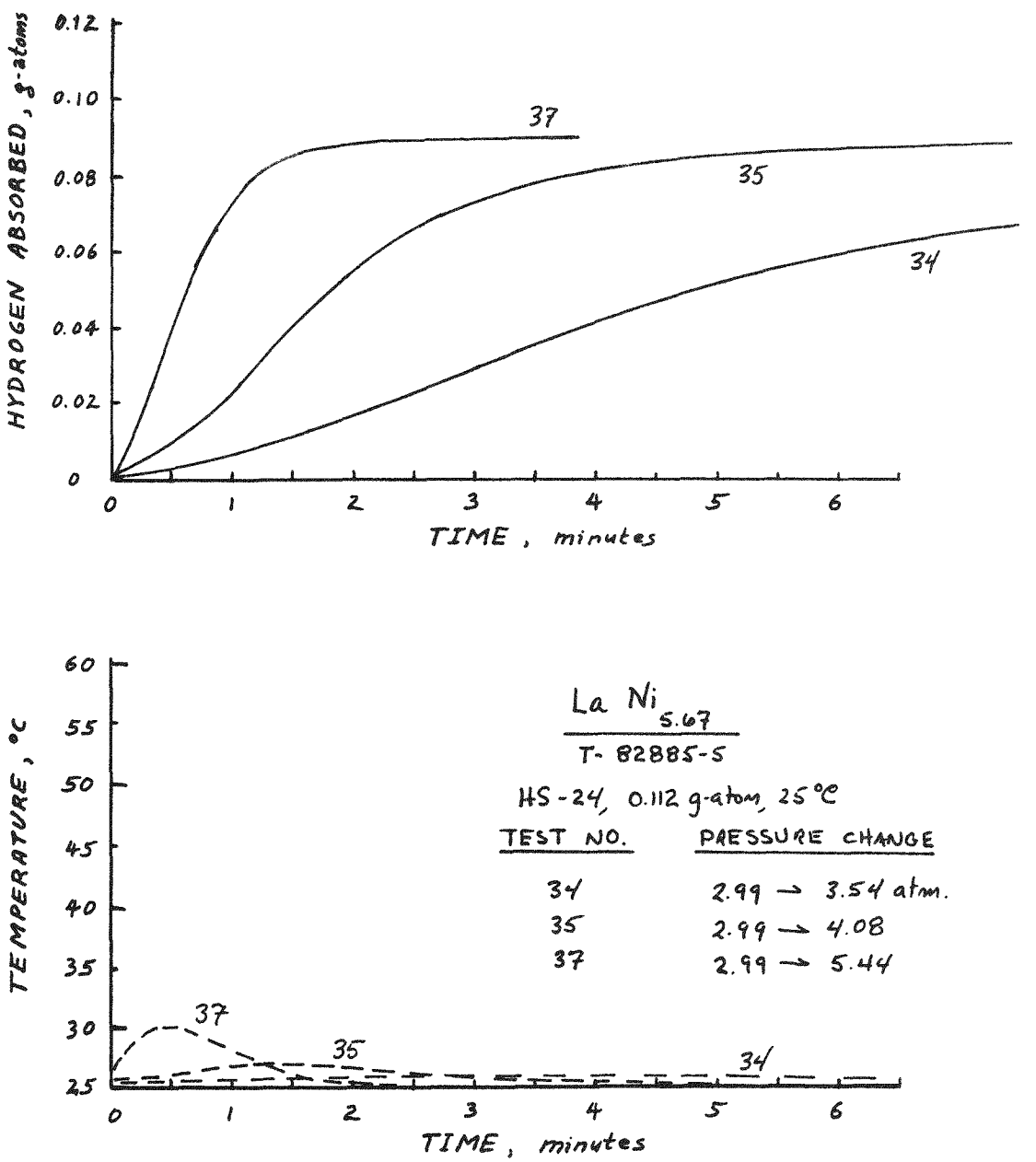

Figure 1-1-4. Time response data for the reaction mass and instantaneous temperature during isobaric absorption at a nominal temperature of 25 C.

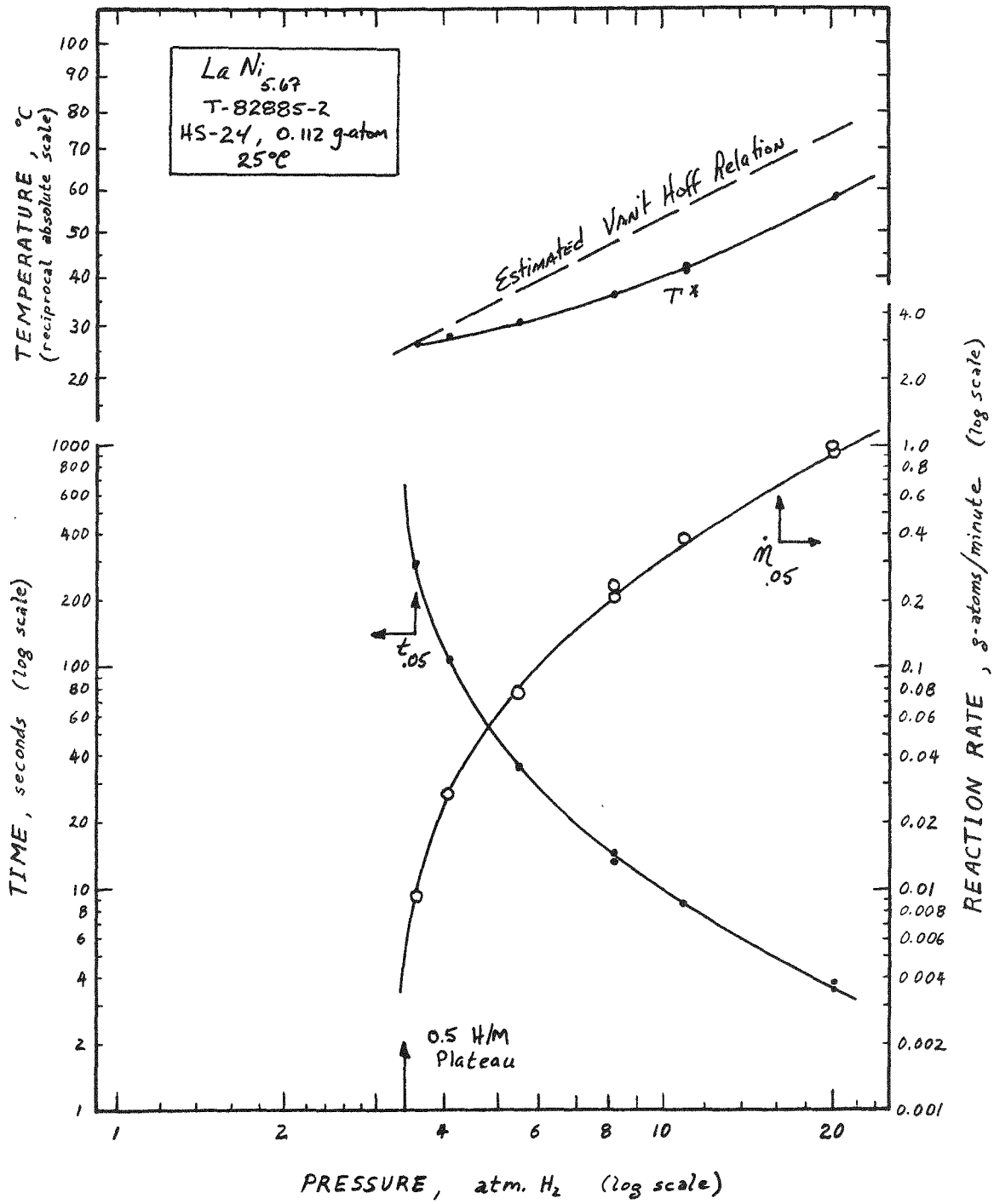

Figure 1-1-5. Summary of absorption kinetic data at 25°C showing the maximum temperature excursion as well as the reaction rate and time at 0.05 g-atoms hydrogen reacted (~0.5H/M).

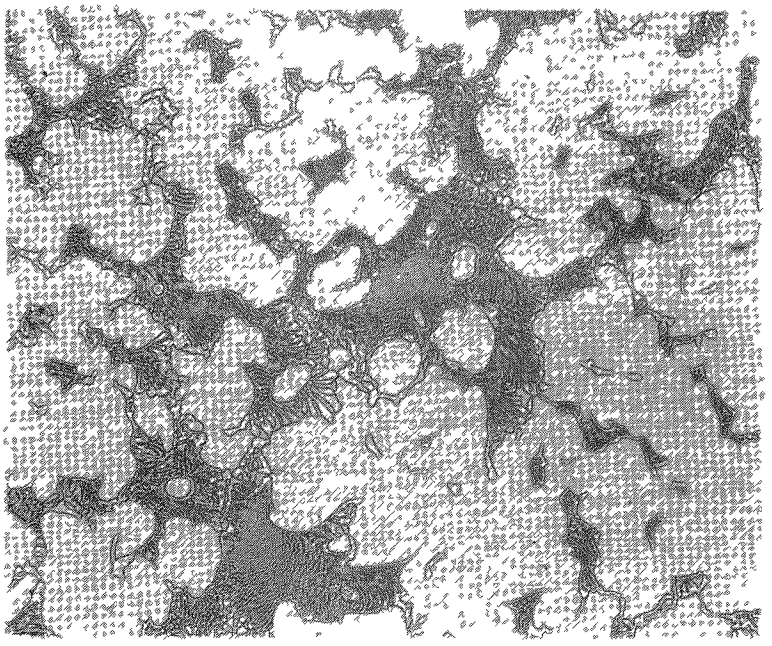

PN 1-72844 250X

Figure 1-2-1. As-Cast Microstructure of $LaNi_7$.

PN 1-72846 250X

Figure 1-3-1. As-Cast Microstructure of $LaNi_{11.5}$.

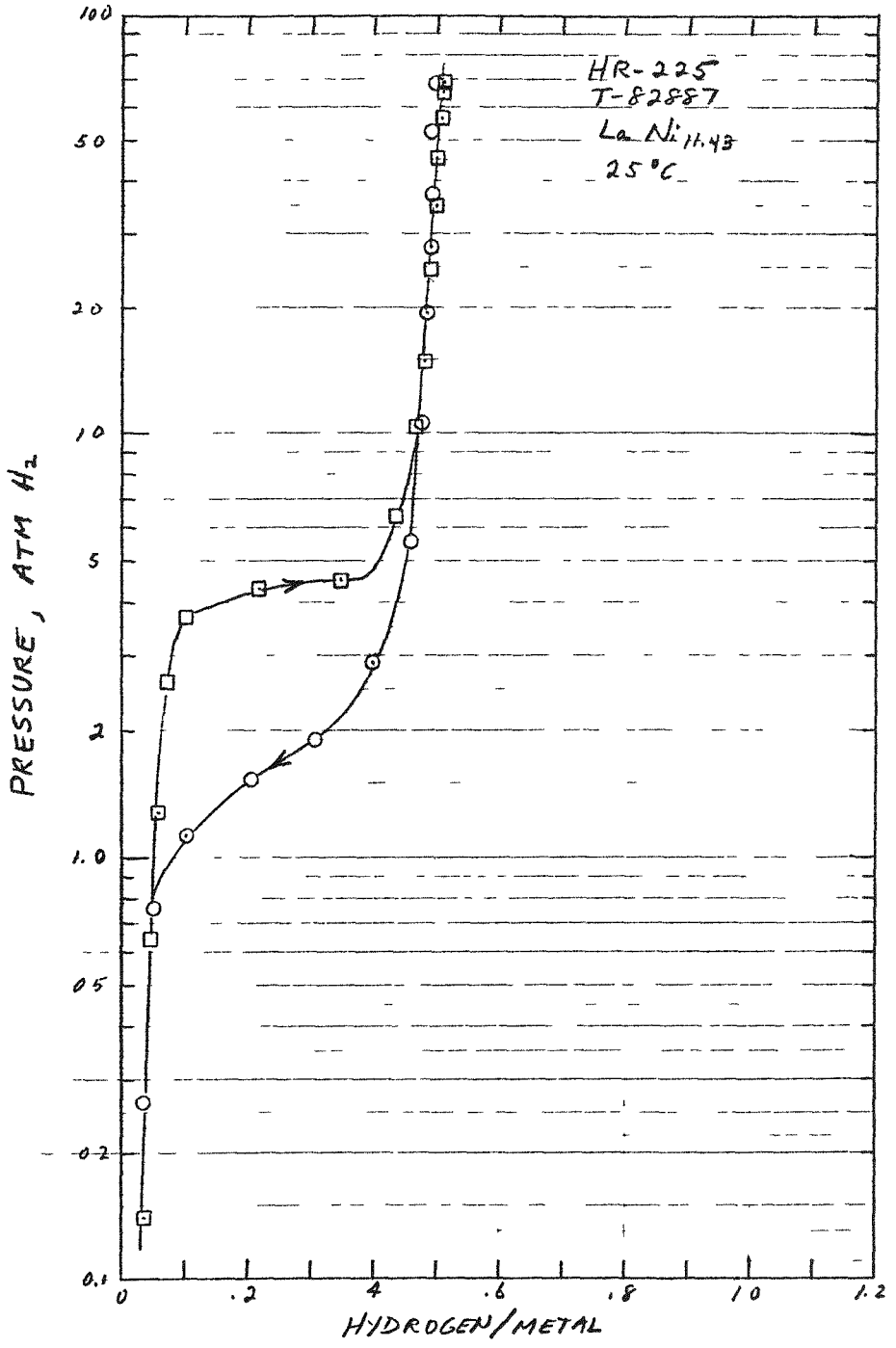

Figure 1-3-2. Static 25°C Isotherms for As-Cast $LaNi_{11.5}$.

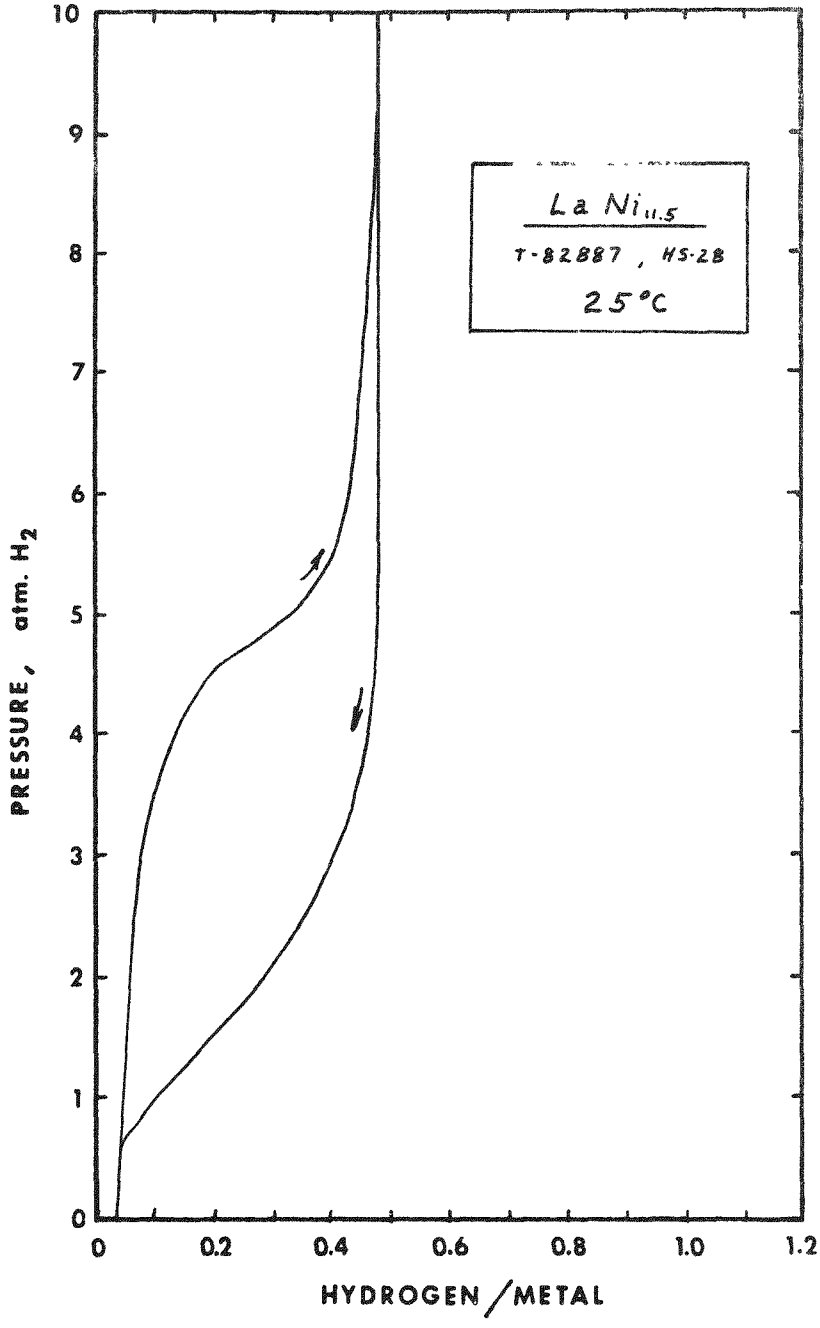

Figure 1-3-3. Dynamic pressure-composition isotherms determined at a reaction rate of 0.0027 g-atom H/min. The actual temperatures differ from the indicated nominal by about 0.3°C.

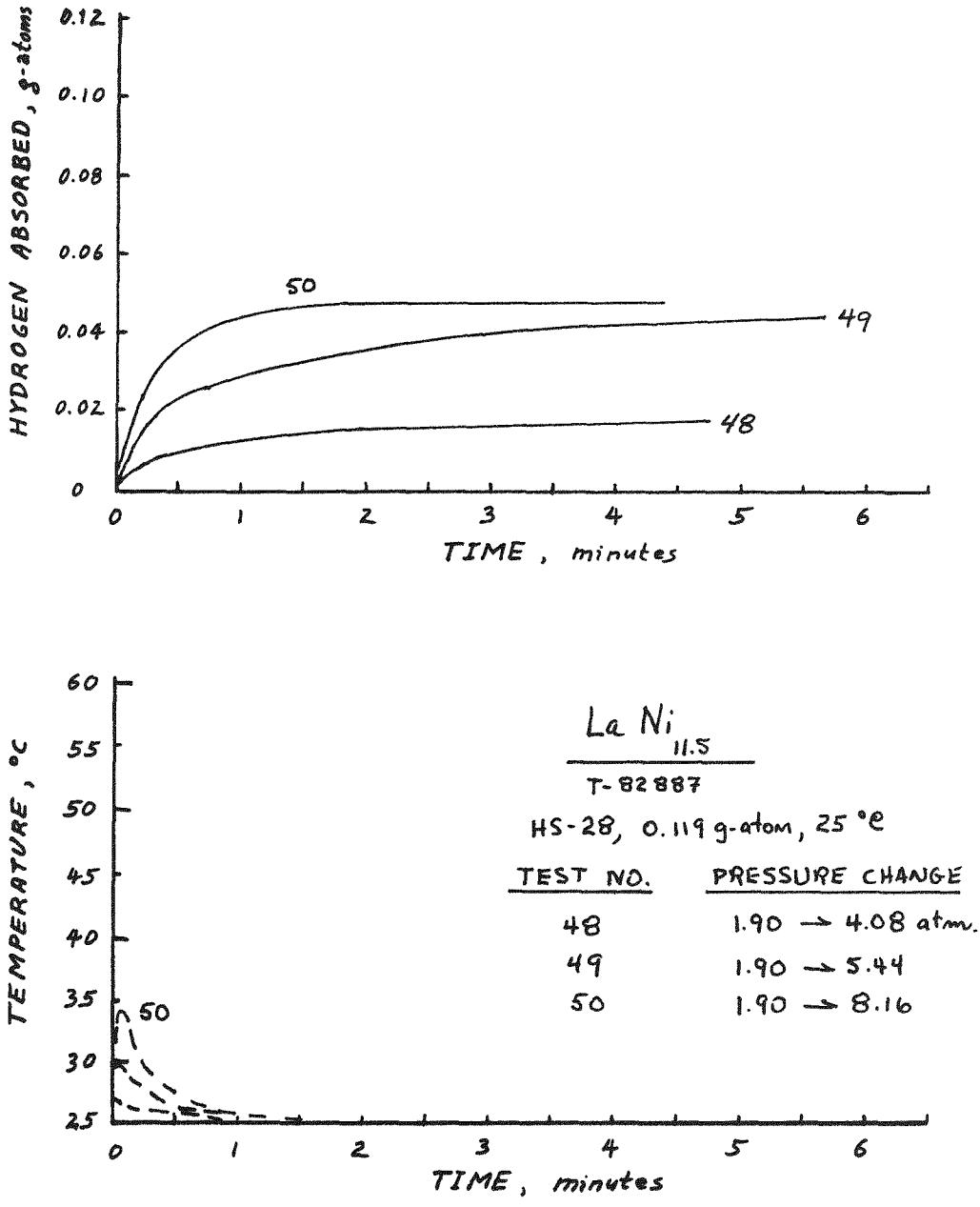

Figure 1-3-4. Time response data for the reaction mass and instantaneous temperature during isobaric absorption at a nominal temperature of 25 C.

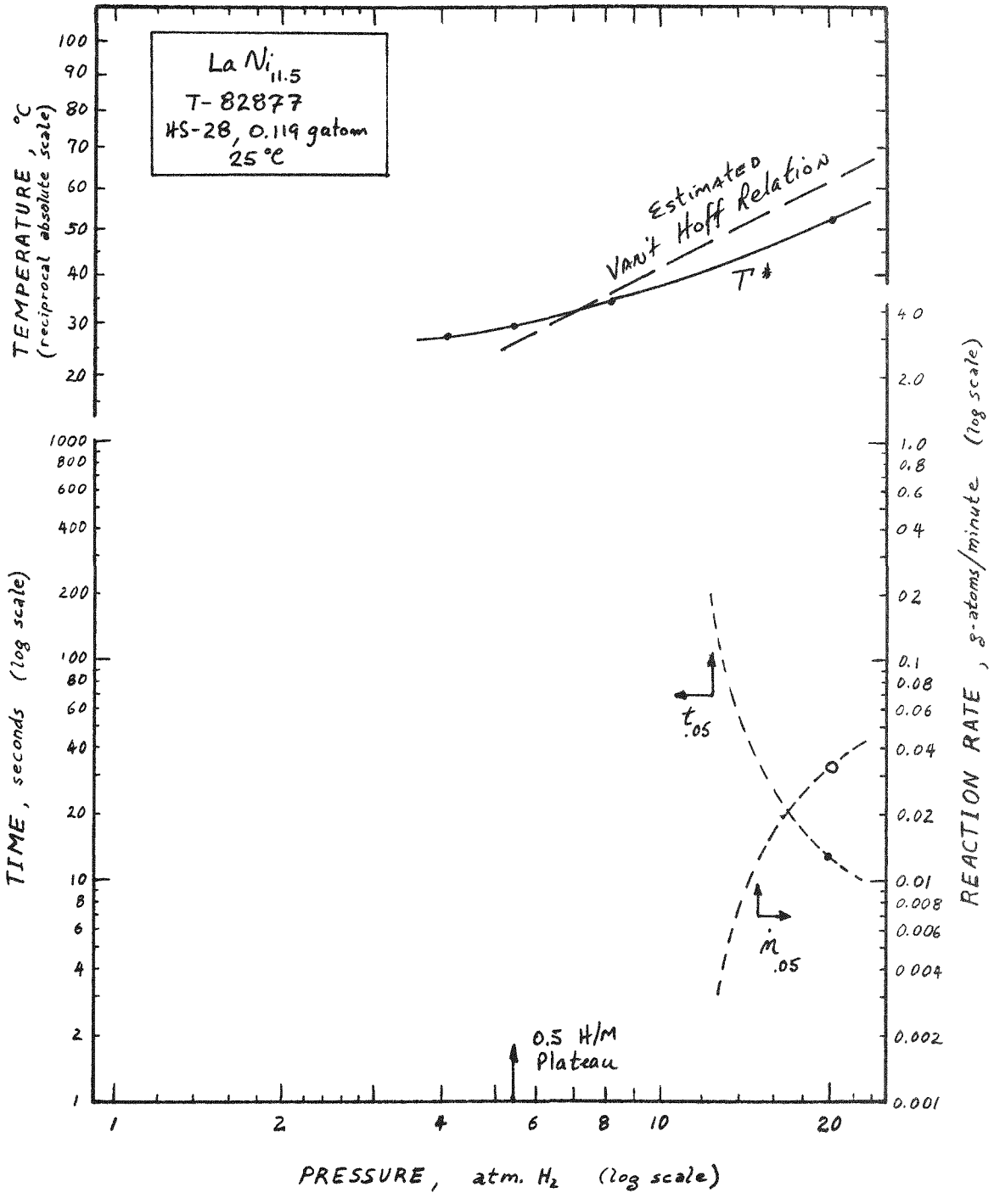

Figure 1-3-5. Summary of absorption kinetic data at 25°C showing the maximum temperature excursion as well as the reaction rate and time at 0.05 g-atoms hydrogen reacted (~0.5H/M).

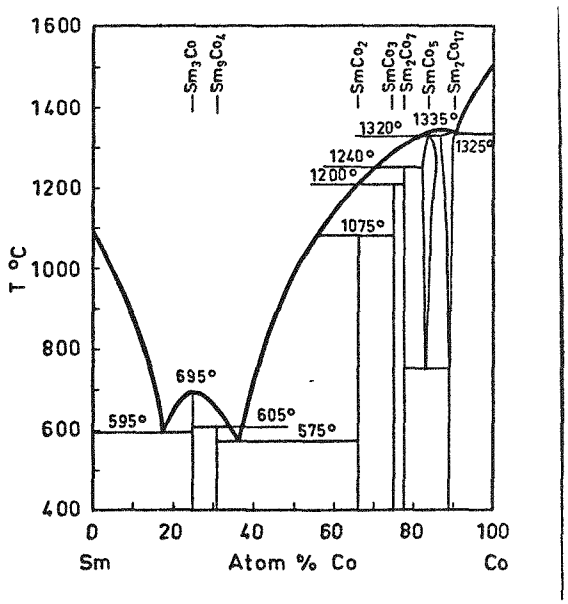

Figure 2-0-1. Sm-Co Phase Diagram (14).

PN 1-71964 250X

(a) As-Cast

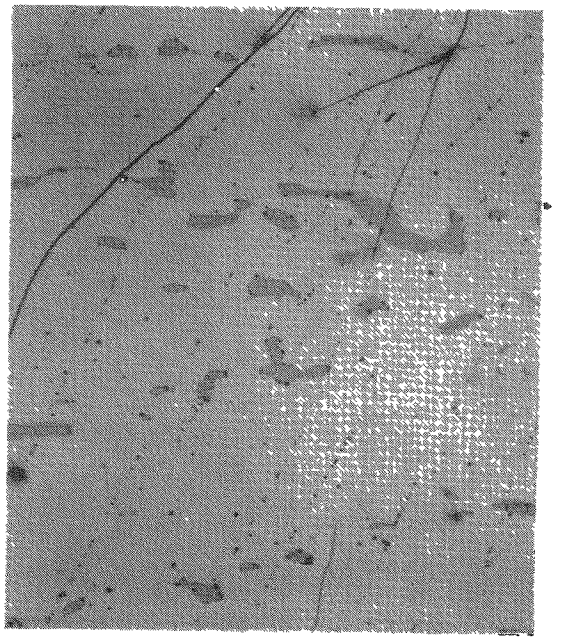

PN 1-72967 250X

(b) S.T. 4 Hours at 1225°C

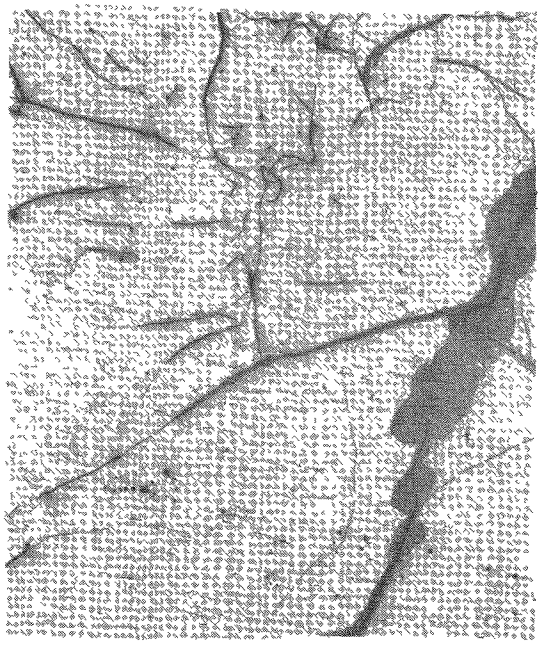

PN 1-72968 100X

(c) S.T. + Aged 24 Hrs. @ 700°C

Figure 2-1-1. Microstructures of $SmCo_5$. (Note the lower magnification for (c).

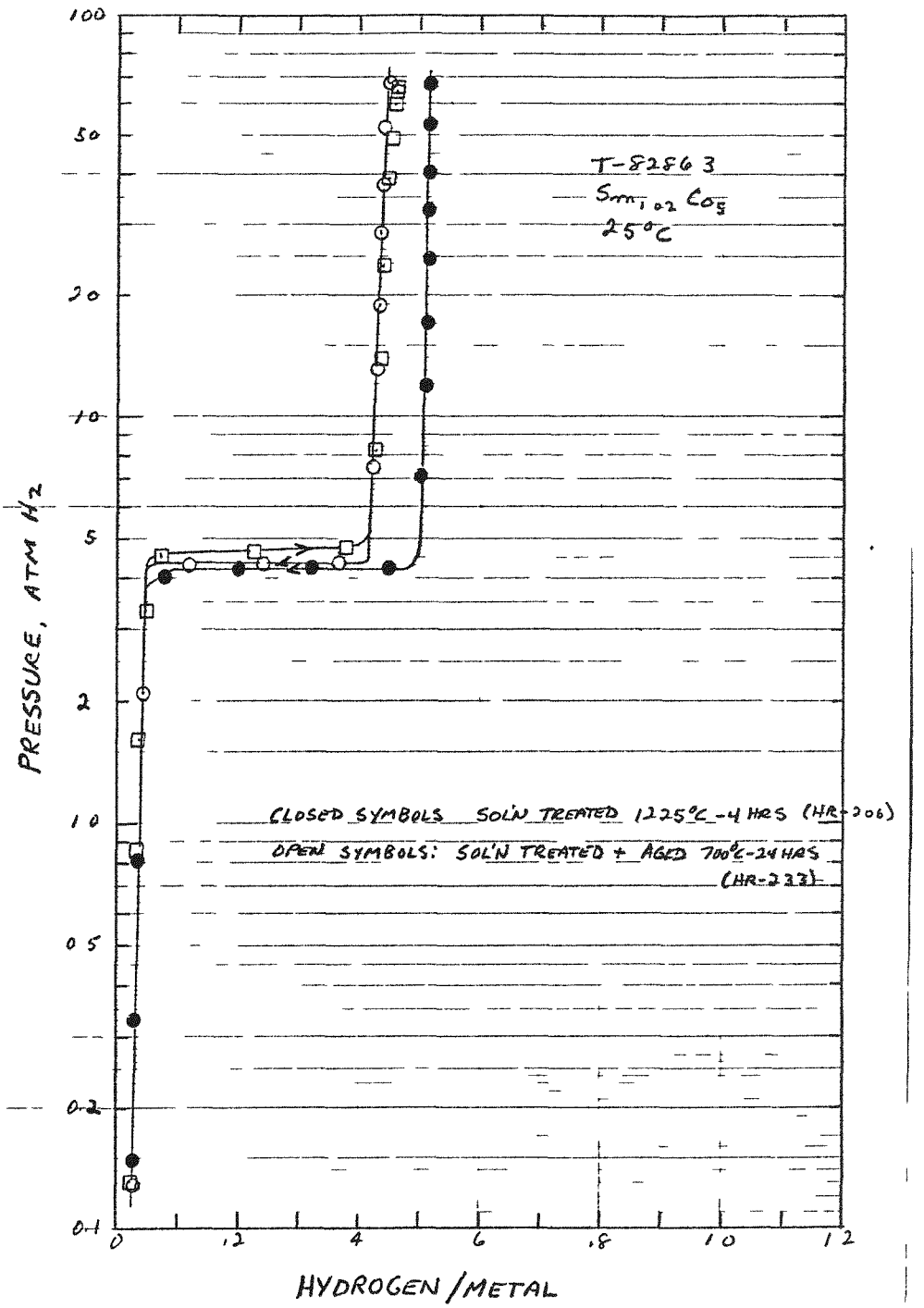

Figure 2-1-2. Static 25°C Isotherms for $SmCo_5$.

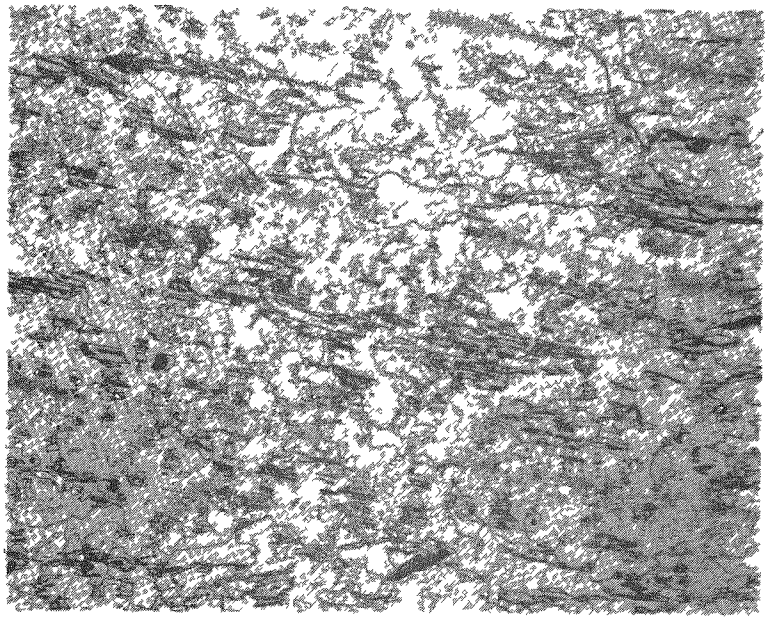

PN 1-72783 250X

(a) As-Cast

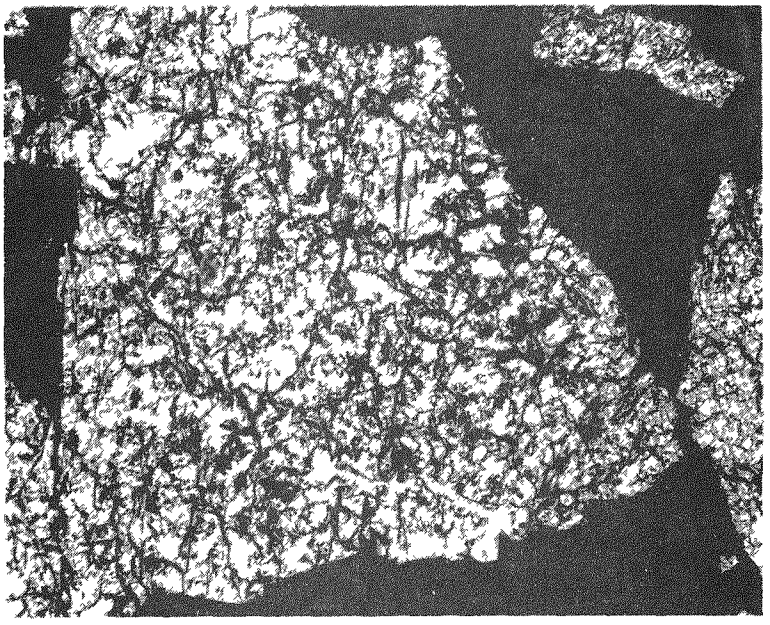

PN 1-73385 100X

(b) Cycled 4 Times

Figure 3-1-1. Microstructures of $LaNi_{3.8}Fe_{1.2}$.

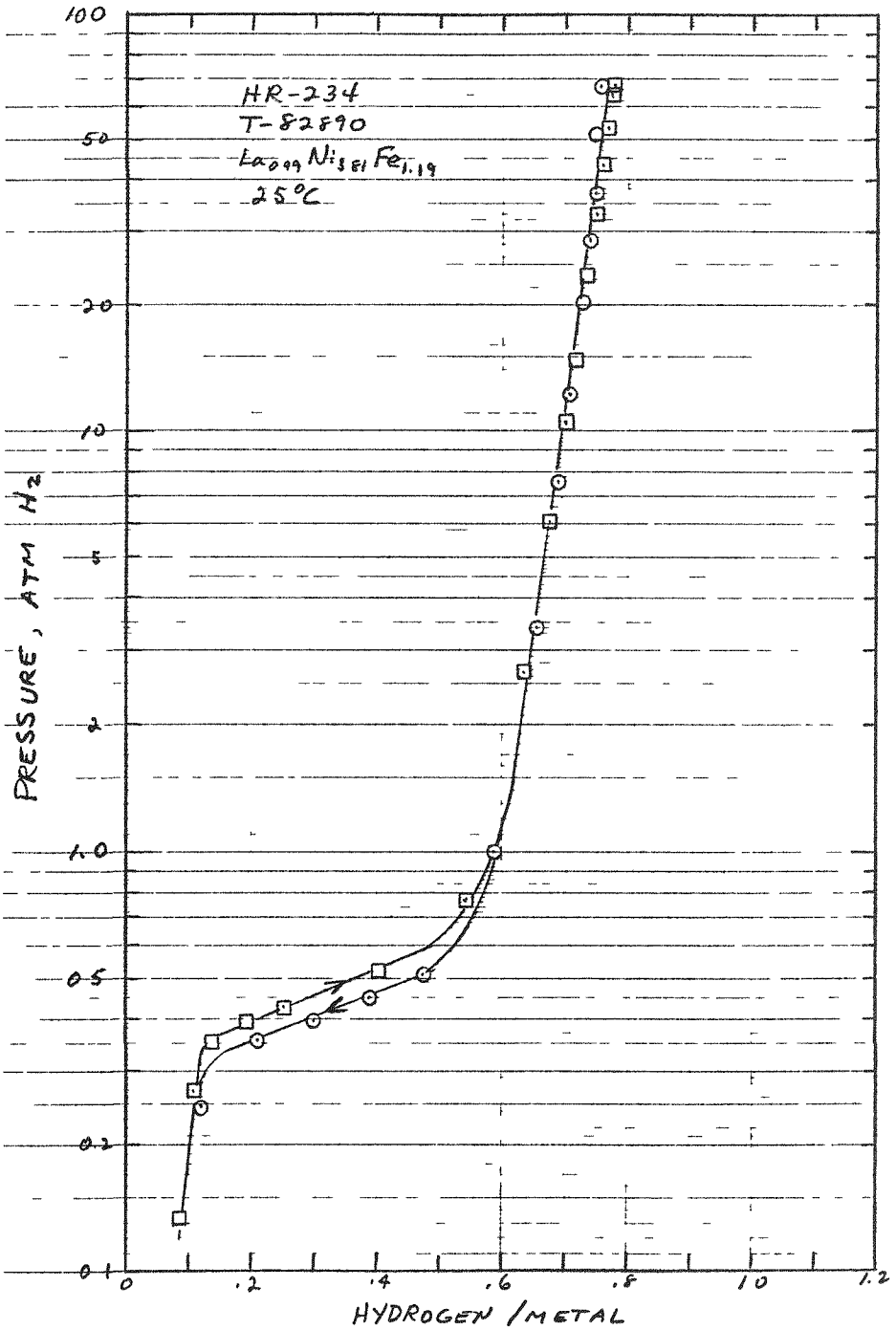

Figure 3-1-2. Static 25°C Isotherms for As-Cast $LaNi_{3.8}Fe_{1.2}$.

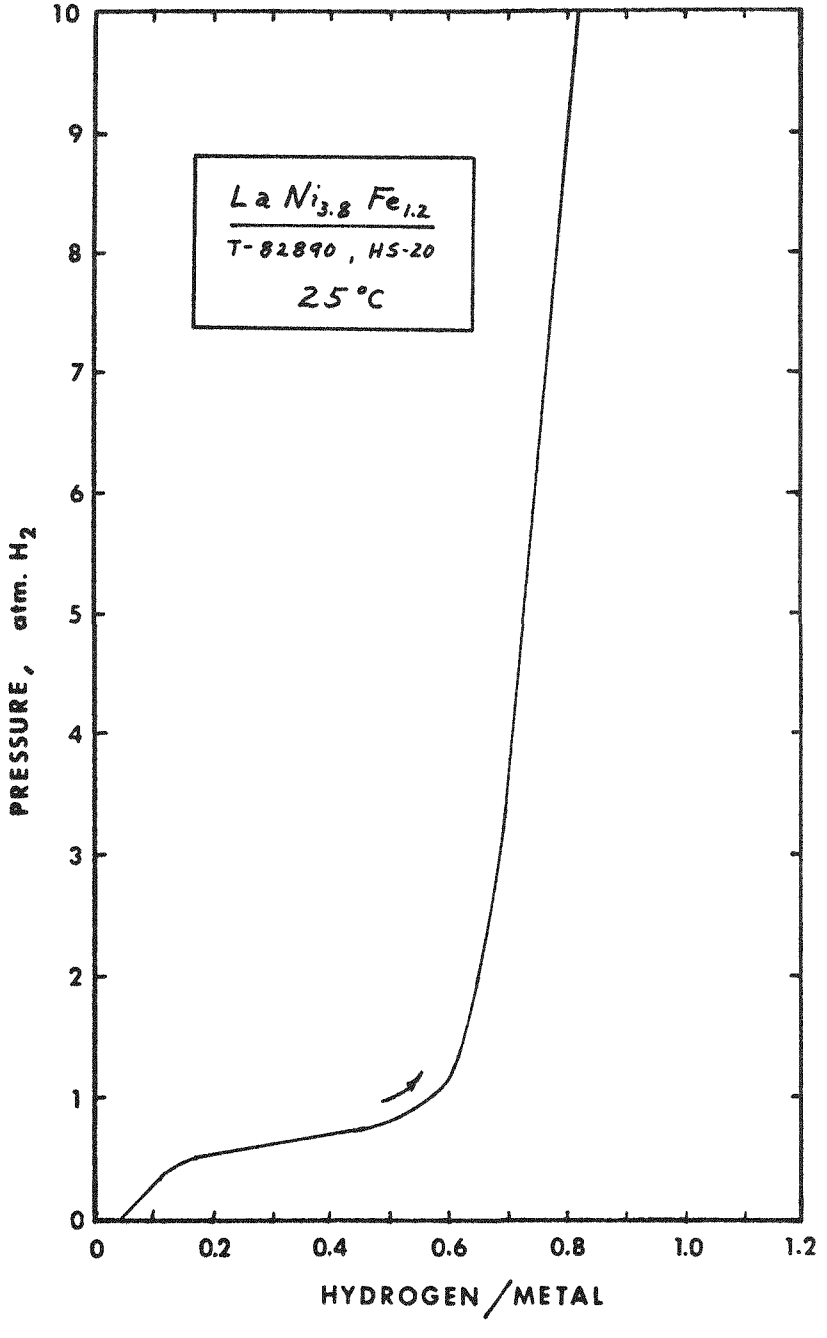

Figure 3-1-3. Dynamic pressure-composition absorption isotherm determined at a reaction rate of 0.0027 g-atom H/min. The actual temperature is about 0.3°C higher than the indicated nominal.

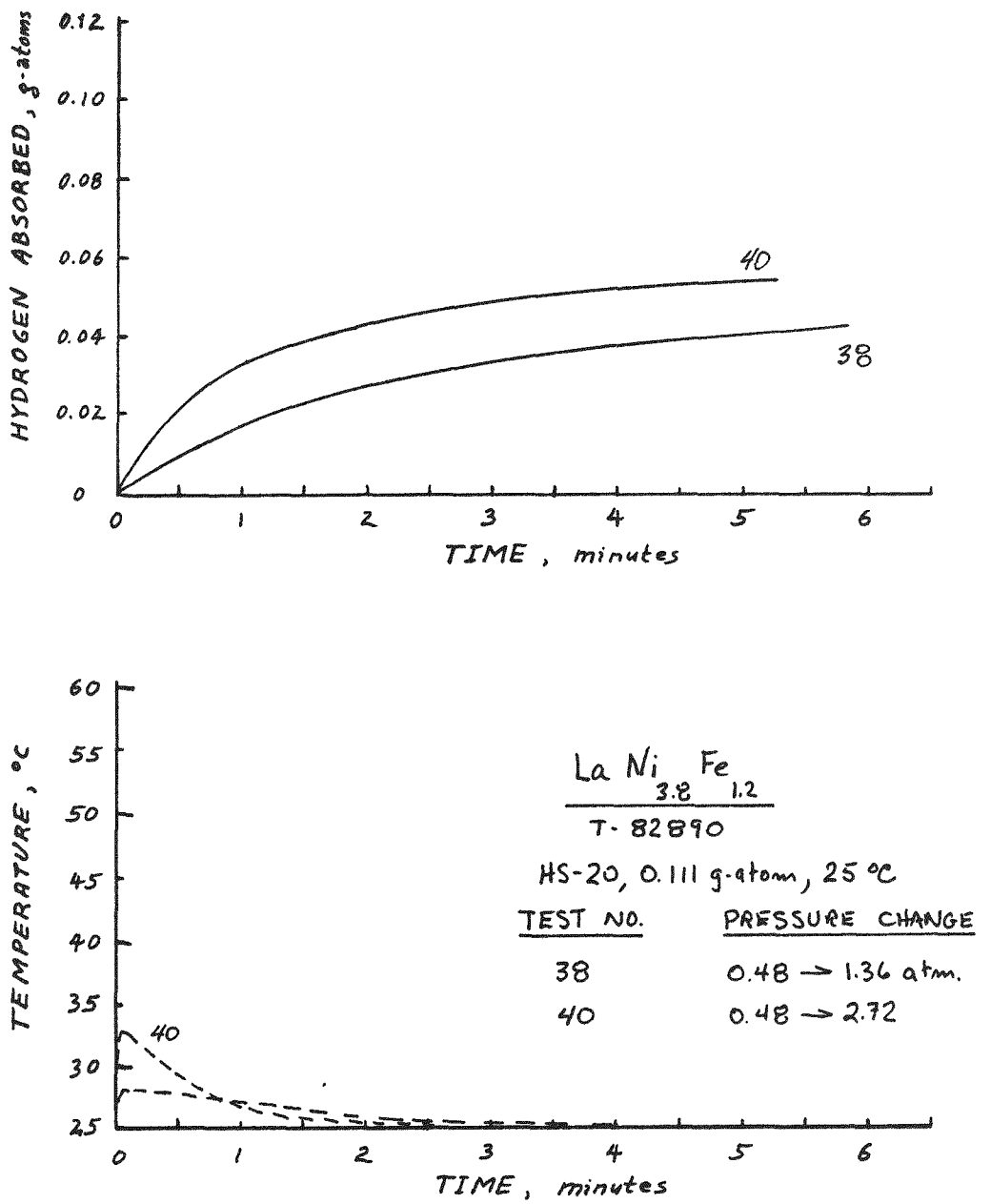

Figure 3-1-4. Time response data for the reaction mass and instantaneous temperature during isobaric absorption at a nominal temperature of 25 C.

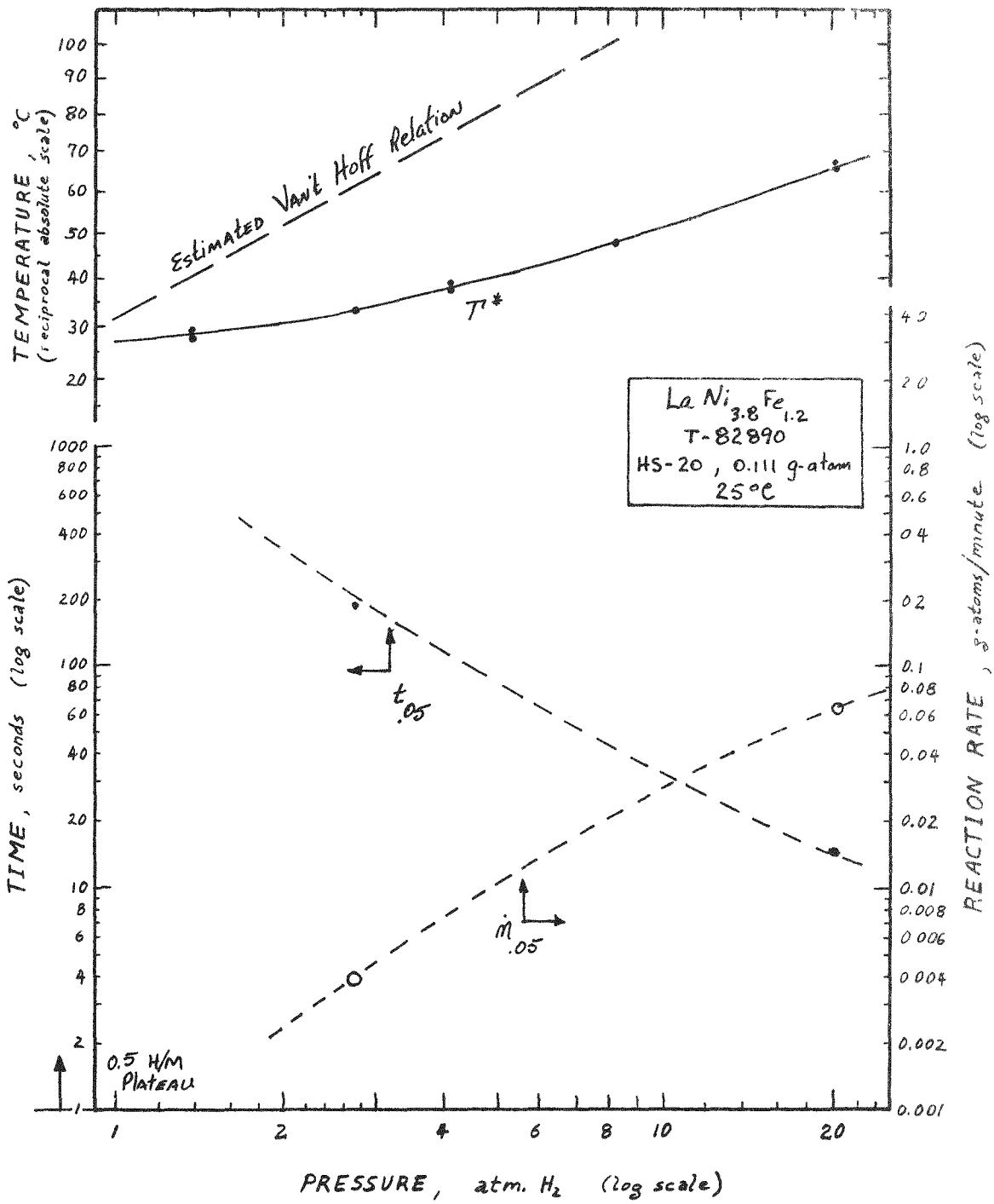

Figure 3-1-5. Summary of absorption kinetic data at 25°C showing the maximum temperature excursion as well as the reaction rate and time at 0.05 g-atoms hydrogen reacted (~0.5H/M).

PN 1-72789 250X

Figure 3-2-1. As-Cast Microstructure of $LaNi_{3.5}Cr_{1.5}$.

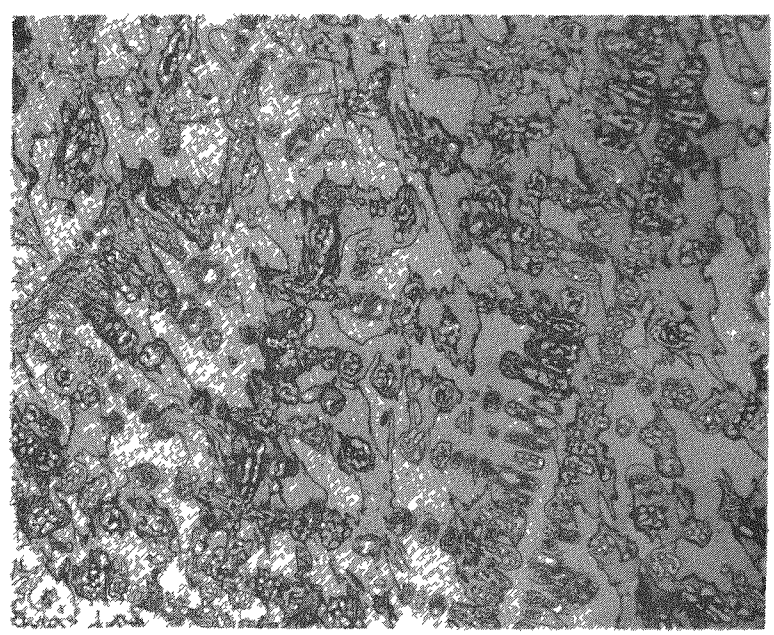

PN 1-73654 250X

Figure 3-3-1. As-Cast Microstructure of $LaNi_4Cr$.

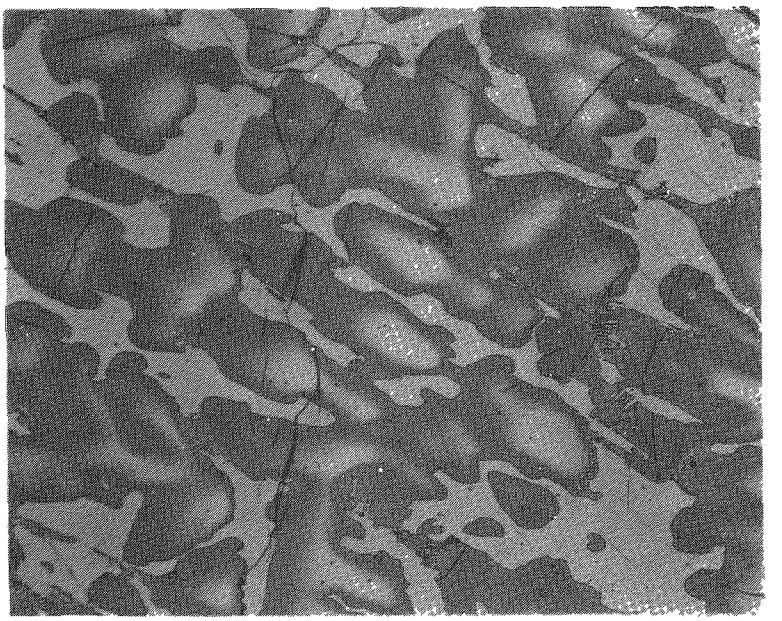

PN 1-72785 250X

Figure 3-4-1. As-Cast Microstructure of $LaNi_4Si$ (Actual Composition $La_{0.90}Ni_{4.04}Si_{0.96}$).

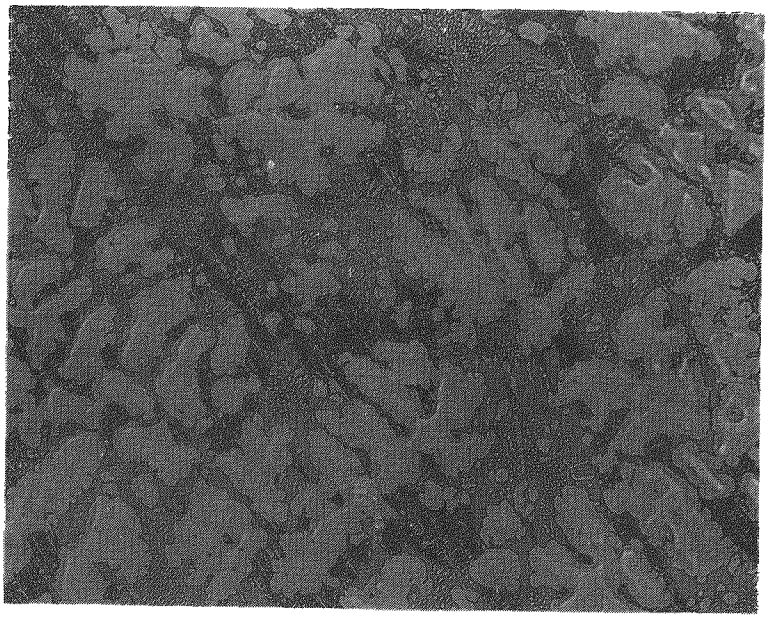

PN 1-72787 250X

Figure 3-5-1. As-Cast Microstructure of $LaNi_4Sn$.

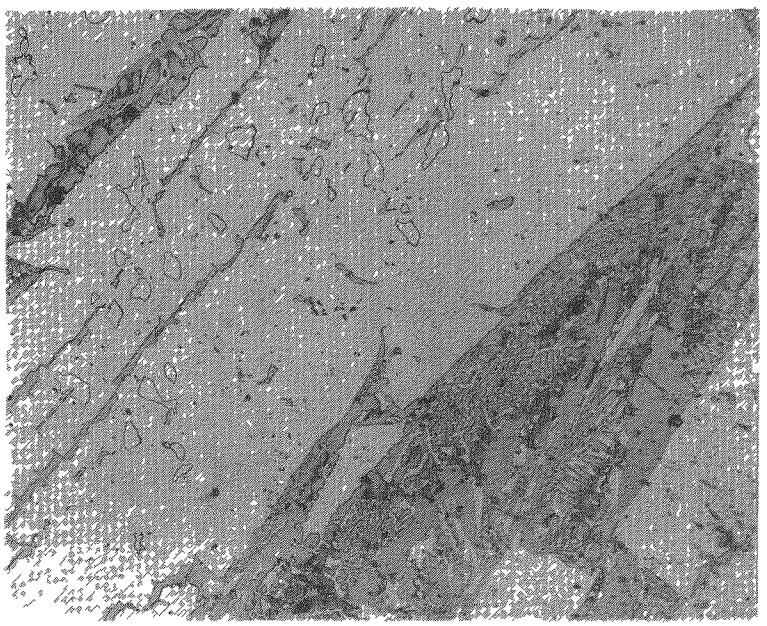

PN 1-73658 250X

Figure 3-6-1. As-Cast Microstructure of MNi_4Sn.

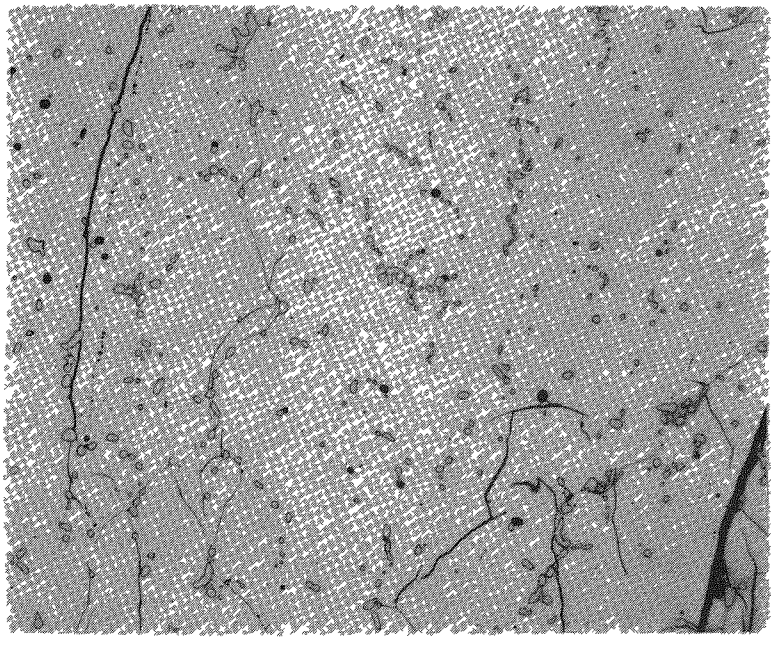

PN 1-72536 250X

Figure 3-7-1. Microstructure of $MNi_{4.3}Al_{0.7}$, Annealed 16 Hours at 1125°C.

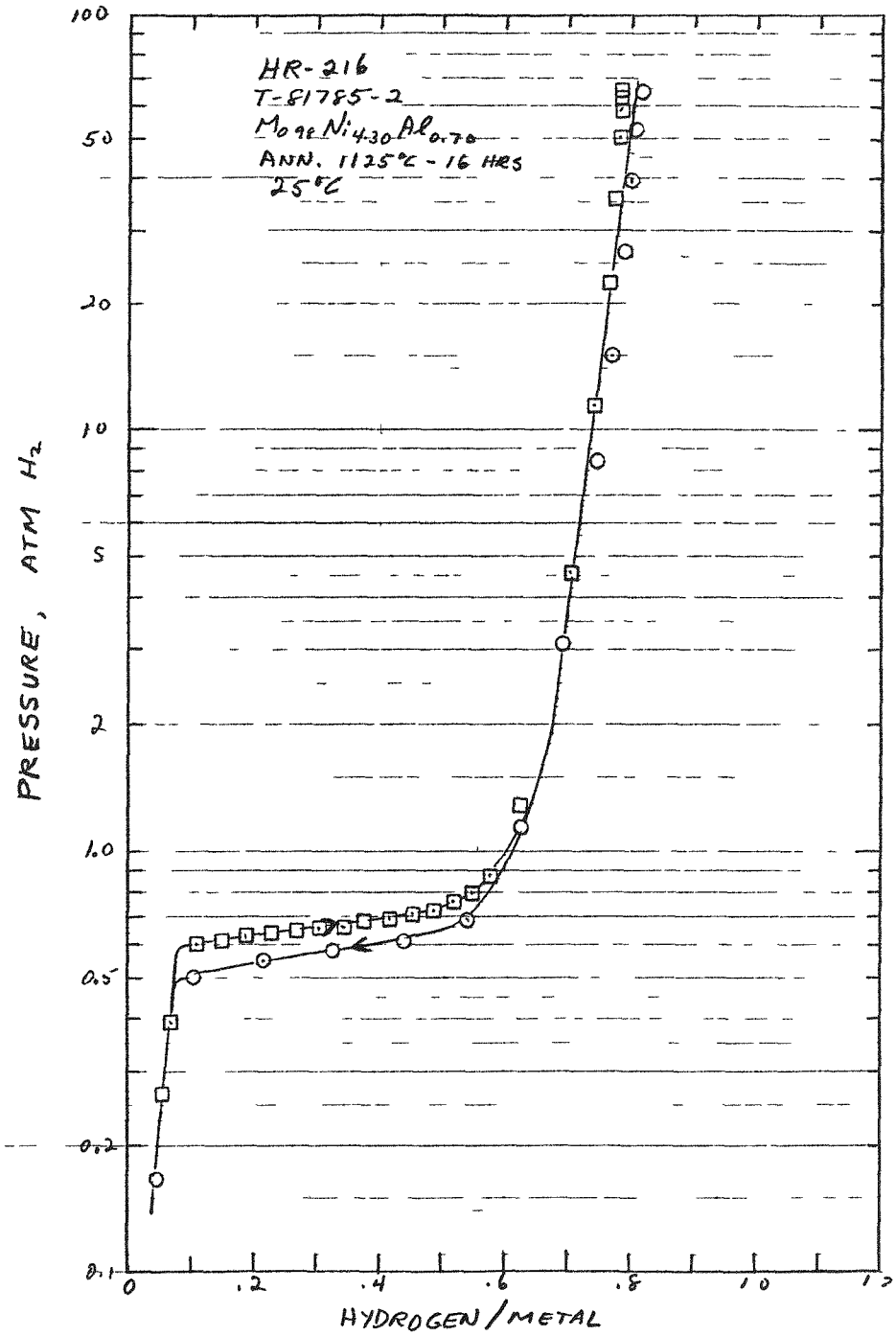

Figure 3-7-2. Static 25°C Isotherms for $MNi_{4.3}Al_{0.7}$, Annealed 16 Hours at 1125°C.

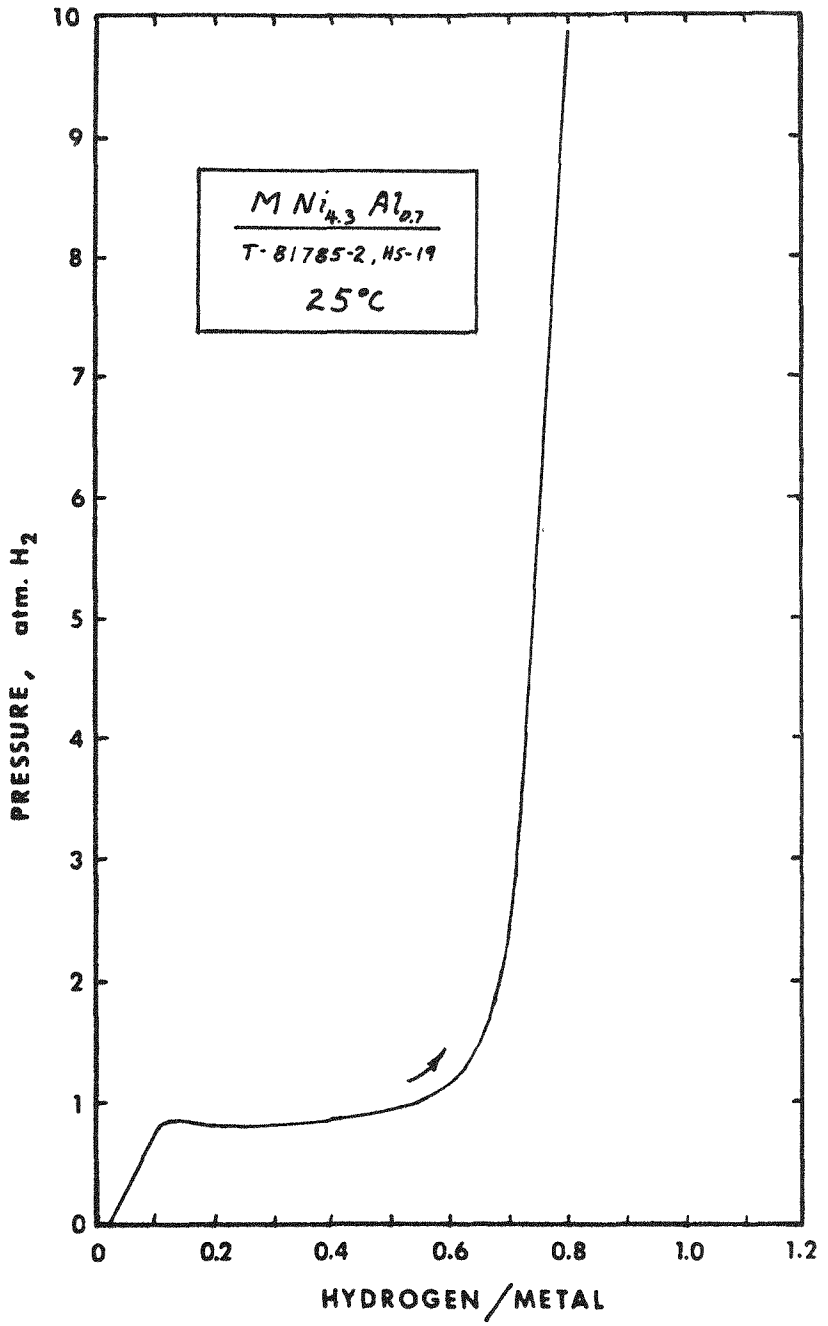

Figure 3-7-3. Dynamic pressure-composition absorption isotherm determined at a reaction rate of 0.0027 g-atom H/min. The actual temperature is about 0.3°C higher than the indicated nominal.

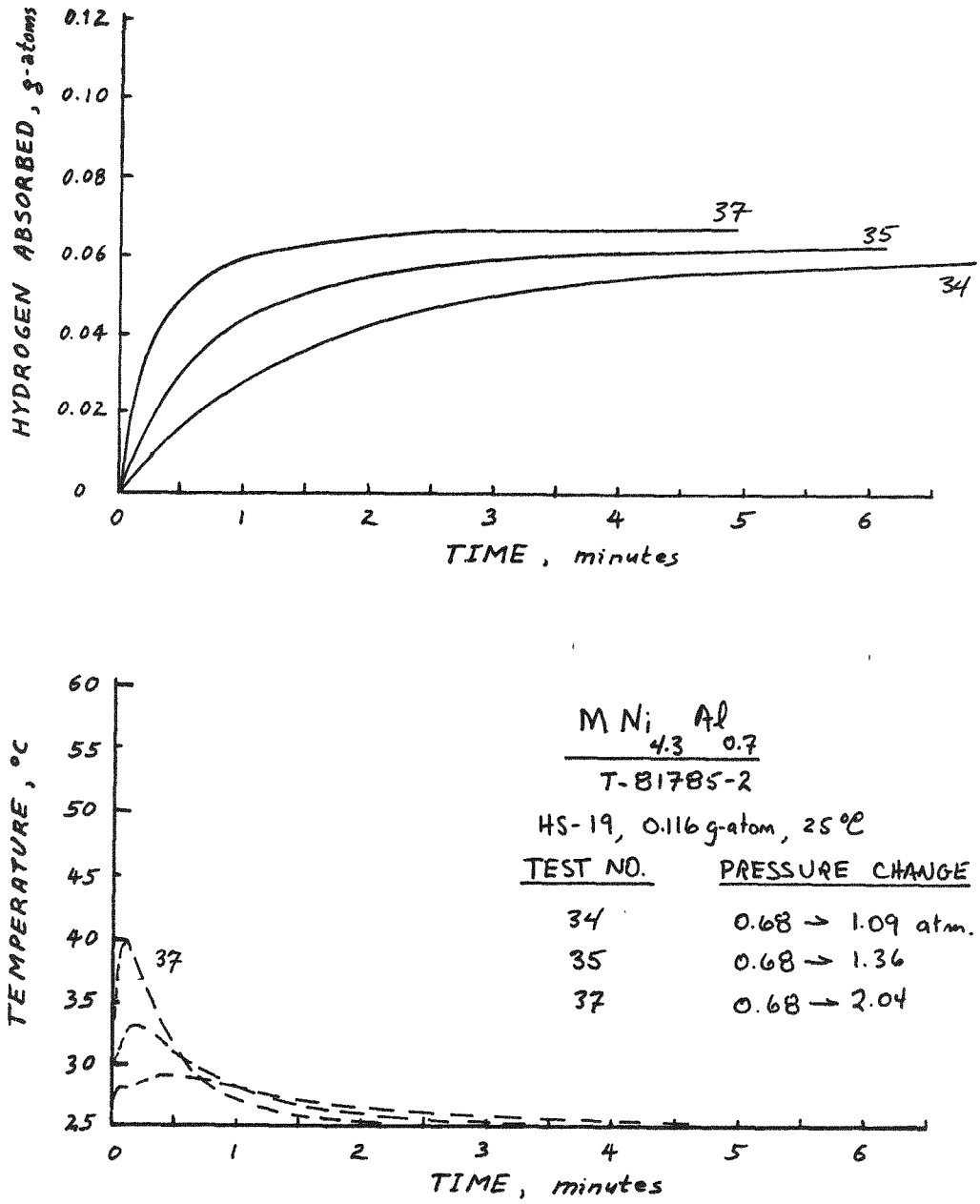

Figure 3-7-4. Time response data for the reaction mass and instantaneous temperature during isobaric absorption at a nominal temperature of 25 C.

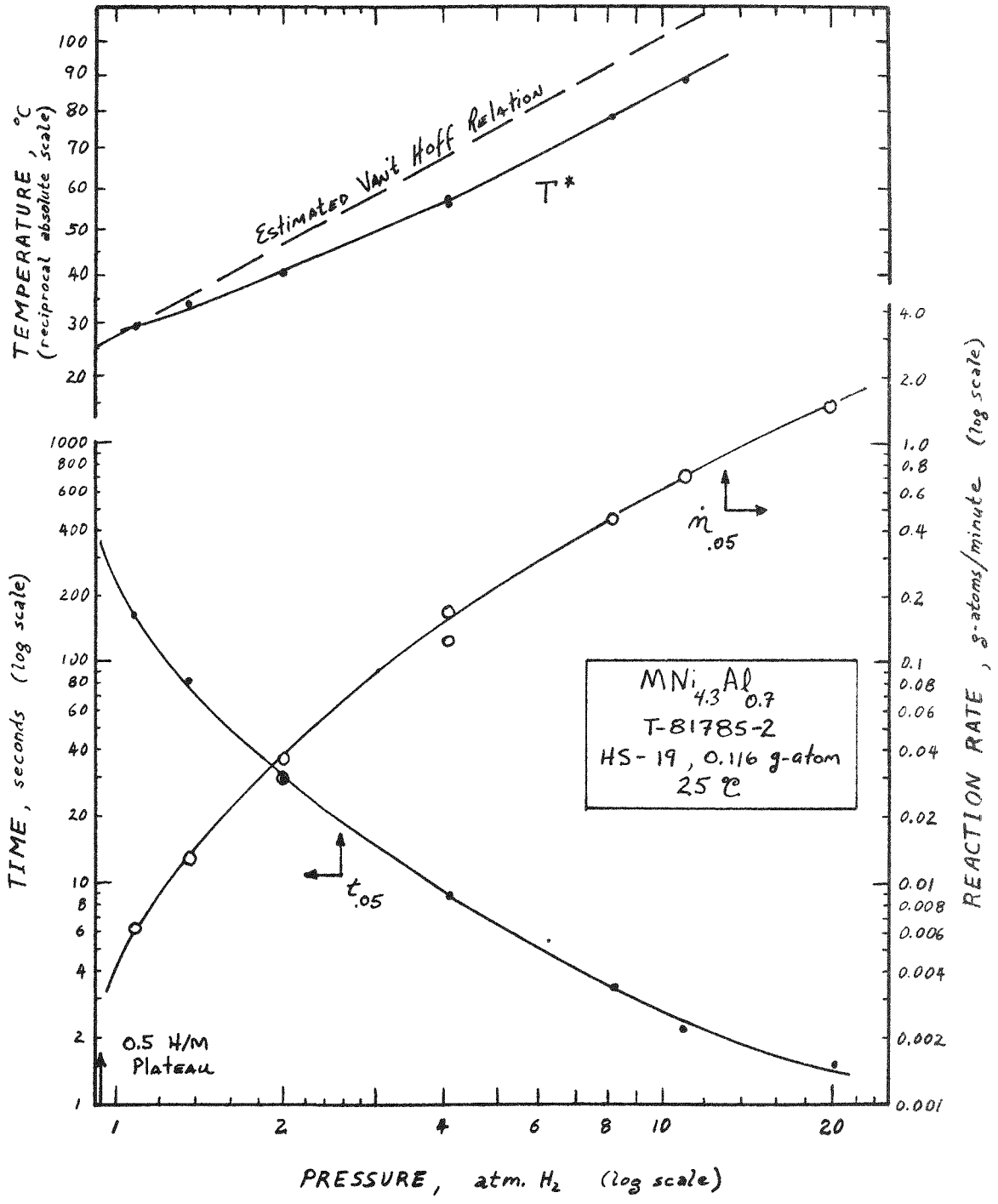

Figure 3-7-5. Summary of absorption kinetic data at 25°C showing the maximum temperature excursion as well as the reaction rate and time at 0.05 g-atoms hydrogen reacted (~0.5H/M).

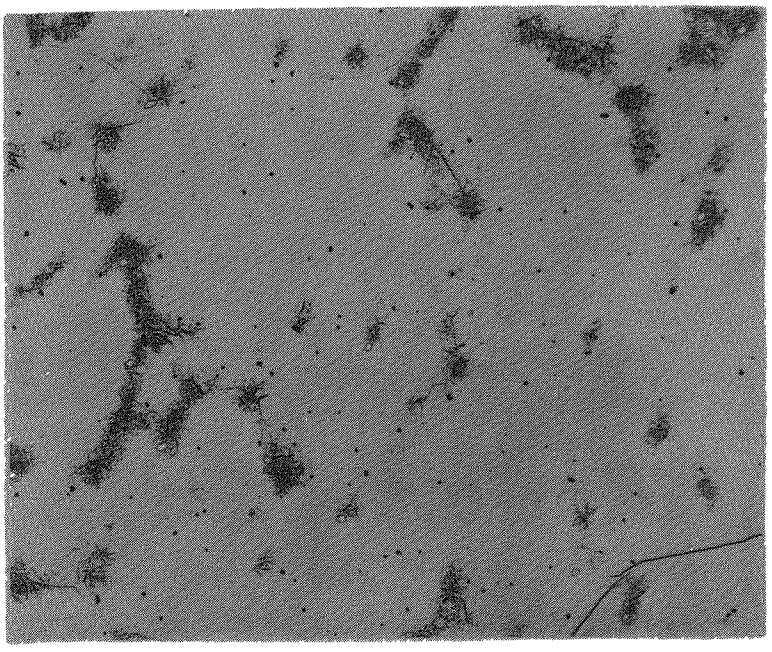

PN 1-72791 250X

Figure 4-1-1. As-Cast Microstructure of $LaNi_4Cu$.

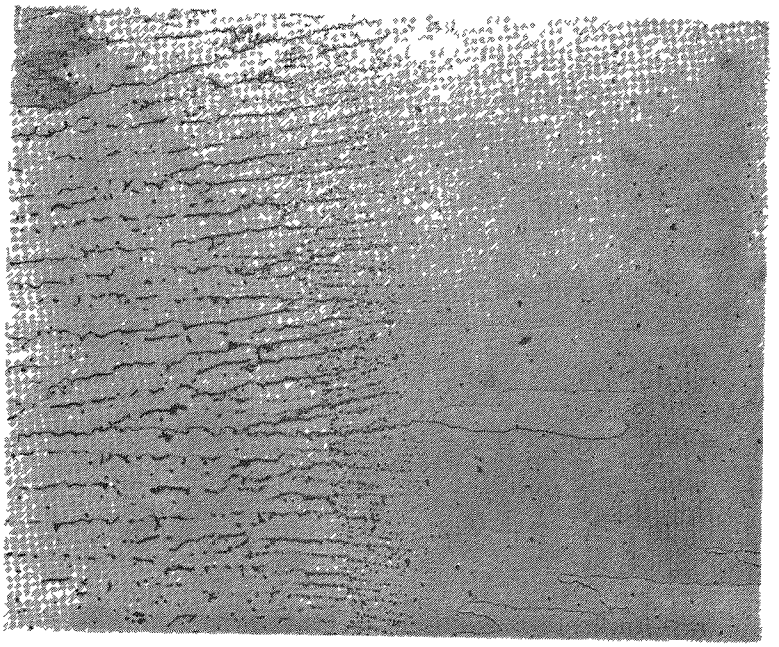

PN 1-72798 50X

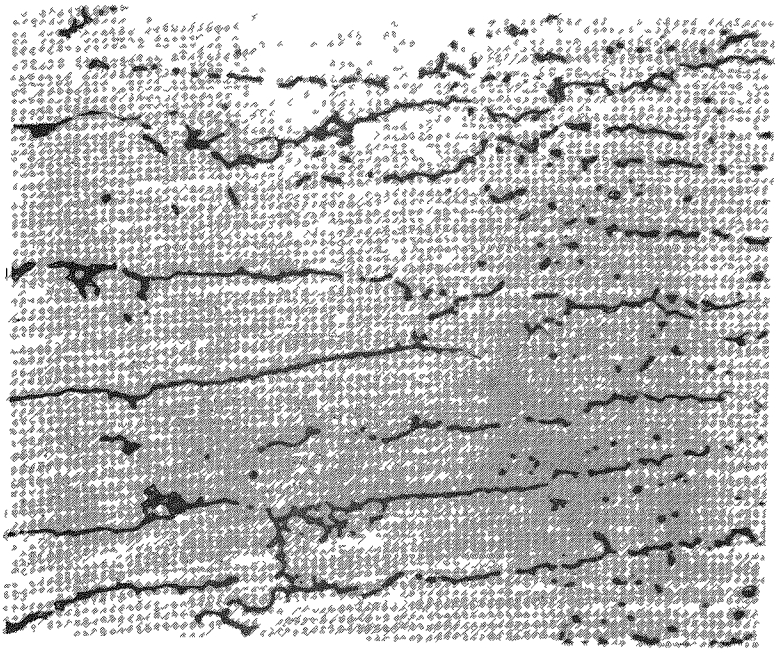

PN 1-72800 250X

Figure 4-2-1. As-Cast Microstructures of $LaNi_{4.5}Pd_{0.5}$.

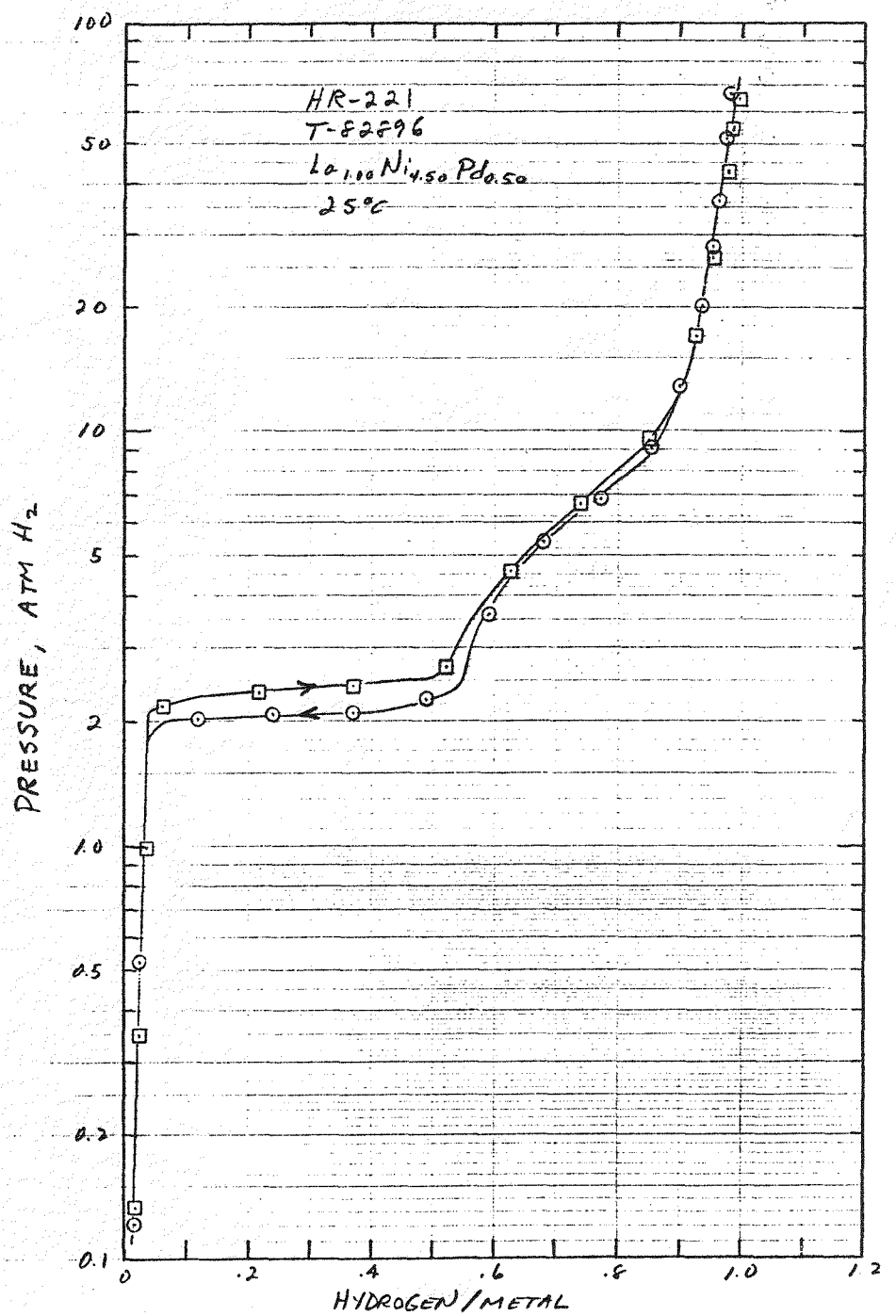

Figure 4-2-2. Static 25°C Isotherms for As-Cast $LaNi_{4.5}Pd_{0.5}$.

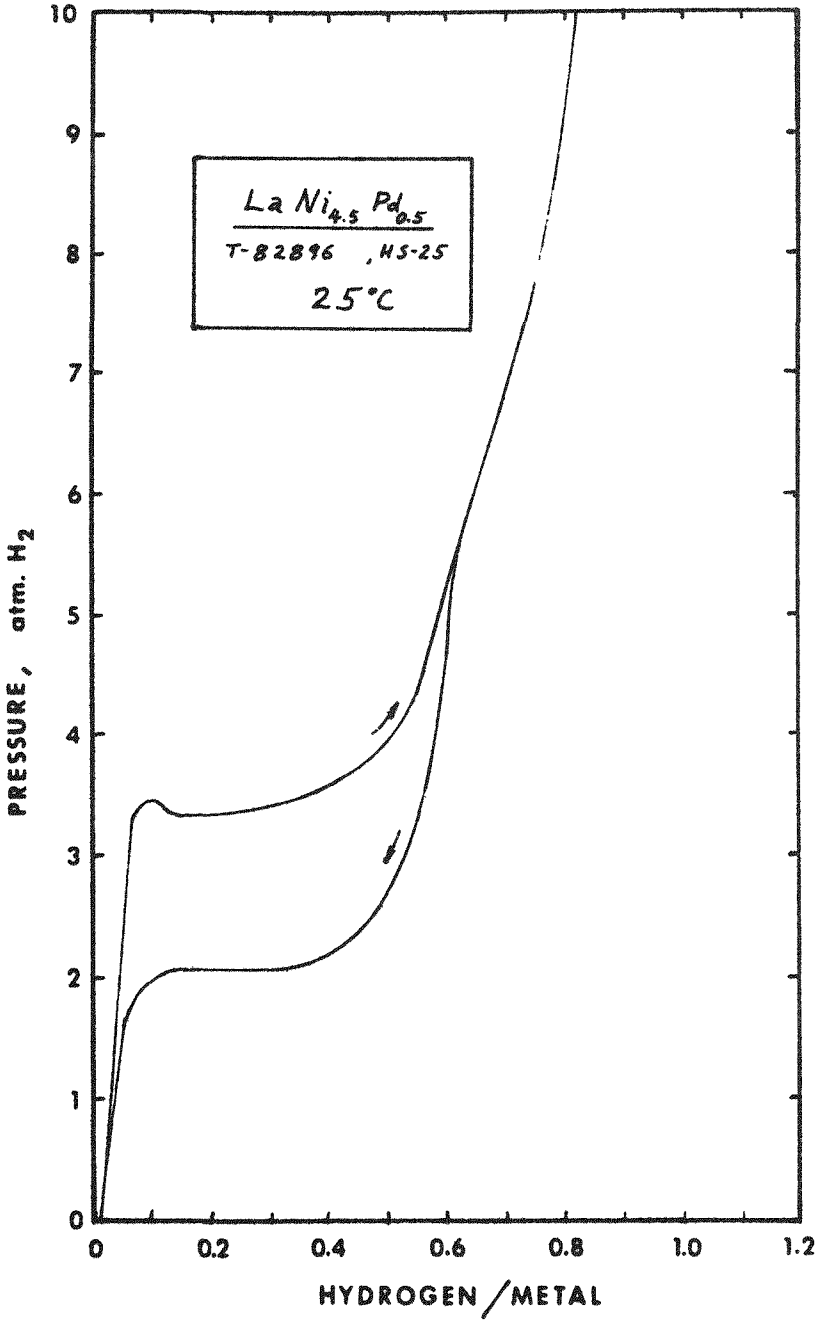

Figure 4-2-3. Dynamic pressure-composition isotherms determined at a reaction rate of 0.0027 g-atom H/min. The actual temperatures differ from the indicated nominal by about 0.3°C.

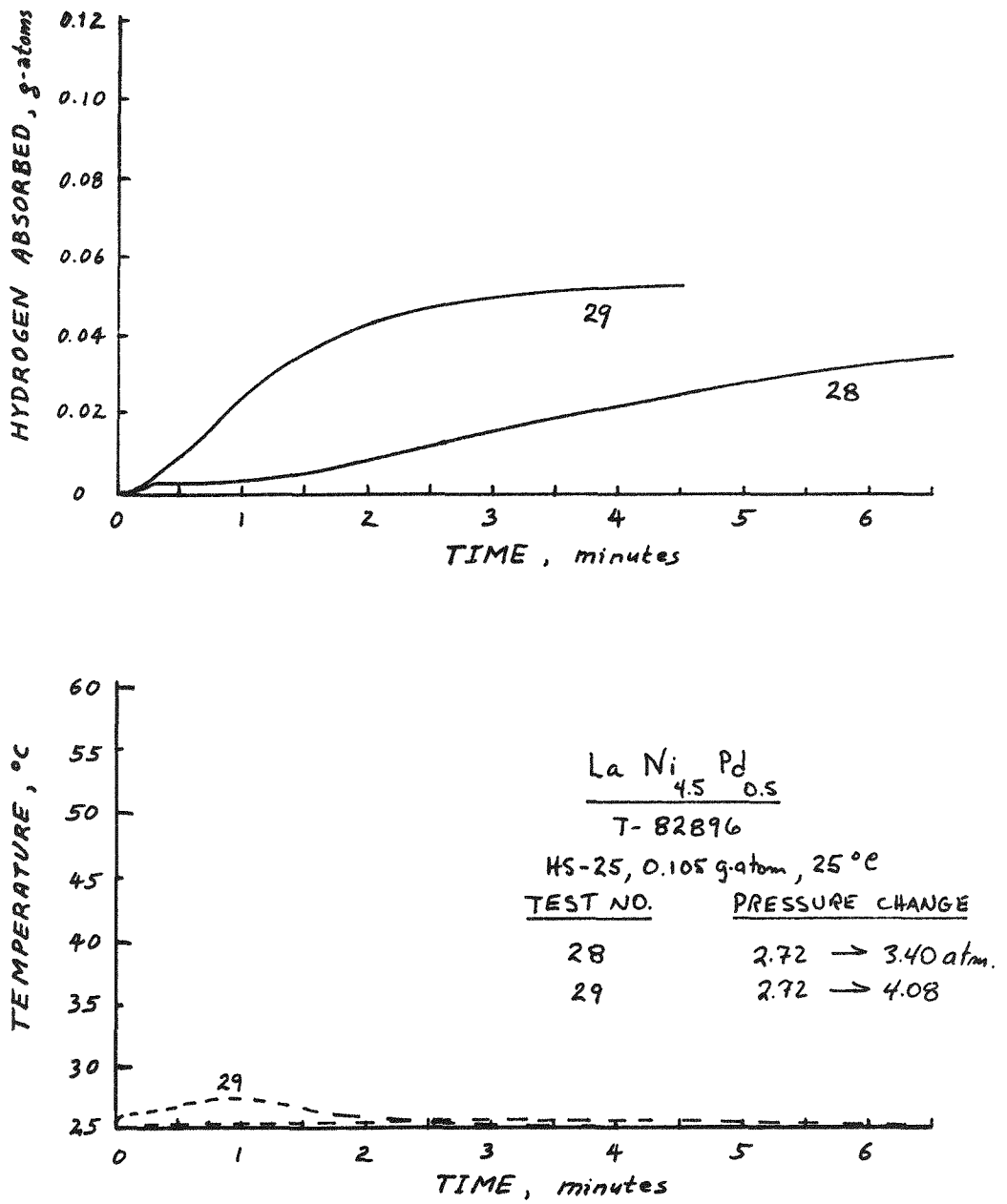

Figure 4-2-4. Time response data for the reaction mass and instantaneous temperature during isobaric absorption at a nominal temperature of 25 C.

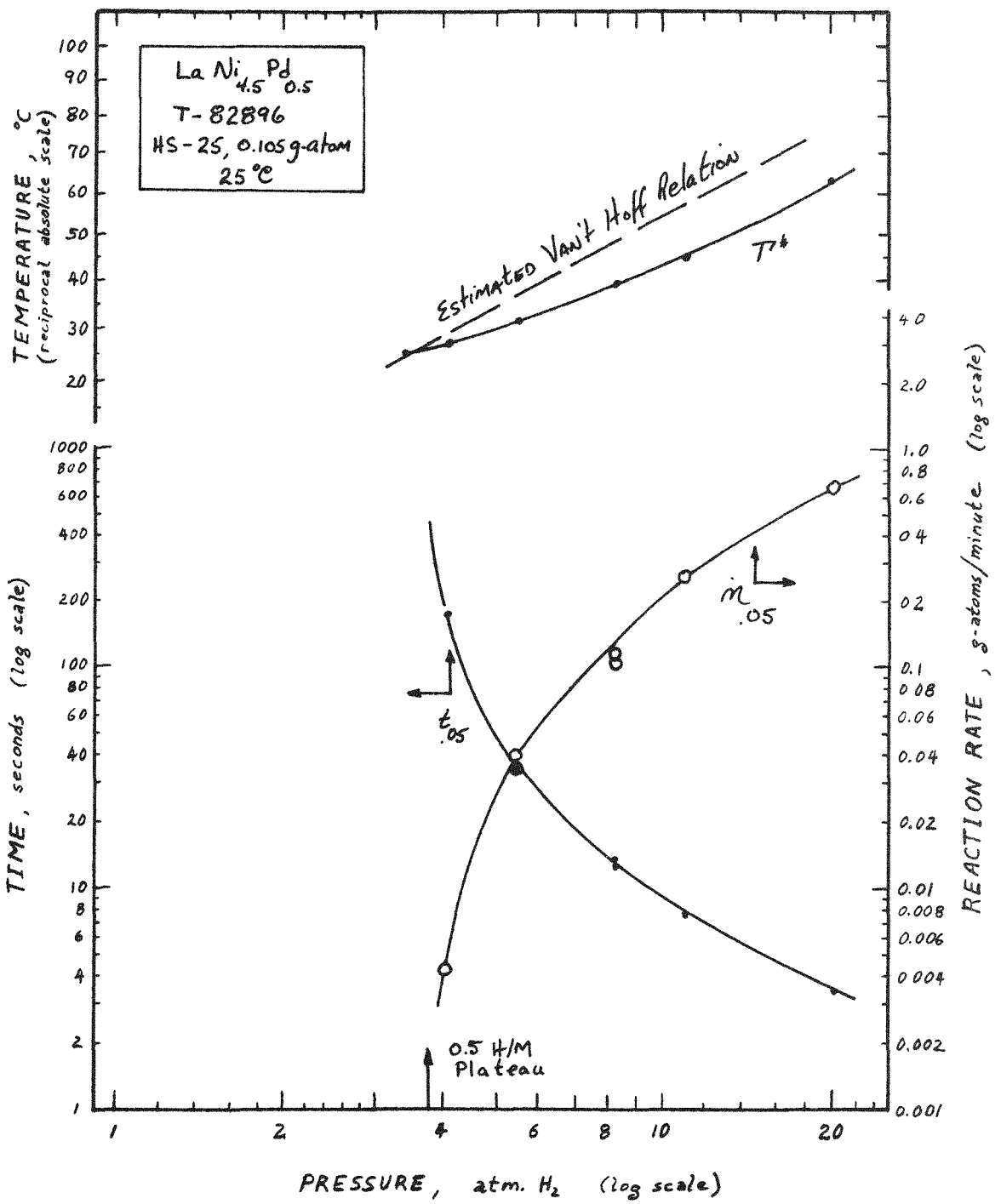

Figure 4-2-5. Summary of absorption kinetic data at 25°C showing the maximum temperature excursion as well as the reaction rate and time at 0.05 g-atoms hydrogen reacted (~0.5H/M).

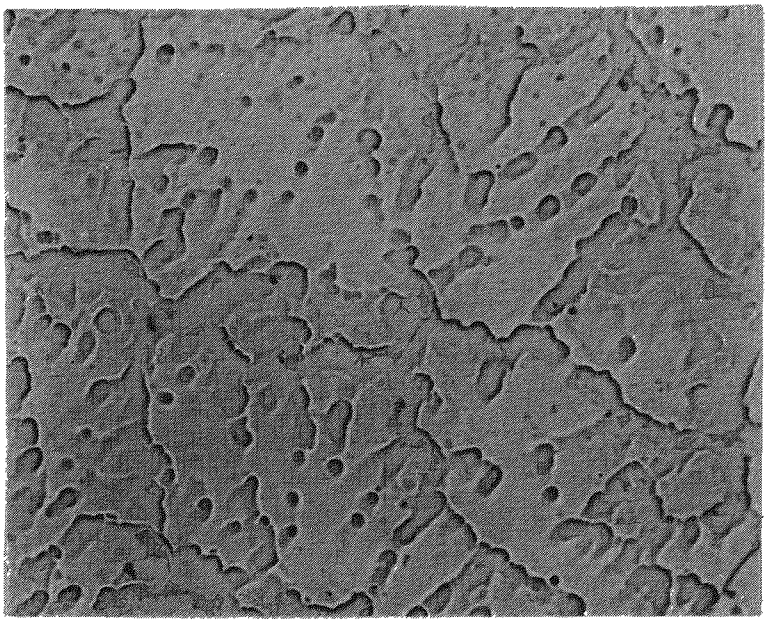

PN 1-73656 250X

Figure 4-3-1. As-Cast Microstructure of $LaNi_{4.7}Sn_{0.3}$.

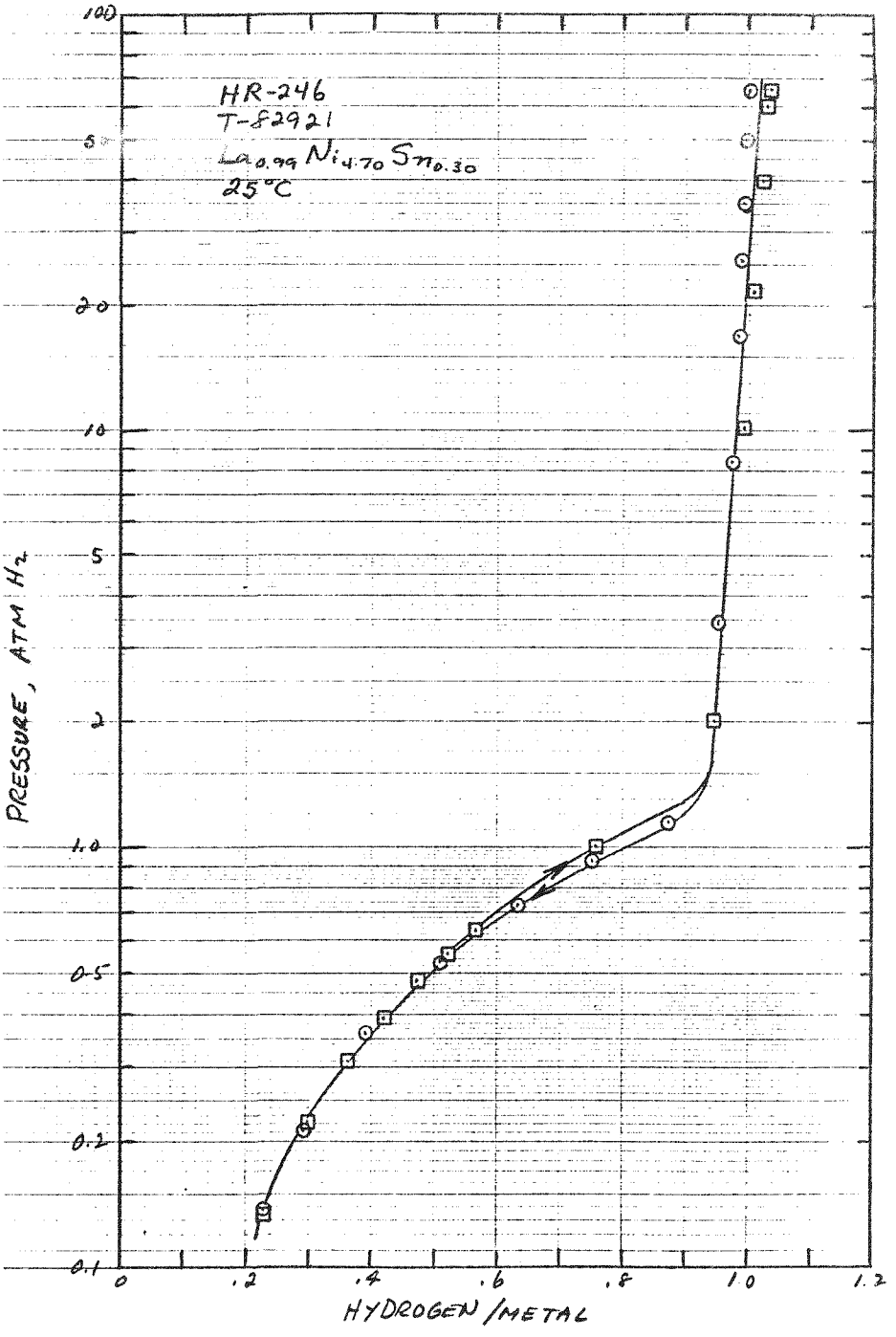

Figure 4-3-2. Static 25°C Isotherms for As-Cast $LaNi_{4.7}Sn_{0.3}$.

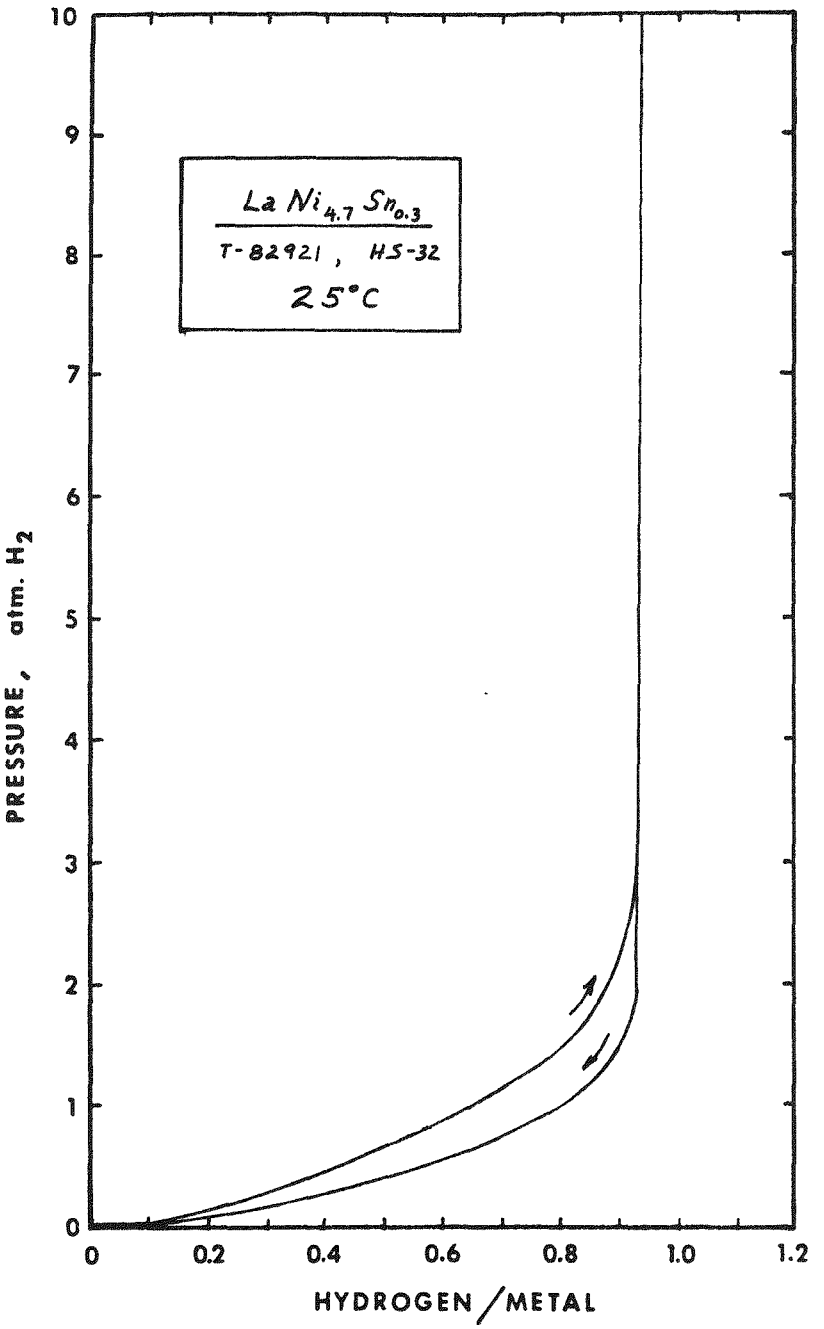

Figure 4-3-3. Dynamic pressure-composition isotherms determined at a reaction rate of 0.0027 g-atom H/min. The actual temperatures differ from the indicated nominal by about 0.3°C.

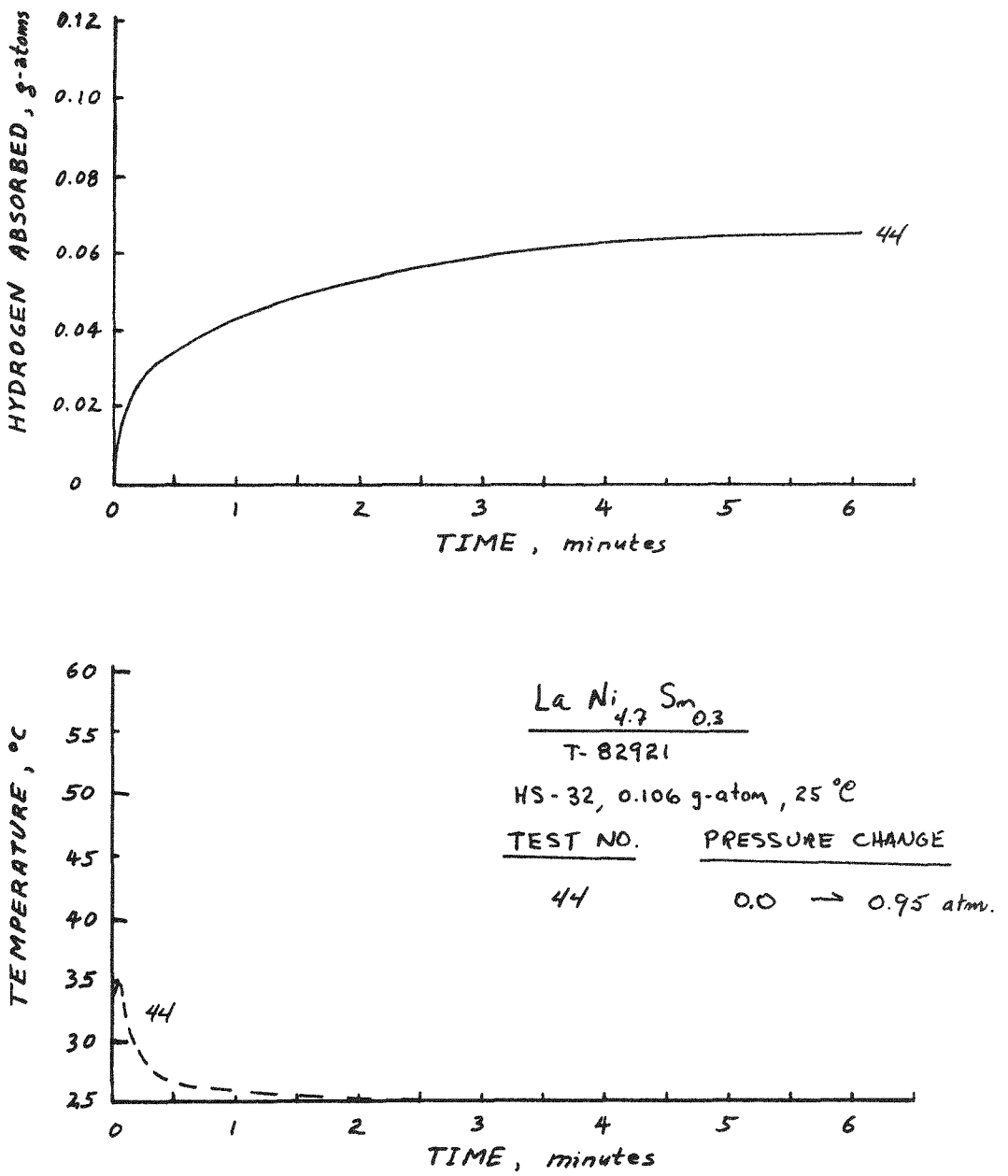

Figure 4-3-4. Time response data for the reaction mass and instantaneous temperature during isobaric absorption at a nominal temperature of 25 C.

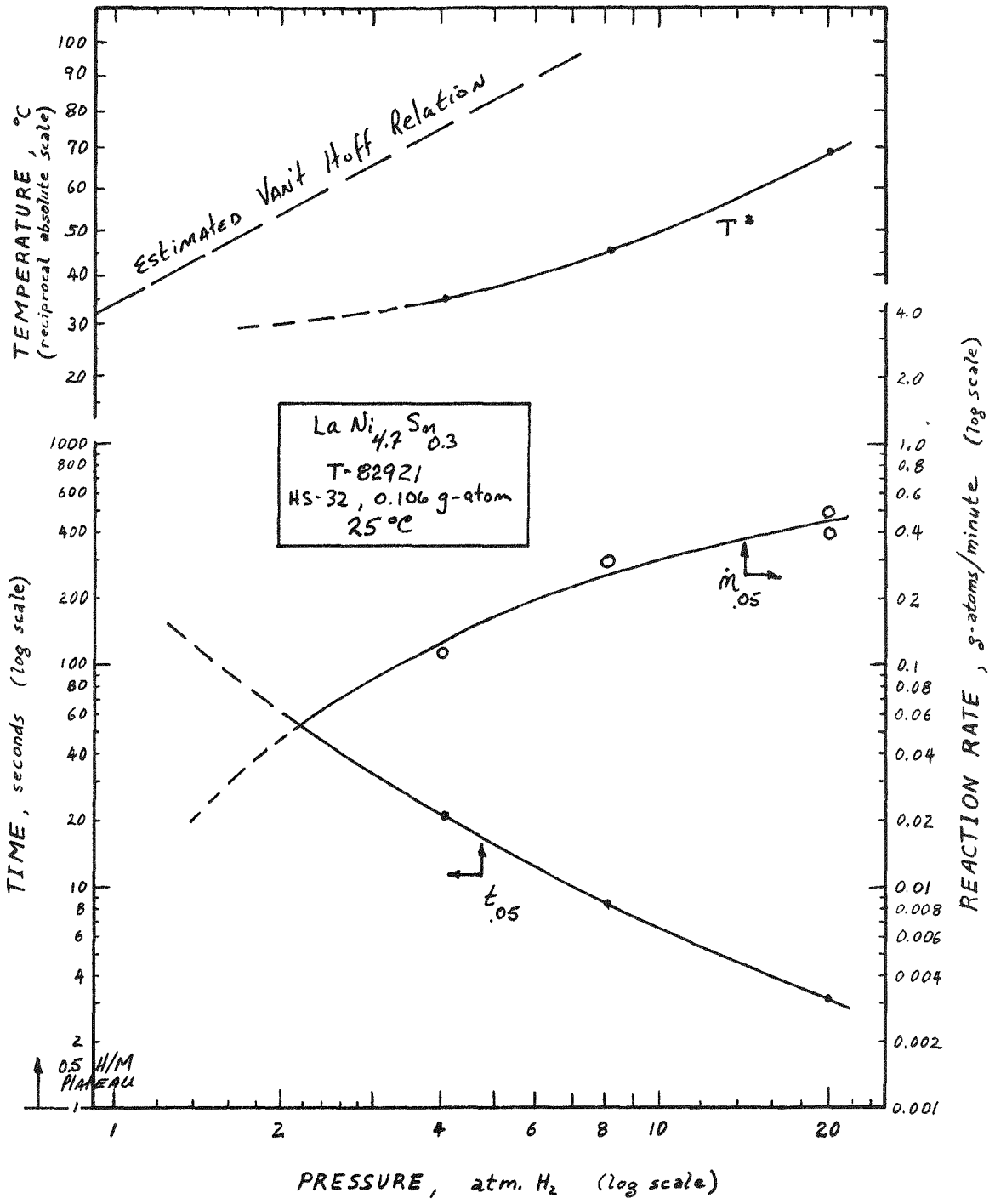

Figure 4-3-5. Summary of absorption kinetic data at 25°C showing the maximum temperature excursion as well as the reaction rate and time at 0.05 g-atoms hydrogen reacted (~0.5H/M).

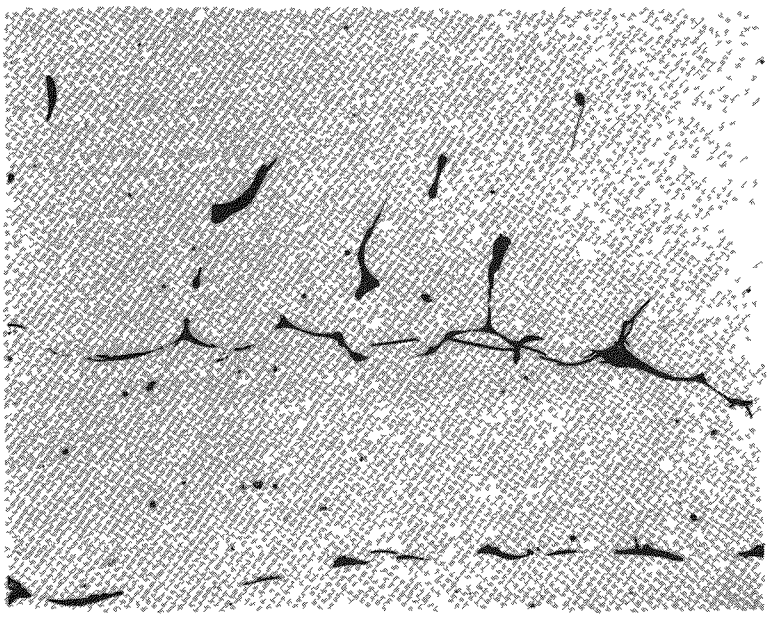

PN 1-73652 250X

Figure 4-4-1. As-Cast Microstructure of $LaNi_{4.8}Co_{.2}$.

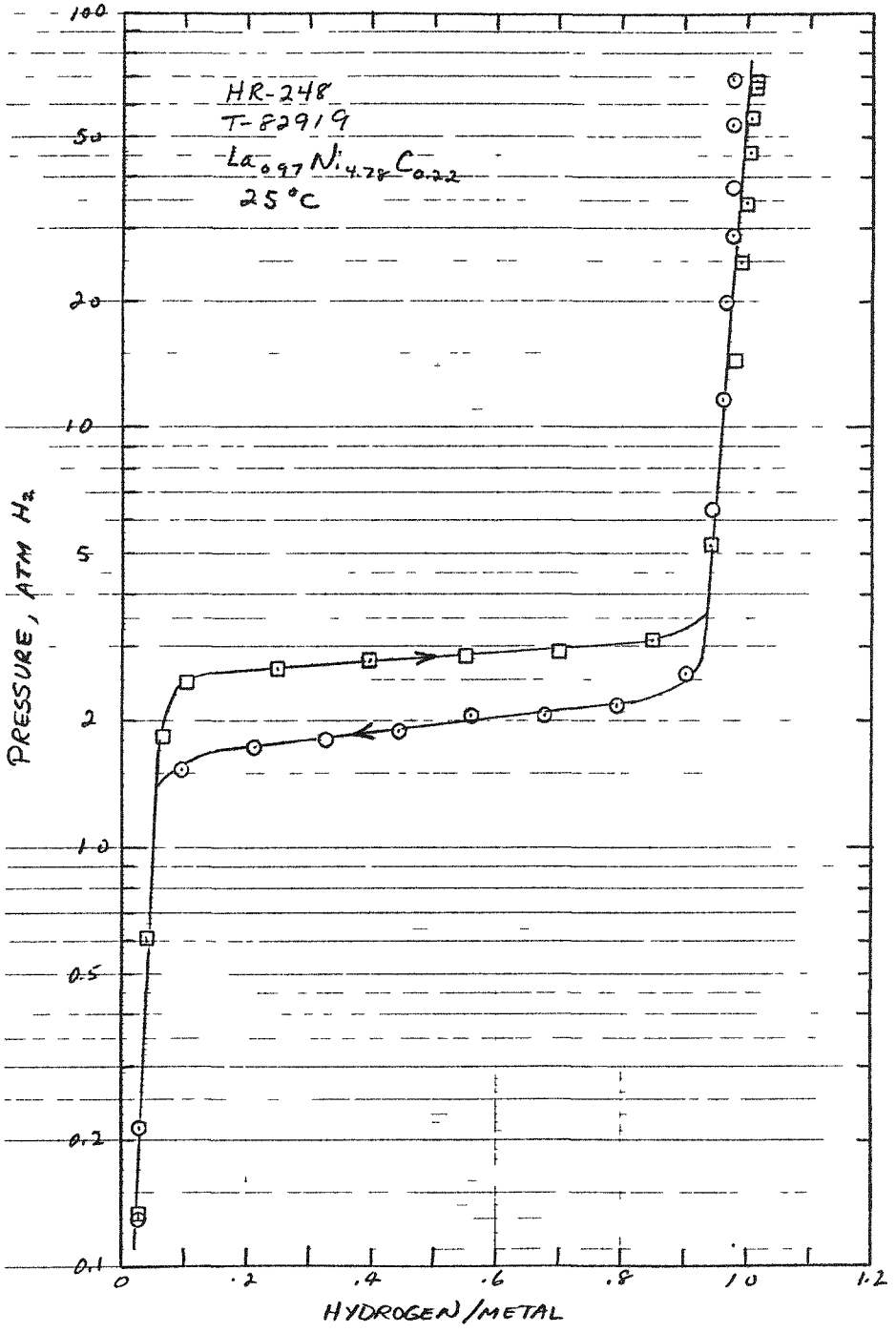

Figure 4-4-2. Static 25°C Isotherms for As-Cast $LaNi_{4.8}Co_{0.2}$.

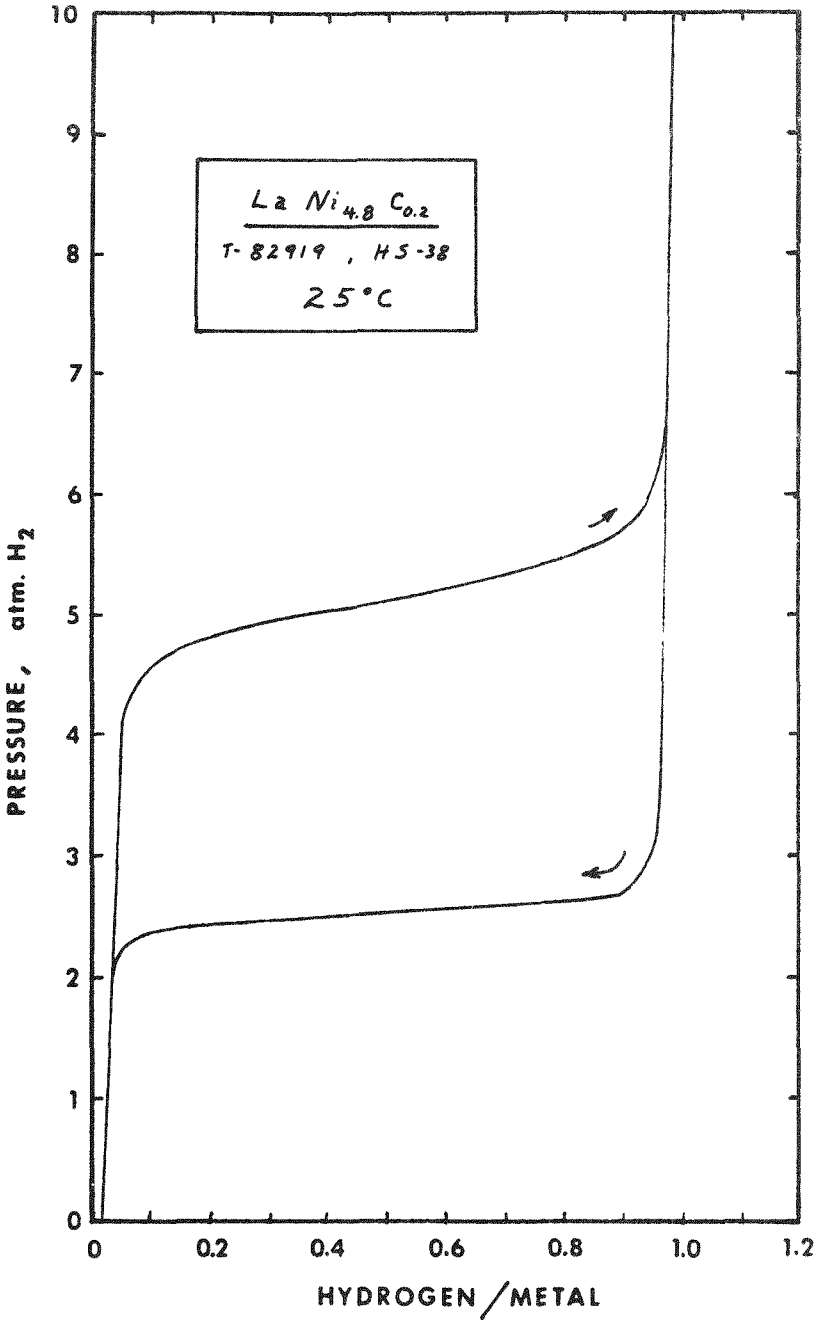

Figure 4-4-3. Dynamic pressure-composition isotherms determined at a reaction rate of 0.0027 g-atom H/min. The actual temperatures differ from the indicated nominal by about 0.3°C.

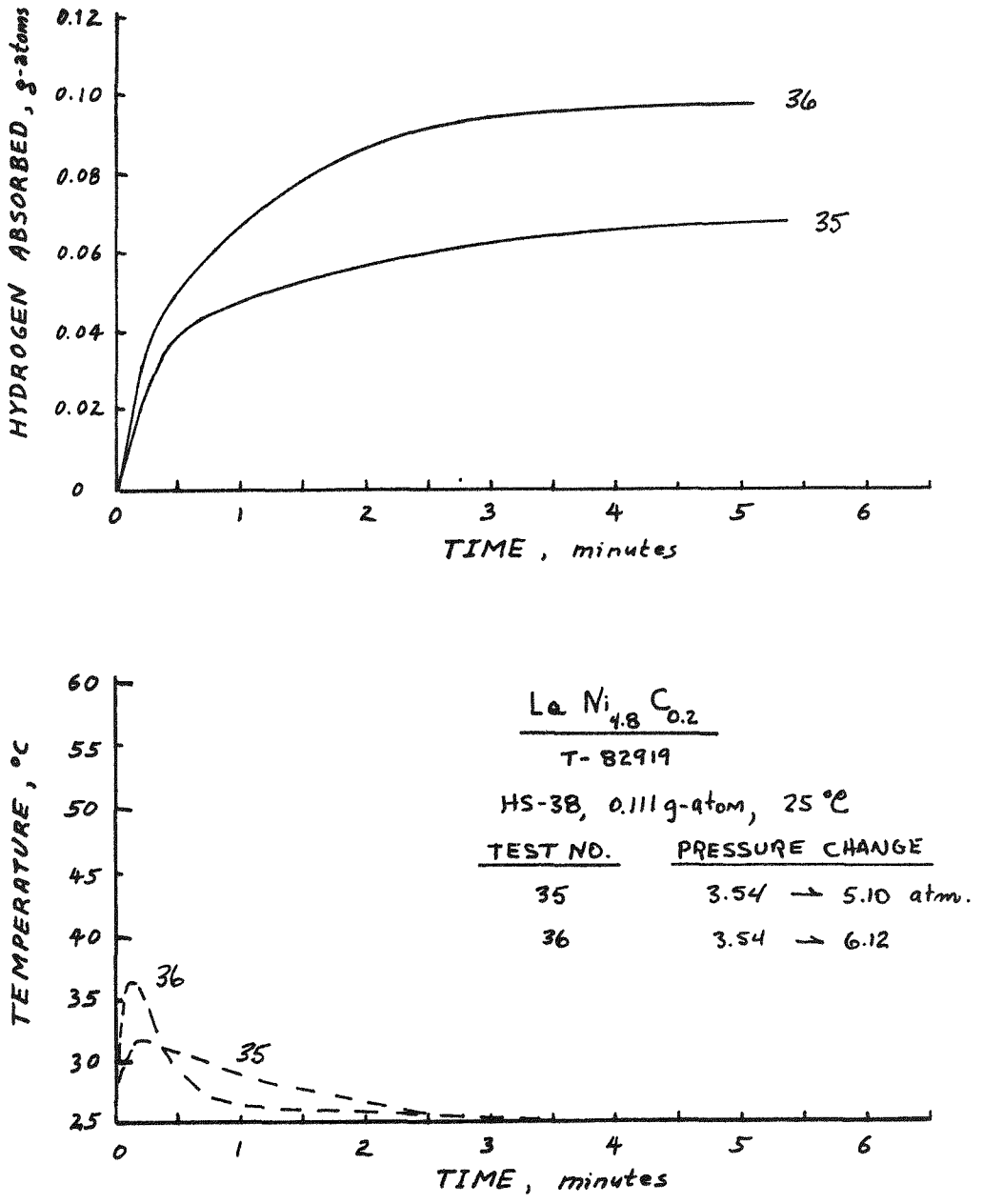

Figure 4-4-4. Time response data for the reaction mass and instantaneous temperature during isobaric absorption at a nominal temperature of 25 C.

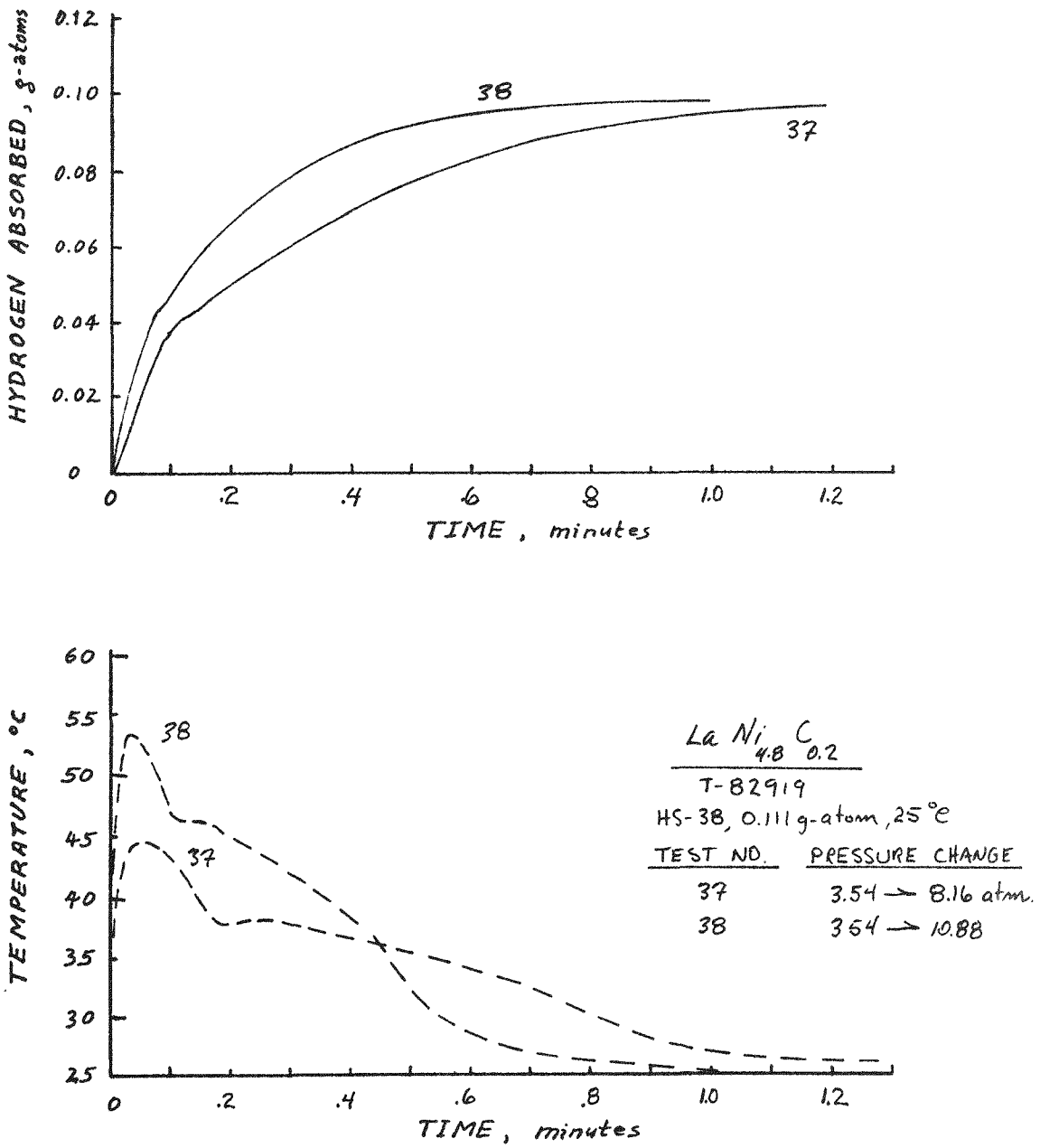

Figure 4-4-5. Time response data for the reaction mass and instantaneous temperature during isobaric absorption at a nominal temperature of 25 C.

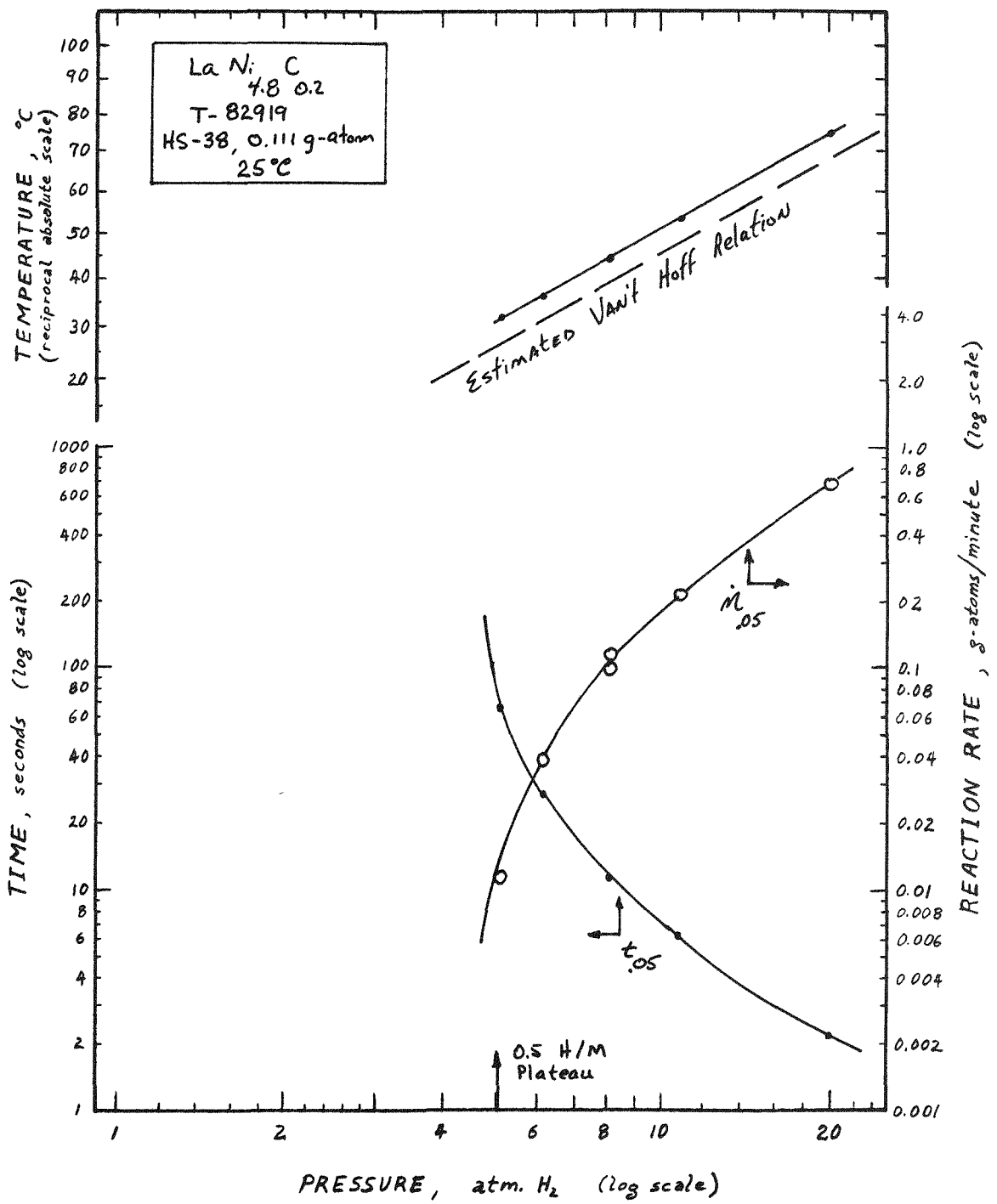

Figure 4-4-6. Summary of absorption kinetic data at 25°C showing the maximum temperature excursion as well as the reaction rate and time at 0.05 g-atoms hydrogen reacted (~0.5H/M).

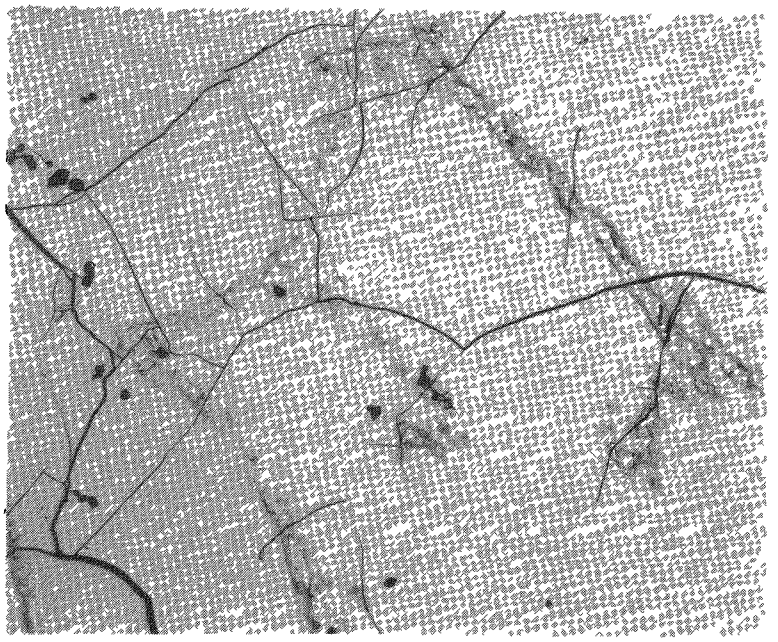

PN 1-73035 250X

Figure 4-5-1. Microstructure of $MNi_{4.3}Mn_{0.7}$, Annealed 16 Hours at 1150°C.

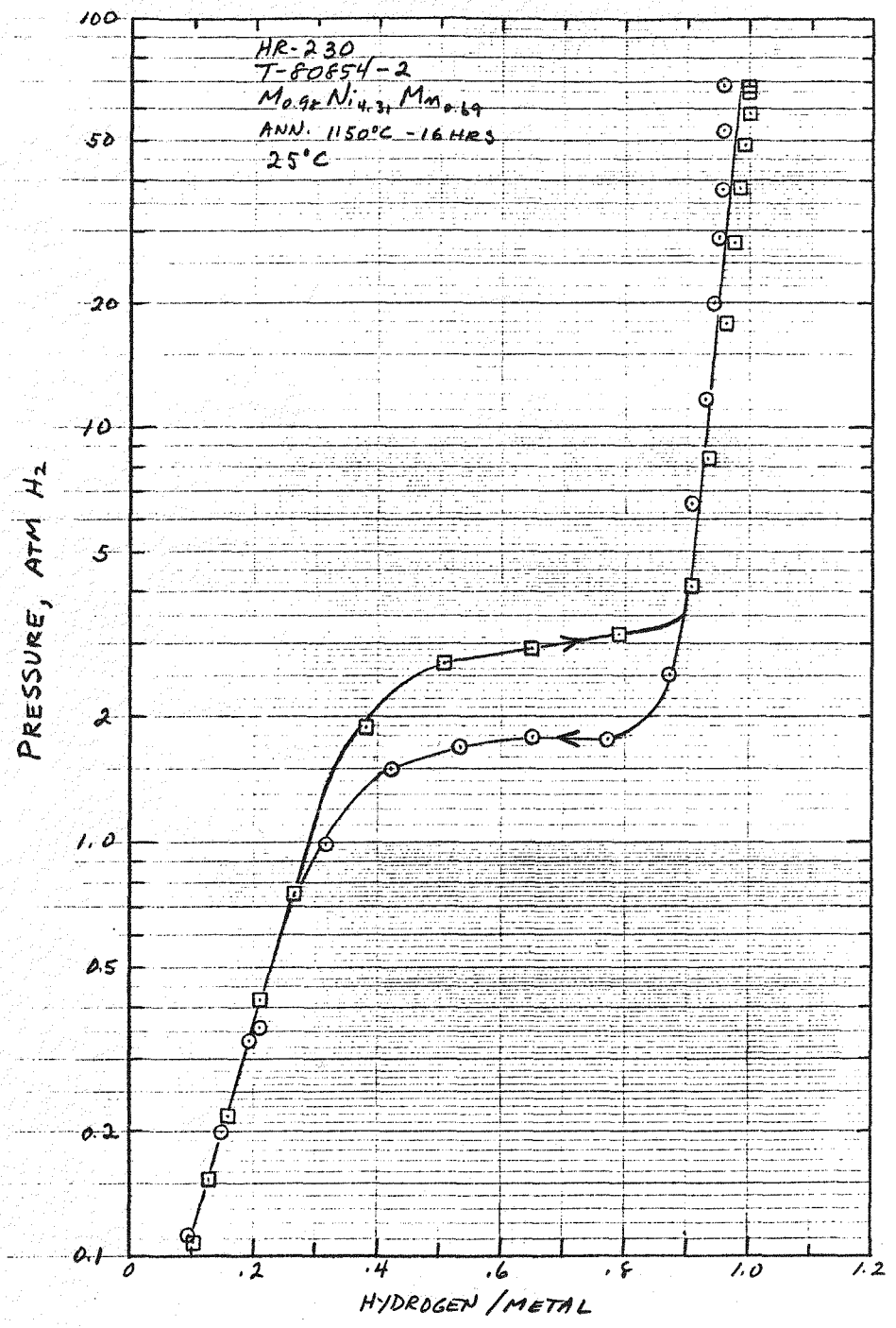

Figure 4-5-2. Static 25°C Isotherms for $MNi_{4.3}Mn_{0.7}$, Annealed 16 Hours at 1150°C.

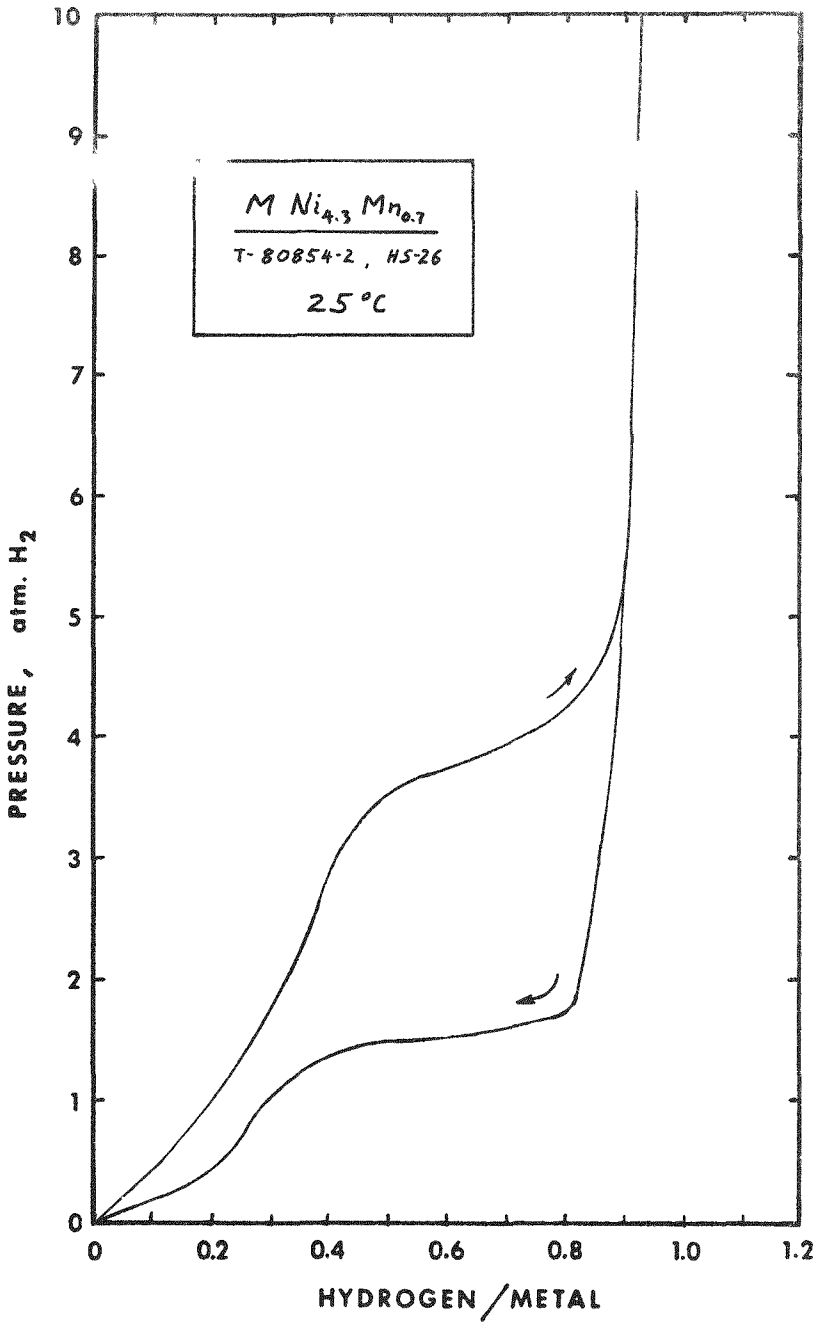

Figure 4-5-3. Dynamic pressure-composition isotherms determined at a reaction rate of 0.0027 g-atom H/min. The actual temperatures differ from the indicated nominal by about 0.3°C.

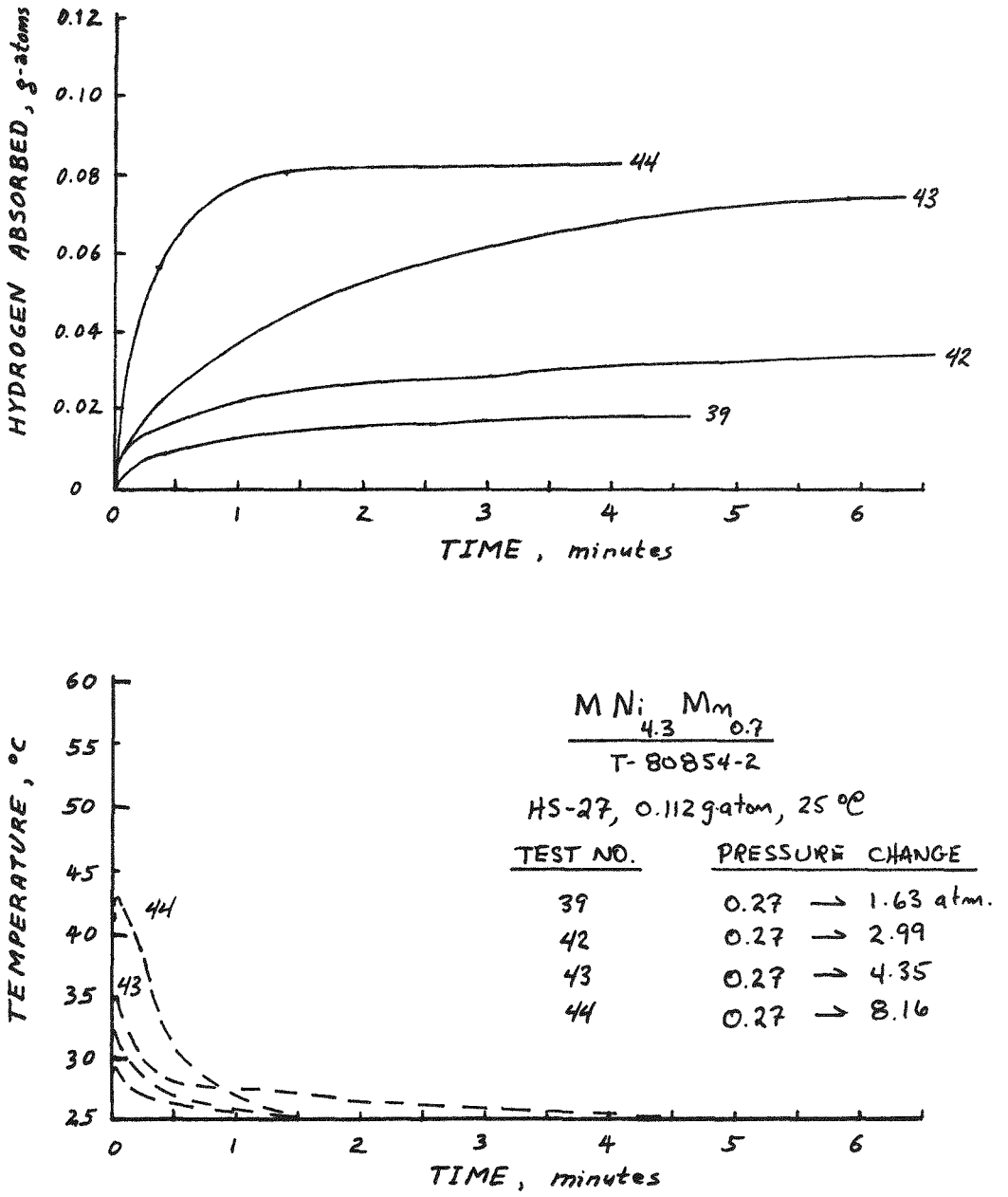

Figure 4-5-4. Time response data for the reaction mass and instantaneous temperature during isobaric absorption at a nominal temperature of 25 C.

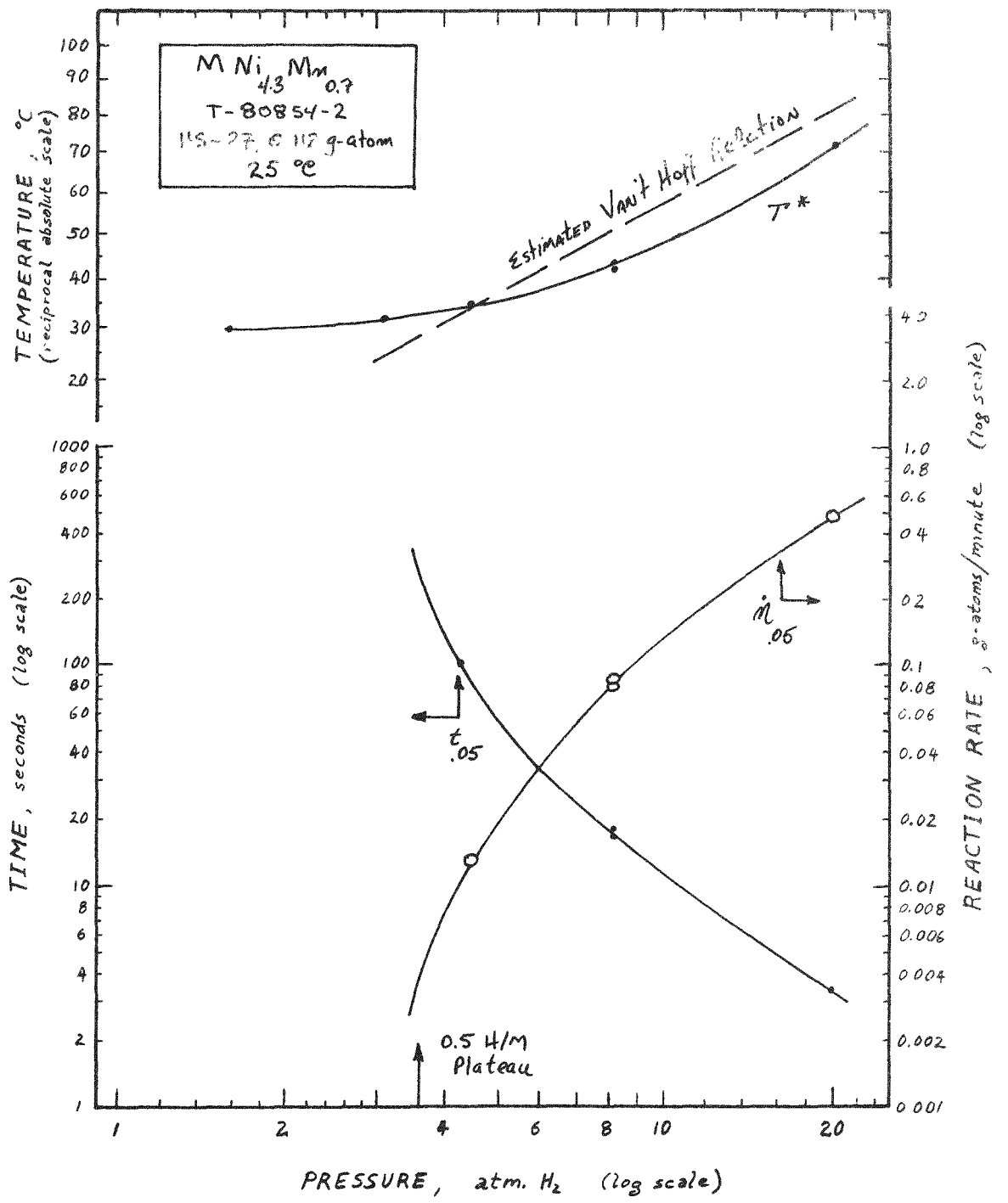

Figure 4-5-5. Summary of absorption kinetic data at 25°C showing the maximum temperature excursion as well as the reaction rate and time at 0.05 g-atoms hydrogen reacted (~0.5H/M).

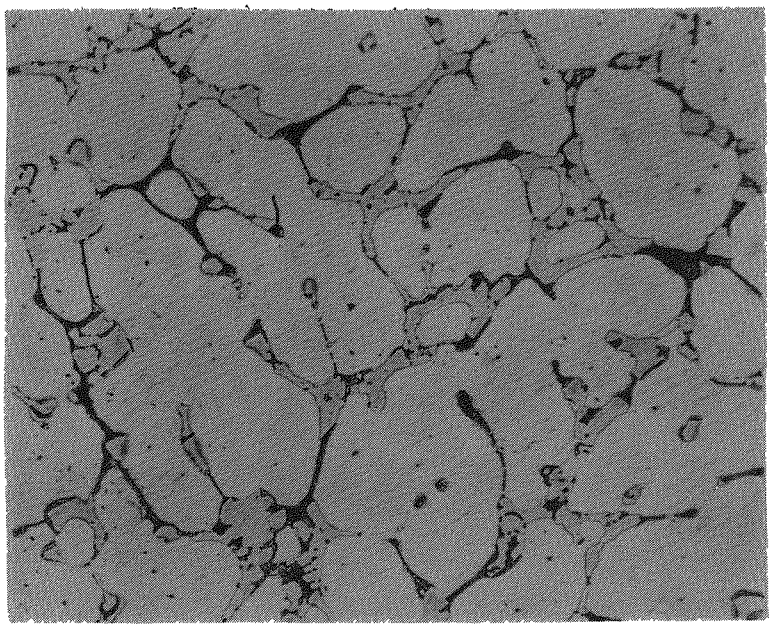

PN 1-72803 250X

Figure 5-1-1. As-Cast Microstructure of $LaNi_{4.8}B_{0.2}$.

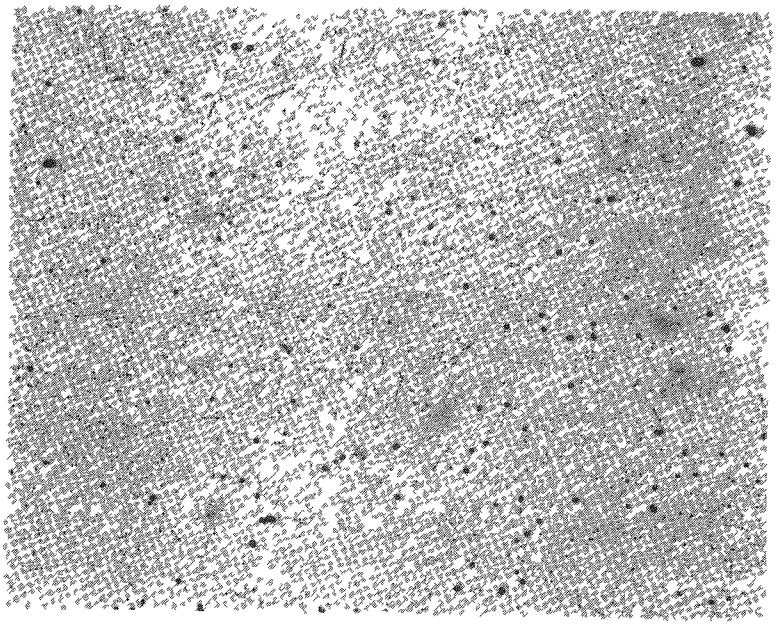

PN 1-72805 250X

Figure 5-2-1. As-Cast Microstructure of $LaNi_{4.9}S_{0.1}$ (Actual Composition $La_{0.94}Ni_{4.998}S_{0.002}$).

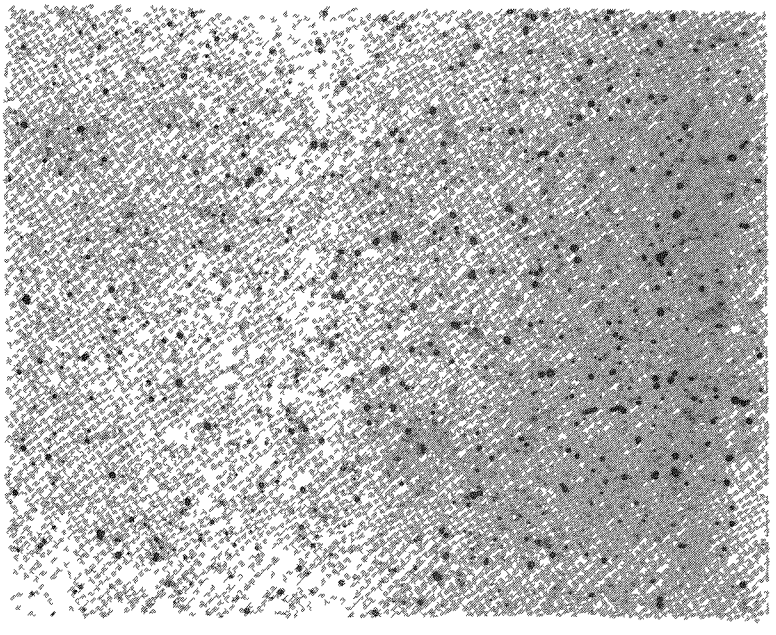

PN 1-72807 250X

Figure 5-3-1. As-Cast Microstructure of $LaNi_{4.9}Se_{0.1}$ (Actual Composition $La_{0.99}Ni_{4.97}Se_{0.03}$).

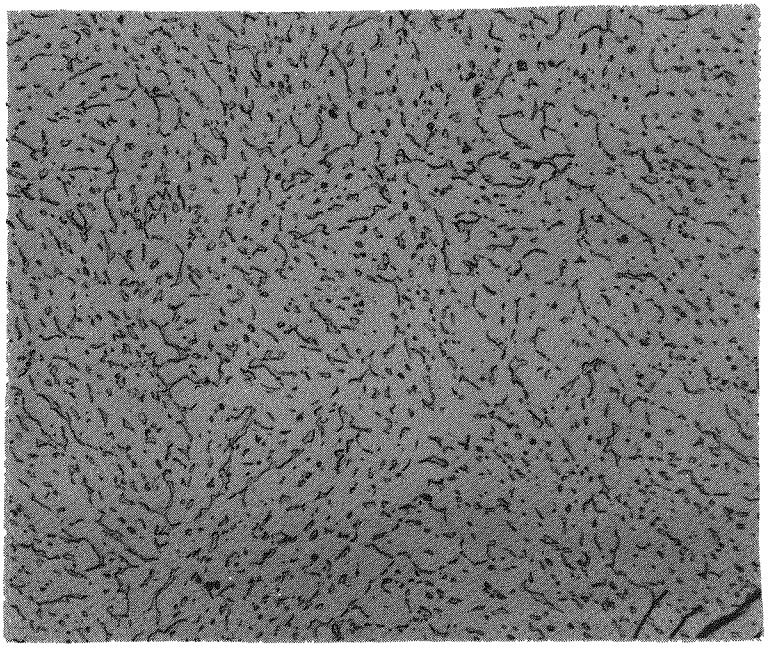

PN 1-72850 250X

Figure 6-1-1. As-Cast Microstructure of $Mg_{0.1}La_{0.9}Ni_5$ (Actual Composition $Mg_{0.19}La_{0.91}Ni_5$).

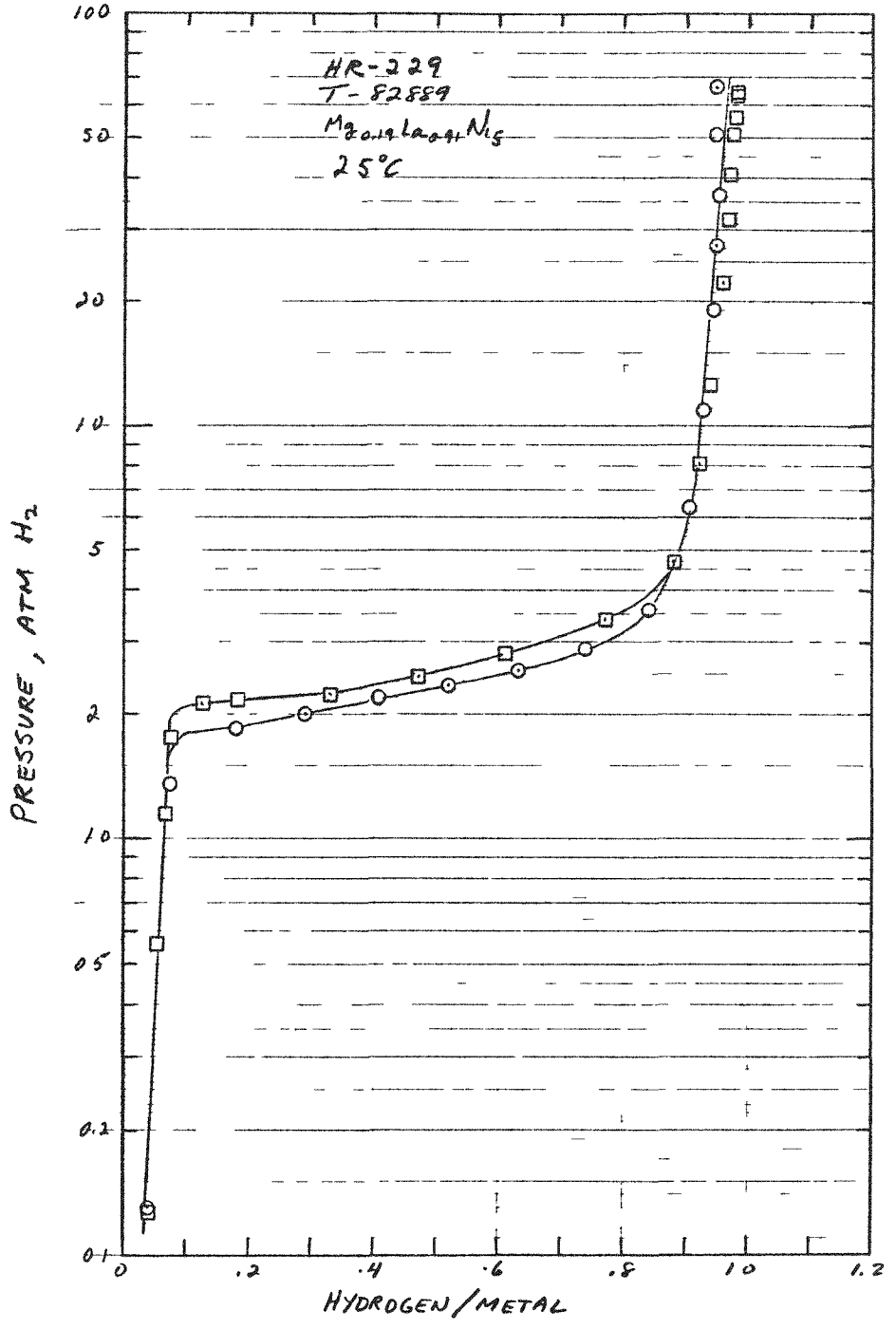

Figure 6-1-2. Static 25°C Isotherms for As-Cast $Mg_{0.1}La_{0.9}Ni_5$ (Actual Composition $Mg_{0.19}La_{0.91}Ni_5$).

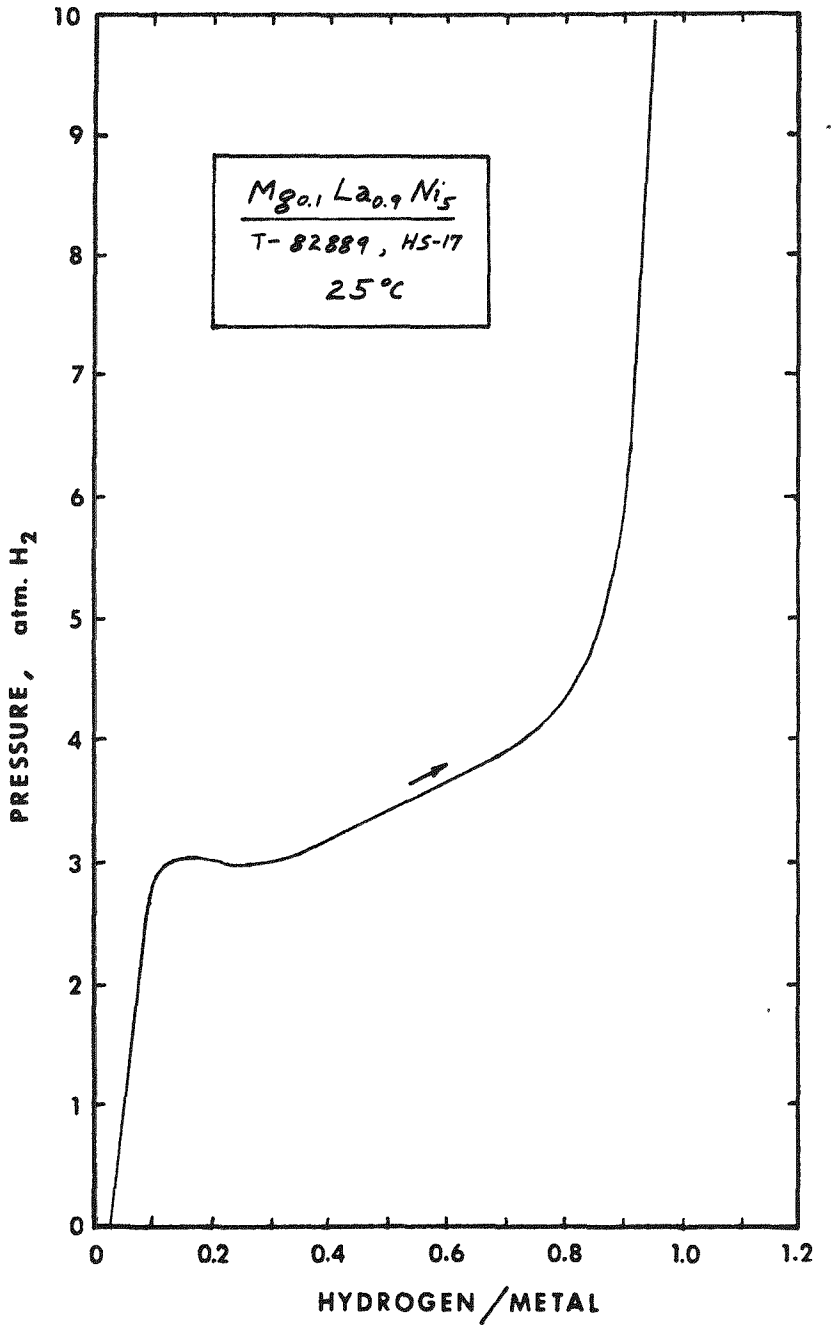

Figure 6-1-3. Dynamic pressure-composition absorption isotherm determined at a reaction rate of 0.0027 g-atom H/min. The actual temperature is about 0.3°C higher than the indicated nominal.

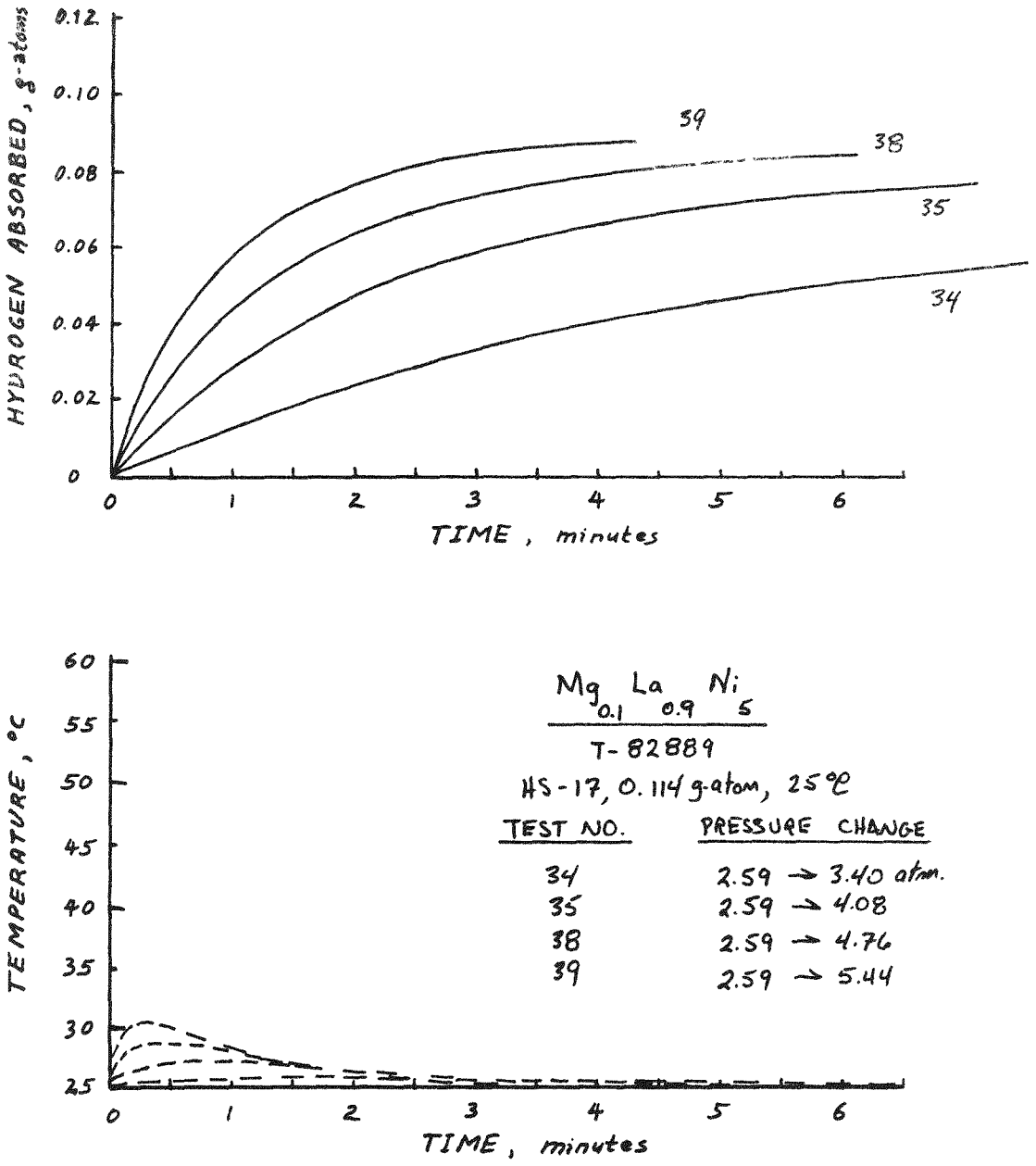

Figure 6-1-4. Time response data for the reaction mass and instantaneous temperature during isobaric absorption at a nominal temperature of 25 C.

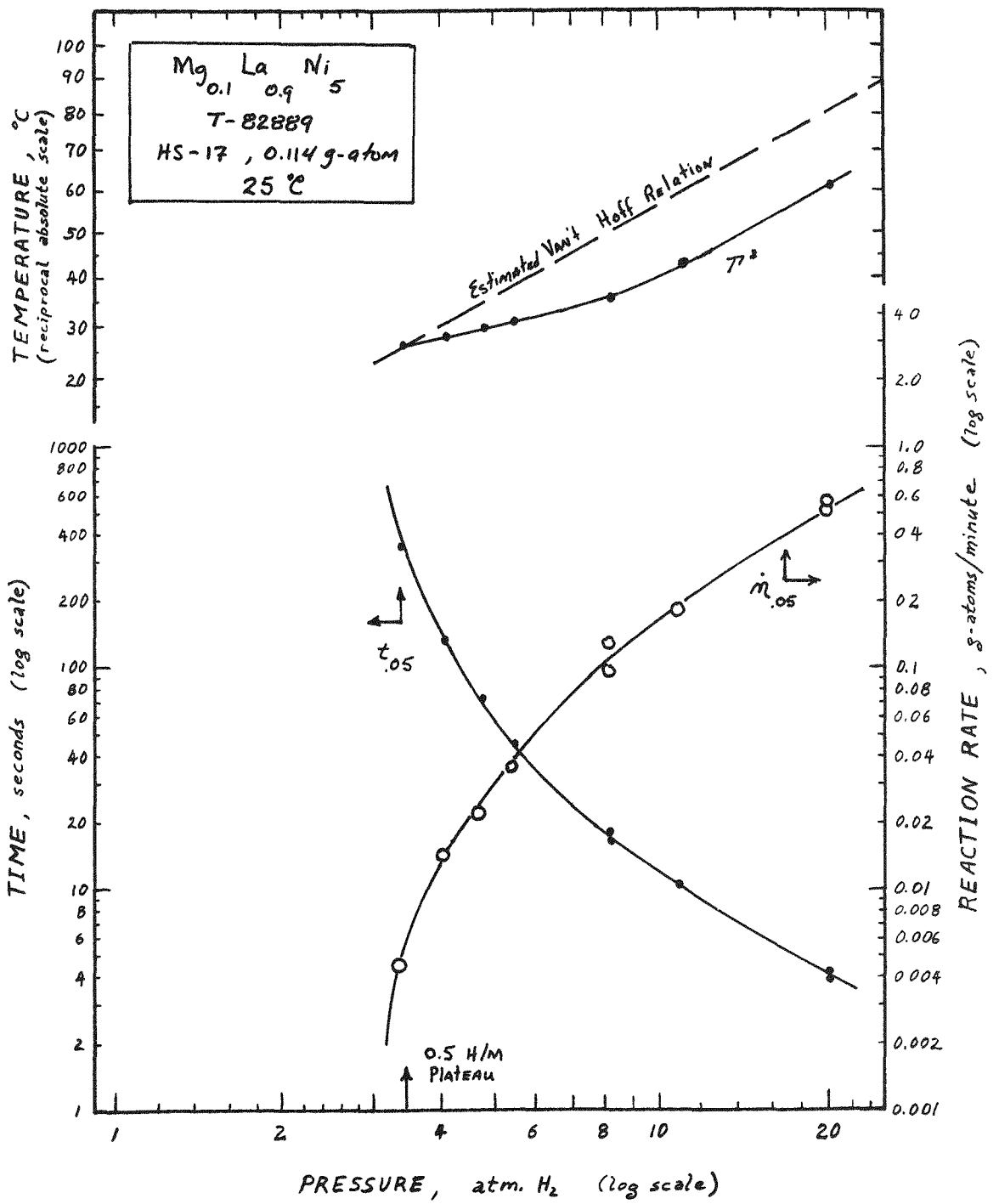

Figure 6-1-5. Summary of absorption kinetic data at 25°C showing the maximum temperature excursion as well as the reaction rate and time at 0.05 g-atoms hydrogen reacted (~0.5H/M).

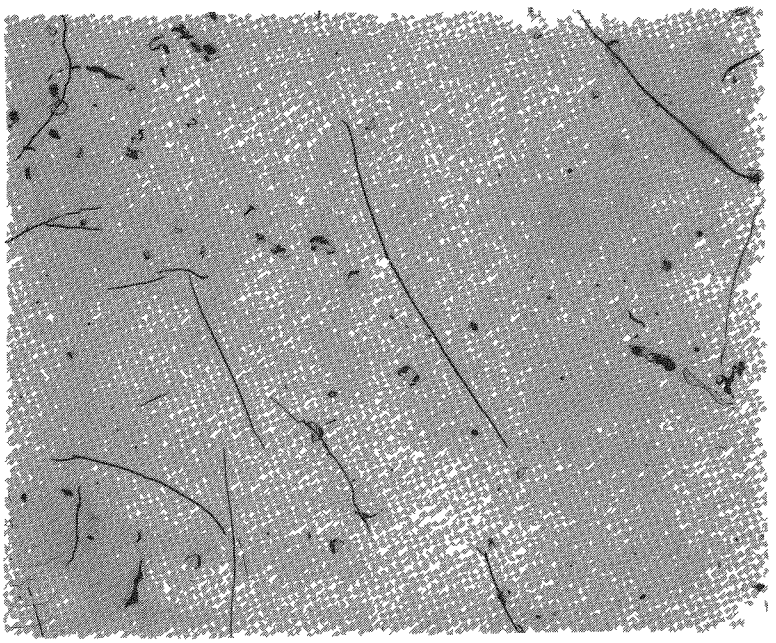

PN 1-72848 250X

Figure 6-2-1. As-Cast Microstructure of $Ca_{0.2}La_{0.8}Ni_5$.

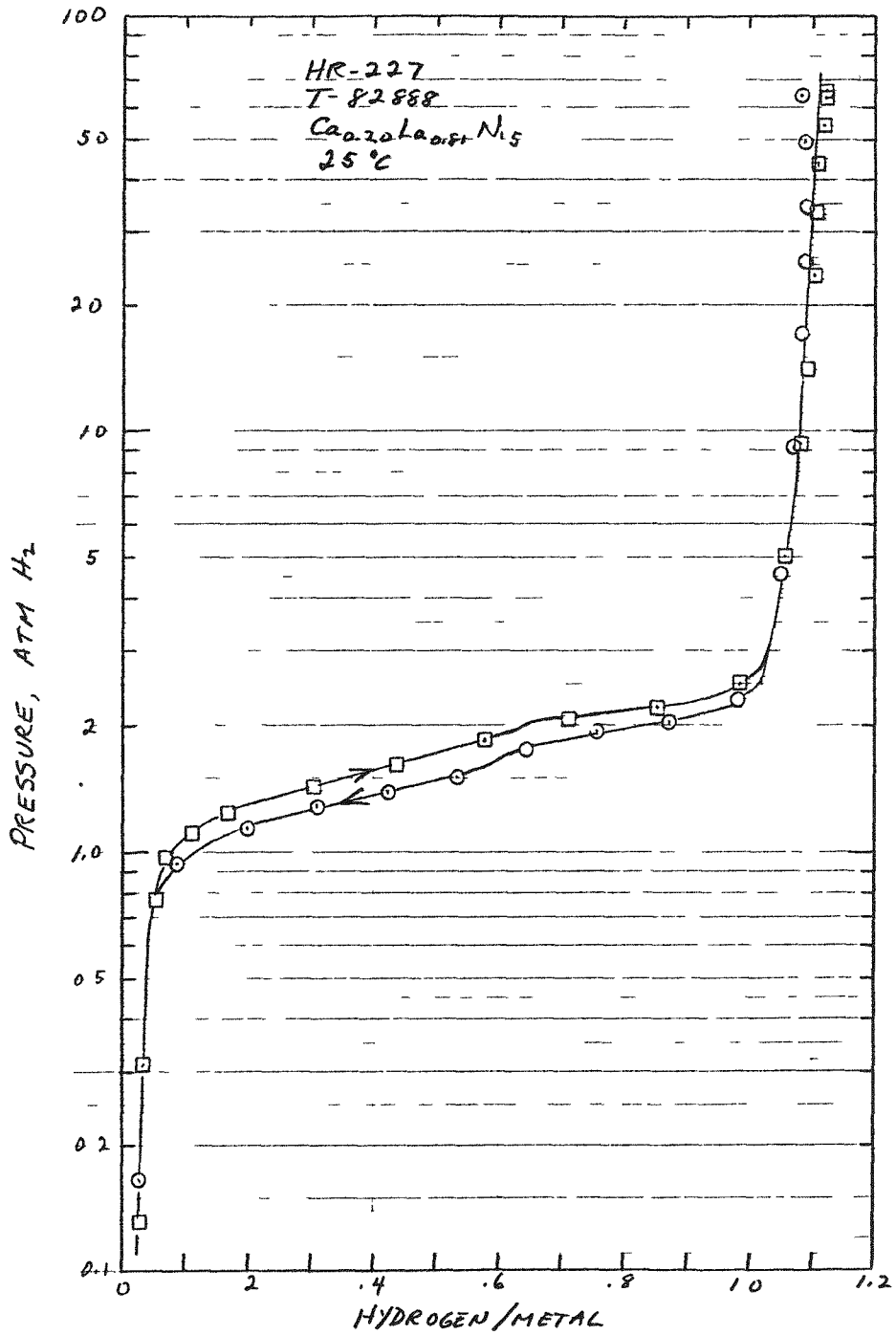

Figure 6-2-2. Static 25°C Isotherms for $Ca_{0.2}La_{0.8}Ni_5$.

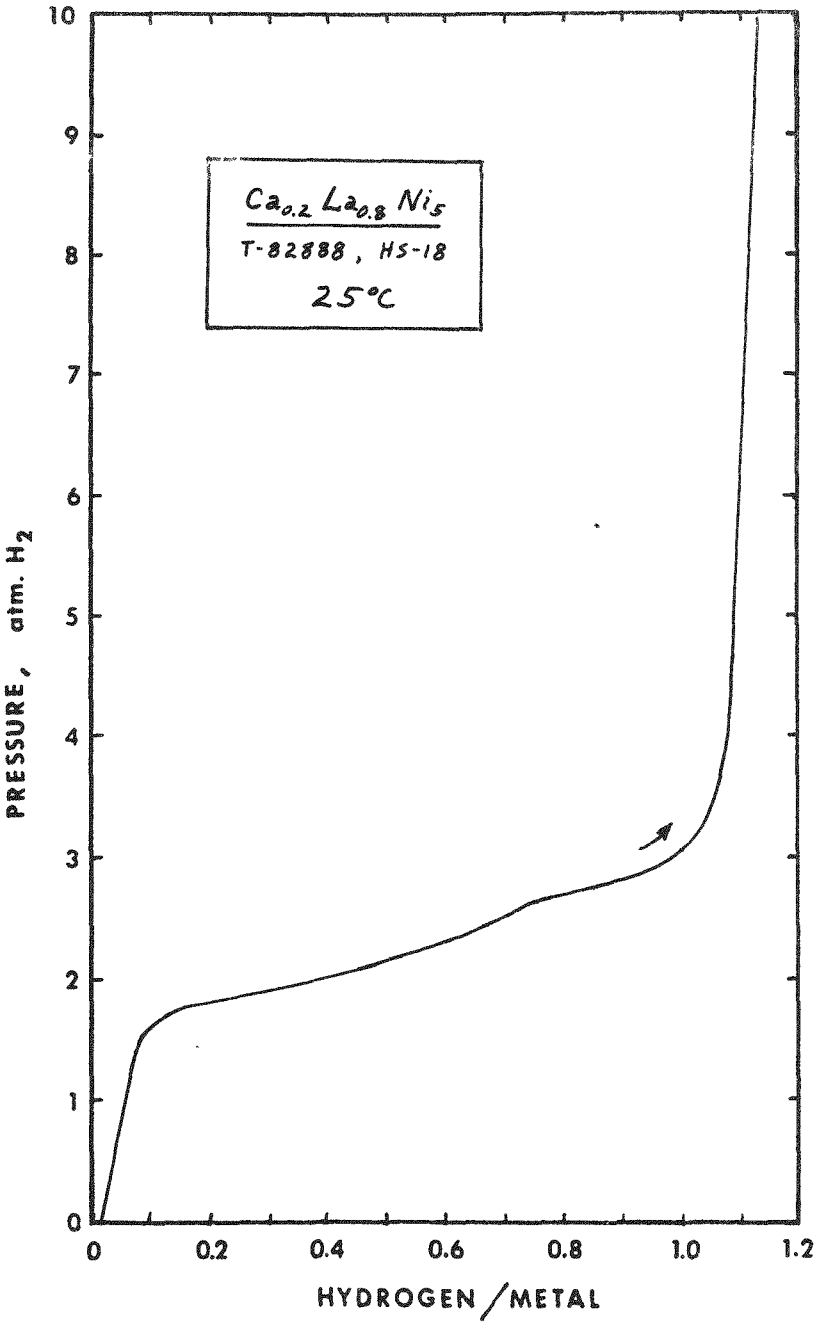

Figure 6-2-3. Dynamic pressure-composition absorption isotherm determined at a reaction rate of 0.0027 g-atom H/min. The actual temperature is about 0.3°C higher than the indicated nominal.

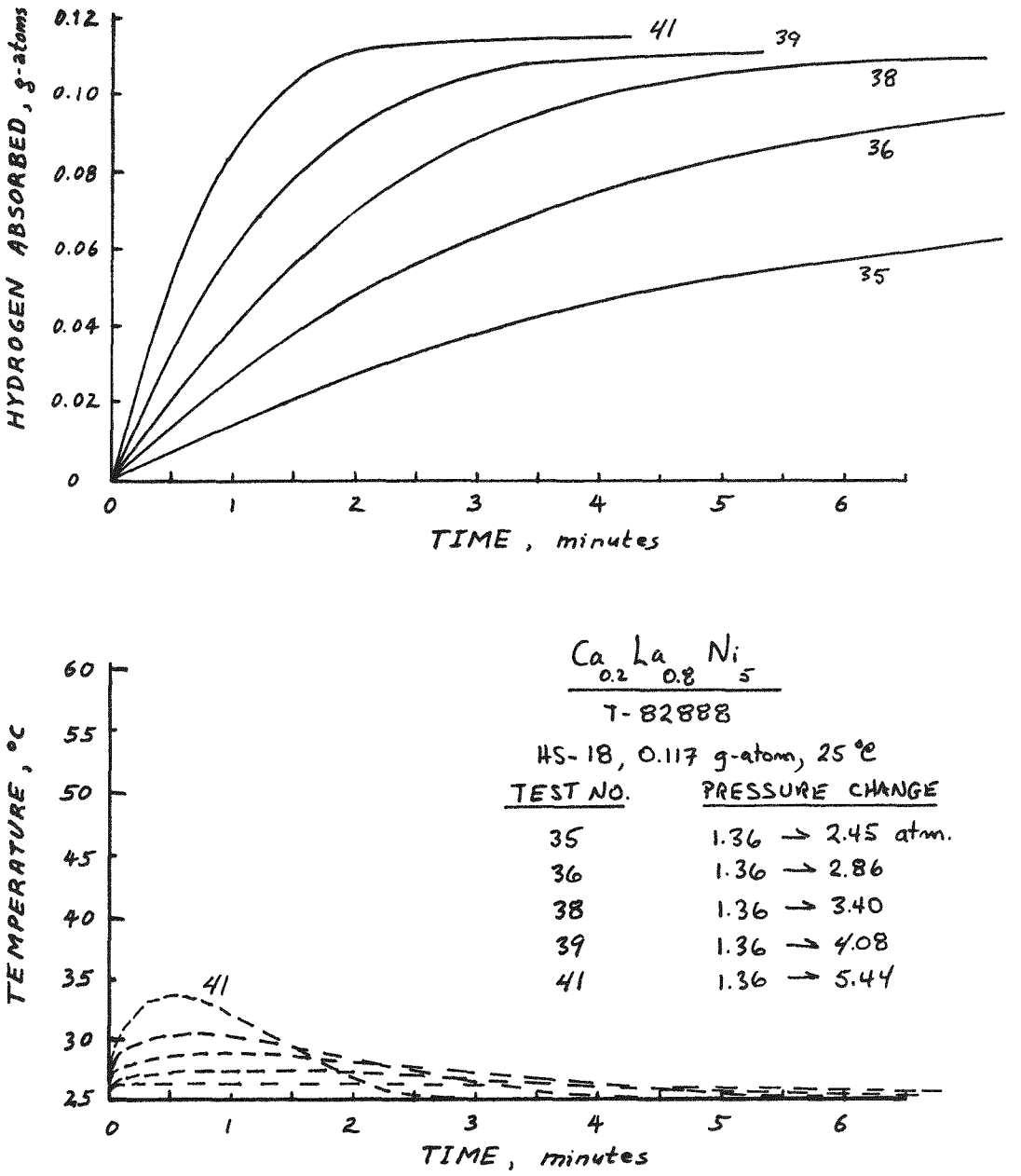

Figure 6-2-4. Time response data for the reaction mass and instantaneous temperature during isobaric absorption at a nominal temperature of 25 C.

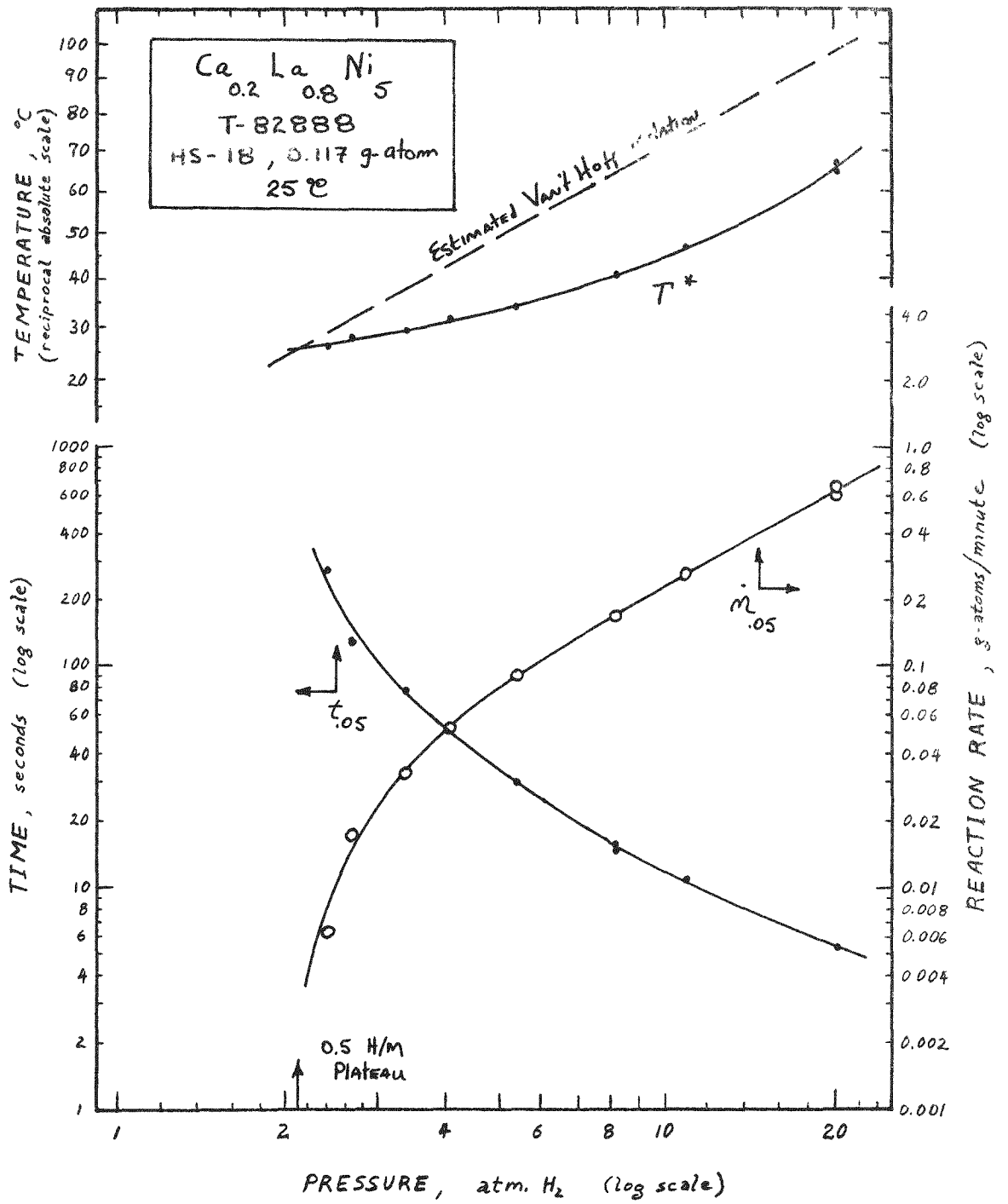

Figure 6-2-5. Summary of absorption kinetic data at 25°C showing the maximum temperature excursion as well as the reaction rate and time at 0.05 g-atoms hydrogen reacted (~0.5H/M).

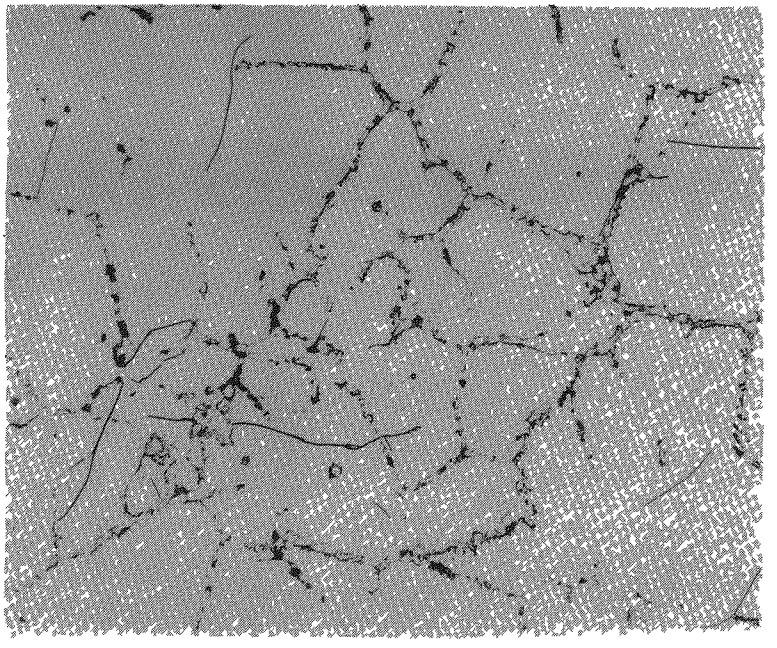

PN 1-72793 250X

Figure 6-3-1. As-Cast Microstructure of $Sr_{0.2}La_{0.8}Ni_5$.

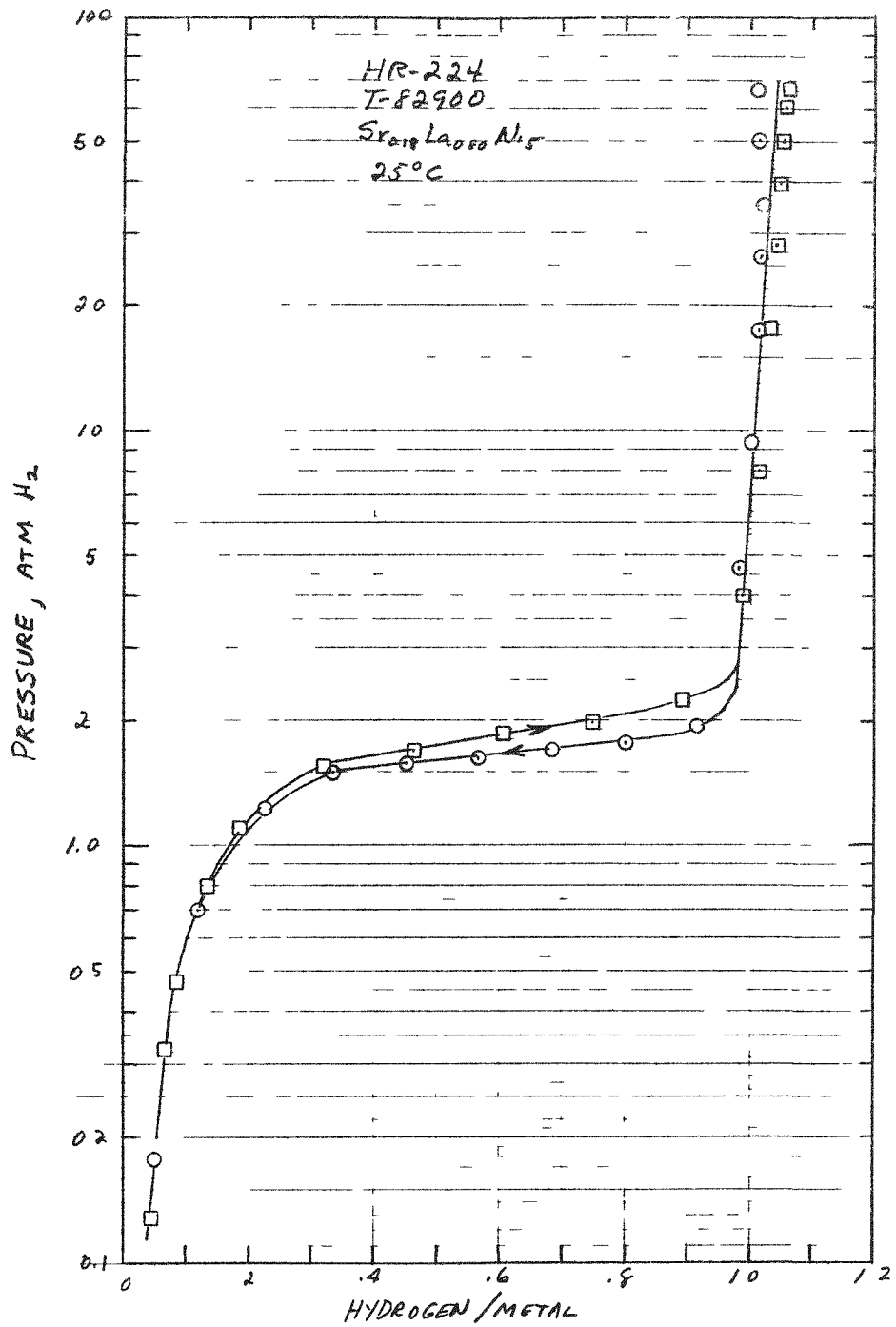

Figure 6-3-2. Static 25°C Isotherms for As-Cast $Sr_{0.2}La_{0.8}Ni_5$.

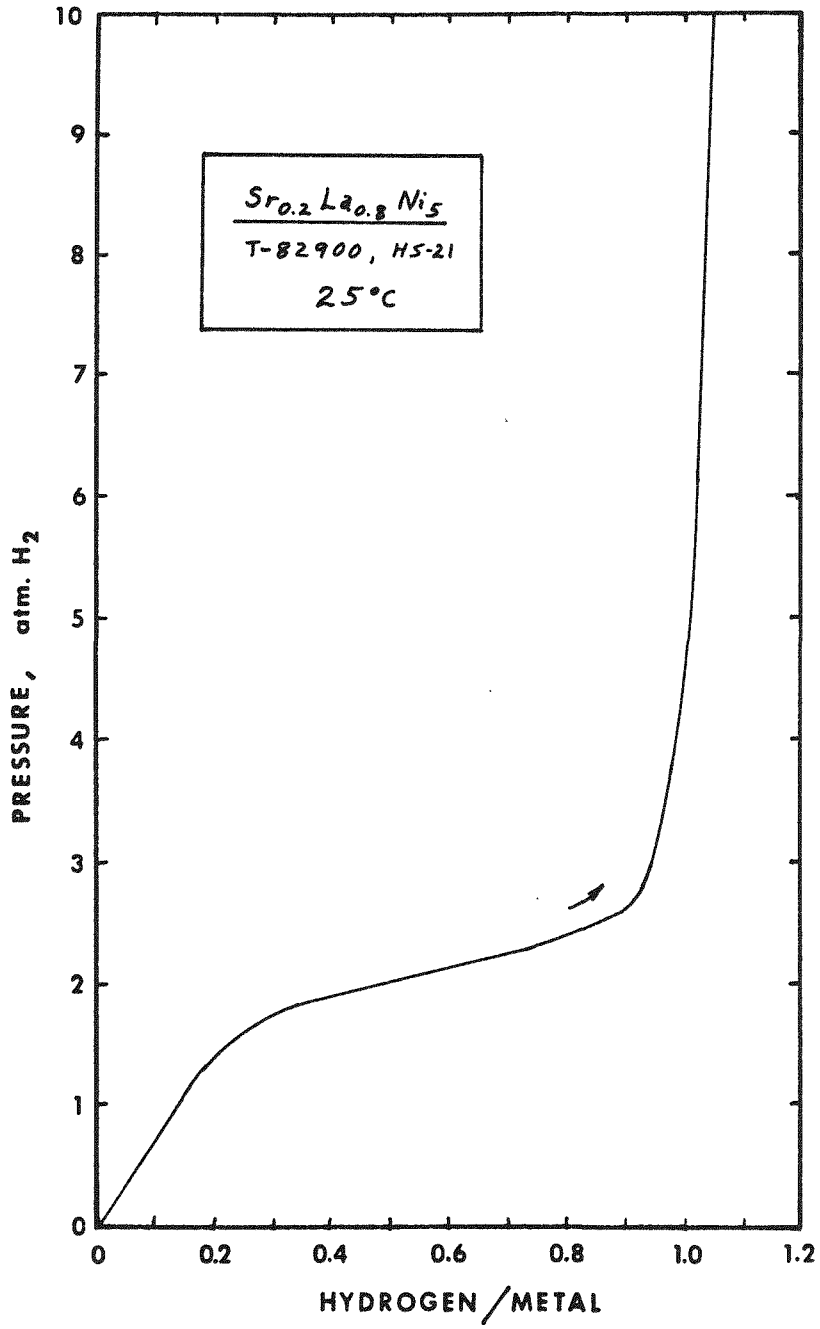

Figure 6-3-3. Dynamic pressure-composition absorption isotherm determined at a reaction rate of 0.0027 g-atom H/min. The actual temperature is about 0.3°C higher than the indicated nominal.

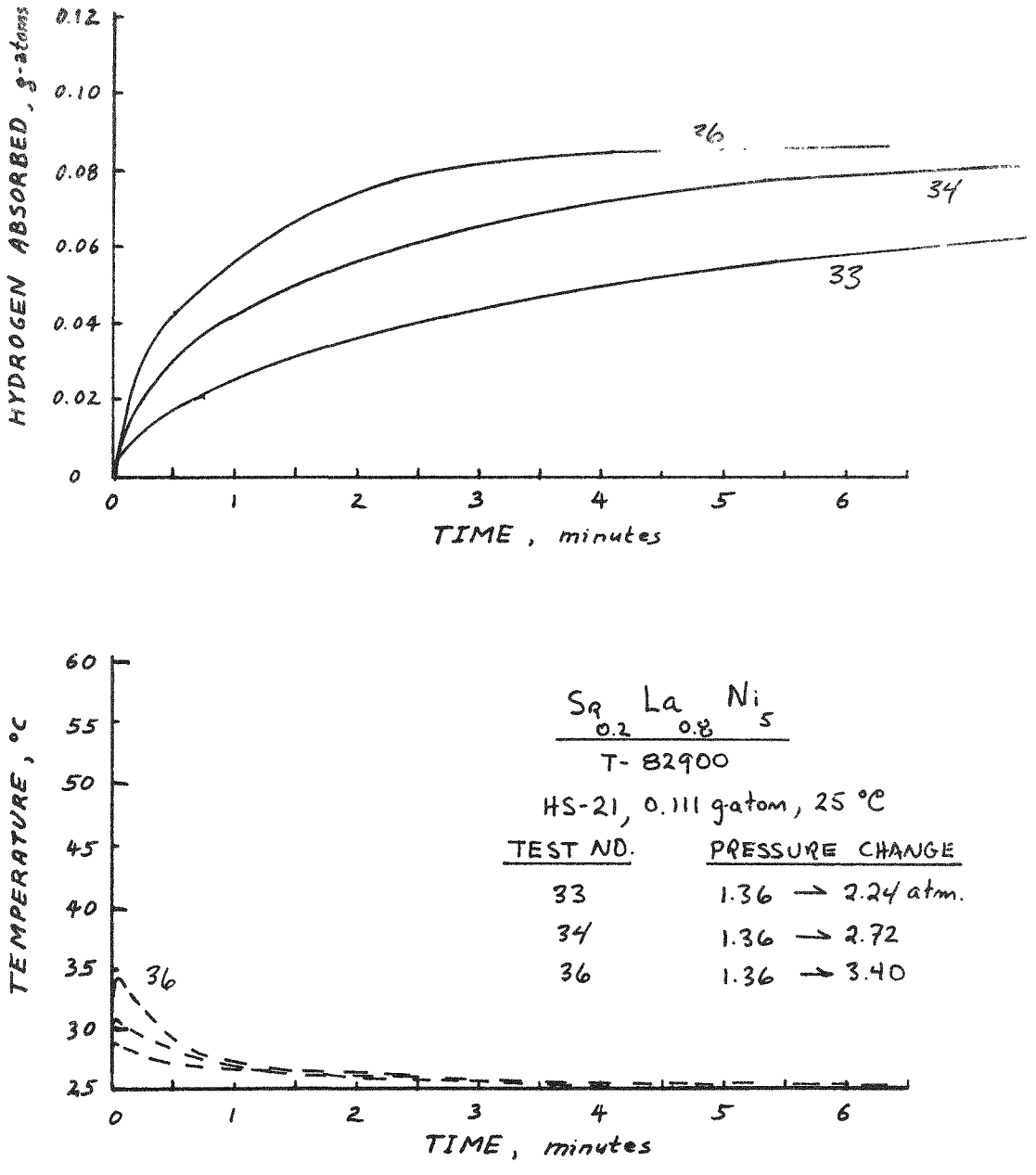

Figure 6-3-4. Time response data for the reaction mass and instantaneous temperature during isobaric absorption at a nominal temperature of 25 C.

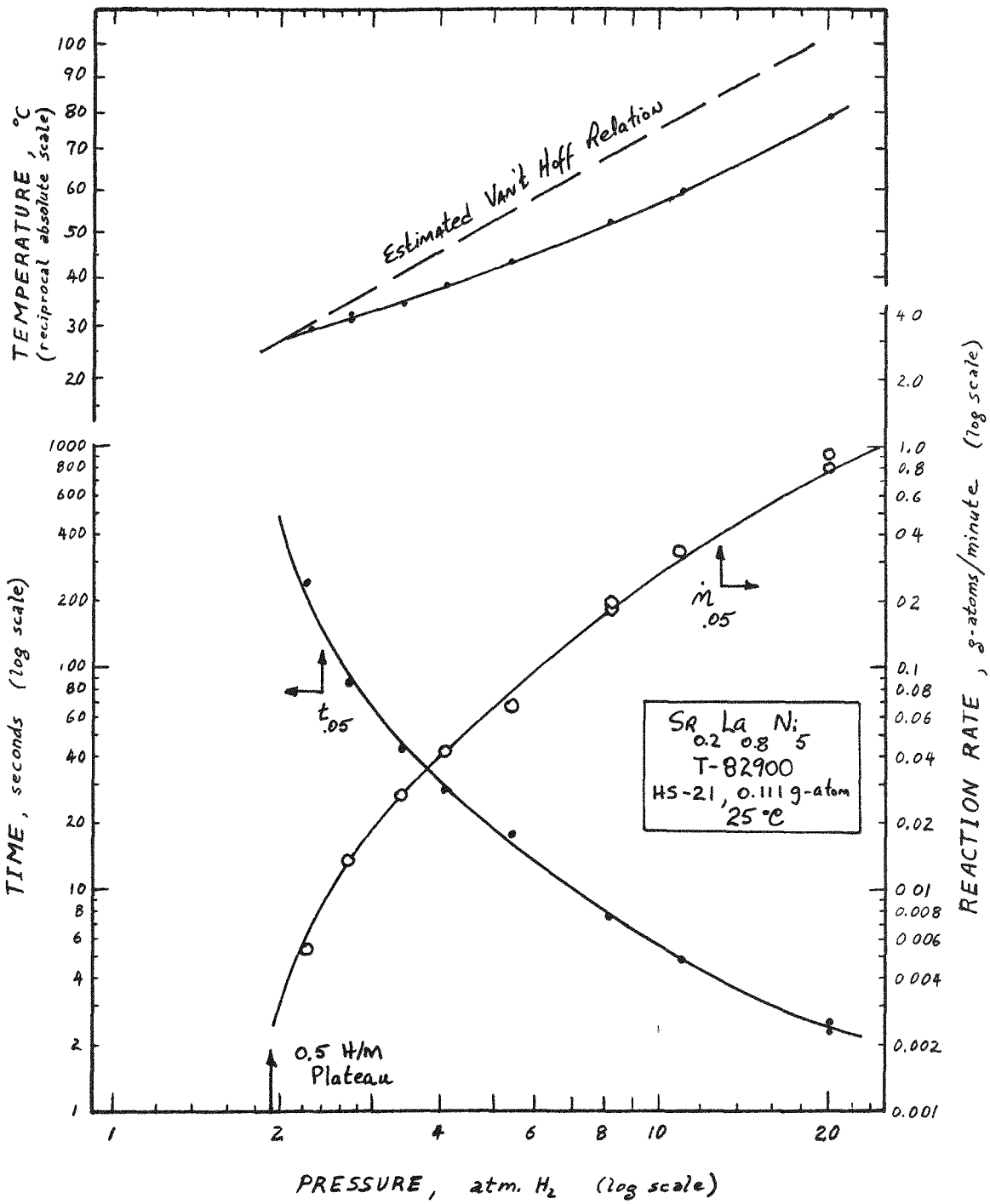

Figure 6-3-5. Summary of absorption kinetic data at 25°C showing the maximum temperature excursion as well as the reaction rate and time at 0.05 g-atoms hydrogen reacted (~0.5H/M).

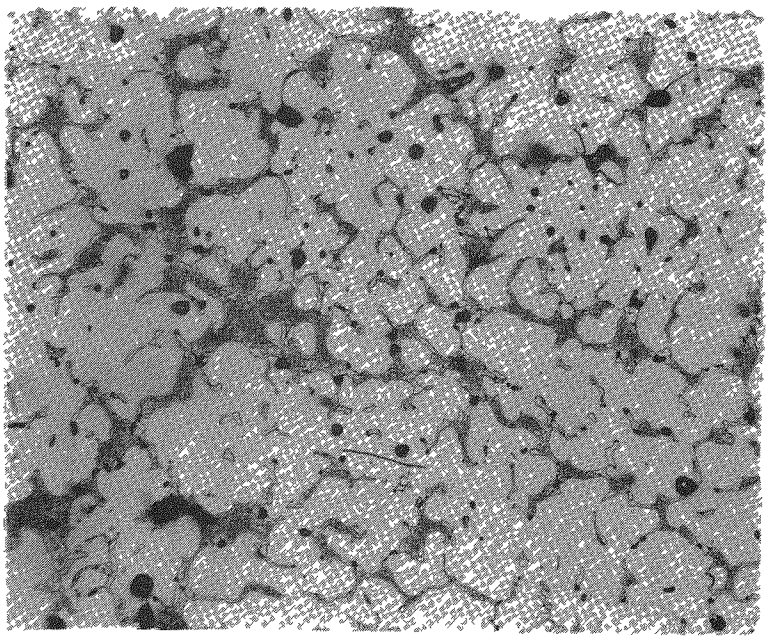

PN 1-72795 250X

Figure 6-4-1. As-Cast Microstructure of $Ba_{0.2}La_{0.8}Ni_5$ (Actual Composition $Ba_{0.13}La_{0.77}Ni_5$).

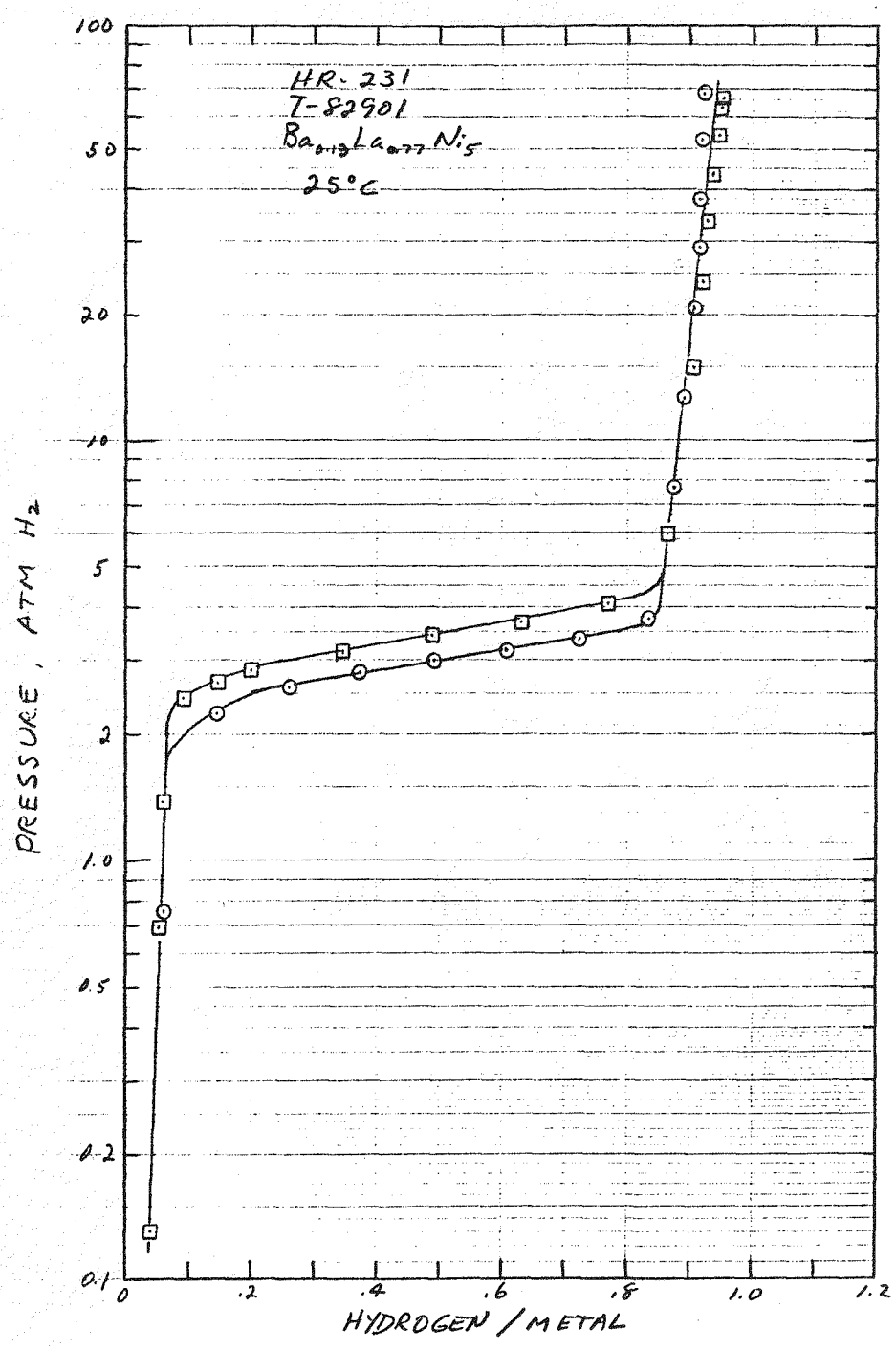

Figure 6-4-2. Static 25°C Isotherms for As-Cast $Ba_{0.2}La_{0.8}Ni_5$ (Actual Composition $Ba_{0.13}La_{0.77}Ni_5$).

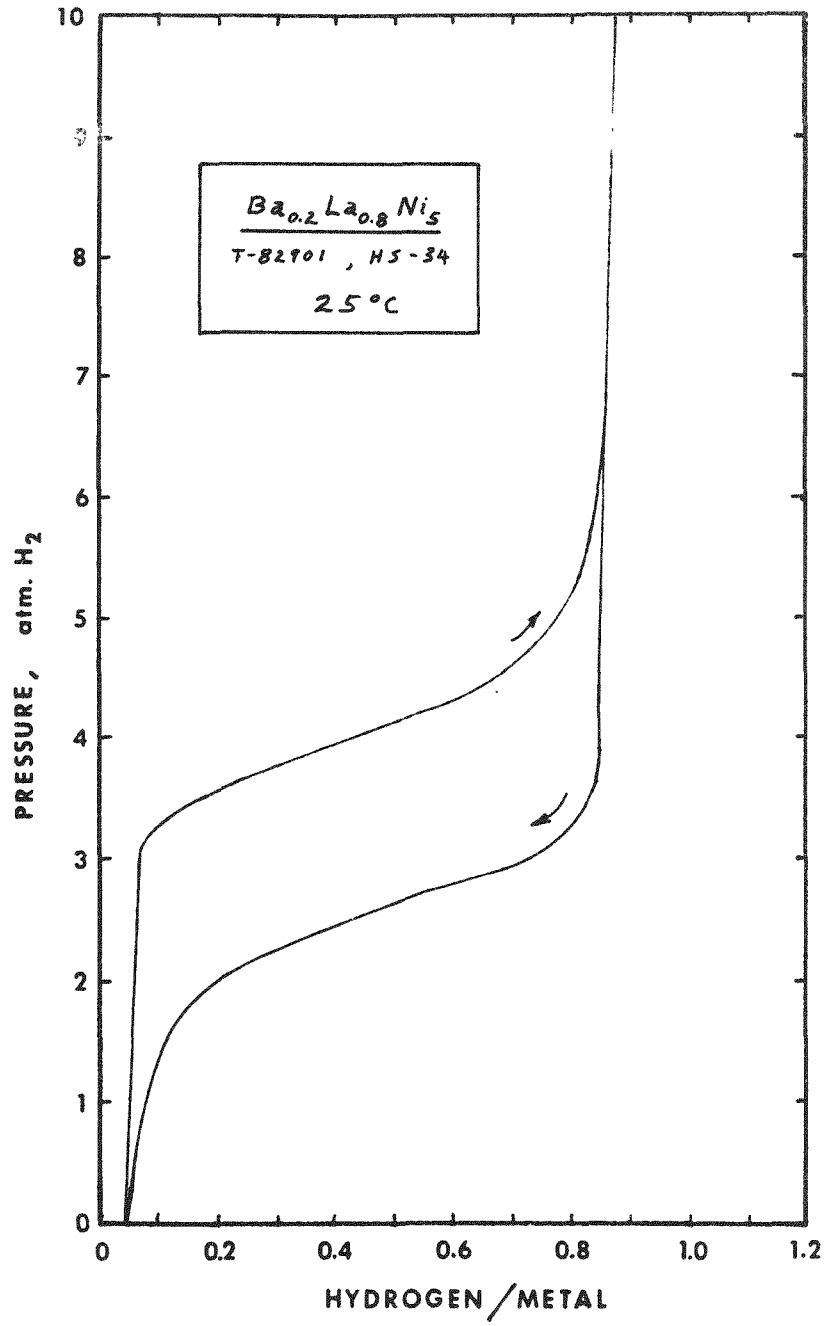

Figure 6-4-3. Dynamic pressure-composition isotherms determined at a reaction rate of 0.0027 g-atom H/min. The actual temperatures differ from the indicated nominal by about 0.3°C.

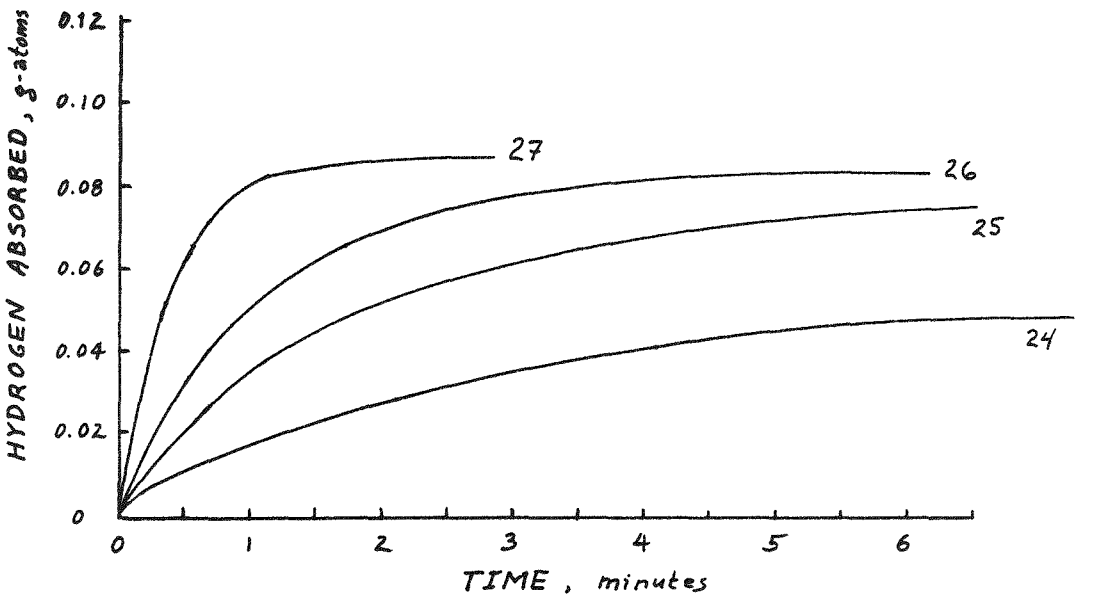

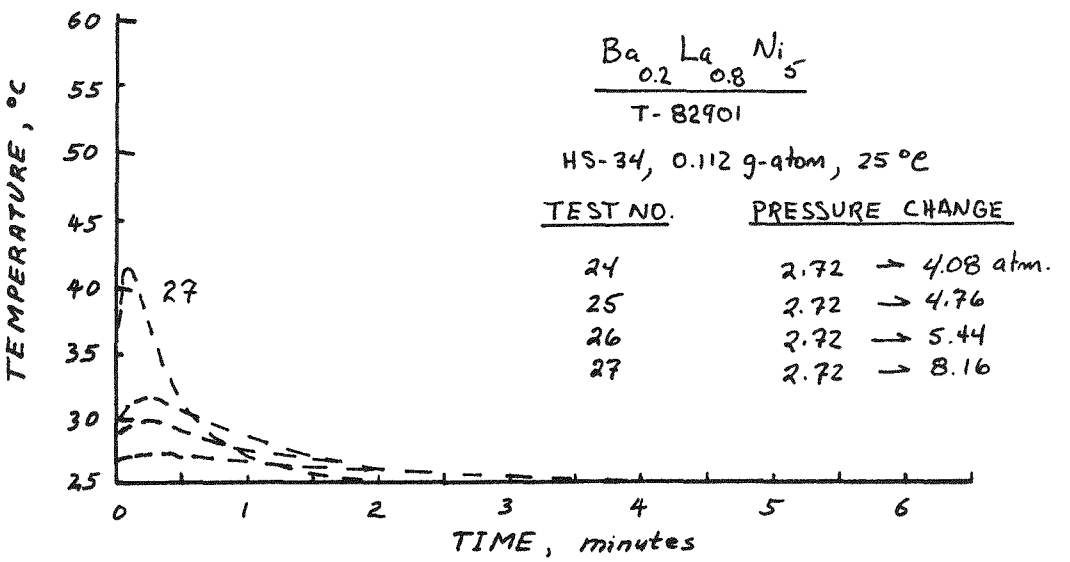

Figure 6-4-4. Time response data for the reaction mass and instantaneous temperature during isobaric absorption at a nominal temperature of 25 C.

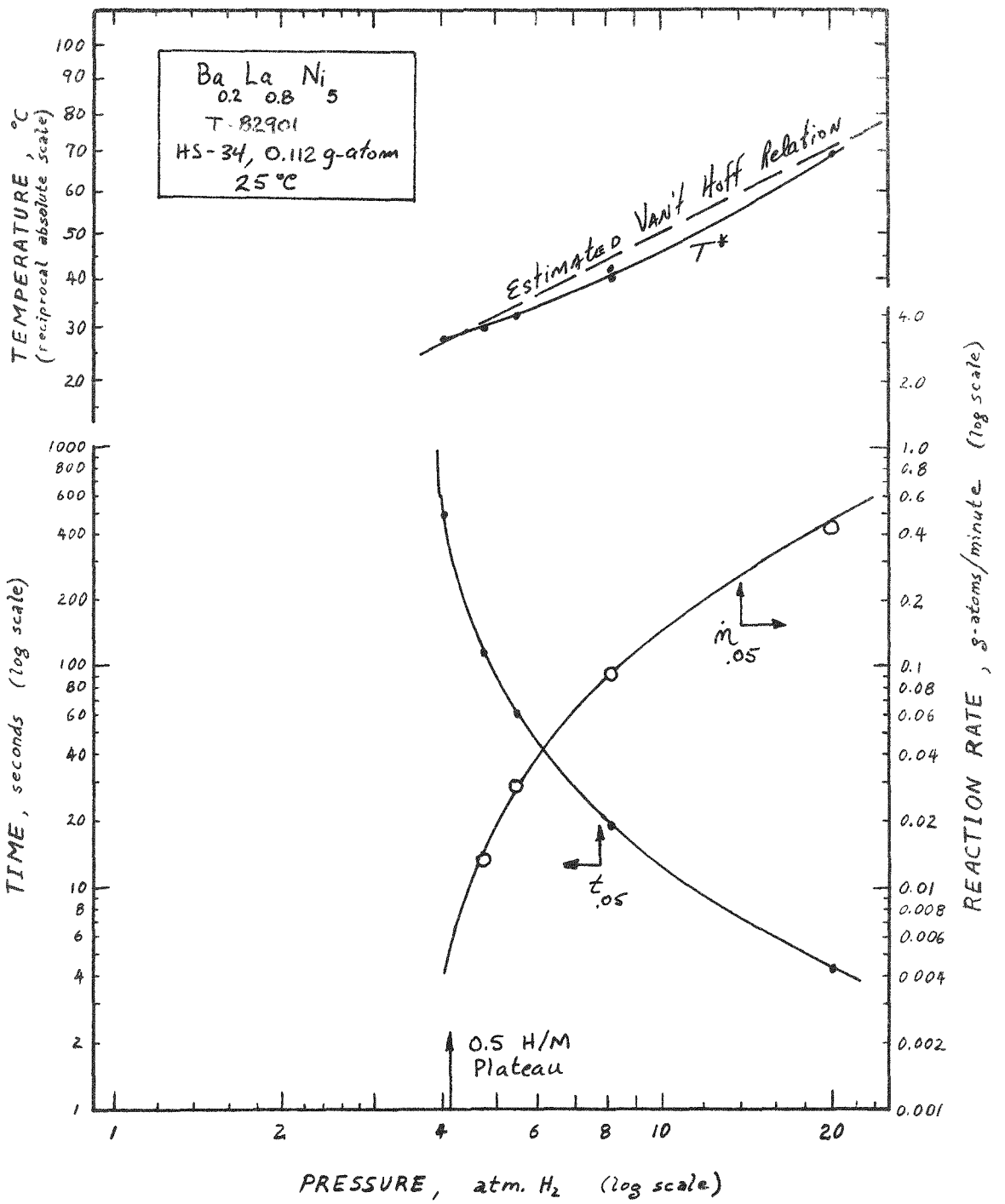

Figure 6-4-5. Summary of absorption kinetic data at 25°C showing the maximum temperature excursion as well as the reaction rate and time at 0.05 g-atoms hydrogen reacted (~0.5H/M).

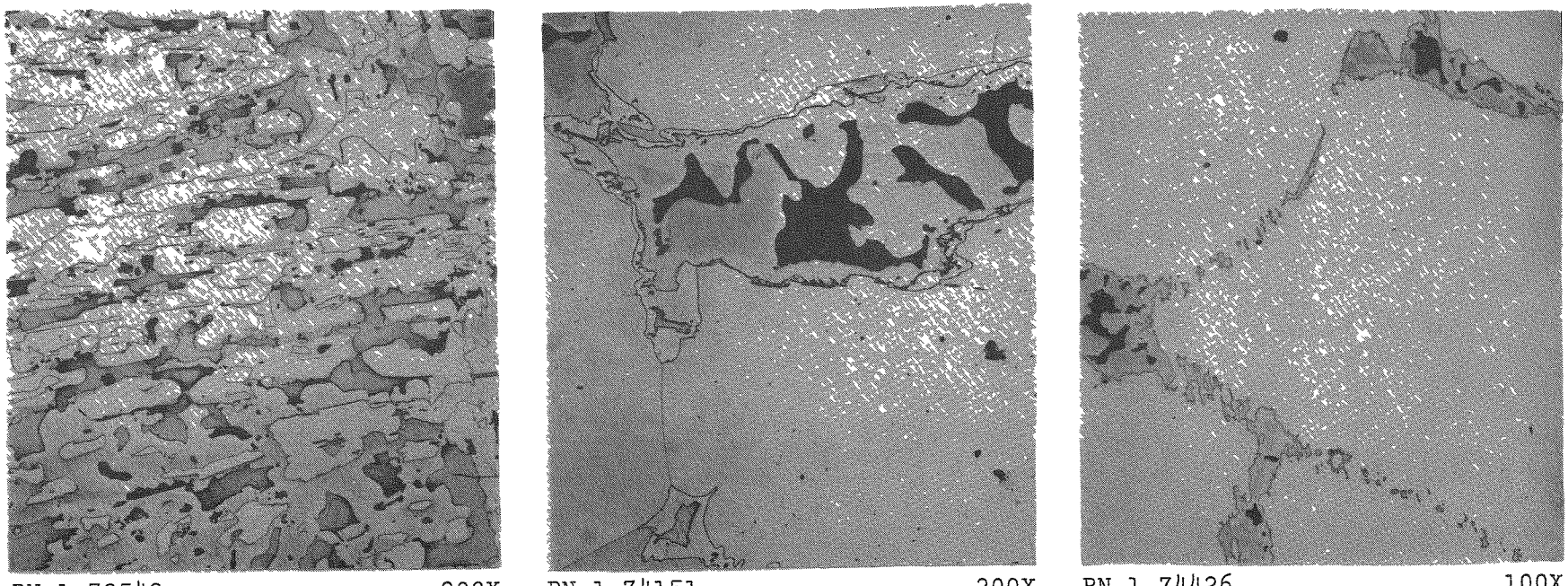

PN 1-73542 200X

(a) As-Cast

PN 1-74151 200X

(b) Annealed 2 weeks at 927°C

PN 1-74426 100X

(c) Annealed 4 weeks at 927°C

Figure 7-1-1. Microstructures of $LaNi_3$. (Note lower magnification of (c).

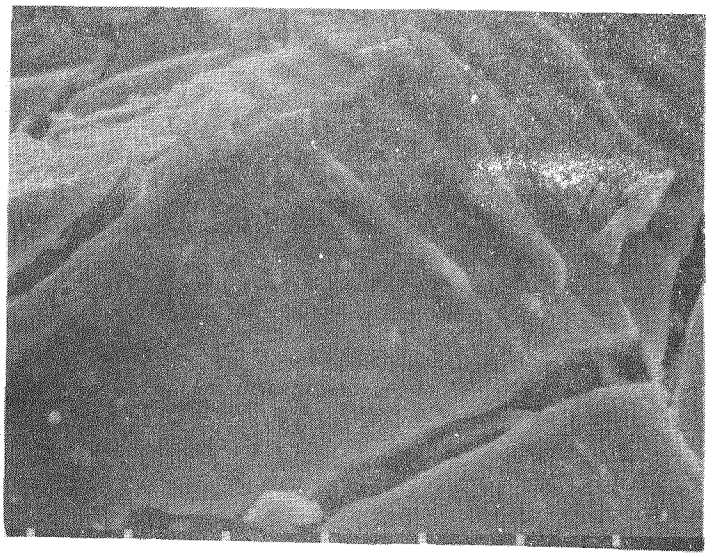

SEM 505-1-2 5000X

(a) $LaNi_5$

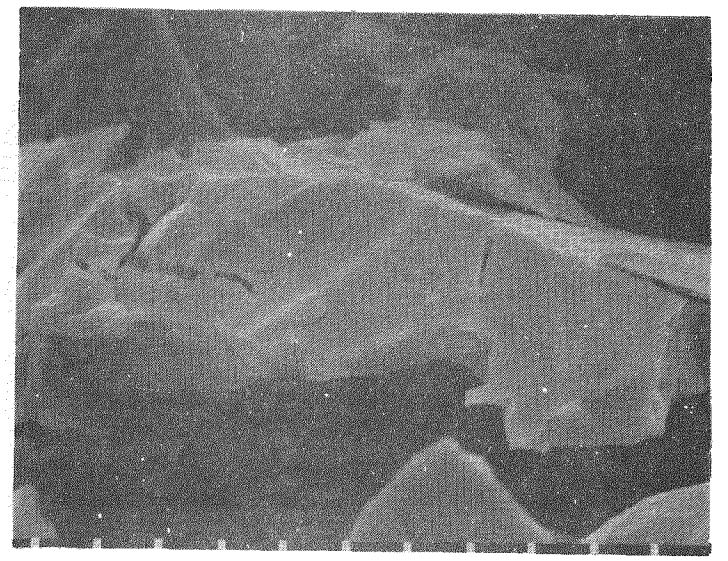

SEM 505-2-4 3000X

(b) $LaNi_{4.9}Al_{0.1}$

Figure 8-1/2-1. Scanning Electron Micrographs of Samples Plated With Pd by Electroless Deposition. (Marker spacings are 3 μm).

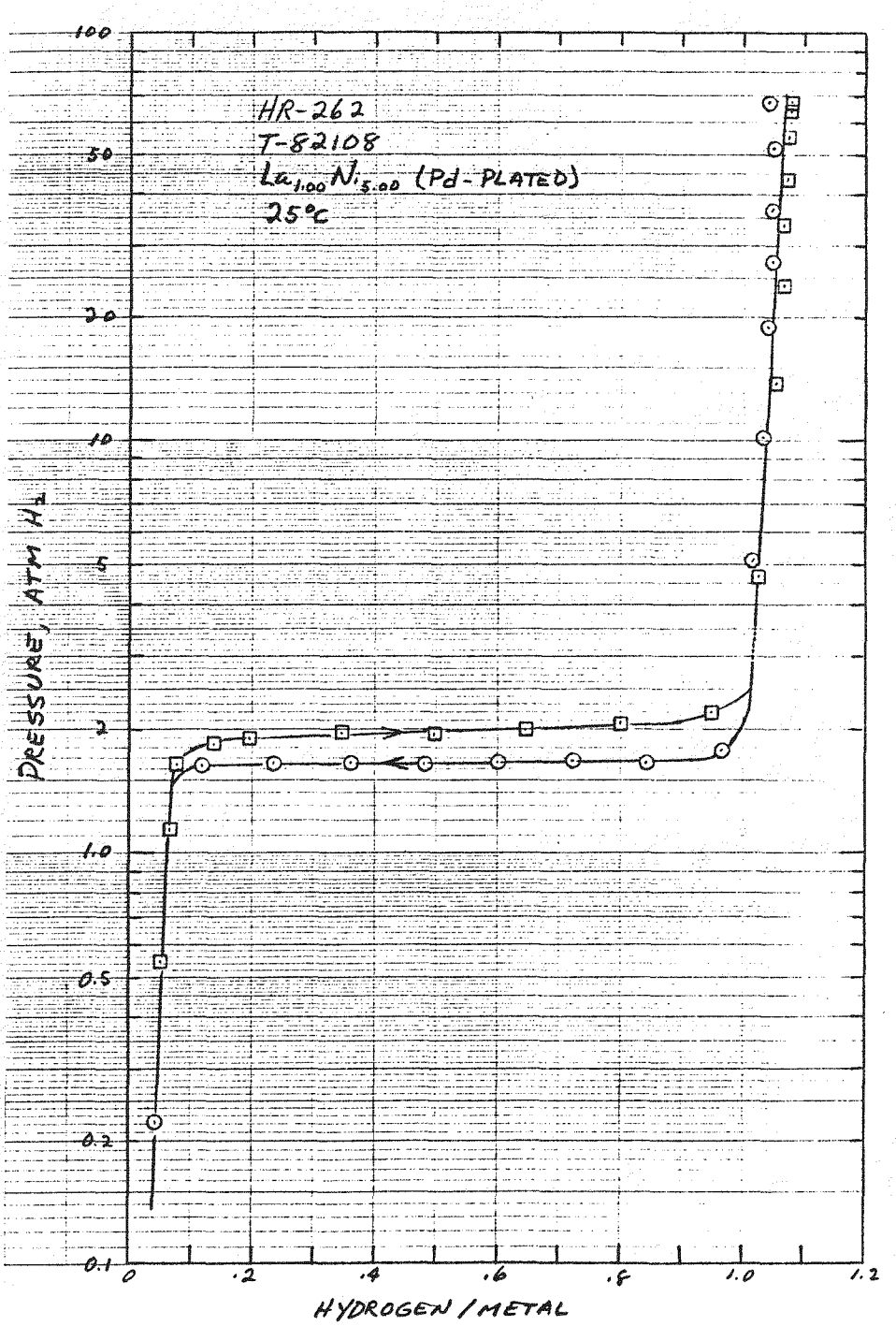

Figure 8-1-2. Static 25°C Isotherms for $LaNi_5$, Electroless Pd-Plated.

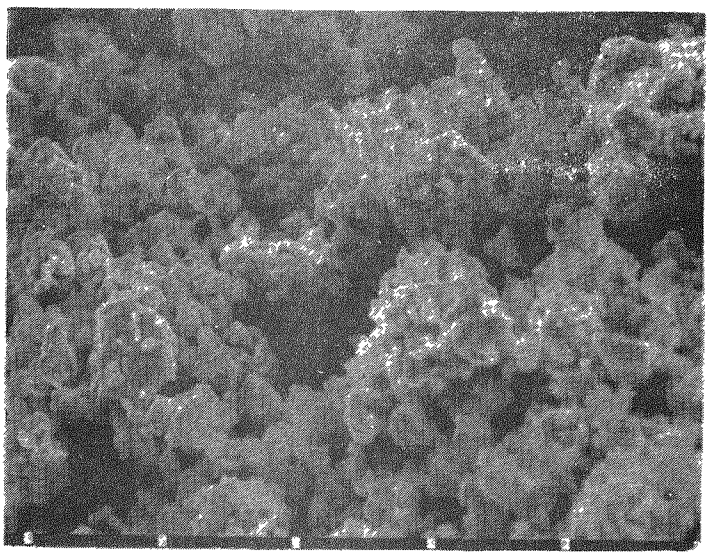

SEM 505-4-8 200X

(a) $LaNi_5$

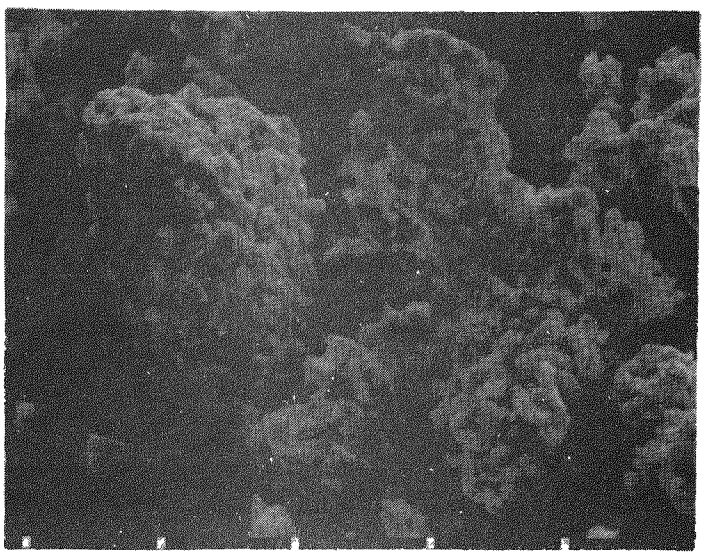

SEM 505-3-6 200X

(b) $LaNi_{4.9}Al_{0.1}$

Figure 8-1/2-3. Scanning Electron Micrographs of Samples Mechanically Alloyed with Pd. (Marker spacings are 10 μm).

APPENDIX A

SYSTEM THERMAL EFFECTS

Thermal characteristics of the test system have been found to significantly affect the kinetic test response of most of the alloys tested in this program. It is appropriate, therefore, to consider somewhat further several characteristics of the test system: temperature measurement, reactor thermal index, and sample conductivity. These comments are offered to provide additional perspective for the test results and hopefully, extend generality of the test results by improving the basis for their comparison to other systems.

The test sample consisted of powder tightly packed in a thin disc configuration in a high conductivity holder reactor. This reactor was designed to maximize heat transfer and to provide straightforward thermal modeling. Instantaneous reaction temperature was measured with an ultra fast response thermocouple (time factor = 0.3 seconds) located in the sample powder bed. Both the thermocouple and reactor are described further in the report (pages 5 and 6, and Figure 2). Thermal response characteristics of the system were evaluated using $LaNi_5$, which of all alloys tested, exhibited the most rapid intrinsic reaction kinetics.

Temperature Measurement

The adequacy of reaction temperature measurement was judged by both the magnitude and speed of the indicated response temperature. In pressure change kinetic experiments, the magnitude of the indicated temperature change was precisely that predicted by the Van't Hoff relation. This is the maximum possible temperature change and it occurs in less than one second. This response is clearly rapid with respect to most of the 'events' used for data analysis and comparison. Also, it is obviously satisfactory with respect to the 'thermal contribution parameter', R, which is the ratio of indicated to maximum possible temperature change.

Reactor Thermal Index

Thermal indexing of a reactor is accomplished by specification of a specific response parameter for a reaction so rapid that response is controlled by heat transfer of the system. This is suggested as a short range and practical technique to characterize a reactor and its influence on kinetic test results. Indexing of this type is not intended to take the place of detailed mass and heat transfer modeling. Rather it is to provide a semiquantitative basis for comparison and scaling between different test systems. The particular choice of index type depends on the information available and/or the intended application.

Any of numerous test results which are system dependent could be used as a thermal index. One example is represented by the time for 75 percent completion of the reaction ($\sim t_{0.08}$) at a pressure equal to double the plateau pressure and at 25°C. For the reactor used herein, this type of index has a value of 100 seconds. This type of index is useful where accurate temperature measurement is not possible.

Another type of thermal index parameter is the 'steady state limit' for the system: the maximum reaction rate achievable at a constant reaction temperature. (For this purpose, 'constant' is taken to mean less than 1°C change per minute.) Estimating this parameter from the kinetic data in Figures 0-1-5 and 0-1-7 gives a value of about 0.023 H/M/minute. The value can also be estimated from constant reaction rate experiments of the type shown in Figure A-1. These data show that the 0.027 H/M/minute rate is the fastest to occur at a nearly constant temperature. (This is a heat flux of 1.68 cal/sec.).

A third type of system index is the thermal time constant. Values of this parameter can be determined from interrupted kinetic tests or from the thermal decay following experiments of the type shown in Figure A-1. From the latter, the thermal time constant for the test system was estimated to be about 10 seconds.

Powder Thermal Conductivity

Conductivity data for hydriding powders is critical to any consideration of system heat transfer; this includes powder container design as well as analytical modeling of rapid reaction kinetics. Fortunately, conductivity data can be determined from several of the experimental results obtained in the thin-disc reactor used in this program. These results give an average thermal conductivity for activated $LaNi_5$ powder of 0.0057 cal/sec. cm/K (2.38 J/sec/m/K). This value is constant over a range of temperature differences of about ±15°C and was determined for powder packing densities of 3.5 g/cc and greater.

The determination of thermal conductivity assumed that the entire heat flux was through the copper base plate of the reactor; the top side of the powder bed, held in place by the stainless steel porous filter disc was assumed to be non-conductive. The copper reactor section was assumed to be free of thermal gradients and to remain at the temperature of the water in the large circulating bath in which it was immersed. The heat of reaction was taken as 7.6 kcal/mole or 3.8 kcal/g-atom (15.9 KJ/g-atom).

Based on the above assumptions, the thermal conductivity, K, of the powder can be approximated by the relation

$$K = QD/A(T_S - T_r) \propto \dot{n}/\Delta T$$

where Q is the heat flux which is determined from the reaction rate, $\dot{n}$, T_S is the sample temperature, T_r is the reactor temperature, D is the bed depth and A the area of the powder disc bed. This equation is valid when $dT_S/dt = 0$, a requirement which in one case is satisfied under steady state conditions (see previous section). It is also satisfied at the instantaneous temperature peak in pressure change, kinetic experiments.

Calculation of the thermal conductivity can be made from the four constant reaction rate test curves shown in Figure A-1 which satisfy the steady state criteria (curves 52, 54, 55, 57). This gives an average conductivity of 0.0050 cal/sec/cm/K; similar tests in a desorption mode give an average value of 0.0059. Note, however, that these values are based on temperature differences which were less than about 4°C (a direct relation to the steady state limit of the system discussed previously).

On the other hand, data from kinetic tests such as presented in Figure A-2, permit evaluation of the thermal conductivity over a wide range of test conditions. This figure shows the reaction rate at the time of peak temperature difference as a function of the peak temperature difference. Between temperature differences of about -15° and +15°C, the data can be approximated by a linear function having a slope of 0.0085 g-atom/min/°C. This value gives a thermal conductivity of 0.0060 cal/sec/cm/K and is very similar to the values determined from constant reaction rate, steady state tests.

The data in Figure A-2 shows further that the conductivity of the powder bed changes significantly for greater extremes of temperature difference. For rapid absorption, the high slope region above +15°C ΔT corresponds to an effective conductivity of 0.0178 cal/sec/cm/K; for rapid desorption, conductivity can drop to as low as 0.0016 cal/sec/cm/K. Such differences might be expected if the charge fraction varied; different levels of powder volume expansion would then change the powder contact pressure (and area). However, for the results shown, the charge fraction happens to be nearly equal for all data (∿0.4 H/M). More likely, the decreased conductivity for rapid desorption may be due to local loss of particle contact due to gas evolution. The increase in apparent conductivity during rapid absorption may be related to convective heat transfer resulting from the increased gas turbulance at high flow rates.

Powder packing density also appears to have some effect on conductivity during absorption at fast rates (high ΔT's). Figure A-2 includes results of more limited tests for which the packing density was decreased from 4.0 to 3.5 g/cc. The lower density results do not show the pronounced increase in conductivity in the 15 to 25°C, ΔT range that is observed in the higher density samples. Significantly, it is the lower packing density which is probably more representative of practical powder beds which must be designed to avoid container swelling. Therefore, the high conductivity value may not be expected in practice.

Combining the results from the steady state and kinetic tests, it is concluded that a single average value of 0.0057 cal/sec/cm/K (0.0239 J/sec/cm/K) represents the most useful expression of thermal conductivity for $LaNi_5H_{2.5}$ powder in the ±15°C, ΔT range. It should be recognized that both the extent of reaction (hydrogen stoichiometry) and fast reaction rates could affect the conductivity, as could the powder packing density if it differed greatly from 3.5 to 4.0 g/cc.

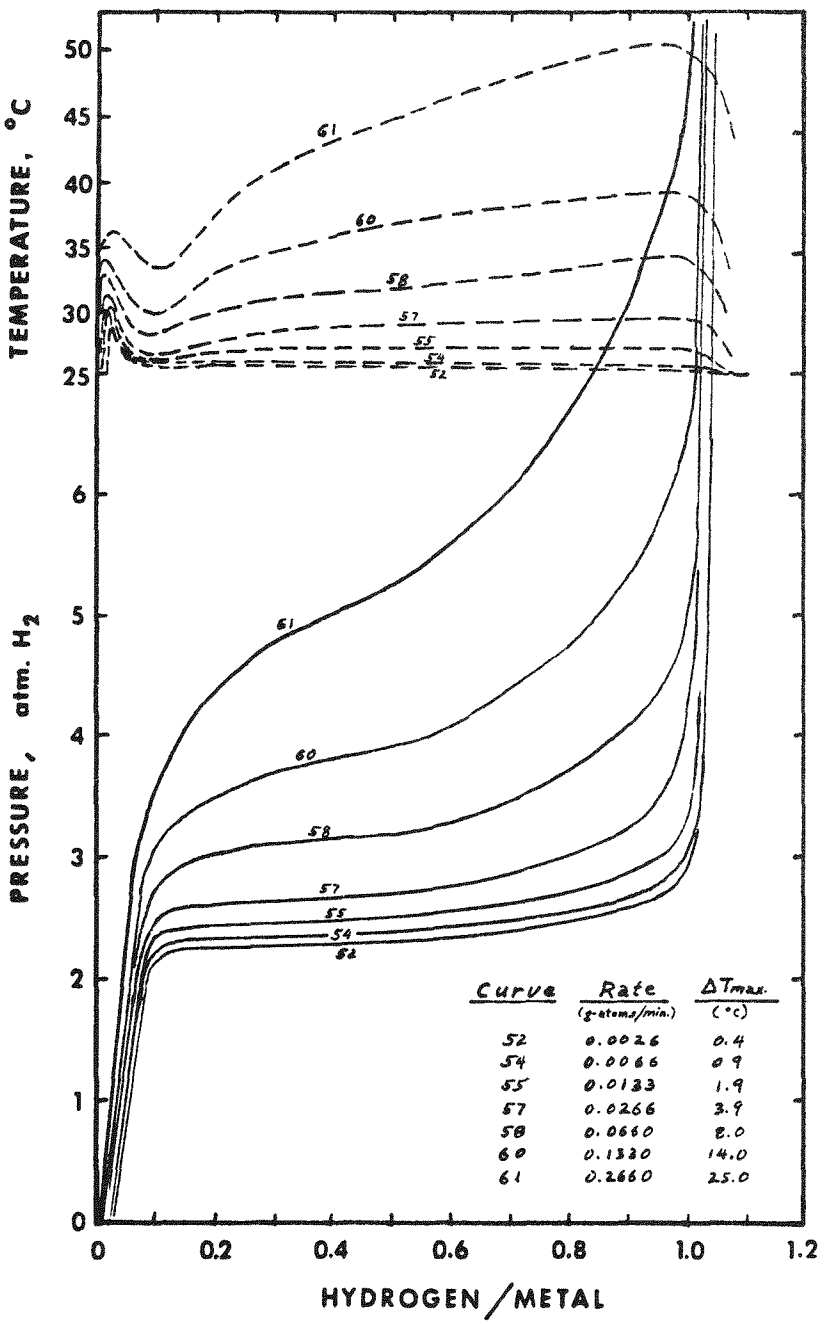

Figure A-1 Dynamic pressure-composition absorption profiles for $LaNi_5$ (T-82108) determined at various gas flow rates. The starting (and bath) temperature was 25.0°C for each test curve; the temperature profiles indicate the sample temperature during the test.

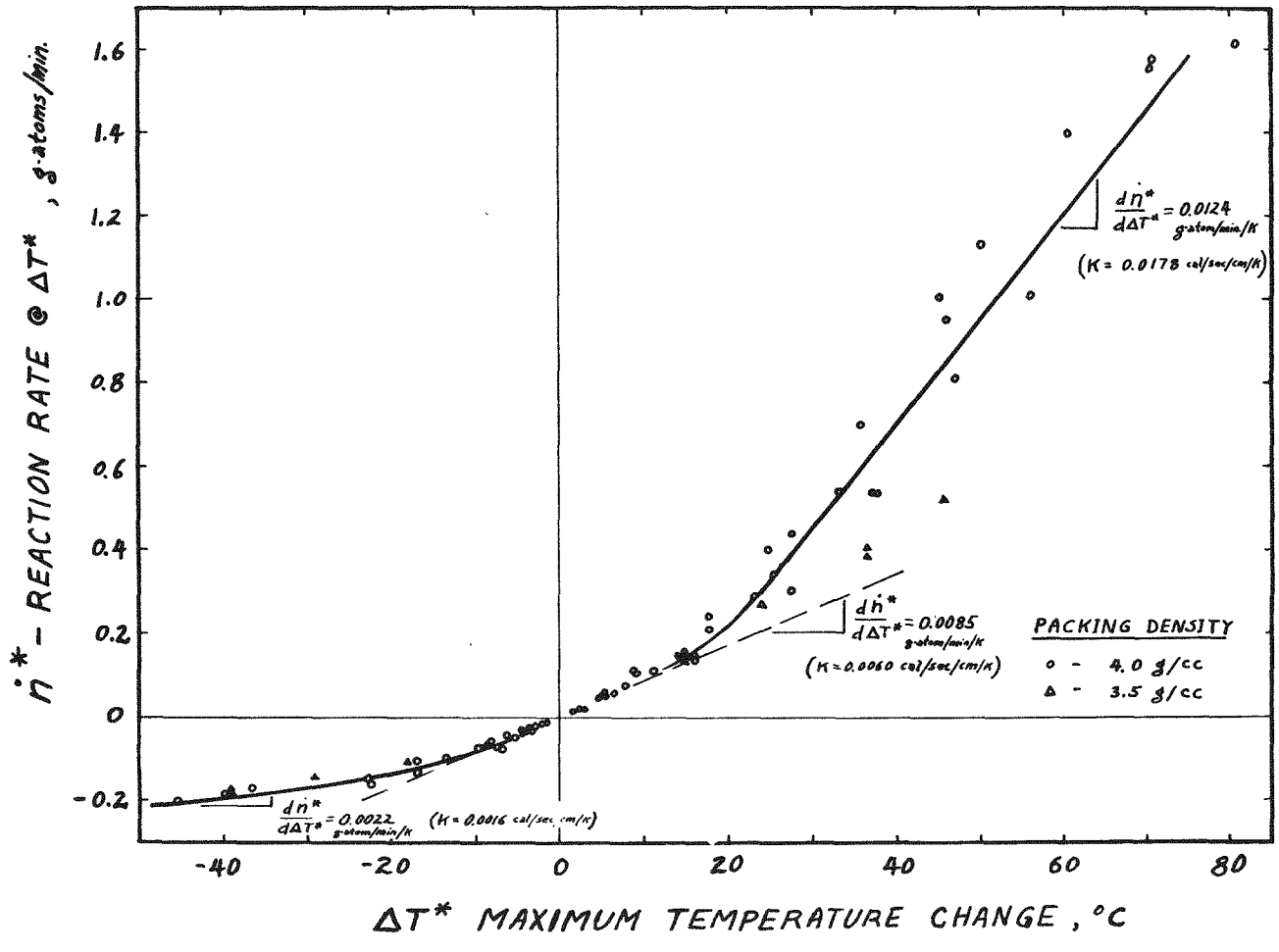

Figure A-2 Kinetic test results at maximum temperature change from which the thermal conductivity, K, of the powder bed was estimated. Data are for $LaNi_5$ (T-82108) at starting temperatures between 15° and 45°C.

Distribution:
Brookhaven National Laboratory
Upton, New York 11973
Attn: F. Salzano
G. Strickland
J. J. Reilly
M. Rosso
R. Wiswall

INCO Research & Development Center
International Nickel Co.
Sterling Forest
Suffern, New York 10901
Attn: L. Huston
G. Sandrock
P. D. Goodell
E. Snape (50)

Energy Research and Generation
Lowell and 57th Street
Oakland, California 04608
Attn: G. M. Benson

Denver Research Institute
Metallurgy and Materials Science Div.
University of Denver
Denver, Colorado 80210
Attn: C. Lundin

Argonne National Laboratory
9700 Cass Avenue
Argonne, Illinois 60439
Attn: D. M. Gruen
I. Sheft

Billings Energy Corporation
P. O. Box 555
Provo, Utah 84601
Attn: R. Billings
B. Campbell
R. Woolley

Department of Energy
Division of Energy Storage Systems
Room 416
600 E. Street, NW
Washington, D.C. 20545
Attn: John Neal
J. H. Swisher
B. Berger
F. Dee Stevenson
Jerome Collins
William Williams

Department of Energy
Division of Solar Technology
600 E. Street
Washington, D.C. 20545
Attn: Jim Rannels
Mike Resner
Joe Weisiger, Jr.

Department of Energy
San Francisco Area Office
1333 Broadway
Wells Fargo Bldg.
Oakland, California 94612
Attn: S. M. O'Brien

Phillips Research Laboratories
Eindhaven, Netherlands
Attn: V. K. P. Biermann
A. R. Miedema

University of New Mexico
Mechanical Engineering Dept.
Albuquerque, New Mexico
Attn: T. Feldman

Iowa State University
Ames Laboratory
Ames, Iowa 50011
Attn: R. Barnes

Allied Chemical Corporation
Box 1021R
Morristown, New Jersey 07960
Attn: G. Libowitz

University of Pittsburgh
Department of Chemistry
Pittsburgh, Pennsylvania 15260
Attn: W. E. Wallace

Institutt für Atomenergi
Kjeller, Norway
Attn: A. F. Andresen

University of Miami
Coral Gables, Florida 33124
Attn: T. Nejat Veziroglu
R. R. Adt, Jr.

Institute of Gas Technology
3424 South Gate Street
IIT Center
Chicago, Illinois 60616
Attn: D. P. Gregory

Israel Institute of Technology
Department of Physics, Technion
Haifa, Israel
Attn: P. S. Rudman

University of California at Los Angeles
School of Engineering and Applied Science
Los Angeles, California
Attn: W. D. VanVorst

Institut fur Festkorperforschung
517 Julich
Federal Republic of Germany
Attn: H. Wenzl

Monsanto Research Corporation
Miamisburg, Ohio
Attn: R. C. Bowman
R. H. DeSando
J. W. Reed
C. H. H. Chong

Los Alamos Scientific Laboratory
Los Alamos, New Mexico 87544
Attn: F. J. Edeskuty

Daimler-Benz AG
Postfach 202
7000 Stuttgart - 60/BRD
Department of Research and Development
Technical Physics/Metal Physics
Federal Republic of Germany
Attn: H. Buchner

2500 J. C. Crawford
2510 D. H. Anderson
2515 E. A. Kjeldgaard
2515 A. A. Heckes (5)
4700 J. H. Scott
4714 R. P. Stromberg
4715 R. H. Braasch
4721 J. V. Otts
4725 R. L. Alvis
4741 S. G. Varnado
4741 T. E. Hinkebein
5151 A. C. Switendick
5800 R. S. Claassen
5810 R. G. Kepler
5812 C. J. Northrup (3)
8310 D. M. Schuster
8313 R. W. Mar
8315 L. A. West
8330 G. W. Anderson
8340 W. Bauer
8425 L. N. Tallerico
8450 R. C. Wayne
8266 E. A. Aas
3141 T. L. Werner (5)
3151 W. L. Garner (3)
for DOE/TIC (unlimited release)